THE TISOL FACILITY,
ON-LINE ISOTOPE SEPARATION AT TRIUMF

by

Marik Dombsky

B.Sc., Simon Fraser University, 1980

M.Sc., Simon Fraser University, 1984

A THESIS SUBMITTED IN PARTIAL FULFILLMENT

OF THE REQUIREMENTS FOR THE DEGREE OF

DOCTOR OF PHILOSOPHY

in the Department

of

Chemistry

SIMON FRASER UNIVERSITY

August, 1990

APPROVAL

Name: Marik Dombsky

Degree: Doctor of Philosophy

Title of Thesis: THE TISOL FACILITY, ON-LINE ISOTOPE SEPARATION AT TRIUMF

Examining Committee:

Chairperson: Dr. P.W. Percival

Dr. J.M. D'Auria, Senior Supervisor

Dr. I.D. Gay

Dr. C.H.W. Jones

Dr. Tom Ruth
Internal Examiner

Dr. Paul Reeder
Pacific Northwest Laboratory
Richland, Washington, USA
External Examiner

Date Approved: Sept. 26, 1990

PARTIAL COPYRIGHT LICENSE

I hereby grant to Simon Fraser University the right to lend my thesis, project or extended essay (the title of which is shown below) to users of the Simon Fraser University Library, and to make partial or single copies only for such users or in response to a request from the library of any other university, or other educational institution, on its own behalf or for one of its users. I further agree that permission for multiple copying of this work for scholarly purposes may be granted by me or the Dean of Graduate Studies. It is understood that copying or publication of this work for financial gain shall not be allowed without my written permission.

Title of Thesis/Project/Extended Essay

The TISOL Facility, On-Line Isotope Separation at TRIUMF

Author: _____
(signature)

MARK DOMBSKY
(name)

Oct 29/90
(date)

ABSTRACT

An On-Line Isotope Separator (ISOL) has been designed and successfully installed as a secondary beamline at TRIUMF. Using medium energy protons on thick targets for isotope production. The separator system was constructed as a test facility (known by the acronym TISOL) in order to establish the feasibility of building a larger high yield system coupled to a post accelerator for the production of accelerated radioactive beams. The separator is based on a vertically oriented quadrupole-quadru-pole-dipole magnetic mass analysing system with a mean dipole radius of 1.25 meters. Using an initial accelerating potential, variable up to +20 kV, singly charged, mass separated, radioactive heavy ion beams have been transported to a first focus 4.1 meters above the target bombardment station after a 6.7 meter flight path. A mass resolution of $\partial M/M \sim 1/2500$ has been measured for the system. In order to further transport the ion beams to an area of low background activity, an additional electrostatic beamline consisting of two electro-static quadrupole triplets and a 90° electrostatic bender was designed, constructed and installed.

Beams of over 120 separate unstable nuclides, with half-lives as short as 20 msec have been observed as positively

charged ions. A high temperature surface ionization ion source coupled to a resistance heated thick target was designed and used to measure the yields of radioactive species produced by 500 MeV proton spallation-/fragmentation reactions and by proton induced fission reactions on a variety of thick (grams/cm^2) refractory targets. Individual nuclides were identified by means of gamma and alpha spectroscopy of the collected beams. Estimates of the mean release times and overall production efficiencies for the observed elements were made from comparison of experimental yields with calculated predictions based on the semiempirical model of Silberberg & Tsao. Estimated mean release times ranged from 1.4 ± 0.2 sec to 1370 ± 950 sec; estimated overall production efficiencies approached a maximum of about 14%.

The construction, testing and optimization of the entire TISOL beamline system is described. The design and assembly of component systems such as the secondary beamline vacuum tank elements, proton irradiation facilities, pumps, valves and diagnostics are discussed. Ion beam generation as well as magnetic and electrostatic beam transport, beam diagnostics and the remote control of the separator by means of a resident interactive computer control system are also described.

for Carol, Katrina

and Nicholas

...the pumps don't work

cause the vandals

took the handles

— Bob Dylan

ACKNOWLEDGEMENTS

I would like to thank all those who took part in constructing the TISOL facility. Principally, but not exclusively, J.Vincent, L. Buchmann, H.Sprenger, D.Jones, H.Biegenzien, D.Harrison, R.Keitel and P.Machule. The TISOL facility would never have been built without the unceasing efforts of my supervisor J.M.D'Auria.

TABLE OF CONTENTS

LIST OF TABLES

LIST OF FIGURES

INTRODUCTION:

On-Line Isotope Separation:

Systematic studies of nuclear properties with the variation in proton (Z) and neutron (N) numbers have proved to be an effective means to a better understanding of nuclear structure and stability. In such studies, it has always been necessary to isolate the particular nuclide under consideration from other radioactive species in order to effectively establish the true properties of only that nuclide under study. In experiments involving long-lived species, purification techniques that depend on chemical or chromatographic separations may be employed with little decay loss of the desired product. However, with studies of nuclides at the extreme edges of stability, rapid separation techniques must be employed to overcome decay losses resulting from the shorter half-lives of the less stable species. Whether a nuclide under consideration is produced by decay or by a nuclear reaction, its rate of production may be so low, and its rate of decay may be so fast as to prevent its isolation by conventional time-consuming "off-line" methods. In such cases, the use of continuous rapid "on-line" separation techniques may allow the observation of the desired product.

One such rapid technique is on-line isotope separation, also more properly called on-line mass separation. The acronym ISOL (for Isotope Separation On-Line) is often used

in reference to both the general technique and to describe the actual separator. Generally, the technique consists of producing a desired nuclide, ionizing the nuclide, separating it from other nuclides by means of electromagnetic mass analysis and collecting the desired product for further study. A separator essentially consists of a target (bombarded by some projectile) coupled to an ion source, some accelerating potential and a mass analysing magnet.

The first to use such a system were Kofoed-Hansen & Nielsen, who studied noble gas nuclides produced from a neutron irradiated uranium oxide target (Ko51a). Their studies, however, were soon abandoned and ISOL methods were not used again until 1965 when Klapisch & Bernas used on-line mass analysis (Kl65, Kl69). Since then, many separators have been constructed at accelarator and reactor facilities around the world. The status of ISOL facilities has been reviewed by Hansen (Ha79) and Ravn (Ra79, Ra89) as well as in the proceedings of the International Conferences on Electromagnetic Isotope Separators [EMIS] (Em80, Em87).

Elements of ISOLS:

The advantages of on-line isotope separators over other isolation techniques are high yield, rapid separation, mass selectivity and possible chemical selectivity. The mass selectivity is achieved by means of the analysing magnet while the other advantages are realized through the

judicious combination of target, projectile and ion source.

The choice of projectile, bombarding energy and target define the reaction cross-section and govern the feasibility of producing a desired nuclide. Three classes of projectile are currently used with ISOL systems: neutrons, heavy ions, and protons.

Reactor based ISOL systems rely on neutron induced fission to produce the desired nuclides. The advantages of such systems include high yields of some neutron-rich species; thermal neutron cross-sections can be of the order of $\geq$ 10 barns. The range of thermal neutrons allows target thicknesses of up to ten grams of uranium and product yields up to $\sim 10^8$ nuclei/sec.(Ra89) The main disadvantage of neutron based systems is that the products are limited to the (mainly neutron-rich) species produced by fission.

Heavy ion based ISOL systems offer an advantage in that any desired product, in theory, should be attainable by the proper choice of a projectile/target combination. Both proton-rich and neutron-rich products can be obtained by use of proton-rich or neutron-rich projectile/target combinations. At bombardment energies of up to ~ 10 MeV/amu, the fusion-evaporation reaction mechanism (HI, xn) can be a very selective way to produce enhanced yields of desired products. At higher bombardment energies, spallation and fragmentation reactions give rise to a greater distribution of products similar to that observed in

proton bombardments. While heavy ion projectiles offer the most favourable production mechanisms, the short range of heavy ions restricts their use to thin targets on the order of 0.1 g/cm^2. This results in maximum production rates of ~ 10^6 nuclei/sec.(Ra89)

Medium energy proton based ISOL facilities rely on a combination of spallation, fragmentation and proton-induced fission reactions for production of both proton-rich and neutron-rich isotopes. The long range of protons allows for target thicknesses on the order of $\geq$ 10 g/cm^2. When such thick targets are used in conjunction with intense (1-10μA) proton beams, production yields of ~ 10^{11} nuclei/sec/μA are obtainable.

Structure & Decay Studies with ISOLs:

Over the last twenty years, ISOL facilities have been instrumental in furthering our understanding of nuclear matter. For example, the ability to systematically measure the atomic masses of a variety of unstable nuclei has provided new insights into nuclear shell structure. On-line mass measurements of long chains of Rb and Cs nuclides (Ep79) and very neutron-rich Na nuclides (Th75) provide evidence of shell closures at N = 52 and N = 82 correlated to the two-neutron separation energies of the Rb and Cs studied. The systematics of the two-neutron separation energies also indicated regions of nuclear deformation around N = 60 and

N = 90 as well as an unexpected onset of strong deformation at N = 20 in the Na nuclide chain.

Furthermore, the ability of ISOLs to rapidly separate significant quantities of nuclei at the edges of nuclear stability has made possible the investigation of "exotic" modes of nuclear decay that are not observed in nuclei close to stability. When the energy available for β-decay exceeds the binding energy of one or more nucleons (or composite light nuclei), the process of β-delayed particle emission be-comes possible. Studies of neutron-rich nuclei conducted at both proton-based and neutron-based ISOL facilities have yielded information on an extensive number of β-delayed neutron emitters.(Re84,Ha85b) Beta-delayed 2-neutron emission has also been observed for ^{11}Li(Az79), $^{30-33}$Na (De80), ^{98}Rb (Re81) and ^{100}Rb (Jo81). Other delayed 2-neutron emitters among Ga, As, Se, Br, Rb, Sb, I and Cs nuclides can be predicted from mass formula calculations. Beta-delayed 3-neutron emission has been observed for ^{11}Li (Az80); the $^{31-35}$Na nuclides as well as potassiums heavier than ^{55}K are expected to be delayed 3-neutron precursors. Delayed composite particle emission in the form of beta-delayed triton decay has been observed for ^{11}Li (La84) and can be predicted for ^{8}He, ^{15,17}B, ^{17,19,20}C, ^{27}F, ^{29}Ne and ^{35}Na from decay energy considerations. Beta delayed alpha emission is known for ^{11}Li, ^{12}B, ^{16}N and ^{18}N.

On the proton-rich side of stability, isotope separated

beam studies have identified numerous cases of beta-delayed proton emission as well as some cases of delayed alpha emission. Two cases of beta-delayed two-proton emission in ^{22}Al and ^{26}P have been observed (Ca82, Ca83). Perhaps the most significant contribution of separated beam research to nuclear decay studies has been the discovery of ground state proton emission decay modes for ^{151}Lu (Ho82), ^{147}Tm (Kl82) and ^{109}I and ^{113}Cs (Fa83, Fa84).

While ISOL beams were not used in the initial discovery of cluster radioactivity (Ro84), subsequent experiments at the ISOLDE facility at CERN confirmed the ^{14}C emission decay mode of ^{223}Ra with a greatly improved statistical uncertianty. Separated ^{223}Ra produced from protons on a thorium target showed over five times the ^{14}C activity that a ^{227}Ac source displayed in the initial experiment (Pr85). At the same time, the ^{14}C decay mode was also observed for ^{222}Ra and ^{224}Ra produced from the same target.

Accelerated Radioactive Beams:

Until recently, most of the information on nuclear structure and properties has been obtained by studying stable nuclei, long-lived radioactive nuclei or the reaction products of stable projectiles and targets. Stable nuclides number less than 300, while the known unstable species number about 2000; current theories predict on the order of 8000 bound species in total.(Ta89) While new techniques

have pushed the limits of the known nuclides farther from stability, the proton and neutron drip-lines have been reached only in the cases of the lightest species. Clearly, the possibility of using radioactive nuclides as either projectiles or targets in nuclear reactions greatly enhances the options available to experimenters.

Isotope separation has been applied in pioneering both radioactive target and radioactive beam experiments. For many years, radioactive targets have been used to synthesize new trans-uranium elements by the process of multiple neutron capture/decay in high flux reactors (Se68). The heaviest nuclide ever produced by this method is ^{257}Fm in quantities of about 10^9 atoms (Ni84). The first experiments using ISOL genererated targets were the studies of the $^{84}Rb(n,p)^{84}Kr$ (An76), $^{76}Br(n,p)^{76}Se$ (An78) and the $^{37}Ar(n,p)$ and $^{37}Ar(n,\alpha)$ reactions (As78). Recently, secondary radioactive beams of 790 MeV/amu He, Li and Be produced at the Lawrence Berkeley Laboratory Bevalac were used on stable targets of He, Be, C and Al to measure the interaction nuclear radii for all the known helium and lithium isotopes as well for ^{7}Be and ^{9}Be (Ta85a, b).

While many different types of experiments using accelerated radioactive beams have been proposed by both nuclear and solid-state scientists, the most emphatic arguments for building accelerated radioactive beam facilities have come from the nuclear astrophysics community (Ac85). The aim of

nuclear astrophysics is to understand the processes involved in stellar evolution both qualitatively and quantitatively. The elemental nucleosynthesis by which stars "burn" is postulated as a series of (p,γ) and (α,γ) capture reactions involving both stable and unstable nuclei interspersed with β-decays. The capture/decay processes can be cyclical and various cycles based on the elements involved have been suggested. For example, the cold-CNO cycle attempts to describe burning in stars of < 100 solar masses, the hot-CNO cycle is postulated for more massive stars and the NeNa- and MgAl-cycles for novae and supernovae. Since the overall balance of such cycles depends on the competition between capture and decay events, a detailed knowledge of both decay constants and capture cross sections is necessary. When the nuclei involved are stable or long lived it is possible to measure the (p,γ) and (α,γ) cross-sections by standard methods. However, when the nuclei have half-lives on the order of minutes or seconds, even radioactive target techniques are not applicable. Many of the cross-sections crucial to the balance of various cycles involve short-lived species: 10 min $^{13}N(p,\gamma)^{14}O$, 70.6 sec $^{14}O(\alpha,\gamma)^{18}Ne$, 6.34 sec $^{26m}Al(p,\gamma)^{27}Si$. The only means of measuring cross-sections on such short-lived species would be by the use of radioactive beams.

Since, in the center of mass frame of reference, it makes no difference which of the two reacting species is target

and which projectile, a reaction analogous to $^{13}N(p,\gamma)^{14}O$ can be produced by an ^{13}N beam incident on a hydrogen target (ie: $^{1}H(^{13}N,\gamma)^{14}O$). Similarly, reactions analogous to (α,γ) can be produced by radioactive beams on helium targets. Whether a radioactive target or a radioactive beam experiment is more advantageous depends on a combination of the production rate of the radioactive species and it's half-life. Some estimates based on production rates from high yield isotope separators suggest that radioactive beams are the best choice for species with half-life < 1 hour and production rates > 10^8 - 10^9 per second (Ha85b). Since the reactions of interest for astrophysical purposes take place at low energies, typical bombardment energies for the radioactive beams would be on the order of several hundred keV/amu to 5 MeV/amu.

The Proposed TRIUMF Accelerated Radioactive Beams Facility:

In 1984, a Canadian ISOL study group was established under the coordination of Professors J.K.P. Lee of McGill University and J.M. D'Auria of Simon Fraser University. That same year, an international workshop on the possibility of building an ISOL facility at TRIUMF was held at Mont Gabriel, Quebec. Since considerable interest was shown in establishing such a facility, a preliminary proposal was presented to the TRIUMF Long Range Planning Committee. That proposal was positively received and a more extensive study,

aimed at identifying technical considerations and estimating costs was jointly funded by TRIUMF and NSERC. The result of that study was a detailed proposal for the construction of a high intensity isotope separator coupled to a linear post accelerator (given the acronym ISAC, for Isotope Separator /Accelerator) that would produce intense beams of radioactive nuclides (Tr85); such a facility would be unique in the world. As well, experimental proposals representing collaborations between some 50 scientists were submitted to the TRIUMF Experimental Evaluation Committee. Since some of these experiments concerned the development of specific technical aspects of ISAC, such as target/ion source studies and post accelerator designs, it was decided that a logical and essential prelude to the construction of a major facility would be to build a smaller test ISOL (TISOL). Such an ISOL would be used to develop targets and ion sources, measure the yields of radioactive beams produced and generally develop on-site expertise in ISOL design and operation.

Originally, the technical aspects of the TISOL project were adressed by a collaboration of scientists from TRIUMF and the Foster Radiation Laboratory at McGill University. Since early 1988, the McGill group has not been an active participant, though it still supports the project in principle.

This thesis describes, in part, some of the aspects of

the construction, development and performance of the TISOL system between 1986 (when design and installation began) and the summer of 1989 (when the surface ionization source on-line tests were finished). Similar to the construction of any other major facility, TISOL has been a collaboration of many individuals. The author has had a major part in all aspects of TISOL development described; particularly TISOL operation, performance testing and the yield measurements. Where certain aspects have principally been the responsibility of others, credit is acknowledged in the thesis.

In the interests of brevity, not all details are included nor all developements described. Only the development and performance of one type of ion source (surface ionization) is described here; the on-line and off-line testing of the plasma source is completely omitted as are the changes to the separator involved in installing the electron cyclotron resonance (ECR) source. The performance of the ECR and isotope yields measured with this source from the fall of 1989 to the present time are also omitted.

A BRIEF CHRONOLOGY OF IMPORTANT EVENTS AT THE TISOL FACILITY:

September 1985: Design of TISOL begins.

April 1986: A surface ionization source in an off-line test stand produces a 20 keV stable Cs^+ beam.

October 1986: The TISOL beam transport system is assembled off-line and beams of $^{85}Rb^{+}$ and $^{87}Rb^{+}$ are extracted and transported through the QQD optics to a focus with an estimated resolution (M/∂M) of about 700.

January 1987: A plasma ionization source is tested and a beam of Ar^{+} is produced.

May 1987: TISOL is installed on-line in beam line 4A.

June 1987: The first proton bombardment of a Sc_2O_3/C target coupled to a surface ionization source in the on-line TISOL system. First radioactive beams extracted (^{38}K, ^{21}Na)

December 1987: A mixed Mo/Ti foil target coupled with the plasma ion source produces beams of Ne, Na & K. A Ta foil target reacts with a BN insulator and destroys the ion source.

June 1988: An electrostatic beam line is added to the TISOL system to move the final beam focus to an area of lower background radiation.

July-Aug 1988: First quantitative measurements of Na, Al & K production yields from a Ti foil target/surface source.

September 1988: A re-designed surface source is used with a Ta target; ^{86}Rb is observed as well as Na & K isotopes.

Dec 1988 - May 1989: Routine yield measurements with a variety of targets using the surface source.

June 1989: The ECR ion source is installed on-line.

July 1989: Ne, Cl & Ar beams are produced from a Ti foil target in the first use of an ECR source coupled to an ISOL.

THE TISOL FACILITY:

TRIUMF Layout:

The TRIUMF meson factory is a national facility for intermediate energy nuclear science situated on the campus of the University of British Columbia and operated by the University of Alberta, Simon Fraser University, the University of Victoria and UBC, under a contribution from the National Research Council of Canada. The heart of the facility is a 6-sector isochronous cyclotron accelerating H^- ions. Extraction of protons is achieved by charge exchange stripping of the hydride ions on a thin foil. This technique allows the simultaneous extraction of multiple proton beams with energies variable from 180 to 520 MeV. Currently, three proton beams are available from the cyclotron. Beamline 1A is a high intensity (120 μA) line used for meson production. Beamline 2C is internal to the cyclotron vault and provides 65-110 MeV protons with 10 μA intensities for radiopharmaceutical isotope production. Beamline 4 transports protons of 180-520 MeV into one of two experimental experimental areas: either beamline 4B, a low intensity ($\leq$ 1 μA) area, or beamline 4A, a medium intensity ($\leq$ 10 μA) area. The TRIUMF site is shown in Figure 1.

The "front end" of TISOL is the irradiation station at the end of beamline 4A, just upstream of the beamline current monitor and the final beam dump. By positioning the

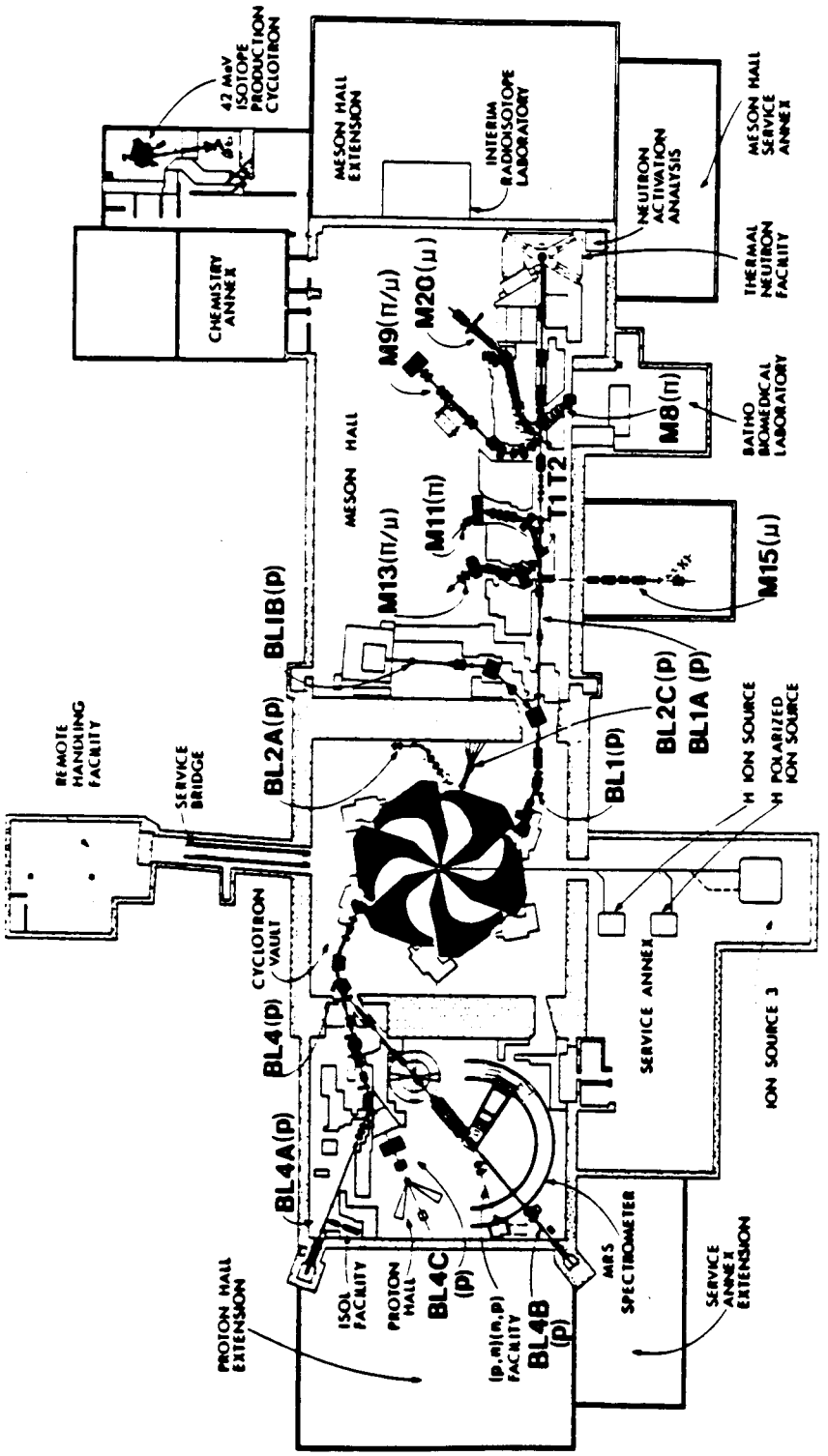

Figure 1: TRIUMF Layout

target/ion source as far downstream as possible, thick targets (on the order of ~ 10 g/cm^2) can be irradiated while minimizing beam spill. Target/ion source combinations are irradiated in a vacuum chamber and a positively charged beam of isotopes is extracted horizontally into a secondary beamline perpendicular to the proton beam. After a flight path of 2.3 m, the beam enters a vertically positioned, mass selecting dipole magnet with a 1.25 m mean optical radius. The isotope beam exits the dipole vertically and after a flight of 2.9 m, comes to a primary focus above the shielding blocks, 4.15 m above the proton beam axis. A further section of beamline containing electostatic beam transport elements guides the beam higher, bends the beam horizontally and brings it to a second focus at the final collection point. The separator system is shown in Figure 2.

The TISOL Containment Room:

During initial installation it was decided to isolate the TISOL area from the rest of beamline 4A to contain any possible release of radioactive contaminants. Since planned irradiations required thick targets of powdered compounds and fissionable material as well as simple metal foils, there was deemed to be a risk of contamination from the "loose" targets during transfer to and from the target vacuum chamber. There was also the possibility that some (or all) components of a target/ion source could melt or

1 TIS Box
2 Faraday Trunk
3 Faraday Cup
4 Wire Scanner
5 Magnetic Quadrupoles
6 Analyzing Magnet
7 Analyzing Slits
8 Electrical Quadrupoles
9 Electrical Bender
10 Electrical Steering

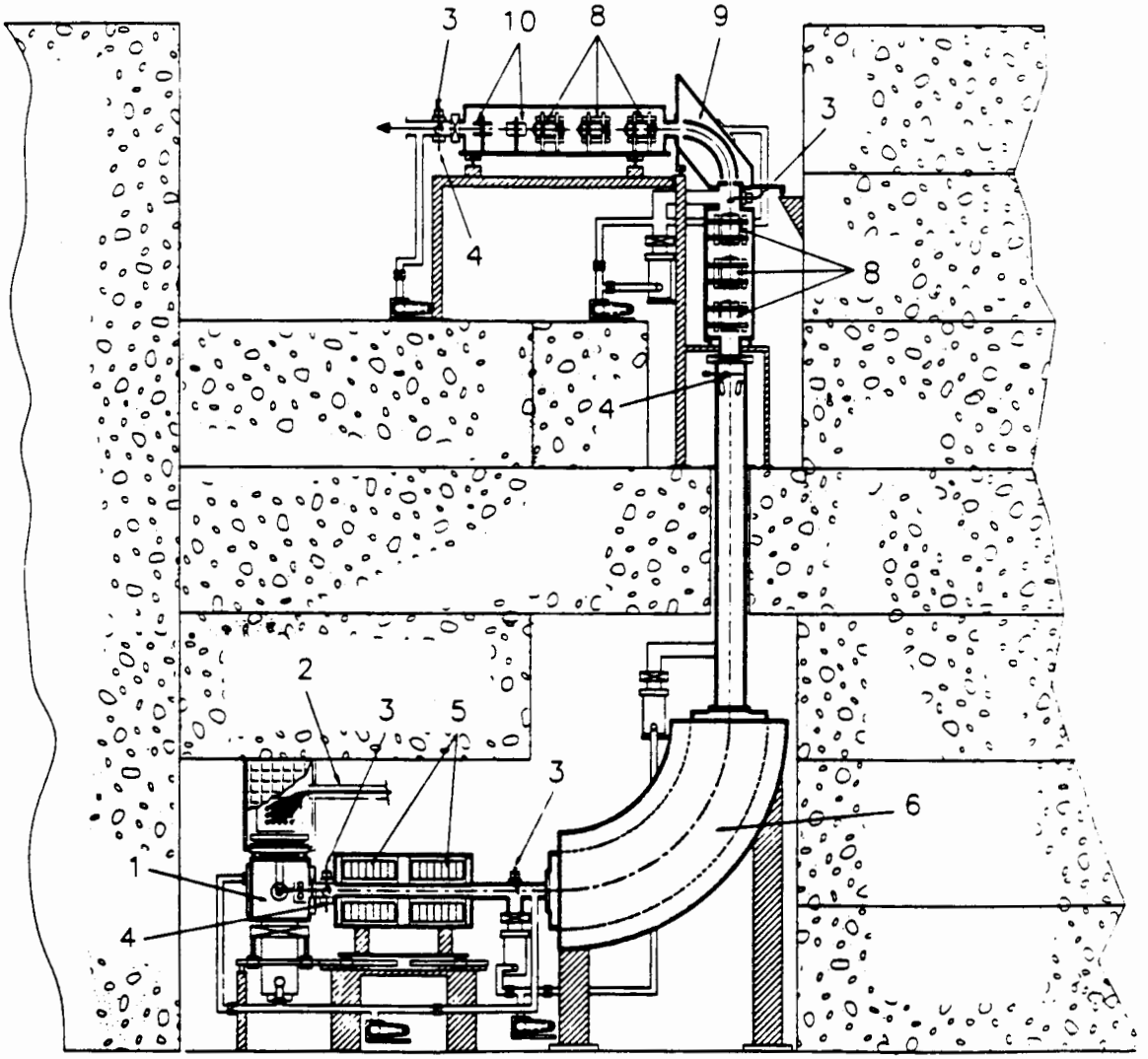

Figure 2: The TISOL isotope separator system.

vaporize and contaminate both the inside of the beampipe and the surrounding area once the target chamber was opened.

Isolation of TISOL was achieved by building a containment room around the back area of beamline 4A. The ceiling and walls of the area (consisting of stacked concrete shielding blocks) were treated by sealing all cracks with silicone caulk and painting with a non-porous paint; the concrete floor was similarly painted. A sealed false wall (using steel framing and aluminum sheet) was constructed on one side of the room and all electrical, gas and water services for the area were routed behind this wall. A similar wall closes off the room from the rest of the beamline area. Access is through a steel door whose lock is part of the beamline safety interlock system; once locked, key access requires intervention of the TRIUMF cyclotron operations staff. The TISOL containment room layout is shown in Figure 3.

When running, the TISOL containment room is kept under negative pressure with respect to the rest of the beamline. Air is drawn from the room through a vent stack attached to a dedicated, high volume fan situated on the roof of the TRIUMF building. The vent line contains a high efficiency "absolute" filter and the exhaust is continuously sampled by the TRIUMF safety group for radioactive contamination. All cooling water for the magnets, vacuum pumps and targets in the area is part of a low conductivity, closed-loop system

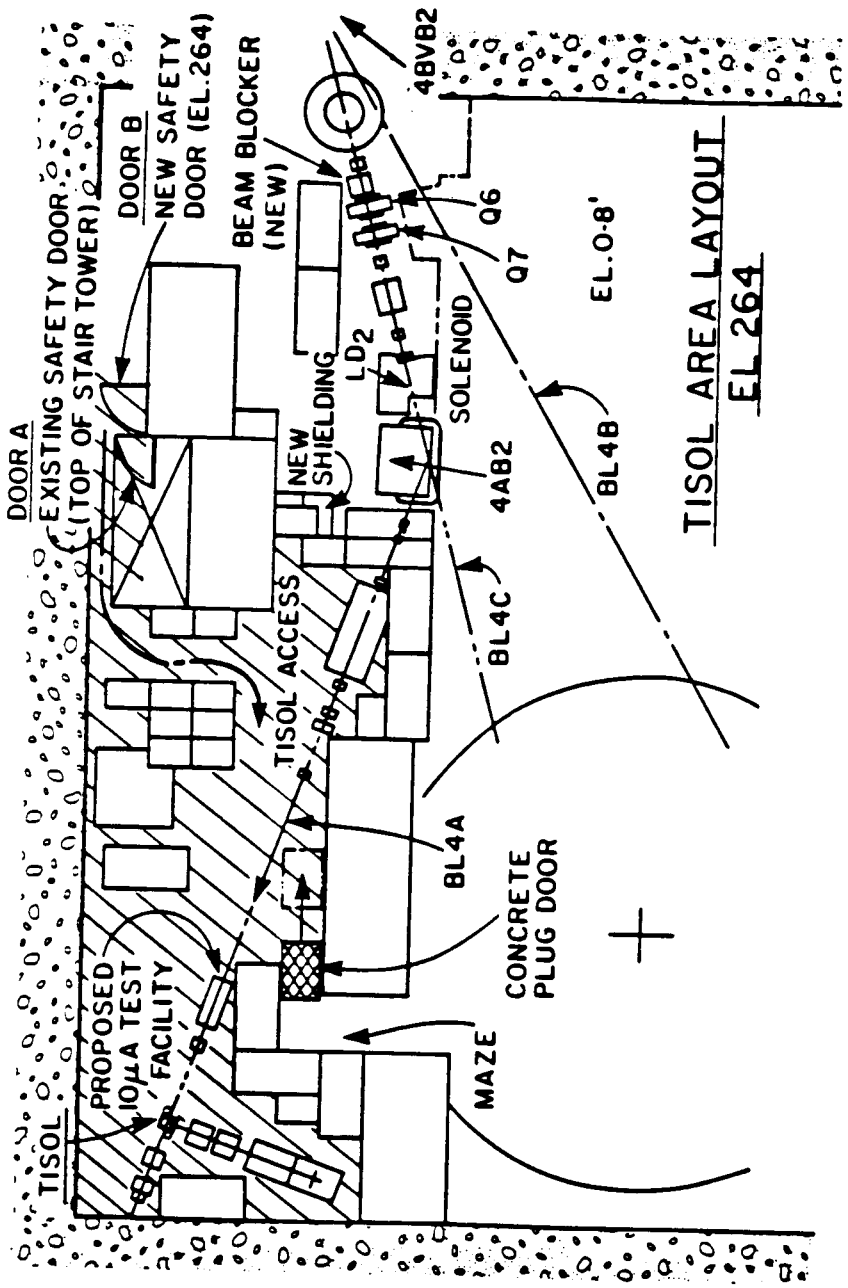

Figure 3: The TISOL containment room on TRIUMF beamline 4A. The sealed area is denoted by diagonal shading.

serving only radioactive areas.

Personnel entering the containment room must wear rubber overshoes and gloves. Anyone working on any equipment in the room is further required to wear disposable coveralls (with hood) and two sets of disposable gloves (the inner pair taped at the wrists). When target/ion sources are first removed from the vacuum chamber after irradiation, all personnel in the room are required to wear respirator masks equipped with general purpose dusts/mists/organic vapour cartridges. Work on the target/ion sources is carried out in an acrylic glove box situated in the containment room. The ion sources are suspended from the roof of the glove box on a teflon surface that allows them to be rotated; two sets of gloves allow two people to simultaneously work on the ion sources. In order to prevent the spread of any contamination, the containment room contains a dedicated set of tools that are never removed from the area; furthermore, all tools, once used in the glove box, remain in the glove box.

General radiation levels and surface contimination in the area are routinely monitored by the TRIUMF safety group. All personnel are required to monitor themselves before leaving the beamline level and again in an area of lower background radiation immediately above the shielding.

THE TISOL VACUUM SYSTEM:

Because TISOL is a test facility, all components of the system were designed based on a philosophy of maximum flexibility. A modular construction and the use of standard fittings and devices permits relatively rapid changes of configuration and replacement. For the vacuum system, this philosophy is manifested by a segmented design and the use of standard components whenever possible; vacuum valves, vacuum gauges and most vacuum tank connections are the same as used elsewhere at TRIUMF. When a device fails, it can be quickly replaced with a similar device that is available or can be "borrowed" from other experimental groups. Similarily, with modular construction, when some design aspect is determined to be inadequate, a redesign of the module rather than the entire system has greatly simplified the work involved.

The current TISOL beamline configuration consists of four vacuum tank sections that can be isolated from each other and evacuated or vented independently. When a component of one vacuum segment fails, that segment is vented during repair; the other segments need not be vented and in some cases, the separator can still be partially operational. The four vacuum sections are: the target/ion source (TIS) irradiation chamber, the mass separator section, the electrostatic beamline section and the final focus chamber.

The TIS Vacuum Chamber:

The target/ion source chamber vacuum system is illustrated in Figure 4. The TIS assemblies are inserted through a 10" ø opening on the top of the chamber. A 1" thick nylon insulator separates the TIS plate (at +20 kV) from the vacuum chamber (at ground). The taret/ion sources are suspended from a circular steel plate that fits tightly inside a steel rim on the insulator, providing the proper lateral positioning. Between the insulator and the vacuum chamber is a 10" ø steel bellows that allows the TIS assembly to be raised vertically up to 4" without breaking vacuum. This allows proton beam tuning with the target raised out of the beam. The bellows is raised or lowered by remotely activating two pneumatic pistons situated diagonally at two corners of the chamber; two linear bearings at the other corners keep the plate and TIS assembly from twisting.

The chamber has removable 0.002" thick steel windows on both the upstream and downstream proton beam ports isolating it from the proton beamline. Of necessity, vacuum in the TIS chamber and the rest of the TISOL system is independent of the beamline vacuum. The beamline vacuum is generally 10^{-5} - 10^{-6} torr, while TIS chamber vacuum as good as 10^{-7} torr has been routinely possible. However, under certain circumstances TISOL has operated with vacuum as poor as 10^{-4} torr. In either case, the TISOL and beamline vacuums are incompatible and must be isolated to prevent one system from

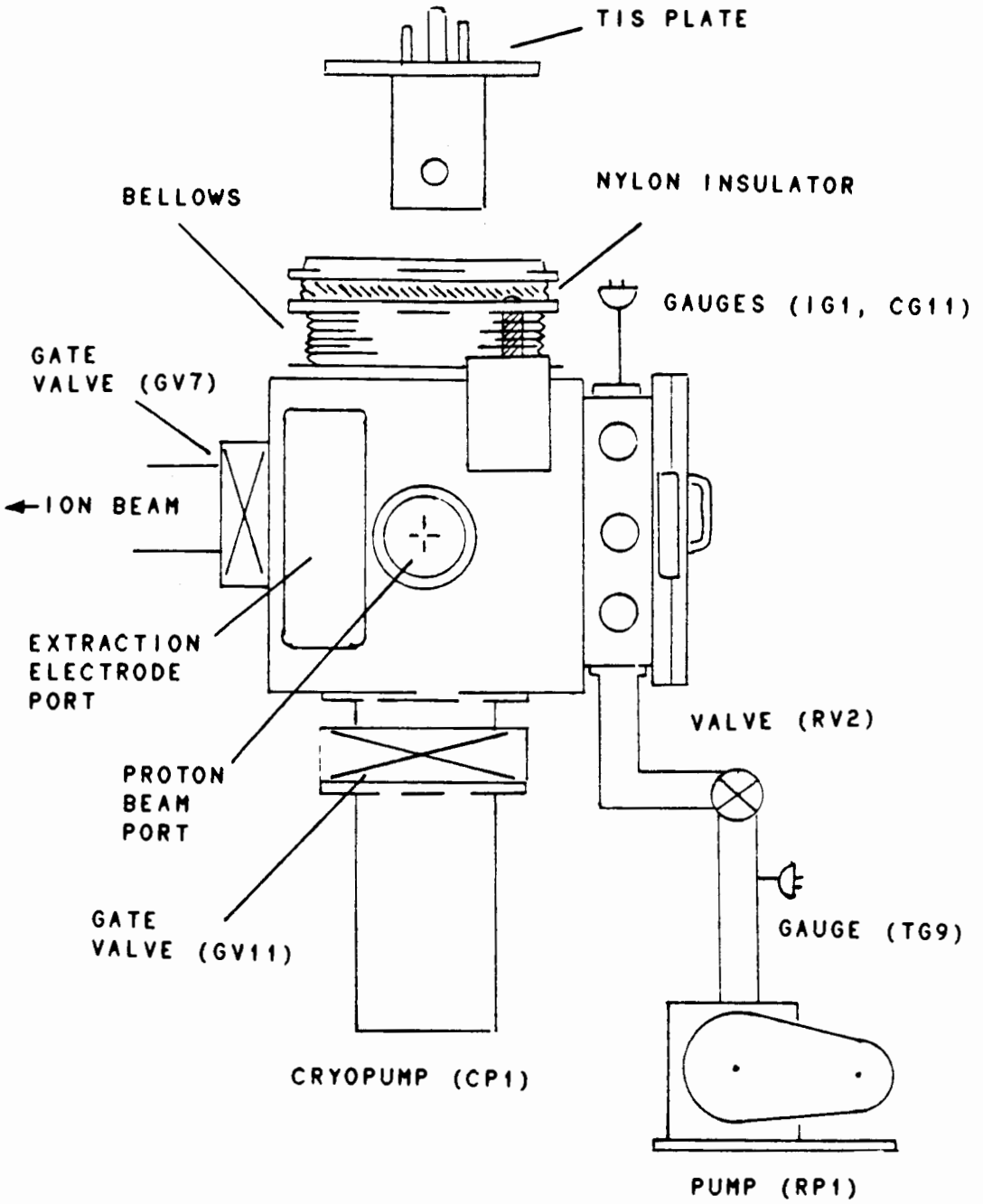

Figure 4: TIS Vacuum chamber. Vacuum gauges and pumping ports are situated around the back ring.

"tripping" the other. The beam windows are also a safety feature; any radioactive contamination, from the thick targets used to produce isotopes, is contained in the TIS chamber rather than being spread along the interior of the beamline. The TIS chamber proton ports are coupled to the beamline with standard TRIUMF 4" ø flanges and quick connect clamps.

The TIS chamber is a steel box 15" by 11.5" by 12" high. Besides the proton port, the upstream face also has a 4" by 6.5" port to accommodate an extraction electrode, while the downstream face has a small port allowing water cooling lines to enter the box. The front face (direction of isotope beam extraction) has a 4" diameter port and gate valve, centered on the ion beam axis, 19 mm above the proton beam axis. The rear face has a 10.5" diameter, hinged, "breech block" type port for access to the interior of the chamber, permitting *in situ* inspection and alignment of TIS components. Vacuum gauges, roughing lines and vent valves are situated on a 4" long ring extension around the rear port. The bottom of the chamber has a 10" diameter port and gate valve leading to a suspended cryopump.

Initial off-line tests with a surface ionization source showed that the TIS vacuum chamber became very hot from the radiated energy of the resistance heated target. In order to protect the integrity of the chamber O-rings, water cooled plates were installed on the interior surfaces of the

four horizontal walls of the chamber. Each plate consisted of two 1/8" thick copper sheets silver soldered on both sides of a cooling loop made of 1/2" copper tubing. The plates have appropriate openings for proton and ion beams and are cooled by independent water lines. In the bottom direction, the cryopump suspended below the chamber was shielded from the radiant heat by a simple baffle of 1/8" copper sheet. In the top direction, the TIS plates are water cooled externally.

With the exception of a manual vent valve and the hot cathode ion gauge, all of the valves, pumps and vacuum gauges are operated and monitored by the TISOL computer control system. All interlock conditions are set (in software) in the control system and may be bypassed or modified as required. Should the vacuum level rise above any of the interlock set points, the control program responds by shutting the gate valves (GV11) and (GV7), isolating the TIS chamber.

The chamber is roughed by a Sargent-Welch 1450 L/sec mechanical roughing pump (RP1) through roughing valve (RV2). This pump is also used to rough the next vacuum section through a second roughing valve (RV1). On the condition that RV1 and the gate valves (GV11) and (GV7) are closed, valve (RV2) may be opened for chamber roughing. Once rough vacuum is achieved (vacuum $\leq$ 50 mtorr, on convectron gauge (CG11)), (RV2) is closed and gate valve (GV11) can be

opened; high vacuum is maintained by the cryopump (CP1).

A cryopump was chosen for the TIS chamber because of the high pumping speeds available and the low maintenance required. Both plasma and ECR ion sources require a support gas and the pump must be able to efficiently remove the non-ionized gas that escapes from the source. Turbo pumps may become damaged with too high a gas load and oil diffusion pumps are too unreliable. The cryopump (CP1) is a CryoTorr-10 high vacuum pump with a Cryodyne closed cycle helium refrigerator, both from CTI-Cryogenics Ltd. Normal operating temperature for this pump is 10 - 20 K. The rated pumping speeds are 5000 L/sec of hydrogen, 3000 L/sec of air or 2500 L/s of argon. Overall capacities (before regeneration is required) are 2000 L for condensable gases and either 12 L (@ $5 \cdot 10^{-8}$ torr partial pressure) or 24 L (@ $\geq 5 \cdot 10^{-6}$ torr partial pressure) for hydrogen. The vacuum range of the pump is quoted as 10^{-3} - 10^{-10} torr by the manufacturer. Vacuums of $5 \cdot 10^{-7}$ torr have been achieved in the TIS chamber, while vacuums in the low 10^{-6} torr region are routine during runs with the target at high temperature (1400° - 1900° C).

The gate valve isolating the TIS chamber from subseqent sections of TISOL is opened on the condition that the vacuum on both sides, as determined by cold-cathode ion gauges (IG1) and (IG5) is below $1 \cdot 10^{-4}$ torr. The TIS chamber is vented either manually, or remotely through a solenoid

activated vent valve (VV1). The condition for remote venting is that all other valves (GV11, GV7, RV2) be closed.

The Separator Tank Vacuum Section:

The second vacuum section consists of the horizontal ion beamline, the dipole vacuum tank and the vertical section of beamline up to the primary ion beam focus — essentially the mass separator elements. This vacuum section is displayed in Figure 5. This section is isolated from the TIS chamber and the following section by two gate valves: (GV7) and (GV10). Rough vacuum is achieved by pumping through the (RV1) roughing valve with mechanical pump (RP1). Vacuum is monitored by the (CG6) convectron gauge and the (IG5) cold-cathode gauge, which is activated when (CG6) reads $\leq$ 50 mtorr. High vacuum in this section is maintained by two 6" ø Turbovac-450 Leybold-Heraeus turbo pumps (450 L/sec pumping speed) positioned at the entrance (TP1) and exit (TP2) of the dipole magnet vacuum tank. These pumps are controlled by Turbotronik NT450 controllers from the TISOL control station above the shielding blocks. The controllers are operated manually but their status is monitored by the computer control system and used as required for interlock purposes. A 1450 L/sec Sargent-Welch mechanical pump (BP2) is used as a backing pump for both turbos. The backing lines branch at the pump throat and each line contains its own valve (BV1 & BV2) and thermocouple vacuum gauge (TG7 &

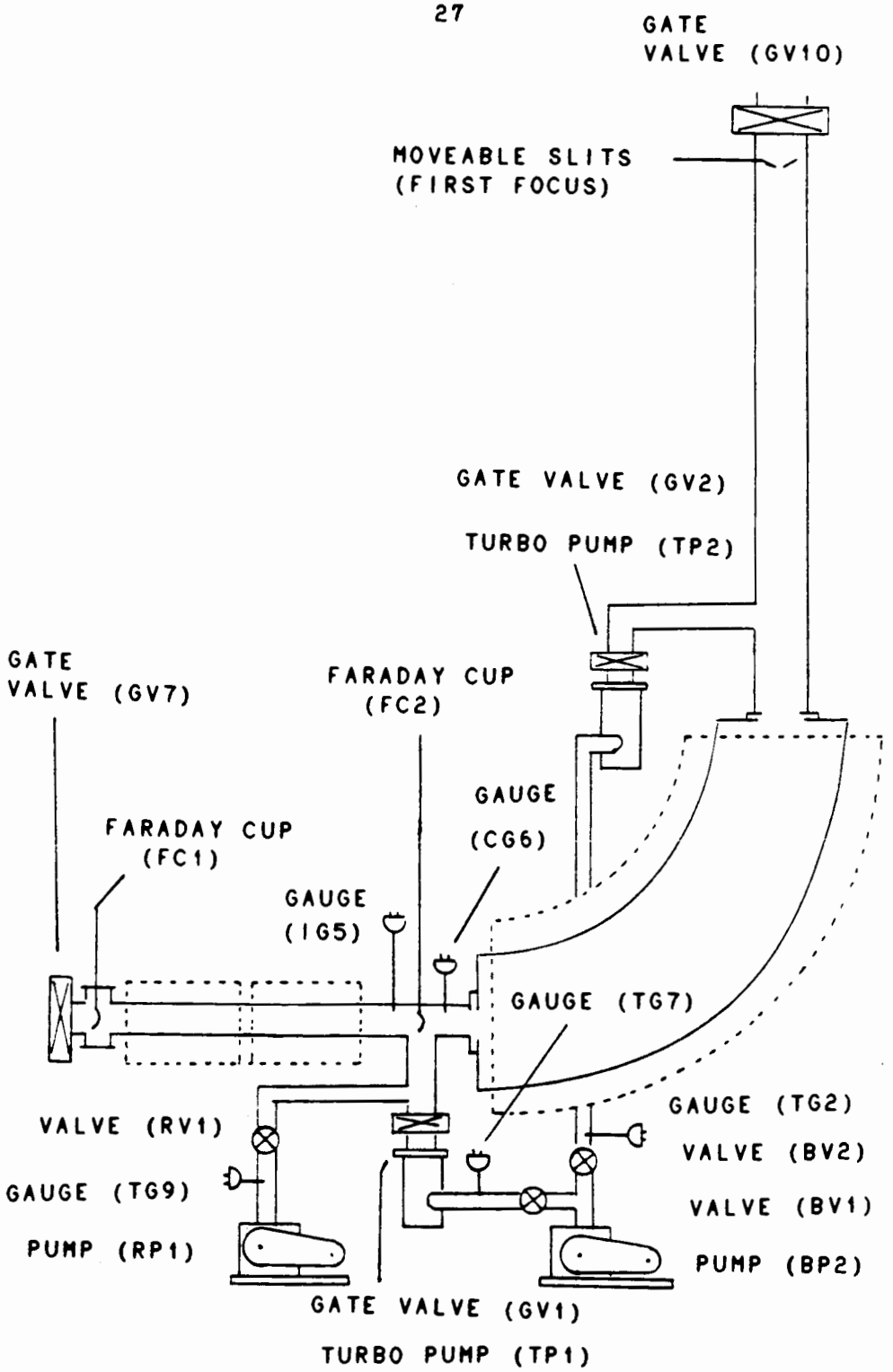

Figure 5: The separator vacuum chamber.

TG2); the turbos are each isolated from the vacuum tank by their own gate valves (GV1 & GV2). This configuration allows the turbos to be used either simultaneously or individually.

As with the TIS chamber, all valves and pumps are interlocked with respect to the relevant vacuum gauges; the interlock conditions are set in the control system software. When the rough vacuum in the tank reads < 100 mtorr on the convectron gauge (CG6), the roughing valve (RV1) is closed and the turbo gate valves (GV1 & GV2) may be opened on condition the turbos are "at speed". Should the convectron gauge vacuum reading rise above 100 mtorr, an alarm condition defined in the control system automatically closes the turbo gate valves to prevent damage to the pumps. Similarly, alarm conditions set on the thermocouple gauges (TC7 & TC2) in the turbo backing lines will also close the turbo gate valves. The (TC7 & TC2) alarm conditions have a one second delay to guard against spurious alarms resulting from an burst of gas in the lines or an erratic gauge reading; action is only initiated if a persistent (> 1 sec) bad vacuum condition is detected.

With both turbo pumps operating, the typical vacuum is in the low 10^{-6} torr range. With only one pump operating, the vacuum is typically an order of magnitude worse. As before, the gate valves to the TIS chamber (GV7) and the electrostatic beamline section (GV10) may be opened on the condition that the cold cathode gauges read $\leq 1 \cdot 10^{-4}$ torr on

both sides of the valve. The mass separator vacuum section is vented by means of a manual valve in the horizontal beamline segment; remote venting is also possible by overriding control system interlocks and venting through the TIS chamber.

The Electrostatic Beamline Vacuum Section:

In the early stages of TISOL construction, only the first two vacuum sections existed and separated ion beams were collected at the first focus. The last two vacuum sections consist of the electrostatic beamline segments and the final focus collection chamber; these are illustrated in Figure 6. As with the previous section, the electrostatic beamline vacuum tank is isolated by two gate valves (GV10 & GV13). This section is roughed by means of a 1450 L/sec Sargent-Welch mechanical pump (RP3).

This is not an ideal arrangement and a typical pump down is somewhat clumsy. With all gate valves closed, (RP3) is started and the roughing valve (RV3) opened when the thermocouple gauge (TG4) condition ($\leq$ 80 mtorr) is satisfied. As with the previous section, tank vacuum is monitored by the convectron (CG10) and cold-cathode (IG7) vacuum gauges. When (CG10) reads below 100 mtorr, (RV3) is closed, isolating the tank while the turbo pump (TP3) is brought to speed. This requires using (RP3) as a backing pump through the (BV3) valve. When (TP3) is "at speed", the

gate valve (GV3) may be opened provided that: (RV3) is closed, (BV3) is open, (RP3) is on, (TG3) reads ≤ 250 mtorr and (CG10) reads ≤ 100 mtorr. In the event that the isolated tank vacuum has deteriorated above the 100 mtorr set point, the turbo backing line is temporarily isolated using the backing valve (BV3) while the tank is pumped through (RV3); the vacuum behind the turbo (TP3) is monitored with (TG3) and is not allowed to deteriorate to the point where the turbo trips off. In practice, the pumping through alternate lines can be juggled for a few minutes without significant vacuum deterioration, until all conditions necessary for opening (GV3) are satisfied.

Once the tank is being pumped by the turbo pump, a ≤ 50 mtorr condition on (CG10) activates the cold cathode gauge (IG7). As before, a $\leq 1 \cdot 10^{-4}$ torr condition on (IG7) and the cold-cathode gauges in the adjacent vacuum sections (IG5 & IG8), allows the isolating gate valves (GV10 & GV13) to be opened. Alarm conditions on any of the vacuum gauges are set in software and the control system automatically shuts gate valves should a bad vacuum be detected. Typically, this section has vacuum in the low 10^{-6} torr range. Since the electrostatic beamline vacuum tank is entirely above the shielding blocks and easily accessed, venting is by means of a manual vent valve.

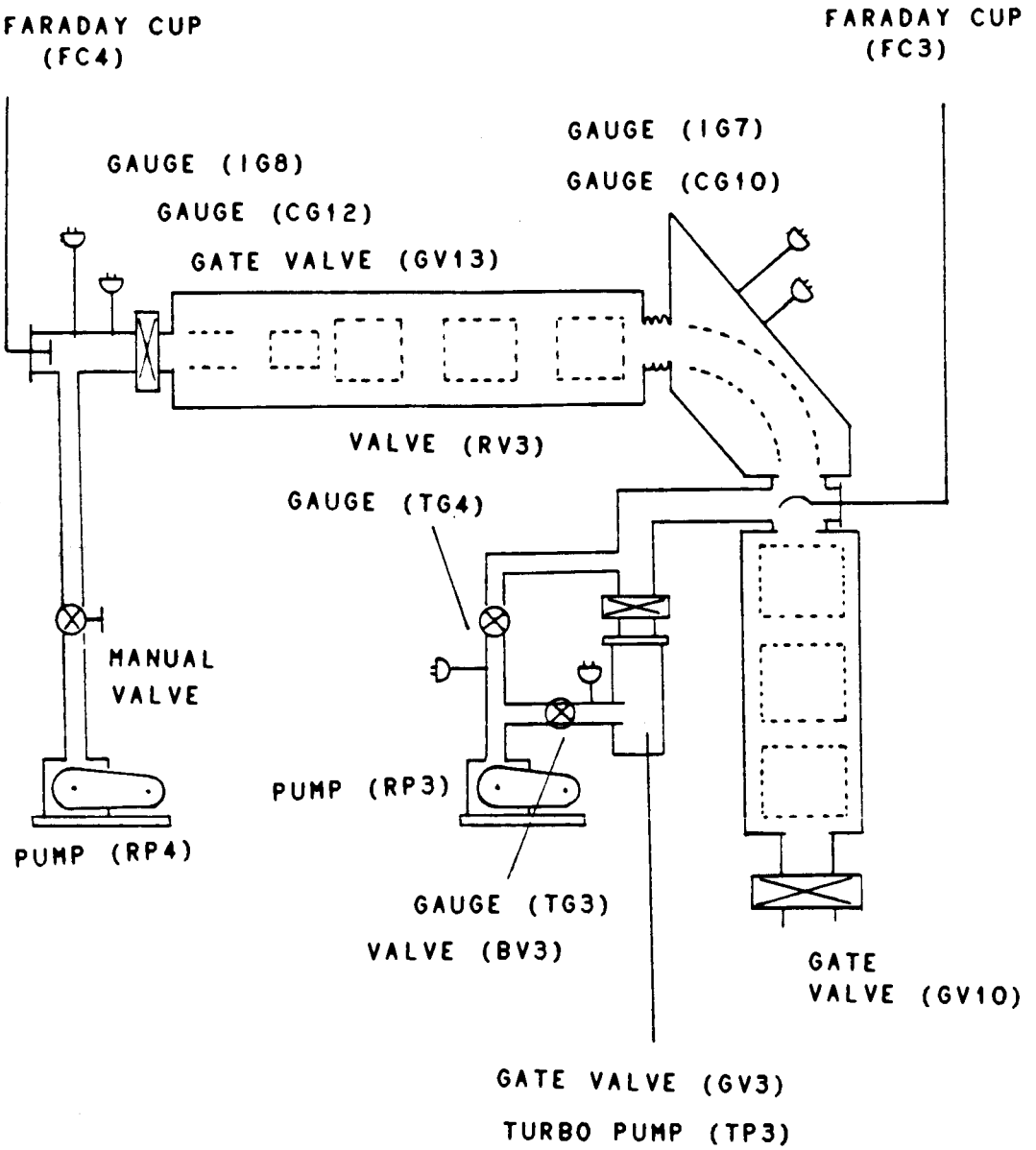

Figure 6: The electrostatic beamline vacuum chamber

The Final Focus Vacuum Section:

The final focus vacuum section currently consists of a 15" long section of 4" ø beamline pipe coupled to a 4" ø four-way cross. The only interaction between this section and the control system consists of monitoring the two vacuum gauges (CG12 & IG8) for purposes of interlocking the gate valve (GV13). The vacuum in this section is essentially tied to that of the preceding section.

In a planned future configuration of the TISOL system, this section is intended to contain a moveable tape for collecting and rapidly transporting separated activity to shielded detectors situated away from the beamline. At that time the pumps and valves will be remotely controlled.

Vacuum Valves & Lines:

Except for a few manual vent valves and the pump and roughing valve of the final focus vacuum section, all roughing valves, gate valves, mechanical pumps, and turbo pumps are operated remotely from the TISOL control area above the 4A shielding blocks. A PC based computer control system (described later) is used to activate and read the status of the vacuum system elements.

Pneumatic roughing valves and gate valves are driven by compressed air and activated by 110 V AC driven solenoids. In order to prevent deterioration from continual radiation exposure, all compressed air lines are of 1/4" copper tube

coupled with brass Swagelock connectors. Each individual air line has its own in-line valve at or near the device it services; this allows servicing of individual components without disrupting the entire system. All roughing valves are wired in a "normally closed" configuration; on loss of AC current, the valves automatically close, isolating the vacuum "modules". This type of configuration not only prevents contamination of the vacuum vessels with pump oil backstreaming from the roughing or backing pumps during a power failure, but also generally confines any disaster to a single vacuum module. The roughing valves also close on loss of compressed air, while the gate valves remain in their current position.

All roughing or backing valves are 2" diameter copper 90° angle valves, with an interior bellows with O-ring seal and ports fitted with KF-50 flanges for quick connection or interchange purposes. All roughing lines are 2" diameter soldered copper tube or stainless steel flexible tube with KF-50 flanges to mate with the valves and pumps. Electrical connections are standardized throughout the TISOL system. AC power connections are made using 4-pin MS connectors for roughing/backing valves and 8-pin MS connectors for gate valves. Low voltage DC switch closure readback connections are made using LEMO "0" 2-pin connectors. Using standardized quick-coupling connectors on vacuum, pneumatic, cooling water and electrical system components not only allows ready

interchange and replacement of these components, but it also reduces the time personnel are required to be in radiation areas.

Vacuum Gauges:

Four types of vacuum gauges are used on the TISOL system: thermocouple, Pirani, cold-cathode and hot-cathode. Except for the hot-cathode gauges, all gauge controller outputs are monitored by the control computer and are used in setting interlock levels for the vacuum system.

The thermocouple vacuum gauges are of the Varian 531 type and are adequate for vacuum estimates in the 760 torr - 50 mtorr range. These gauges are placed in the vacuum lines adjacent to roughing pumps, backing pumps or crucial valves. The nature of some of the vacuum system components prevents the easy use of readback devices. When a mechanical pump or roughing valve is remotely activated, there is no absolute indication that it is indeed pumping or open — there are no available readbacks to indicate its true status. The control system indicates only that contactors or solenoids have been energized. The readings of thermocouple gauges at pump throats and on either side of valves must be monitored to verify the condition of such devices. Current for the thermocouple gauges is supplied by a TRIUMF manufactured, double width NIM module that contains twelve independent 16 mA DC sources. Each gauge is serviced by a shielded 22 AWG

2-twisted pair cable that carries the heater current and the voltage readback. The readbacks are fed directly into the control system ADCs and the vacuum reading is displayed on the control computer.

The Pirani gauges are 275 series Granville-Phillips convectron gauges with a range of 1000 torr to 1 mtorr. Each gauge is operated by its own controller — the TISOL control system monitors the status of each gauge through the 0 - 9 V recorder output of each controller. Gauge readings are displayed both by analog meter readouts on the controllers and by the control system computer. The convectron gauges are used to set system interlocks at specific vacuum levels in the applicable range with an accuracy that the thermocouple gauges cannot provide. Each of the four existing TISOL vacuum sections has one convectron gauge.

The cold-cathode ion gauges are the highest order vacuum gauge that is controlled and read by the computer control system. These are Varian 524-2 gauges coupled to Varian 860 gauge controllers; the accurate range for this combination is rated at $1 \cdot 10^{-2}$ torr to $1 \cdot 10^{-7}$ torr. As with the convectron gauges, each vacuum section is equipped with one cold-cathode ion gauge. Because of the 10^{-2} torr top end requirement of these gauges, the gauge controllers are activated (by the computer control system) only after the convectron gauge in the same vacuum section reads below 10^{-3} torr; on loss of vacuum, the controllers are turned off at

the same vacuum level. This switching is accomplished by supplying or denying 110 V AC to the outlets servicing the controllers. (Since each gauge head requires 4 kV high voltage from its controller, shutting off the controllers also provides some measure of safety for personnel working on the vented vacuum tanks.) The gauge readings are monitored by the TISOL control system through the 0 - 10 mV recorder output of the controllers and are displayed by both the controller analog meter and by the control system computer. These gauges are used to set high vacuum interlock conditions for TISOL operation — the gate valves isolating the four vacuum sections will only open when the cold-cathode gauges on either side read below $1 \cdot 10^{-4}$ torr. Unfortunately, because a high vacuum condition (10^{-7} torr as read by these gauges), gives a recorder output of 0 mV, the same as an "off" condition. This results in a high number of false vacuum "trips".

The most accurate vacuum estimates on the TISOL system are provided by a hot-cathode (Bayard-Alpert) ion gauge with a reliable range of 10^{-3} torr to 10^{-9} torr. This gauge is located on the TIS chamber and is operated independent of the TISOL control system. Since the best vacuums achieved in the TISOL system are in the high 10^{-7} torr range, in principle, the cold-cathode gauges should provide adequate readouts. However, in practice, the cold-cathode gauges may become contaminated and give erroneous or erratic vacuum

readings. The hot cathode gauge is less prone to contamination, and can be outgassed remotely when it is contaminated. It is used for accurate vacuum readings in the TIS chamber periodically during on-line running. The disadvantage of the hot-cathode gauge, that precludes its constant use during on-line running, is that it is affected strongly by the 20 kV accelerating potential applied to the target/ion source. Consequently, accurate vacuum readings are obtained only periodically and large fluctuations are monitored by the cold-cathode gauges. The hot-cathode gauge is also extensively used during the initial pumping out and conditioning of the target/ion source. Its faster and more sensitive response with respect to that of other gauges allows the outgassing of the target with increasing temperature to be monitored.

SERVICES AT HIGH VOLTAGE

The initial acceleration of the ions to be separated by TISOL is due to a variable 0 - 20 kV potential applied to the target/ion source; the extraction electrode and the rest of the separator system is at ground. The source is suspended in the vacuum of the TIS chamber from a plate electrically insulated by a 1" thick nylon ring. Services required for the source (cooling water for electric connectors, DC current for target heating or support gas in

the case of plasma or ECR sources) enter the vacuum chamber with the source, through the TIS support plate. These services must be reconciled to the potential on the TIS plate.

The cooling water required for parts of the ion source is most easily dealt with. Water is supplied to the source from the beamline 4A closed-loop low conductivity cooling system. Quick connect couplings and 1/2" ø natural rubber hose are used on both supply and return lines. Approximately 7' lengths of the rubber hose effectively isolate the source (at +20 kV) from the cooling system (at ground).

Similarily, a support gas (when required) can be supplied through a length of insulating tubing, such as polyethylene. If the gas pressure is low, as is generally required, the ion source is effectively insulated from the supply.

Electric current (DC) for resistance heating the target and an ionizer (surface source) or cathode (plasma source) must couple directly to the source and, with the source at high voltage, the conductors and power supplies must also be at high voltage. At TISOL, the power supplies required for the target/ion sources are enclosed in a Faraday cage and biased to the accelerating voltage. Conductors run from the cage, through an enclosed Faraday trunk, down to the TIS chamber. Control and monitoring of the power supplies is accomplished using the computer control system through an optical fiber link.

The Faraday Cage & Faraday Trunk:

The Faraday cage is situated above the shielding blocks at the 9.1 m level above the beamline floor, on a steel platform containing the TISOL control area. Its dimensions are 9' by 11' by 8' high and it is constructed of a steel channel frame covered by aluminum mesh on three sides; the back side (which holds the circuit breaker panels) is entirely sealed by 1/8" thick aluminum sheet. Entrance is through a sliding door at the front of the cage.

During initial TISOL tests, the Faraday cage was placed on a concrete floor — the floor of the cage was of 1/2" thick polyethelene sheet covered by 1/2" plywood serving as an insulator between the services at high voltage and ground. The power supplies were placed immediately on top of this floor and its insulating properties were sufficient to operate the Faraday cage contents at a potential of +20 kV without significant leakage current. However, when the Faraday cage was installed in its final position on the steel platform, a 1/16" thick aluminum sheet was used to cover the plywood. This resulted in an insulator sandwiched between two large area conductors, one of which was raised to +20 kV — essentially, a large leaky capacitor. Charging the contents of the Faraday cage to +20 kV resulted in a prohibitively high leakage current from the high voltage power supply. The 1/16" aluminum sheet could not be removed as its presence was deemed absolutely necessary (by

those charged with TRIUMF safety concerns) to act as a barrier to molten components in the event that the power supplies should somehow malfunction simultaneously with their circuit breakers and melt through their steel cases causing the plywood and polyethelene insulation to catch fire. After several attempts at finding practical insulators to insulate the services from the "capacitor" floor, the power supplies and gas bottles were elevated above the floor using 6" X 6" ø PVC pipe couplings set on end. With these insulators, the observed leakage current with the system at +20 kV potential was no higher than could be attributed to the extracted ion beam current alone.

Electrical power is supplied to the Faraday cage by a Tracon Engineering Inc, 480 V, 3 phase isolation transformer situated adjacent to the cage. Currently, the contents of the cage consist of two 10 V/500 A DC power supplies manufactured by Philtek Industries Ltd., a 10 V/300 A DC power supply (also from Philtek), a 600 V/25A DC power supply from Hewlett-Packard, a helium gas bottle and a small vacuum pump used to pump out the gas line. A cabinet containing electronics for remotely controlling the power supplies is also situated on a rack in the Faraday cage and powered from within the cage.

The DC current from the power supplies and any required gas is supplied to the target area through an enclosed Faraday trunk that runs from the cage, down through the

shielding blocks, to the target station. The Faraday trunk is constructed of a 14" by 6" steel cable tray covered with 1/8" aluminum sheet. Nylon supports are mounted in the tray to serve as insulators for the electrical cables and the gas lines. The electrical conductors consist of 7 pairs of rigid 4/0 AWG rubber insulated copper cables, 1 pair of 3 AWG cables, 1 pair of 4 AWG cables and two 1/4" ø steel gas lines. Three 22 AWG/2 conductor shielded cables, used for thermocouples at high voltage, also run through the Faraday trunk. At the Faraday cage end, the conductors are connected to quick-coupling brass female connectors on a switching panel at the entrance to the Faraday trunk; flexible insulated lines from the power supplies carry the mating male quick connectors.

With the surface ionization source, only two of the power supplies (both 500 A) are used; one to heat the target, the other to heat the ionizing metal foil. Each 500 A supply uses a total of four Faraday trunk cables: two 4/0 cables (in parallel) for the positive connections and two 4/0 cables (also parallel) for the negative. At the target station end of the Faraday trunk, the rigid cables are spliced to short lengths of flexible conductor that end in male quick connectors; these mate with connectors on the target/ion source systems. Both female and male connectors are color coded red or black and are labeled at both ends of the faraday trunk. By changing connections at the switching

panel and the source, the configurations of the power supplies can be altered to suit the power requirements of a variety of ion sources.

The High Voltage System:

The accelerating high voltage for TISOL is supplied by a Spellman 12 mA power supply variable up to ± 20 KV. This power supply is situated in a rack at the TISOL control station adjacent to the Faraday cage. High voltage is supplied to the Faraday cage through an insulated high voltage cable running overhead. For further safety, the cable was enclosed in a 2" ø PVC pipe over its entire run from the rack to the Cage. In the Faraday cage, the cable connects to a small distribution strip that feeds lines to all components required to be at high voltage. All components insulated from the Faraday cage walls and floor are "floated" to a potential of +20 KV with respect to the ground of the Faraday cage. Great care is taken to insure that any conductor in the Faraday cage is either connected to absolute ground (the cage itself) or to the high voltage. The cases of the power supplies, the gas bottle and its regulator, the vacuum pump and the electronics rack and cabinet are all interconnected and tied to the + 20 KV "ground" of the Faraday cage circuit breaker panels. The high voltage is transmitted to the target/ion source through the Faraday trunk conductors by tying the negative terminals

of the power supplies to their cases, and therefore, to the +20 kV potential; any unused conductors are shorted to the +20 kV "ground" to avoid any free floating conductor in the HV system. Similarily the Faraday trunk gas lines are either tied to high voltage through connection to the gas bottle or shorted to a +20 kV surface if unused. During times when the Faraday cage contents are not at high voltage, the isolated components are connected to absolute ground by a grounding hook with a flexible connector and an insulated handle. This hook is removed for HV running and used to ground out the Faraday cage contents immediately after the HV has been turned off.

High Voltage Safety Considerations:

For obvious safety reasons, the high voltage power supply is interlocked to the door of the Faraday cage and to the door of the TISOL containment room. Both doors have two switches (wired parallel for redundancy) that must be activated (by closing the doors) before the high voltage power supply can be turned on. These switches are not part of the computer control system but were wired directly into the circuitry of the HV power supply to prevent possible defeating of the safety interlock conditions through software manipulation. In case of personell entering the Faraday cage or TISOL containment room, an open condition

power to the HV power supply. This interlock is not entirely "idiot proof", but it requires a more dedicated idiot to defeat it.

As a further safety consideration, the high voltage power supply can only be activated by a keyed switch; the power supply can effectively be "locked out" by simply removing the key from the switch. This feature allows personnel to safely access the containment room (taking the key with them) by preventing anyone from turning on the high voltage in their absence from the control station. Conversely, entrance to the TISOL containment room may be prevented during high voltage running by locking the room with the radiation lockup system key, which is then kept at the control station. Obviously, these considerations only apply during off-line test runs, during on-line operation the entire area is made inaccessible by the radiation lockup safety system.

During high voltage running, visual indicators of the presence of high voltage are furnished by two flashing amber lights, one situated in the containment room the other on the Faraday cage. Turning on the HV power supply activates these lights. As well, the TRIUMF cyclotron operations control room is appraised of the high voltage conditions by a remote line running directly from the HV power supply.

ION BEAM TRANSPORT

The ion beam transport and mass separation of the TISOL system is provided by a vertical quadrupole-quadrupole-dipole (QQD) magnet configuration. Since vertical beam transport and mass separation was planned for the proposed radioactive beams facility, the TISOL system was built to mimic the basic geometry of the proposed system.

The QQD System:

The dipole and quadrupole magnets were built by the University of Colorado (Boulder) Nuclear Physics Laboratory as part of their energy loss spectrograph. (Ri75) The magnets were donated to TISOL after the facility was decommissioned.

The quadrupoles each have an effective length of 43 cm, hyperbolic poles and a 3" ⌀ aperture. The quad pair is rigidly mounted on a support structure that is, in turn, mounted on three linear bearings. This allows the quad pair to slide along the ion beam axis, changing position by up to 23.7 cm. This design element was incorporated for the purpose of accommodating a variety of ion sources. For small ion sources, such as surface or plasma sources, the distance between the target and the beam exit orifice (the "object" of the magnetic optic system) is small: the source is located close to the target. However, an electron cyclotron re-

sonance (ECR) source is large and must be accommodated in position along the ion beam line: the source "object" may be several feet upstream (along the ion beam line) of the production target. The sliding quad pair allows for both possible source configurations. With an ECR, the quads are moved upstream to accommodate the large source, with a plasma or surface ionization source, the quads have room to slide downstream. Positioning the quads close to the source exit orifice increases the acceptance of the magnetic optics system.

Each quadrupole magnet is water cooled and powered by a Research Industries Ltd. 22 V/0-50 A power supply. The power supplies are hardware interlocked to individual thermal switches on each magnet pole coil and to water flow switches on the cooling lines of each magnet. The quadrupole magnets are not part of the TISOL computer control system but are activated and controlled manually. Individual 10 turn potentiometers are used to set the quadrupole power supply currents. The magnetic fields of the quads are not routinely monitored, only the power supply currents are visually checked using LED displays. The quad pair is configured to provide bend plane focusing in the first magnet and non-bend plane focusing in the second.

The TISOL mass analysing magnet is a 90° H-frame dipole weighing ~ 8000 kg. Originally, the dipole was a split-pole magnet with a pole-tip gap of 4.45 cm. For use at TISOL,

the magnet was modified by converting it to a single pole design with a 10 cm pole-tip gap; the effective bend plane aperture is 20 cm. The physical radius of curvature is 1.38 m, while the pole-tip redesign was based on a calculated mean optical radius of curvature of 1.25 m. The pole face design was determined, using beam transport modeling, by K.Oxorn of the Foster Radiation Laboratory (McGill University).(Ox87) Given the proton beamline spatial limitations and the limitations of the quad and dipole acceptance apertures, beam transport modeling was performed using the computer codes TRANSPORT (Br73) and REVMOC (Ko84).

The dipole is powered by a Philtek 300 A/40 V power supply and controlled through the TISOL computer control system. In practice, the dipole field is initially set using a rough estimate of the required current, then stepped to the exact field required with reference to a Hall probe. The Hall probe is suspended in the magnet gap, far enough from the edges of the pole pieces to ensure a homogenous field is being measured. An F.W.Bell BH-701 Hall probe with a 100 mA control current is used; the probe output is 7.269 mV/kG ± 20%, with a linear deviation < 1/4% below fields of 10 kG.

Calculated & Measured Performance:

Initial predictions of TISOL beam transport were based on a slit ion source exit aperture. A horizontal slit 1 mm by

20 mm was envisaged for both plasma and surface ionization sources. First and second order optics calculations, using TRANSPORT and REVMOC estimated a magnification of 2 in the bend plane and a magnification of 2.3 in the non-bend plane at the first focus of the separator system, this corresponds to a calculated mass resolution of $M/\partial M = 1100$. Beam losses were calculated at 8%. Calculations based on an ECR ion source with a circular 1 mm ⌀ orifice yielded a magnification of 3.3 and a mass resolution of $M/\partial M = 400$ with 4% beam loss. These initial calculations did not include accurate estimates of the dipole fringe fields.

Once the redesigned magnet pole faces had been installed, the dipole was completely field mapped. The field map was used as an input parameter in subsequent computer modeling using the RAYTRACE program. (Ha81) The results were quite different from the earlier values. The surface/plasma object geometry produced a predicted bend plane magnification of 6.1, a non-bend plane magnification of 4.4, a transmission of 82% and a resolution of $M/\partial M = 334$. The ECR geometry predicted a bend plane magnification of 5, a non-bend plane magnification of 2, 99% transmission and a resolution of $M/\partial M = 223$. Clearly, the effects of the dipole fringe fields had been underestimated. By the time the calculations were complete it was not practical to change the pole geometry and the system was installed with the existing field aberrations.

In the early stages of off-line testing, estimates of the actual transmission and resolution of the system were obtained. All of these studies were conducted prior to the installation of the electrostatic beamline, and used the surface ionization source with a 1.5 mm by 19 mm slit exit aperture. Beams of stable ^{85}Rb and ^{87}Rb, from thermal decomposition of Rb_2CO_3 were used. Transmission was defined simply as the ratio of summed beam currents at the first focus over the total beam current at Faraday cup 1, located just upstream of the TIS chamber.

In order to measure beam mass resolution, a 30 mm by 1 mm collimating slit was positioned just in front of the Faraday cup at the first focus, with its long axis in the non-bend plane. The slit was centered on the beam axis, but could be moved (in the bend plane) using a worm gear and vacuum bellows. A pointer and linear scale, exterior to the vacuum chamber allowed accurate positioning of the slit to ± 0.5 mm.

Mass resolution was determined by scanning the two rubidium isoptope beams. With a rubidium beam focused on the slit, the accelerating high voltage was oscillated by feeding a 0.1 Hz ramp from a signal generator into the HV power supply's remote control circuitry. This caused the ion beam to sweep over the collimating slit at 10 sec intervals. The ion current measured on the Faraday cup behind the slit was passed through a current-to-voltage

converter into the vertical channel of a Tektronix 564 storage oscilloscope; the scope time base was triggered by the signal generator. In this manner, a mass scan of the two rubidium stable isotopes was obtained.

The 10 sec sweep cycle allowed relatively quick beam tuning using the scope display. The peak beam current could be roughly calibrated by comparing the signal level on the scope to the actual current measured with a Keithley 504 electrometer. Stable rubidium beams are ideal for this type of mass resolution estimates. ^{85}Rb and ^{87}Rb have isotopic abundances of 72% and 28% respectively and both beams are easily observed. Furthermore, the rubidiums are medium mass nuclei providing a good estimate of an average mass resolution.

The optical performance of an isotope separator is partially defined in terms of its mass resolution, that is, its ability to separate beams of adjacent mass. If the distance between adjacent mass beam images (M and M + ∂M) with image widths (FWHM) is given by ∂x, the images are resolved on the condition that:

$$FWHM \leq \partial x/2$$

However, the mass resolution is defined from the condition that:

$$FWHM = \partial x$$

Then, the spectometer mass resolution is defined in terms

of the width of the image of the ion beam mass peak:

$$\text{Resolution} = M/\partial M = DM/FWHM$$

and

$$D = \partial x/\partial M$$

where: $M \equiv$ mass of the ion beam

$FWHM \equiv$ full width at half maximum of the beam image

$D \equiv$ dispersion per unit mass (A168)

Rough estimates of mass resolution were obtained by reference to the peak separation on the scope screen. For example, if the peak separation is 5 screen division units corresponding to two mass units between ^{85}Rb and ^{87}Rb, the dispersion is: $D \sim 2.5$ divisions/mass. Taking a mean mass of 86 gives:

$$DM \approx 86 \cdot 2.5 \text{ div/mass} \approx 215 \text{ div/mass}$$

If the FWHM of each peak is further estimated at ~ 0.1 divisions, that is FWHM $\approx$ 0.25 div/mass, the mass resolution becomes:

$$M/\partial M \approx DM/FWHM \approx 215/0.25 \approx 860$$

Using this method, mass resolutions were routinely measured during the early stages of TISOL development. Resolutions up to ~ 2500 were observed. However, these high resolutions were obtained at the cost of beam transmission. For estimated mass resolutions of 1500 - 2000, the transmission was routinely about 20%. Transmissions of up to 50% could be obtained with resolutions of 700 - 900. In all measurements using the slit orifice geometry, transmission never exceeded the 70% mark. Figure 7 shows a mass scan with an

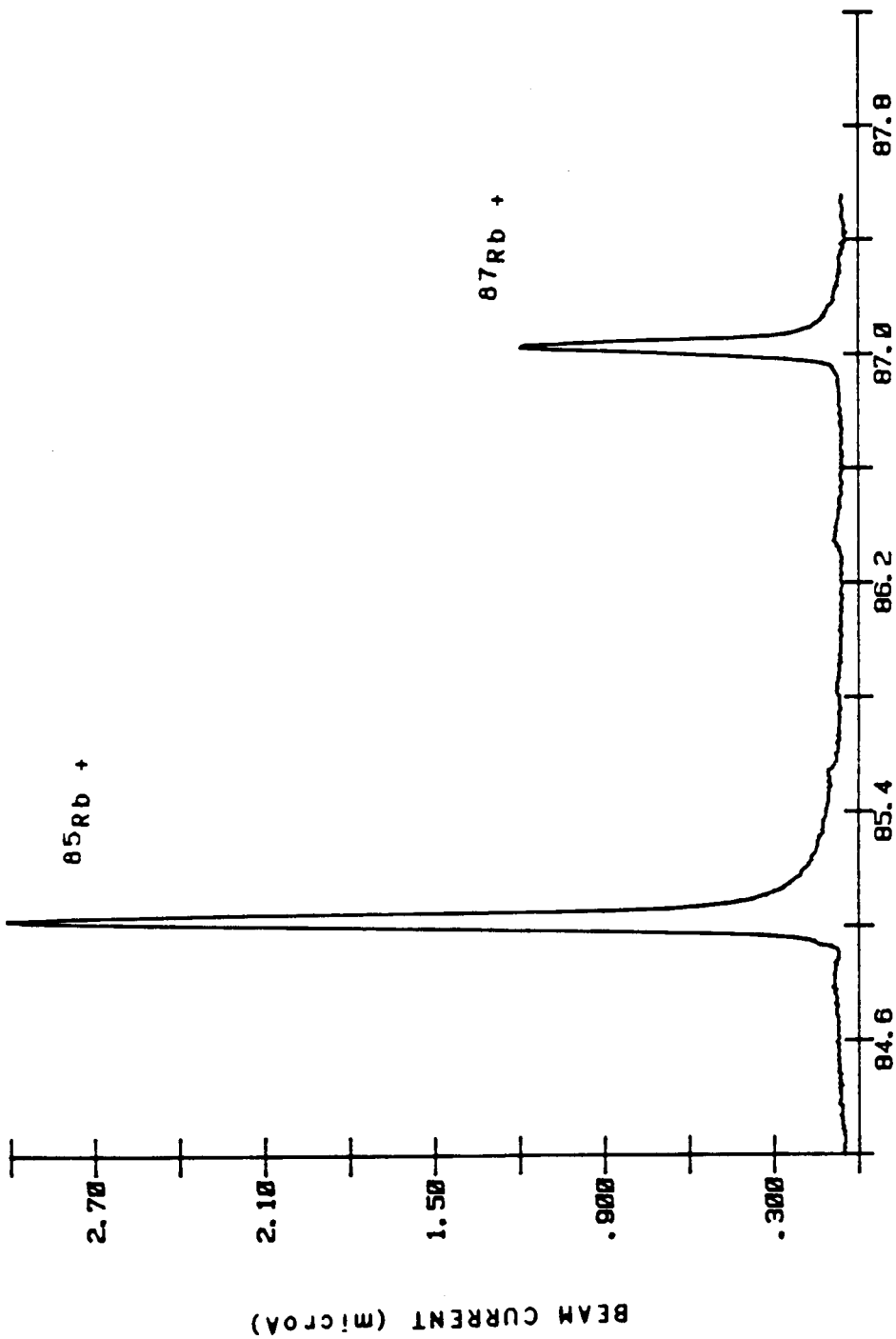

Figure 7: A high resolution rubidium beam scan.

estimated mass resolution of 1500; transmission is ~ 20%. In order to obtain an estimate of the final beam image size, a stationary ion beam was scanned by moving the collimator slit across the beam in the bend plane. With the ^{85}Rb beam initially centered on the collimator slit, the slit was moved in 2 - 3 mm increments and the beam current measured on the Faraday cup immediately behind the slit. A FWHM of ~ 7 mm was measured for a 0.023 μA ^{85}Rb beam; this corresponds to a magnification of ~ 4.5, slightly better than the predicted value of 7. With further optimization of the system, a ~ 2.5 mm FWHM was measured for a 0.09 μA beam with a $M/\partial M \approx 860$; this corresponds to a bend plane magnification of ~ 1.7, much better than predicted.

The two rubidium beams were also used to estimate the contamination factor for adjacent mass positions. The 2 mass rubidium separation allows a good estimate of the position of the intermediate mass (A=86); measuring the current at this position relative to the peak currents (at A = 85 and A = 87) gives an estimate of the contamination. The system was tuned to a mass resolution of 1200 - 1300. The ^{87}Rb beam was centered on the collimating slit and the ion current scanned as before. A FWHM of ~ 3 mm was estimated for mass 87 with a peak current of 2.5 μA. Both mass peaks could not be scanned with one magnet field setting due to the limited travel of the slit bellows, however, the mass 85 current was later measured at 7.7 μA.

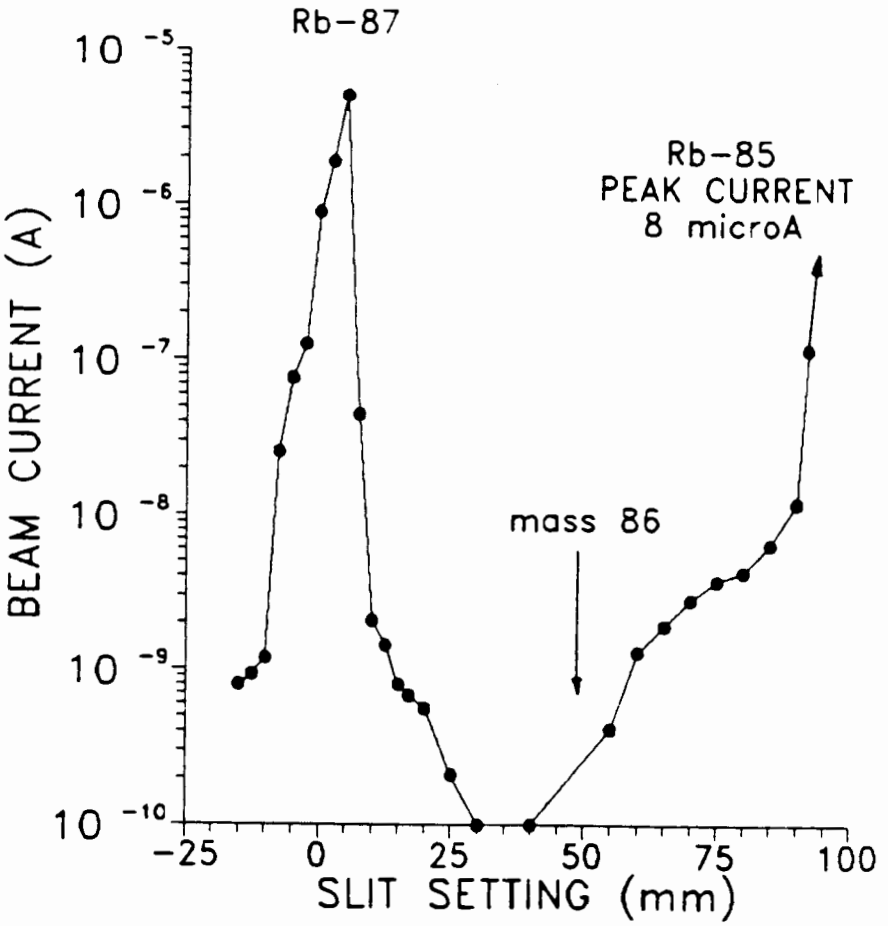

Figure 8: Scan of rubidium beams. The mass 86 position is at 42 - 49 mm; ^{87}Rb FWHM ≈ 3mm; mass resolution ≈ 1250. Adjacent mass contamination is ≈ $1/10^4$.

Figure 8 shows the results of the mass scan, the tail of the mass 85 beam can be seen at the edge of the graph. The estimated FWHM is ~ 3 mm; for a resolution of ~ 1250 and an average mass of 86, the unit mass dispersion is ~ 44 mm. This corresponds to a slit position of 42 - 49 mm, depending on the estimated mass 87 peak center. In this region there is less than $4 \cdot 10^{-10}$ A of detectable beam current. Based on a 7.7 μA peak current at mass 85, the contamination factor is $\approx 4 \cdot 10^{-5}$ for a 1 mm slit. The full width at 1/10 maximum of the ^{87}Rb beam is 5 mm. A rough estimate of the contamination factor at the 90% level is $\approx 2.5 \cdot 10^{-4}$; a perfectly acceptable factor. The "resolution" estimated at several widths of the mass 87 beam is given in Table 1.

Table 1

Mass Resolution of ^{87}Rb Ion Beam

Position	Beam Width (mm)	Mass Resolution (M/∂M)
FW1/10M	5	750
FW1/100M	11	340
FW1/1000M	14	270

The size of the beam spot, in the non-bend plane, was never measured. The use of the slit exit orifice geometery was abandoned due to the poor beam transmissions. The slit source orifice was replaced by a circular 5 mm ⌀ "object".

By this time, the electrostatic beamline had been installed and it was not possible to repeat the scanning slit measurements. However, transmission could still be estimated from the ratio of summed beams at the final focus to that of total beam at Faraday cup 1. Using stable beams of ^{23}Na, ^{39}K and ^{41}K, the transmission was estimated at 100% ± 10% for the circular orifice. During the transmission measurement a 1/2" ϕ circular collimator was positioned in front of the final focus. The fact that transmission is essentially 100% through this diameter, suggests that the beam magnification is < 2.6. This is supported by observation of beam "burn" marks on aluminum foil placed at the final focus. These "burn" spots are less than 1 cm ϕ, implying a magnification of < 2.

Though the measured beam transport (using the slit geometry) falls short of the predicted design performance, mass resolution and image magnification were determined to be much better than first feared. The measured adjacent mass contamination factor of only $1/10^{-4}$ is very good. Using a circular ion source orifice results in a transmission and beam spot size that are adequate for all purposes.

The Extraction Electrode:

During initial tests with the slit orifice source, a slit extraction electrode orifice was also used. The exraction electrode had a chromium plated copper face with a

4 mm by 40 mm opening for the ion beam. Immediately behind the front face were two electrostatic deflection plates (6 cm by 9 cm) that could be biased (≤ 1.5 KV) to steer the ion beam in the vertical plane. Behind the deflection plates was a 7 cm ϕ by 1.5 cm long "focusing" ring. A voltage of up to 12 KV could be applied to this ring to help focus the extracted beam. The electrode face, deflection plates and focus ring were mounted on a sliding track and could be manually positioned (along the ion beam axis) from outside the TIS chamber using a rack and pinion gear mechanism with an O-ring vacuum feedthru. The deflection plates proved to be of little use, but the focusing ring was needed to improve beam transmission; without the focusing ring, transmissions were on the order of only a few percent.

For on-line operation a new remotely positioned extraction electrode was designed. The new electrode had a stainless steel front face with a 1/2" ϕ circular opening; a focusing ring was positioned behind the front face. The electrode could move in the vertical, horizontal and axial planes with respect to the ion beam. The 3 degrees of motion were made possible by mounting the electrode frame at the end of an arm that pivoted at a point outside the TIS chamber. The arm was surrounded by an internal steel vacuum bellows and positioned by three stepping motors that moved the arm on linear bearings. The extraction electrode position, relative to the source, was determined by reference

to 3 calibrated linear potentiometers; a linear pot for each if the directions of motion. The moveable electrode greatly increased the amount of beam that could be extracted. It could be used to adjust for small errors in initial source alignment and also to adjust for misalignment from thermal stresses during operation.

The Electrostatic Beamline:

After a few initial on-line runs with TISOL it became apparent that radiation background levels at the first focus position were too high to permit isotope yield determination. Further beam transport was required to bring the beam to an area of low background; it was decided to build a beamline extension using electrostatic optic elements. The space limitations at the TISOL facility required a 90° bend (in the magnetic dipole bend plane) to a accomodate slit source geometry. Though the use of slit sources has essentially been abandoned, the electrostatic beamline extension was designed to accommodate both slit and circular beam "objects".

The requirements for the electrostatic elements were calculated, by L.Buchmann of the TRIUMF ISIS group, using computer modeling with the electostatic transport code SPEAMVI (Fo74); the first focus beam spots were used as the "objects" for the elecrostatic optics. The calculations showed that to accommodate both slit and circular

geometries, 2 electrostatic quadrupole triplets were required: one before and one after the the 90° electrostatic

Table 2

Geometry of the Electrostatic Beamline

Element	Beam Drift Length (in)	Aperture (in)	Total Position at Element Start (in)
D1	15	> 7	0
Q1	10	7	15
D2	2	> 7	25
Q2	10	7	27
D3	2	> 7	37
Q3	10	7	39
D4	11	> 5	49
B	29.8	> 4	60
D5	4	> 5	89.8
Q4	10	4	93.8
D6	2	> 4	103.8
Q5	10	4	105.8
D7	2	> 4	115.8
Q6	10	4	117.8
D8	~ 40	4	127.8
IMAGE			~ 168

D ≡ driftspace, Q ≡ quadrupole, B ≡ 90° bender

bender. The final design geometry is given in Table 2. The first quad triplet brings the beam to a focus just after the exit of the bender, the second triplet then recaptures the beam and can be used to produce a final focus (over a wide range of distance) at the end of the beamline. The quad pairs Q2-Q3 and Q5-Q6 are used to confine and focus the beam, Q1 and Q4 are used to remove asymmetries caused by the initial "object" and the selective bender focusing. Additional beam steering was provided by installing horizontal and vertical electrostatic deflection plates (5 " long) after the final quad (Q6) just in front of the final focus. Also, the poles (opposite pairs) of Q3 could be biased up to ± 3 KV to provide further steering.

In operation, the electrostatic elements require ~ 3.25 KV for the 90° bender and ≤ 1.5 KV for the quads. The bender, quads and steerers are controlled by the TISOL computer control system. Individual power supplies are paired in a master-slave configuration such that setting the desired potential on the positive power supplies automatically sets the equivalent potential on negative power supply of the pair.

Unlike the magnetic transport system, the performance of the electrostatic beamline has been entirely as predicted by the initial design. Final beam spots < 1 cm ϕ have been observed using nominal potential settings. In practice, the addition steering described above is never used because it

is not necessary. The electrostatic beamline is schematically shown in Figure 9.

Beam Diagnostics:

The main beam diagnostic elements are 4 internal Faraday cups placed along the beamline. The first three are movable copper plates that can be rotated in or out of the beam axis by triggering pneumatic pistons. Faraday cup 1 is situated just outside the TIS chamber and is used to monitor the total beam current leaving the extraction electrode. Faraday cup 2 is situated at the entrance to the dipole and monitors the beam current after the magnetic quads. Faraday cup 3 is located after the first electrostatic quad triplet, at the entrance to the 90° bender. The last Faraday cup (4) is the stationary beam collector at the final focus. Faraday cups 2 and 3 are of limited utility because they are not at positions corresponding to a focussed beam. At these positions the beam may be larger than the surface of the Faraday cup and the measured beam currents are not used for accurate calibration.

Additionally, two helical wire scanners were installed at the Faraday cup 1 and 2 positions. A wire helix is rotated about an axis perpendicular to the beam and at 45° to the horizontal and vertical planes. This wire cuts the beam twice in each rotation: first in the vertical then the horizontal plane. The current measured on the rotating wire

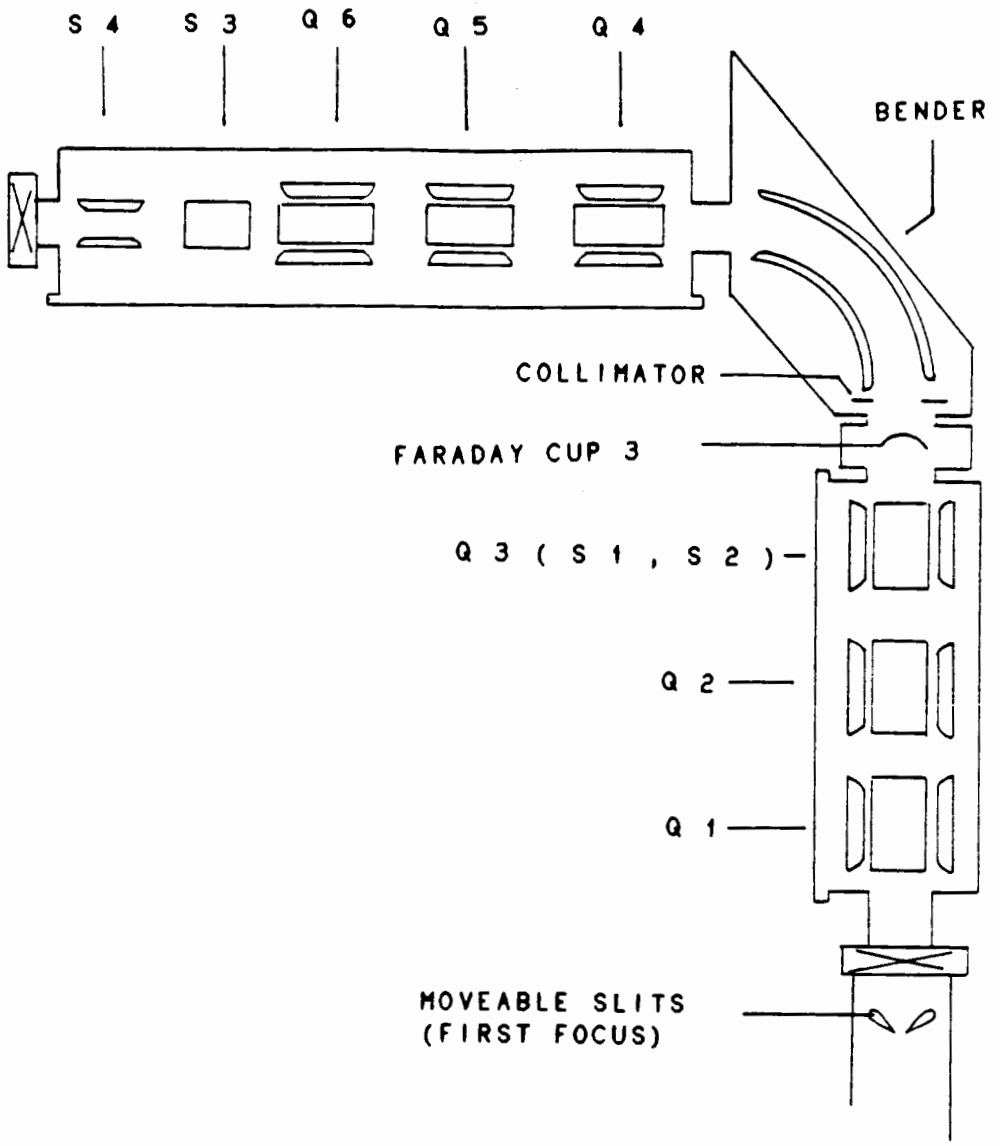

Figure 9: Schematic representation of the electrostatic beamline.

is processed by an independent control unit and displayed as a trace on a storage scope or PC terminal. As with the Faraday cup, the wire scanner in front of the dipole is of little use. The beam profile at this point is so large that the wire is essentially in the beam at all times.

The manual scanning slit at the first focus, used for initial beam diagnostics, has been replaced with a remotely controlled adjustable collimating slit. The slit opening can be varied from 0 - 50 mm in the bend plane. Both sides of the slit are isolated and can be independently used to monitor the beam striking each side. Additionally, a horizontal wire can scan the beam in the non bend plane at this position.

THE TISOL COMPUTER CONTROL SYSTEM

Design Criteria:

The TISOL separator is essentially a secondary beamline at TRIUMF. With the requirement of simultaneous control of beamline vacuum elements, beam transport elements and ion sources at both high temperature and high voltage, the operation of TISOL is as complex (or more complex) as that of the muon channels of beamline 1A. System components must be monitored and controlled remotely, since access to most areas of TISOL is denied during on-line operation. A further difficulty arises in the need to control and monitor

those system components that are at high voltage. Both practical and safety considerations require the use of a control system that can continuously monitor the TISOL system status and can react quickly to potential problem situations. Since TISOL is a test facility, the control system must also be flexible; system changes and expansions must be easily accommodated. Since TISOL also has the potential to be an experimental facility, the control system must be relatively easy to operate; control must be available to experimenters without specialized system programming skills. Finally, there was an additional financial design constraint; the TISOL budget limited the type of system that could be acquired. The initial purchase price had to be modest and the system had to be such that components could be acquired as the need arose, and the budget permitted.

Fortunately, it was possible to assemble such a system. The TISOL control system is based on a modestly priced host computer (originally an XT clone, currently an AT clone) that communicates with a series of modular input/output controllers. Both digital and analog controllers are available and the system is expandable to a maximum of 4096 controllers. Experimenters can access the control system through the host computer keyboard using a simple "conversational" set of commands. A schematic representation of the TISOL system is displayed on the host computer monitor screen and

TISOL components can be quickly activated by highlighting the required graphics "icon" and pressing a key for confirmation. The control system was developed, for TISOL, by TRIUMF staff; the expert services of R.Keitel (software) and D.Harrison (hardware) are most gratefully acknowledged. Conversion of system components to remote operation, cabling and interfacing to the control system were TISOL responsibilities.

Control System Hardware:

The TISOL control system hardware consists of a host IBM PC clone computer (running the MS-DOS operating system) connected via an RS422 serial port to an industrial OPTOMUX™ system (Op22) of intelligent addressable input/output (I/O) control modules; these modules are, in turn, connected to the TISOL devices. The modules are located on OPTOMUX I/O boards; each board has a Motorola 6803 microprocessor which coordinates I/O and communications protocol. Both digital and analog OPTOMUX boards are available, each with up to 16 plug-in positions for digital-input, digital-output, analog-input, analog-output, analog-to-digital (ADC) or digital-to-analog (DAC) controller modules. Different I/O boards are used for digital and analog modules. The analog boards accommodate 12 bit ADC's or DAC's. The digital boards accommodate a combination of AC and DC I/O modules; all of the I/O channels are optically

isolated (4 kV rms). Commands from the host computer to the modules are interpreted by OPTOWARE^{TM} software. The OPTOMUX system architecture allows for a maximum of 256 remote I/O boards (for a total of 4096 I/O points) at distances up to a mile from the host computer. The modular nature of this system makes it ideal for an expanding and changing application such as TISOL.

The OPTOMUX boards are mounted in an equipment rack adjacent ot the host computer on the TISOL control platform. Additionally, a "satellite" rack controlling the electrostatic beamline elements is located adjacent to the final focus of the separator. A second "satellite" rack, containing modules that control the devices at high voltage, is located inside the Faraday cage. Since both the devices and their OPTOMUX modules are at a potential of up to +20 kV, communication with the rest of the system (at ground potential) is maintained through a two channel fiber optic link. Some appreciation of the complexity of the TISOL control system can be gained from its OPTOMUX module requirements. In 1989 the OPTOMUX module list was roughly as follows:

<u>Digital 110 V AC outputs:</u>

4 mechanical pump "on" drivers

8 gate valve "open" drivers

10 solenoid valve "open" drivers

3 Faraday cup "in" drivers

3 extraction electrode motor "forward" drivers

3 extraction electrode motor "reverse" drivers

6 extraction electrode "forward/reverse" limits

2 1st focus collimator slits motor "open/close" drivers

5 cold cathode ion gauge "on" drivers.

Digital 110 V AC inputs:

10 solenoid valve internal "open" readouts

Digital 24 V DC inputs:

4 mechanical pump "contactor in" signals

3 turbo pump "at speed" signals

6 Faraday cup "in/out" limits

2 1st focus collimator slits "open/close" limits

16 gate valve "open/close" limits

3 "watchdog" emergency shutdown inputs (internal)

Digital 5 V DC outputs:

3 dipole magnet range readout extension outputs

Analog 0 - 10 V DC ADC's:

5 cold cathode ion gauge readouts

4 convectron gauge readouts

11 thermocouple vacuum gauge readouts

3 extraction electrode position readouts

6 proton beam position readouts

1 1st focus collimator slits position readout

1 dipole magnet power supply current readout

1 Hall probe readout

Analog 0 - 10 V DC DAC's:

1 dipole magnet power supply current control DAC

Satellite Modules at High Voltage:

15 digital "on/off", "ramp up/down" I/O modules controlling 3 power supplies

3 0-10 V ADC power supply current readouts

3 0-10 V ADC power supply voltage readouts

3 0-10 V ADC target themocouple probe readouts

Satellite Electrostatic Beamline Modules:

5 5 V DC electrostatic bender control outputs

2 5 V DC steerer #3,#4 "inhibit/enable" outputs

2 110 V AC steerer #1,#2 p.s. contactor drivers

2 110 V AC steerer #1,#2 p.s. contactor readbacks

1 110 V AC quadrupole p.s. contactor driver

1 110 V AC quadrupole p.s. contactor readback

1 0-10 V electrostatic bender control DAC

2 0-10 V electrostatic bender +/- voltage monitor ADC's

2 0-10 V steerer #3,#4 p.s. voltage control DAC's

2 0-10 V steerer #3,#4 p.s. voltage monitor ADC's

6 0-10 V quad p.s. (+/-) voltage control DAC's

6 0-10 V quad p.s. (+) voltage monitor ADC's

6 0-10 V quad p.s. (-) voltage monitor ADC's

2 0-10 V steerer #1,#2 p.s. voltage control DAC's

2 0-10 V steerer #1,#2 p.s. voltage monitor ADC's

Since the end of 1990, further modules controlling a variety of new elements necessary for operation of a more complex

ion source, have been added. The OPTOMUX hardware racks and modules were constructed and assembled by D.Harrison of the TRIUMF microprocessor controls group.

Control System Software:

As with the hardware, the software requirements of the TISOL control system demanded flexibility. For example, changes in the type of ion source (surface, plasma, ECR) require different vacuum, magnet and power supply configurations. The control system software must be able to be readily redefined to adapt to a reconfigured hardware system. The TISOL control system (TICS) software was developed by R.Keitel of the TRIUMF microprocessor controls group. Though TICS was initially designed for TISOL, one of the design goals was to provide a standard in-house system that would replace the "one of a kind" control systems existing at TRIUMF. TICS was designed to run on IBM compatible PC's and provide a fully functional stand-alone control system that was flexible and general enough to service, not only TISOL, but any similar secondary beamline, complex experiment or process control at TRIUMF.

The TICS software system is based around a data base language (TICSLanguage) which is used to describe the configuration of the system (system definition) and its graphic display on the host computer (display definition) in two ASCII text files. The two definition files (TISOL.DEF &

TISOL.DSP) can be edited using any ASCII text editor. The TISOL.DSP file contains the layout of the graphics display of the system: number of pages, icon location, window sizes, display parameters for logged data. The TISOL.DEF file contains :

i) hardware commands for all devices in the system

ii) device interlocks

iii) alarm conditions

iv) reactions to alarm conditions

v) unit conversions for device readbacks. eg: Volts per bit

vi) instructions for logging device status

Within the TICSLanguage, there are standard definitions for device classes such as PUMP, POWER SUPPLY, VALVE, GAUGE, MOTOR, etc. Special devices merely require a new device definition rather than a change in the entire control system. In this way, the software, as well as the hardware, is "modular".

Once the .DEF and .DSP files have been edited to reflect the desired system configuration, they are compiled by a TICSLanguage compiler (TICSCMPL) that generates system tables for the main control program TICS. Compilation is automatically invoked at system startup and the command "start <*name*>" will automatically compile the <*name*>.DEF and <*name*>.DSP files. Thus, more than one set of files can be generated to reflect different system configurations. TICSLanguage syntax errors simply abort compilation and the

user is given a (usually) meaningful error message. Once operational, an on-screen help facility is available.

The main program TICS does the actual system control. It continuously reads and checks the defined devices, handles commands from the user and updates the display. The average turn around time for checking every device in the system is 400 - 600 μsec, depending on system configuration. The program has a data logging utility that can be configured to write the status (or value) of selected devices to a disk file at specified time intervals. Using this utility provides a means of tracking the condition of the system over extended periods of time. A graphic display of one or more device parameters is also immediately available on a second display monitor. Display ranges and sampling rates can be set by simple commands and the monitored devices can be readily changed. This feature is very useful since it provides a quick visual means of monitoring, for example, the change in vacuum gauge reading (device #1) as a function of target oven power supply current (device #2). However, the primary utility of the computerized control system is in its ability to detect alarm conditions and react accordingly, much faster than a human operator. The second most useful feature is the definition of device interlocks; a device is activated only when all its interlock condition are satisfied. Both alarm and interlock conditions are defined in the .DEF file, but may be bypassed at any time by

commands from the operator. An example of the TICS system control screen is shown in Figure 10. Figure 11 shows an example of a section of a system definition file, with primitive OPTOMUX commands, interlock conditions and alarms. Further details of the control system architechture are available in references (Ke87) and (Ke90).

Device Connection:

Each of the control system OPTOMUX modules had to be connected to its corresponding device, to activate it or to read its status. Running individual cables to each device is not practical and, furthermore, defeats the "modular" design approach of the control system. In order to maintain a flexible philosophy at the actual device connection level, a system of distribution boxes was used. Distribution boxes were situated at various locations of the separator and connected to the OPTOMUX racks by multiconductor cables; shorter lengths of the appropriate cable were then run from the "octopus" boxes to individual devices. Separate boxes were used for 110 V AC (to drive devices) and for low voltage DC (device status); three AC boxes and two DC signal boxes were located in the TISOL containment room. Four more (two of each) were located above the shielding blocks near the first and final focus positions. In addition, dedicated "octopus" boxes were used for the extraction electrode (driver, status and position signals) and for the two turbo

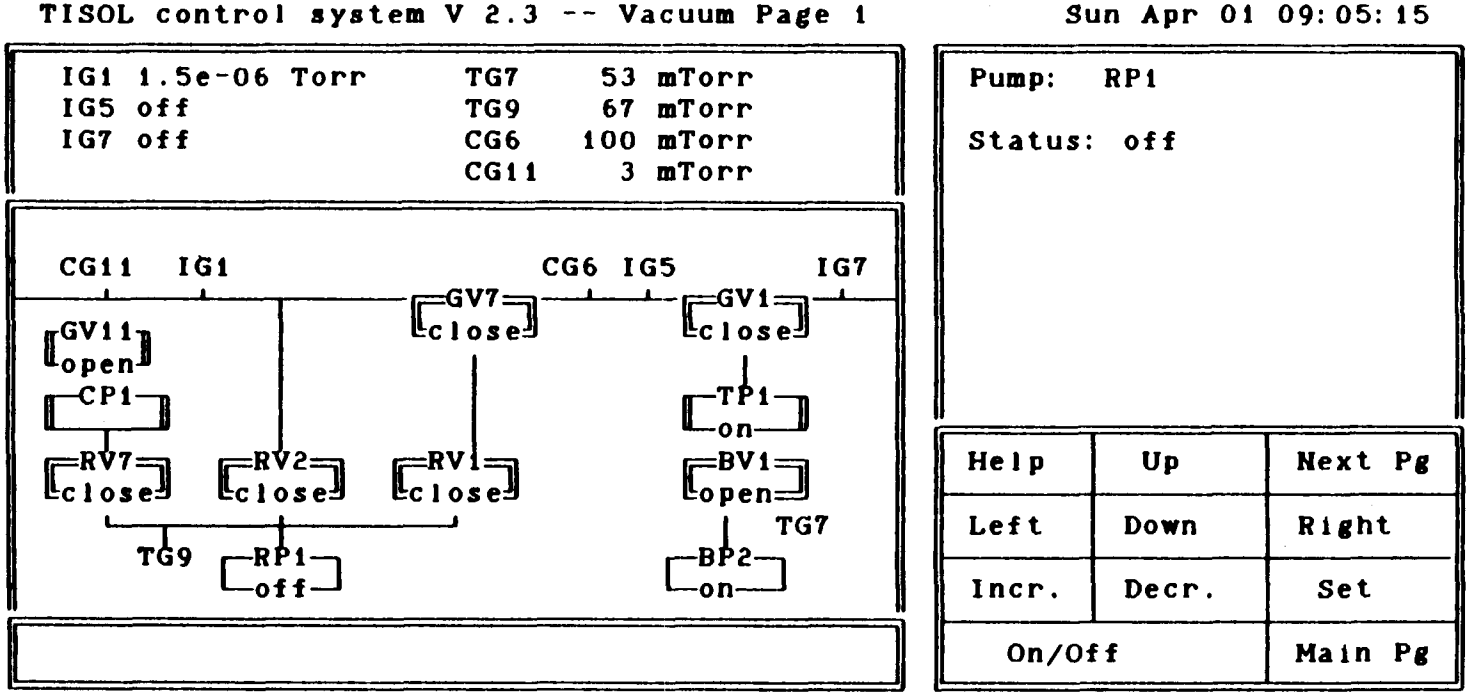

Figure 10: A page from the TICS screen display. Vacuum gauge readings are at the top of the screen. The upper right frame gives detailed device information, the lower right frame shows the numeric keypad map.

```
definition TISOL
devices
   pump TP1
      turbo
      commands
         on                  b253 p0 c10   (a)
         condition TG7 < 0.25 Torr         (b)
         condition BV1 open                (b)
         off    default      b253 p0 c11   (a)
         read_status         b253 p2 c12   (a)
         read_status2        b253 p2 c12   (a)

   valve VV1
       commands
         open                b250 p0 c10    (a)
         condition GV11 closed              (b)
         condition GV7 closed               (b)
         condition RV2 closed               (b)
         close  default      b250 p0 c11    (a)
         read_status         b250 p2 c12    (a)

   gauge IG5
       conversion output
         table cldcat.tbl
         volts_per_bit 0.00244              (c)
       commands
         on                  b251 p14 c10   (a)
         condition CG6 < 0.05 Torr          (b)
         off    default      b251 p14 c11   (a)
         read_status         b252 p8 c12    (a)
         read_value          b255 p1 c37    (a)
..
alarm_if RV2 open            action close RV1       (d)
                             action close GV11
                             action close VV1
                             action close RV7
alarm_if BP2 on              action RP1 off         (d)
..
log IG1                                             (e)
log TG7
log CG6
log PS2
log_time 20 seconds
end_of_definition
```

Figure 11: Excerpt from of a control system definition file.

(a): OPTOMUX commands: board 253, position 0, command code 10

(b): interlocks, (c): unit conversion, (d): alarm definition,

(e): device logging instructions.

pumps in the containment room.

For AC boxes, 16 conductor, 16 AWG cables with 16 pin MS connectors at both ends were run for lengths ranging from ~ 150' (containment room) to ~ 70' (above the shielding blocks). The OPTOMUX rack and the "octopus" boxes were equipped with mating MS connectors. Distribution lines from the "octopus" boxes to the individual devices were 3/16 AWG rubber-insulated cabtire with 4 pin MS connectors at the device end. Mating MS connectors and neon indicator lights were installed on metal junction boxes on all AC devices. At the "octopus" box, the distribution lines were connected to a terminal block using crimp connectors. Allowing two conductors for ground and neutral lines, a maximum of 14 devices could be driven from each "octopus" box. In order to add a new device, an OPTOMUX module is plugged into the appropriate position on a card, the software is redefined and an additional cable is run from the "octopus" box to the new device; the modular flexible nature of the system is maintained, long runs of new cable are unnecessary, and a minimum of time is spent in a radioactive environment connecting the new device. By wiring all devices with standard connectors, the lines assigned to devices are easily reallocated with system reconfiguration.

The DC signal "octopus" box construction is analogous to that of the AC boxes. Since the DC levels are used merely to indicate switch closures, a lighter cable gauge is used.

Cables are 25 conductor 22 AWG with DB-25 connectors at both ends, as before, mating connectors at the boxes and the OPTOMUX rack are used. Between the "octopus" boxes and the devices, shielded twisted pair conductors with LEMO "0" 2-pin connectors are used; the boxes are prewired with mating connectors. One of the 25 pins of the conductor is used for a "common ground" allowing a maximum of 24 signals per "octopus" box. New devices or new limit switches are added as before: an OPTOMUX module is plugged in, the software redefined, the new lines connected at the "octopus"box.

Unlike the limit switches and AC driven devices, all vacuum gauges are cabled independently. The vacuum gauge requirements do not have to be as flexible as other devices. Furthermore, using "common" lines for several gauges is not appropriate. Initially, spare lines were provided for possible expansion of gauge requirements and these have generally accommodated systm expansions. Similarily, lines for Faraday cups and wire scanners are cabled independently.

THE SURFACE IONIZATION SOURCE

At the beginning of TISOL construction, it was decided that the first ion source to be built would be a surface ionization source. This decision was based on practical considerations. Surface ionization is probably the simplest means of obtaining an ion beam: unlike plasma or electron

cyclotron resonance (ECR) sources, no support gas or magnetic field is required, only a clean, hot, metal surface. Furthermore, the surface ionization efficiencies for some elements (especially the alkalis) are very high; the theoretical efficiency for Cs^+/Cs can be essentially 100%. A simple efficient source was considered ideal for initial testing, developing and commissioning of TISOL.

Principles of Thermoionization:

Thermal ionization takes place in metallic enclosures containing atoms and charged particles, both with thermal energies. Unlike discharge ion sources, the energy of the charged and neutral species is roughly equal and essentially defined by the temperature of the enclosure. About 1920, M.N.Saha (Sa20, Sa21, Sa23) derived an equation describing the ionization efficiency of a thermal plasma, in such an enclosure, based on the principle of quasi-neutrality: that is, that the density of electrons and ions in the plasma is

roughly equal. According to the Saha equation, the ionization efficiency (η) is given by:

$$\eta = \frac{n_i}{(n_i + n_0)} = \left[\frac{\gamma}{(1 + \gamma)}\right]^{1/2}$$

where: n_i, n_0 ≡ density of ions and atoms respectively

and:

$$\gamma = 2(g^+/g^0)(2\pi m/h^2)^{3/2}p^{-1}(kT)^{5/2}\exp[-W_i/kT]$$

where:

g^+, g^0 ≡ statistical weights of ionic and atomic states; ≈ (2J + 1), where J is the total angular momentum of the ion or atom ground state.

m ≡ electron mass

P ≡ plasma pressure = $kT(n_0 + n_i + n_e)$

W_i ≡ ionization potential of the atoms

T ≡ absolute temperature

π, k, h ≡ the usual famous constants

In 1925, Langmuir and Kingdon (La25) discovered that practically 100% efficiency was experimentally achieved for cesium vapour ionized on a tungsten surface at 1200 K; the efficiency predicted by the Saha equation was only ~ 0.1%. The discrepancy was attributed to the inapplicability of the quasi-neutrality assumption. The electron density (n_e) was instead defined by the density at the tungsten surface:

$$n_{e0} = 2(2\pi mkT/h^2)^{3/2}\exp[-\phi/kT]$$

where: ϕ ≡ the work function of the electron emitting surface

When the redefined density was substituted into the Saha equation, a new surface ionization efficiency (β) defined by the so-called Langmuir (or Saha-Langmuir) equation is given by:

$$\beta = \frac{n_i}{(n_i + n_0)} = \left[\frac{\alpha}{1 + \alpha}\right]$$

where: $\alpha = n_i/n_0 = (g^+/g^0)\exp[(\phi - W_i)/kT]$

For the condition $W_i < \phi$, there is a high efficiency with little dependence on temperature. For $W_i > \phi$, the efficiency is strongly dependent on both temperature and ionization potential. The Saha-Langmuir equation described the experimental data very well and was used for theoretical predictions of thermoionization until the early 1970's. At that time, groups at Livermore (Jo73) and Dubna (Be71) again discovered anomalously high ionization efficiencies while studying the ionization of lanthanides in high temperature cavities. One possible explanation was the formation of a molecular oxygen layer on the metal ionizing surface, which increased the effective work function. However, Latuszynski & Raiko (La75) found that the ionization efficiency was dependent on the extracted ion current. Kirchner and Piotrowski (Ki78) then showed that the Latuszynski & Raiko efficiency formula was identical to the Saha equation except for a 1.47 normalization factor. Kirchner (Ki81) went on to describe the characteristics of thermoionization in light of both Langmuir surface ionization and an ion current, plasma pressure dependent Saha formalism. Kirchner concluded that for a cavity with a large exit orifice and a temperature below ~ 2500 K, the ionization efficiency is described by the Langmuir equation. For ionization of trace amounts of material in a high temperature cavity with a small orifice (~ 0.1 mm) the efficiency was governed by the vapour

pressure of the ionizing surface (with W_i < 8 eV) and the Saha equation was a valid. The Saha equation was also considered to be valid for ionization of macroscopic amounts of material, in which case the ionization efficiency was dependent on the vapour pressure of material; in such a case the orifice size was less important.

In summary, it appears that surface ionization (Langmuir equation) is dominant for the conditions W_i < ϕ in all cases. For W_i > ϕ, surface ionization is also dominant if the exit orifice of the ionizing cavity is large and the temperature is < 2700 K for a rhenium ionizer or < 3000 K for a tungsten ionizer. At higher temperatures, with a small exit orifice, "thermal plasma" ionization (Saha equation) is dominant, or at least a good approximation. The limiting temperatures may be lower if impurities (with sufficiently high vapour pressures) are present in the ionizer materials.

The McGill Surface Ionization Source:

The first surface ionization target/ion source used at TISOL was designed at the Foster Radiation Laboratory (McGill University) and assembled at TRIUMF. Preliminary development and the first on-line runs used variations of this source. The source was inserted vertically into the target chamber. Both target and ionizer were suspended from the vacuum feedthru connectors used to deliver current

through the top sealing plate of the target chamber. Commercial ceramic isolated feedthrus (Varian) were welded to the top plate. These solid copper connectors for DC current heating of the target were rated for 600 Amps maximum while those for heating the surface ionizer were rated for 250 Amps maximum. An additional feedthru for a thermocouple was also welded to the top plate. Figure 12 shows the feedthru orientation on the TIS plate.

The target oven was a cylindrical tube with a 0.016" wall thickness, machined from a single piece of high purity graphite. At the ends of the tube the graphite increased to 0.125" thickness for 0.500" on each side. These thicker portions were clamped by 1/2" thick by 4.00" by 1.500" graphite support pieces that carried the current necessary to resistance heat the oven. Threaded graphite screws were used to supply adequate clamping pressure and make a good contact. The graphite oven clamps were connected to molybdenum rods that were clamped in turn by copper support pieces connected to the vacuum feed thrus. The support structure was constructed such that lateral and rotational freedom was available to align the oven correctly. The top of the oven had a 0.745" by 0.245" opening to allow for diffusion of products into the ionizer assembly. Crucibles containing the actual target materials were placed in the oven and the oven was sealed by thin graphite foils held in place by graphite split rings. A cylindrical 0.020" thick

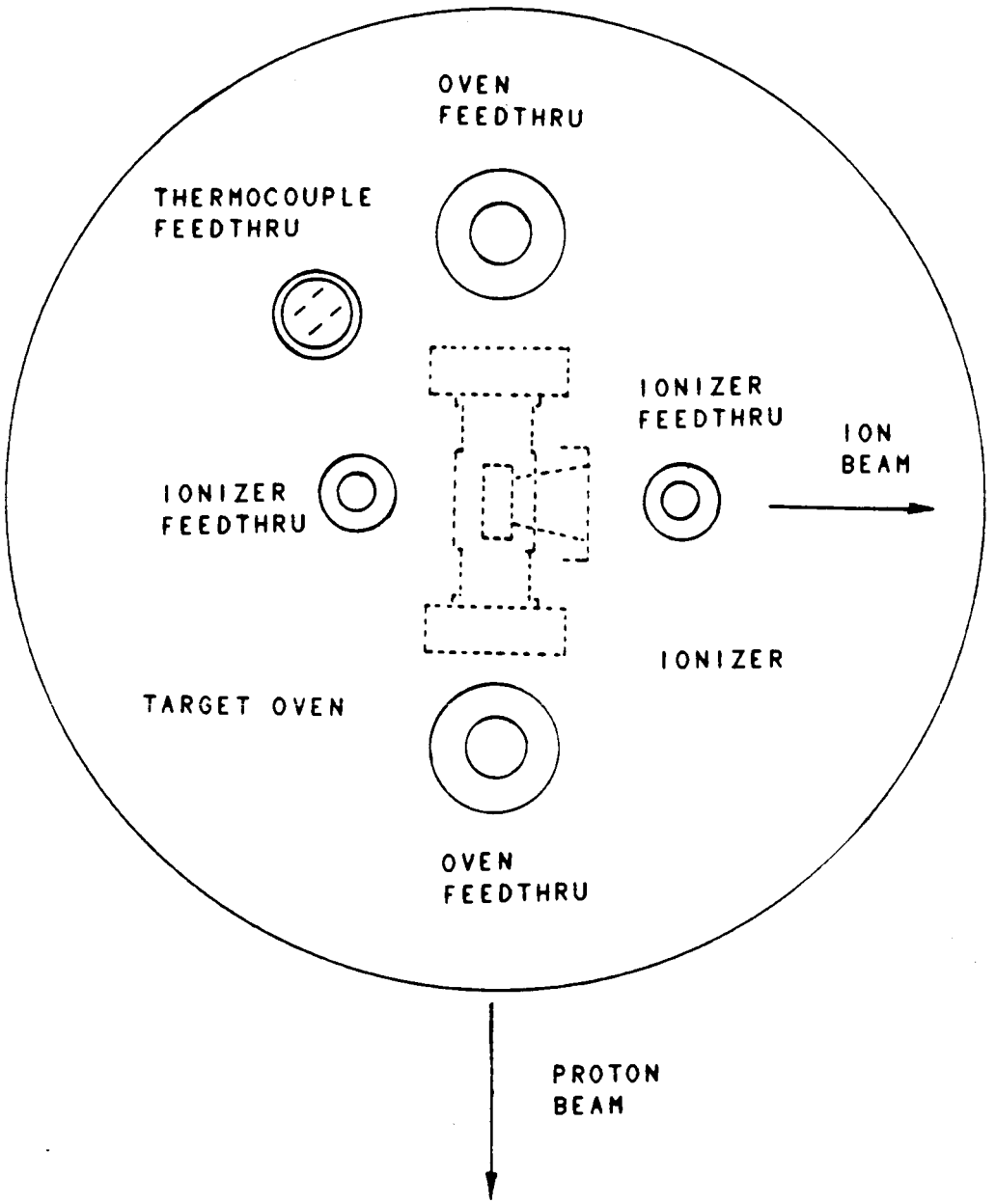

Figure 12: Feedthru orientation of TIS plate.

Ta metal heat shield resting on boron nitride support rings surrounded the oven. The oven assembly is schematically shown in Figure 13.

The ionizer assembly consisted of a thin (0.001") metal foil cavity (1.250" long) spot welded to thicker (0.020") Ta metal support pieces. For economic considerations, a tantalum foil was used to ionize Cs and Rb for initial tests. Later, rhenium and platinum foils were used to obtain higheryields of the lighter alkali elements. The rear support piece consisted of a rectangular chimney that fit into the oven exit orifice through a boron nitride insulator. The front support piece defined the exit orifice of the ionizer. Initially, the ionizer had a slit geometry: 0.75" by 0.062", later a circular (~5 mm ø) ionizer was used. The center axis of the ionizer (the TISOL ion beam axis) was 0.750" above the central axis of the oven (the proton beam axis). As with the oven, the tantalum ionizer support pieces were connected to the vacuum feedthrus by a series of intermediate copper connectors allowing for lateral and rotational positioning. The ionizer assembly is schematically illustrated in Figure 14.

The temperatures achieved by resistance heating both the ionizer and oven were measured by using an optical pyrometer and later, *in situ*, by a W-5%Re vs. W-26%Re high temperature thermocouple with a maximum operable temperature of 2760° C. The temperature curves were calibrated in terms of the power

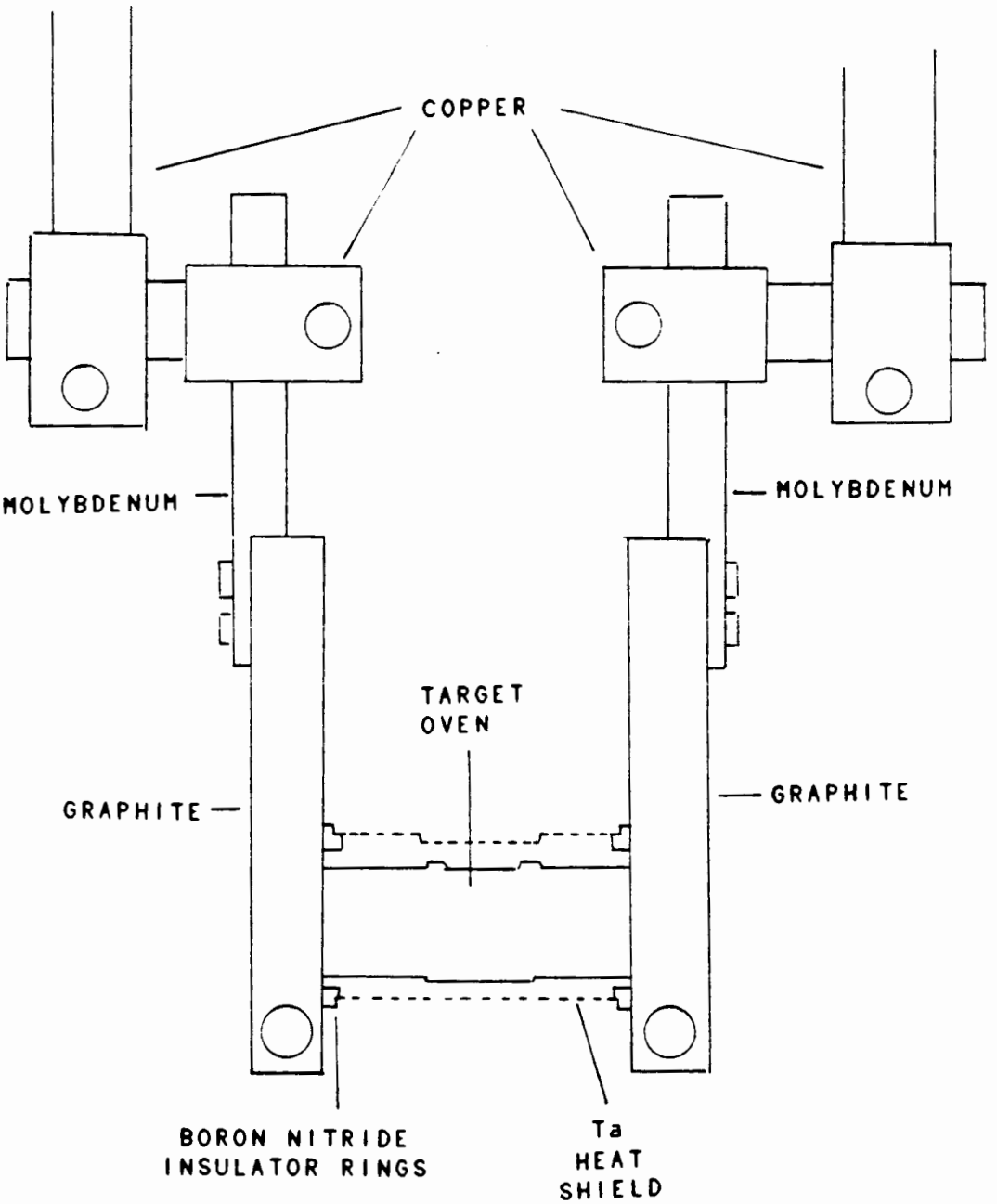

Figure 13: McGill surface source oven assembly.

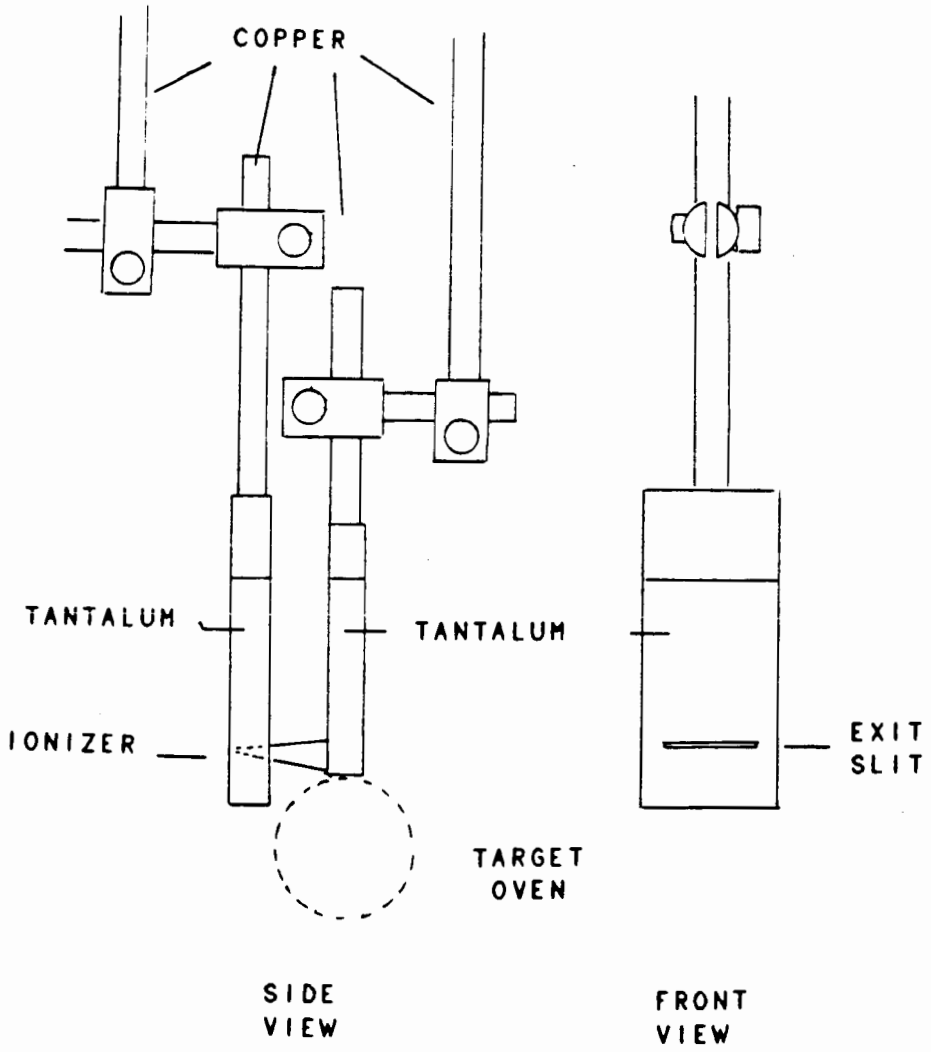

Figure 14: McGill surface source ionizer assembly.

supply currents and estimated accurate to about ± 200°.

Off-Line Testing & Performance:

Prior to on-line operation, the target/ion source was extensively tested in an off-line mode. The main purpose of the off-line tests was to examine the beam transport properties of the separator, calibrate the magnets and generally become familiar with its operation. The operational properties of the ion source also became apparent during these tests.

Ion beams were generated using small quantities of alkali carbonates placed in the oven; these carbonates decompose at relatively low temperatures and provided a source of alkalis for ionization. The surface source ionized all the alkalis from Cs to Li. Generally, the rubidium beams were used since the two stable isotopes provided a good means estimating mass resolution.

During the tests it immediately became apparent that the source, as designed, was unsuitable for high temperature operation. Radiant heat from both the oven and, to a lesser extent, the ionizer was high enough to compromise the integrity of the target chamber O-rings. As well, the operation of the cryopump was seriously compromised by radiant heating from the source. To alleviate the heat problems, water-cooled copper plates were installed (to act as heat shields) on the interior of the target chamber walls

and between the ion source and cryopump. Further heat shielding in the form of a water-cooled copper shield was installed on the TIS plate. This cylindrical heat shield completely covered the ion source except for the front ionizer support. Thin steel windows were spot welded over cutouts on each side of the heat shield "can" to minimize material in the proton beam path. After installation of the heat shields, no excessive temperatures were detected on the walls of the target chamber and the cryopump operation was much improved.

Further problems with the ion source became apparent with subsequent operation. The thin walled oven and ionizer were subjected to stresses due to their thermal expansion and the expansion of their support arms. The stress on the oven was not critical and an oven could be subjected to relatively long heating periods before it deteriorated to the point where it cracked. The oven lifetime could not be accurately predicted, but generally an oven would last long enough to allow for at least three on-line runs (1-2 beam shifts) and the required preconditioning (2-3 days per run). The ionizers were much more fragile due to the very thin (0.001") foils used in their construction. The lifetime of an ionizer was even less predictable than that of an oven and the use of platinum ionizers was completely abandoned. The platinum foils were found to burn out too easily with relatively small (but abrupt) changes in heating current.

Typically, an ionizer would not survive more than one (and often less than one) on-line run.

While the eventual failure of an oven or ionizer is unavoidable, changing either is very difficult once the ion source has been running. The primary difficulties are the result of high temperature; screws and connections are invariably seized and often impossible to separate. Furthermore, any repair is acerbated by the fact that the entire source is radioactive and repairs are encumbered by the necessity of working in a glove box during limited exposure periods. Increasing the wall thickness of the oven was not considered viable. To achieve a temperature in excess of 2000° C, a current on the order of 400 A was required. The 500 A limit of the DC power supply used to heat the oven is probably not sufficient to effectively resistance heat a thicker walled oven. Since the oven lifetimes were not critically short and the graphite components were relatively easy to disassemble, it was decided to continue using the existing oven design.

However, the repair of the ionizers was considered too difficult to continue. Since the typical ionizer current was ~ 130 A from a 500 A power supply, a thicker sturdier ionizer could be accommodated. At first, the ionizer design was changed to a circular tube constructed by spot welding a 0.010" thick tantalum foil; a tungsten foil was inserted into the Ta tube to act as the ionizing surface. This

proved slightly more rugged than the previous design. The final design consisted of a commercially purchased 0.020" ϕ Ta tube turned down to ~ 0.016" ϕ (using a lathe) and welded to the front and back ionizer supports. As before, the Ta tube was lined with a W or Re foil that acted as the ionizing surface. This ionizer could withstand 2-3 on-line runs.

Two additional problems with the surface source led to its eventual redesign. Both problems related to the high temperature operation of the source. The first manifested itself during changes in heating current during ion beam separation. It was noticed that with a change in ionizer current (and to a lesser extent with oven current) the measured ion beam intensity would often decrease. Sometimes, the beam intensity could be regained by repositioning the extraction electrode. This suggested that the position of the ionizer exit orifice was changing under the heating load. The approximately 9.5" length of the relatively thin (3/8") ionizer supports apparently produced sufficient torque under heat stress to misalign the ionizer. Since the misalignment could not always be corrected by repositioning the extraction electrode, a more rigid ionizer support design was clearly in order.

The second problem was more obvious and more critical. With increased oven temperature, the target chamber vacuum would seriously deteriorate even after long periods of

conditioning and outgassing. Above an estimated temperature of ~ 1500° C, vacuum conditions were poor enough (10^{-4} torr) to cause high voltage arcing in the target chamber. Clearly, components of the ion source, that were insufficiently cooled, were vapourizing. This was conclusively demonstrated after the final run using the McGill source. During this run the ion source was heated to an estimated temperature of ~ 1900° C. A post mortem of the source showed that virtually every metal to metal connection was irreparably seized and droplets of copper (sublimed from the oven supports) were found condensed on the heat shield. Since the feedthru connectors for both the oven and ionizer were only water-cooled on the exterior of the TIS plate, a redesign with cooling closer to the actual heat sources was indicated.

The TRIUMF Surface Source:

In order to correct some of the problems with the McGill surface source, a redesigned ion source was constructed. Due to time and material constraints, a complete redesign was not possible; the new source was built using the a spare TIS plate of the same design as that of the previous source. The oven and oven heat shield designs were also identical to the McGill source.

The major differences in the new source design were an attempt to rigidly position the source so as to eliminate

thermal misalignment and the inclusion of water-cooling, *in vacuo*, close to the heat sources. The source was designed such that the ionizer, the oven and their respective supports were rigidly clamped to a 0.5" thick, 3.25" by 4.0" copper support block. This block was, in turn, clamped by three aligning screws to a second water-cooled copper block (0.75" by 4.0" by 5.5") suspended from the TIS plate on 1/2" diameter steel threaded rods. Aluminum spacer sleeves (1" O.D.) were placed over the steel rods to rigidly position the cooled support block. The oven and ionizer supports were connected to the vacuum feed thrus in the TIS plate by flexible copper braid conductors. On the previous source, water-cooling was only provided by cooling blocks on the feedthru connectors on the exterior side of the TIS plate. It was hoped that the *in vacuo* cooling and the addition of more efficiently cooled exterior connectors would increase heat dissipation to levels where the vapour pressure of the source components would not cause vacuum deterioration.

The oven, Ta oven heat shield and graphite oven clamping supports were the same as with the previous source. However, the clamping supports were, now, clamped to the aligning block by 0.375" thick copper support pieces. The flexible copper braid conductors, carrying the heating current, were also connected to these supporting pieces. The oven assembly is schematically shown in Figure 15.

As with the oven, the ionizer assembly was also supported

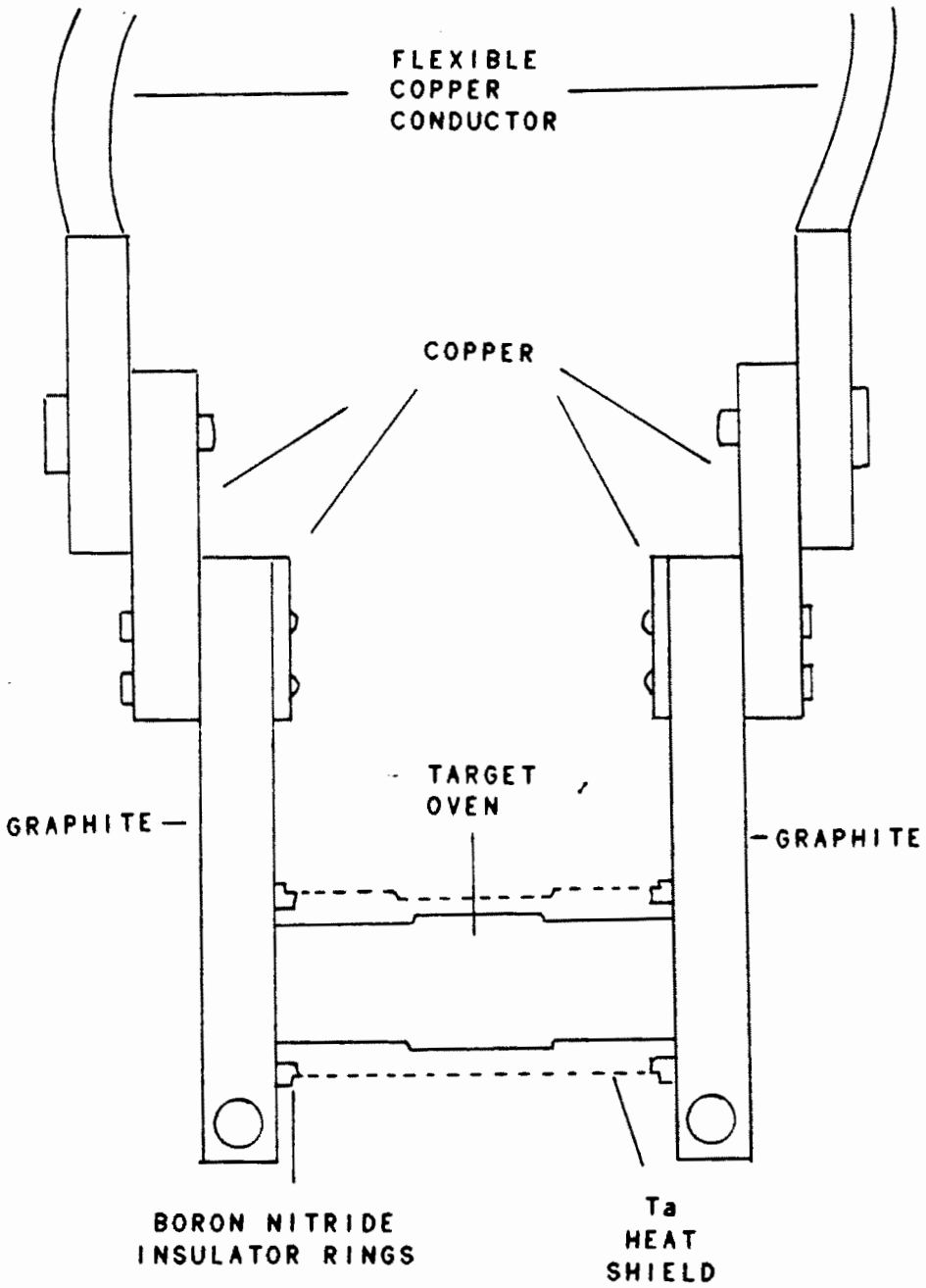

Figure 15: TRIUMF surface source oven assembly.

from the aligning block by copper supports to which the flexible braid conductors were attached. A rectangular chimney of boron nitride connected the oven and ionizer. As before, the ionizer consisted of a tantalum tube welded between two tantalum sheets that were screwed to the copper supports; a rhenium foil was used to line the tube. The ionizer assembly is illustrated in Figure 16. To prevent shorting of the ionizer and oven heating circuits to the alignment block, the copper supports in both cases were insulated from the alignment block (and from their connecting screws) with MACOR™ machinable ceramic. All screws, with the exception of the graphite clamping screws on the oven clamps, were of stainless steel. A stainless steel heat shield lined with several layers of thin tantalum foil surrounded the source and was directly connected to the cooling support block.

The oven and ionizer temperatures were calibrated as a function of heating current using an optical pyrometer. Additionally, a thermocouple placed in the center of the oven was used to study the contribution to oven temperature from the ionizer. With no direct oven heating, an ionizer temperature of ~ 1400° C resulted in a temperature of ~ 400° C at the center of the oven. The oven temperatures, with and without ionizer heating, were not measured so the contribution from the ionizer at high oven temperatures is not known. However, it can be reasonably estimated to be of

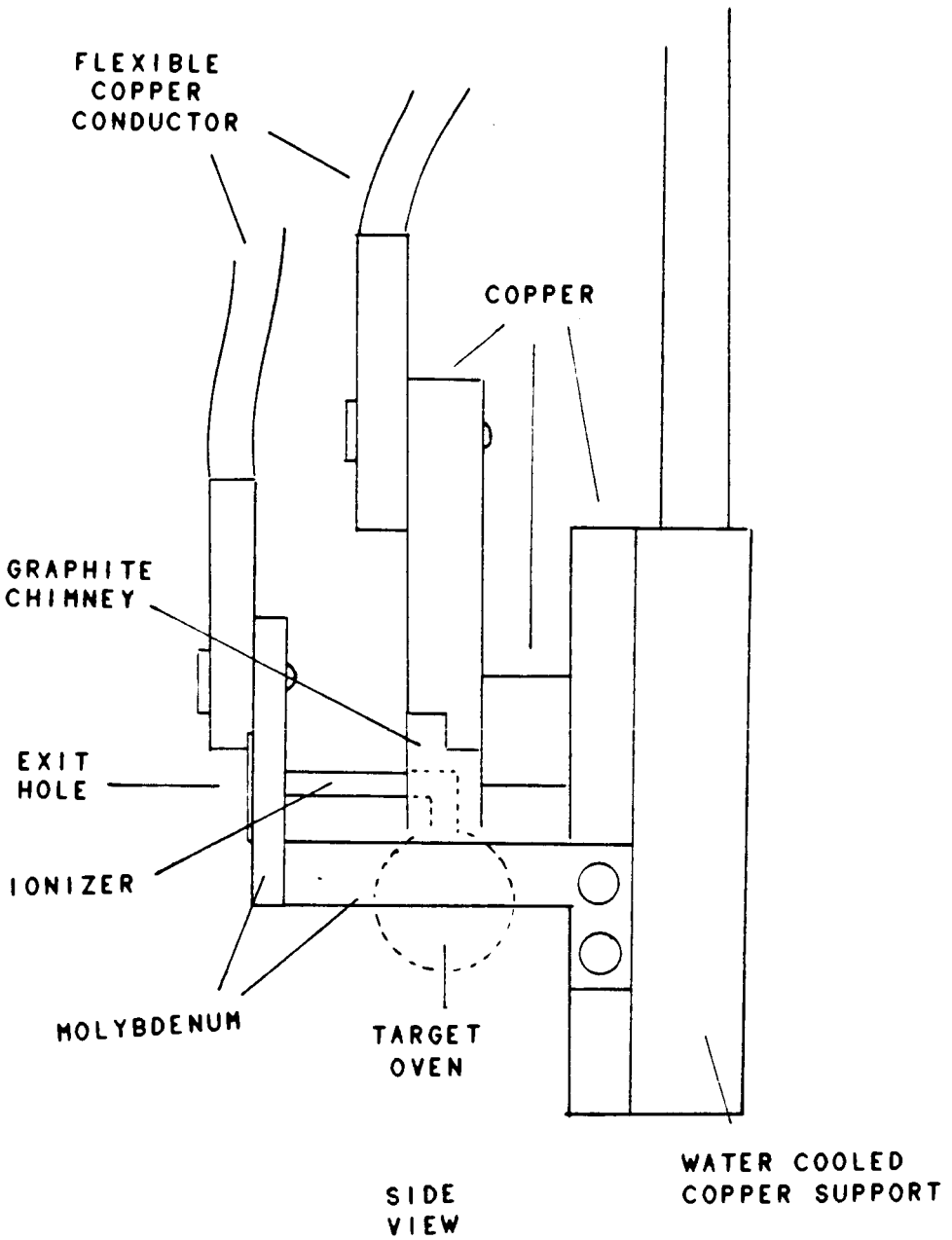

Figure 16: TRIUMF surface source ionizer assembly.

the order of several hundred degrees. A similar increase in ionizer temperature from radiant heat from the oven is also likely. All on-line runs were conducted with an ionizer current corresponding to ~ 1900° C without regard to indirect heating contributions from the oven; the actual ionizer temperature may have been higher by a few hundred degrees. Oven temperature calibrations, using the thermocouple, were conducted with the ionizer heated to operating temperature and can be considered esentially accurate. Temperatures in excess of 2000° C in the oven were achieved with accompanying vacuums in the high 10^{-6} torr range. The absolute temperature could not be determined above 1950° C because the Al_2O_3 insulation of the thermocouple probe vapourised above this temperature. That these temperatures were indeed attained was demonstrated by the observed disintegration of the portion of the insulator that had been in the oven.

The performance of the new ion source was much better than that of the previous model. Not only could higher temperatures be achieved, but thermal misalignment could not be detected. The new source was also generally easier to align. With a source suspended vertically from a circular plate, misalignment is a problem. A small rotation of the top plate can alter the angle of the extracted beam. A small angular misalignment results in a large beam displacement over the flight path to the dipole entrance.

With the previous source, the position of the ionizer exit orifice could not be accurately determined. The source had to be aligned visually through the upstream proton beam port of the target chamber each time it was inserted. With the new source, the rigid configuration allowed a scribe mark to be placed on the back of the cooling block, corresponding to the elevation and center of the ionizer exit orifice. This scribe mark was initially aligned with the beamline center using a surveying theodolite. The TIS plate and mating target chamber surface were then scribed in the aligned position and the source could be aligned at any time by matching these marks.

Though superior, the new source also had its problems. The original BN chimney channeling the product elements from the oven to the ionizer had to be replaced with a graphite chimney. The cooled boron nitride proved to be such a good thermal conductor that volatile elements were condensed in the chimney during diffusion to the ionizer. The original copper front support piece of the ionizer was replaced by a molybdenum substitute, as were the original steel screws on the support. The radiant heat reflected from the extraction electrode was sufficient to melt the heads of the steel screws and anneal the copper. Even using molybdenum did not entirely solve the problems with this piece. The temperature at this point was high enough to often seize the screw making ionizer replacement difficult.

All but three of the on-line runs for yield measurements presented in subsequent sections were made with the TRIUMF surface source. At the end of the surface source runs, the source had not yet burned out.

STUDIES RELATED TO PRODUCTION OF AN ISOTOPICALLY PURE ^{22}Na TARGET

There is considerable interest among the nuclear astrophysics community in measuring the cross-sections for the ^{22}Na(p,γ)^{23}Mg reaction below proton energies of 1 MeV. These cross-sections are deemed important as the reaction is thought to be the most likely mechanism for destruction of ^{22}Na in a Ne-Na cycle presumably occuring in proton-rich stellar environments. Interest in such a cycle stems from the discovery of an isotopic anomaly in Ne inclusions in carbonaceous chondrite meteorites (Eb79). It is believed that the decay of ^{22}Na (formed in explosive stellar events and later incorporated into the meteorites) is responsible for the Ne anomaly. Most likely, the production reaction for ^{22}Na in a stellar environment is ^{21}Ne(p,γ)^{22}Na. Since ^{21}Ne is a stable isotope, it is not difficult to measure cross-sections for such a reaction. However, measuring cross-sections for the ^{22}Na(p,γ)^{23}Mg reaction is more difficult. Theoretically, it would be possible to use a radioactive beam approach and bombard a hydrogen target with a sodium beam, but the long half-life of ^{22}Na

($t_{1/2}$ = 2.6 yr) makes it a suitable candidate for a radioactive target. Practically, this is the only current means of measuring the cross-section in question, since no accelerated radioactive beams facility exists at present.

A typical target thickness for a low energy cross-section measurement is ~ 10^{17} atoms/cm^2, this corresponds to a ^{22}Na activity of ~ 27 mCi. It is crucial that any target used for such a measurement be isotopically pure. Unfortunately, commercially available sources of ^{22}Na have unacceptable levels of ^{23}Na contamination. A mass separator with good mass resolution could be used for preparing a monoisotopic target. A mass separator already used for radioactive species, such as TISOL, is ideal for preparing a radioactive isotopically pure target. Concurrent with the separator developement program and measurement of production yields at TISOL, an isotopically pure ^{22}Na target (~ $6 \cdot 10^{12}$ atoms/cm^2) was prepared.

Production and Separation of ^{22}Na:

Rather than purchasing commercial sodium solutions, more than enough ^{22}Na for the target was obtained from discarded irradiated accelerator parts. Virtually anything made of aluminum that spends some time near an energetic proton beam contains large quantities of ^{22}Na that has been accumulated as the product of the ^{27}Al(p, 3p3n) reaction. Initially, activated aluminum was obtained from LAMPF (courtesy of

R.Kavanaugh, Kellog Laboratory, Cal. Inst. of Tech.). Later, local supplies were obtained as aluminum components from TRIUMF beamline 1A became available.

Even though large amounts of ^{22}Na were present in the aluminum pieces, the Na/Al ratio was too small to consider a chemical separation of the two. Since there is a large difference in the vapour pressures of the two elements, it was decided that the best way to separate sodium from aluminum would be by evaporation. To this end, the melting behaviour of aluminum and its release of sodium were studied. Rather than use the long-lived ^{22}Na in these studies, ^{24}Na ($t_{1/2}$ = 14.97 hr) was used. The ^{24}Na was produced by irradiating aluminum foils in the TRIUMF CP42 radioisotope production cyclotron (42 MeV H^-, 200 μA max.). Target thicknesses were on the order of 2 - 3 g/cm^2 and irradiation times were about 10 - 30 minutes with a 5 μA beam. Normally, 20 - 30 μCi of ^{24}Na were produced and each foil was cut into several pieces allowing several studies.

Initial studies consisted of simply observing the changes visible when aluminum melted. Small (< 10 g) pieces of Al (nonactivated) were placed in boron nitride crucibles and slowly heated in a vacuum evaporator. The temperatures of the resistance heated Ta evaporator boat were determined using an optical pyrometer. Several stages of melting were observed:

i) at about the melting point of aluminum (660° C) no

physical change was observed.

ii) at ~ 850° C the aluminum coalesced into a ball with a dull, darker, outer skin; bright shiny metal could be seen underneath through small cracks in the outer skin.

iii) At ~ 1150° C the "ball" breaks up and aluminum flows freely and creeps out of the container.

The preceding behaviour can be interpreted as follows. Below a temperature of ~ 850° C the molten aluminum is contained in an Al_2O_3 shell and no visible change is seen. Above this temperature, the oxide shell is partially cracked by internal thermal forces and the molten aluminum forms a droplet with an oxide skin. Above ~ 1150° C thermal motion completely overcomes the containment of the oxide layer and the molten aluminum flows freely. In all subsequent studies, care was taken to keep the temperatures well below 1100° C while still ensuring that sodium could be efficiently released.

Once the melting behaviour of aluminum was determined, the release of sodium was investigated. Irradiated pieces of aluminum (containing ^{24}Na) were heated to the "ball" formation stage in the vacuum evaporator. Cooled catcher foils of various materials (steel, Al, Ta) were suspended above the sample in attempts to condence the sublimed ^{24}Na. Gamma counting of the Al samples before and after melting showed that almost all of the sodium was effectively releas-

ed at the "ball" formation temperature; less than 2% of the initial ^{24}Na was present in the Al "ball" after heating. The attempts to condense the sodium on the cooled catchers, however, were not successful. Activity from ^{24}Na was found to be dispersed over the entire interior of the vacuum evaporator.

In order to minimize the amount of bulk material that would have to be placed in the TISOL target/ion source, to produce a sufficiently thick ^{22}Na target, a method of concentrating the sublimed sodium on a catcher foil was investigated. Since the evaporator method had not worked, another technique was tried. Aluminum samples were placed at the bottom of a steel test tube that was, in turn, held upright, by a graphite insert, in a typical quartz sublimation apparatus. The quartz vessel was evacuated and heated to the appropriate temperature in a small tube furnace; temperatures were measured using a thermocoule inserted into the tube furnace. Tantalum, molybdenum or steel catcher foils were affixed to the water-cooled cold finger of the sublimation apparatus, just above the mouth of the steel tube. Gamma counting indicated that while some sodium was deposited on these cooled foils, most (as with the vacuum evaporator) was dispersed over the entire inner surface of the sublimation vessel.

In an attempt to contain the evaporated sodium, a 2 - 3" long chimney made of rolled thin (0.002") Ta foil was placed

over the mouth of the steel test tube. After evaporation, ~ 80% of the ^{24}Na activity was found to be condensed, in a band only a few millimeters wide, inside the Ta foil chimney. This band could be easily cut out and used in subsequent tests in the TISOL system.

Final tests consisted of measuring the ionization efficiency of sodium using the surface ionization source. Either small pieces of irradiated Al or the Ta catcher foils (with condensed ^{24}Na) were placed in BN crucibles in the target oven of the source. Faraday cup 1, located just after the ion beam port of the TIS chamber, was lined with aluminum foil. The ion source was operated at the appropriate temperature, and the extracted beam collected on Faraday cup 1. The ionization efficiency was determined from the initial ^{24}Na activity and the final activity on the Faraday cup liner; typical ionization efficiencies were 5 - 15%. No difference was observed between runs using sodium condensed on catcher foils or released directly from aluminum. Gamma counting the remains in the BN crucibles showed that, as in the evaporator studies, essentially all of the sodium was released. During heating, the extracted beam current on Faraday cup 1 was monitored with an electrometer. In runs using aluminum pieces, beam currents of a few hundred nanoAmps were always present, even with no oven heating. At an oven temperature ~ 600° C a temporary increase in beam current (as high as 1 - 2 μA) was usually

observed for about 5 minutes. The beam current would then decrease to ≤ 500 nA until a temperature of ~ 800° C was reached. At this point a strong sustained increase in beam current (up to 2 μA) was observed for up to 10 minutes. These beam current increases can be interpreted in terms of an initial partial release of Na at the Al melting point followed by a larger, more complete release at a temperature corresponding to the aluminum "ball" formation.

The ^{24}Na ionization efficiency studies were important because they provided the only direct means of measuring the efficiency of the source and separator. Efficiencies for ^{24}Na deposition on Faraday cup 1 were determined on several occasions and never exceeded 15%. When the ^{24}Na beam was brought through the entire separator and deposited at the final focus, a similar efficiency was determined. This suggests a transmission efficiency of ~ 100% for the TISOL beam transpport system. Estimates of transmission efficiency with beams of stable alkalis also suggest that, with a good tune, essentially no beam is lost between Faraday cup 1 and the final focus. Therefore, the limiting 15% value must arise from inefficiencies inside the TIS chamber, either from source leakage, poor ionization or ineffective extraction. In an attempt to trace the missing ^{24}Na, the ion source, extraction electrode and swipes from all interior surfaces of the TIS chamber were surveyed for activity. An essentially even distribution of ^{24}Na activity was found on

all of the TIS chamber walls. The ion source was also active, but no specific areas of concentrated activity could be determined without completely disassembling the source. No ^{24}Na activity was found on the front of the extraction electrode, but this area recieves so much radiant heat from the ionizer that any deposited sodium would quickly be evaporated. It appears that some of the sodium probably remains trapped in the graphite oven of the source. The rest of the missing sodium either leaks out of the source and is distributed about the target chamber, or is deposited and re-evaporated from the extraction electrode.

The theoretical surface ionization efficiency (calculated using the Saha-Langmuir equation) for sodium in contact with a Re surface at 1900° C is ~ 30%. An overall efficiency of 15% suggests that about half of the sodium is lost either before or after ionization.

^{22}Na Target Implantation:

In spite of the low efficiencies measured for sodium beam production, it was decided to implant a ^{22}Na target. Since beam transmission was of the order of 100%, contamination of the separator was not a problem. ^{22}Na contamination of the ion source and TIS chamber could be tolerated since regular on-line operation had already contaminated them.

Two pieces of aluminum having an estimated combined ^{22}Na activity of ~ 1 mCi were placed in a BN crucible in the

target oven of the ion source. Prior to heating the target oven, the separator transmission was optimized using a ^{23}Na beam. Stable sodium is always present in some component of the source and a mass 23 beam is always observed. After optimization, the dipole magnet was set to the calculated mass 22 position and the oven temperature was slowly increased. A 24 mm ø tantalum disk, centered on the final focus Faraday cup, was used used to collect the separated ^{22}Na. The beam current at the collection position was monitored and displayed behavior similar to that previously observed at Faraday cup 1. An initial small current was observed close to the aluminum melting point followed by a stronger sustained current increase at higher temperature. Increasing the oven temperature produced corresponding increases in beam current that would then slowly decay. The average mass 22 beam was ~ 10 nA with maximums as high as 50 nA; occasionally rapid oscillations were observed. After about 20 minutes, oven temperature increases would no longer sustain the beam current which steadily decreased with time. At a current of 2nA, collection was terminated. The collection foil was removed and surveyed for ^{22}Na. It was discovered that the final beam spot had not been tightly centered on the rather large (3.5" ø) Faraday cup. A total of about 50 μA of ^{22}Na had been deposited on the Faraday cup, but only 6 μA was on the collector foil. Since beam spots of ≤ 1 cm ø have been routinely observed at TISOL, the

poor focusing must be attributed to a malfunction of the electrostatic beam line elements.

In conclusion, it has been shown that a ^{22}Na target, although thin, can be prepared using TISOL and a surface ionization source; a 100-fold increase in deposition is easily possible with greater attention to the beam focusing. The sodium release properties of aluminum are now known and sodium activity can be concentrated on a catcher foil. With an improvement in the sealing of the target oven of the ion source, it is likely a further 2-fold increase in deposition can be achieved. Further details of the preceding studies can be found in reference (Da90)

ISOTOPE YIELD MEASUREMENTS

Two of the primary purposes of constructing the TISOL facility were to determine the yields of isotopic beams that could be routinely produced, and develop target/ion sources that maximized those yields. To this end, targets consisting of refractory metal foils and refractory binary compounds were irradiated and ion beams generated using a surface ionization ion source. The yields of isotopes of the ionized elements (mainly alkalis) were systematically measured by gamma and alpha spectroscopy of the deposited beams at the final focus of the spectrometer.

Target Preparation:

With the 500 MeV proton beams available at TRIUMF, two types of nuclear reactions are possible for purposes of isotope production. Spallation reactions of the (p,xpyn) type, where several nucleons are emitted in the exit channel, produce a product mass distribution with a maximum peaked at about 10 - 20 masses lighter than the mass of the target; a subsequent decrease in production towards lighter mass products is exhibited. With heavier targets, proton induced fission reactions are also possible. Here, the products have a broad mass distribution centered roughly about half the target mass. For a target such as U^{238}, both reaction mechanisms are expected to contribute and the product mass distribution consists of a superimposition of both mass yield curves. For a heavy neutron-rich target, the fission mechanism also produces isotopes that tend toward neutron excess when compared to the products of spallation reactions. The choice of an appropriate target requires consideration of both the production cross-sections for the desired isotopes and the ability of the target matrix to efficiently release the product elements.

Choosing targets with regard to production cross-sections was relatively straight forward. Since a surface ionization source was being used in the TISOL yield measurements, the products most efficiently ionized would be the alkali elements. To maximize production of alkali

species, targets containing elements of slightly higher Z than the desired alkalis were chosen, in order to make best use of the spallation reaction mechanisms. A target containing U^{238} was also investigated to measure the yields of neutron-rich rubidium and cesium species.

Choosing an appropriate target on the basis of efficient release of products from the target matrix is anything but straight forward. The rapid release of reaction products may be considered to depend mainly on the speed of two processes: the diffusion of the product through the target matrix and the desorption of the product from the surface of the target. Other factors contributing to the delay of product species are diffusion times to the ionizing surface, adsorption and desorption on ion source surfaces and possible chemical reaction with the target matrix, target impurities or ion source components. Carraz et al. (Ca78, Ca79) have characterized the diffusion and desorption effects on release properties in a variety of high temperature powder and molten target matrices by use of a temperature dependent parameter related to activation energies, diffusion coefficients and target particle dimensions. While these discussions are useful in understanding the principles of release from a target, the prediction of specific release rates for product/target combinations is not easily accomplished. Usually, reliable values of diffusion coefficients and activation energies are

not available for the product/target combinations under consideration. Even when reasonable estimates of the necessary parameters are made, the behavior of a target matrix in the high radiation environment of an on-line production run may be radically different from the behavior predicted by parameters derived from off-line laboratory measurements. Rather than attempt to predict the possible release behavior of product/target combinations from theoretical considerations, it is more productive to measure experimental release rates and production yields, either in actual on-line studies or in off-line studies of previously irradiated targets. Such studies, measuring the release properties of a variety of refractory solid targets and molten metal targets, have been conducted at the ISOLDE (CERN) facility (Ca78, Ca79, Bj81, To81, Ho84, Ra87) and at the ISOCELE (Orsay) facility (Pu81). From these studies, suitable targets for rapid release of many elements have been determined, As well, general indications of the types of elements and compounds that make appropriate targets are gained.

Whatever the difficulties in predicting release behavior, one principle can be relied on with certainty: increasing the temperature of the target matrix will increase the rate of product release. Both diffusion and desorption are directly proportional to temperature. A high temperature in the target/ion source also enables the desired reaction

products to successfully evaporate out of the target matrix and reach the ionizing surface without condensing. Clearly, targets of refractory elements or compounds, with low vapour pressures, are good choices. Initial targets for the TISOL yield measurements consisted of thin foils of refractory metals. For safety considerations, loose powder targets were not allowed in the initial test stages. Target foils of pure titanium, zirconium, niobium and hafnium were chosen; these elements could be expected to produce high yields of potassium, rubidium (from both Zr and Nb) and cesium nuclides respectively. In later yield measurements the safety restrictions were relaxed, and refractory powders loosely pressed (using an organic binder) into pellets were also used as targets. A zirconium carbide target was chosen for comparison with the zirconium foil target and a silicon carbide target was used in an attempt to maximize sodium yields. A pressed powder uranium oxide/graphite target was also used to measure yields of neutron-rich fission products.

Proton Irradiations:

All yield measurement runs were conducted using 500 MeV protons for target irradiation. Beam intensities varied from 200 nA to 600 nA. Beam current was determined by the beamline 4A secondary electron monitor (SEM) situated downstream of the TISOL target; the SEM is calibrated to

read the beam current in nanoAmps for an integration time of 1.6 seconds. The SEM signal was routed into two visual scalers and the beam current read directly in nanoamperes. Usually, several SEM readings were taken during a data acquisition interval and their average value used in yield calculations; an uncertainty of ± 10 nA was assumed. Proton beam alignment was accomplished using a horizontal/vertical split plate beam monitor immediately upstream of the TISOL target. This beam monitor was periodically checked throughout the irradiations to insure that the proton beam had not drifted off target.

Isotope Beam Tuning & Calibration:

In order to tune the separator beamline for maximum transmission to the final focus at Faraday cup 4, the targets were doped with small (microgram) quantities of powdered alkali carbonates. These carbonates slowly decomposed under target heating and produced constantly available beams of stable alkali ions, of known masses, which were used to tune and calibrate the spectrometer. Typically, once the desired operating temperature of the target was reached, the accelerating potential was applied to the target/ion source and a beam current of one of the stable alkali beams (^{7}Li, ^{23}Na, $^{39,41}K$, $^{85,87}Rb$, or ^{133}Cs) measured at Faraday cups 1 and 2. The extraction electrode position and focus ring potential were then varied to

maximize the beam current at Faraday cup 2. Next, the beam current was maximized on Faraday cup 3 using the dipole and the quadrupoles; the slits at the first focus position were closed down to some arbitrary opening (usually 5 mm) during beam tuning to ensure a finely focused beam. The electrostatic beamline elements were tuned next to bring the ion beam to the final focus at Faraday cup 4. After maximizing the beam current at the final focus, the entire tuning procedure was repeated in attempts to increase the beam current. Usually, the most sensitive elements of the tune were the position of the extracion electrode and the quadrupole fields. The electrostatic beamline, once tuned, required little adjustment.

Once a tune had been established for a known "calibration" ion beam mass, the quadrupole and dipole settings were noted. The settings for a desired mass were calculated by a first order approximation:

$$\frac{B_2}{B_1} = \frac{\sqrt{m_2}}{\sqrt{m_1}}$$

where: $\sqrt{m_2}$ ≡ mass of desired ion beam

$\sqrt{m_1}$ ≡ mass of known ion beam

B_1 ≡ dipole field at known mass position

B_2 ≡ required dipole field for desired mass

The quadrupole settings were calculated using the same method. However, since the quad fields are not directly determined, the reference voltages of the quad power supplies were substituted for the fields in the above equation.

The dipole magnetic field was determined using an F.W.Bell model BH-701 Hall probe suspended in the dipole field. This probe has an output of 7.269 mV/kG ± 20% with a linear deviation of < 1/4 % in the field region < 10 kG. Typically, with an accelerating potential of 20 kV, the dipole field required to bend a ^{133}Cs ion beam was about 1.66 kG. Since this field is well within the limit of < 1/4 % linear deviation boundary, the first order approximation discussed above was quite adequate for mass tuning.

While the Hall probe intrinsic linearity was sufficiently accurate, the linearity of the mV-to-Gauss conversion table resident in the control system software proved to be inadequate. Using the control system to set and read the dipole fields of stable, known, mass beams, discrepancies on the order 5-6 Gauss in calculated vs. observed fields were encountered for Na-to-K or K-to-Rb field changes. Greater discrepancies were found in setting fields for K masses from observed Cs beam values, or fields for Na masses based on Rb beam values. This linearity problem was solved by splitting the Hall probe signal and feeding it into both the control system and into a Hewlett-Packard 3456A digital voltmeter for additional visual display. The voltmeter is is capable of readings down to 10^{-4} Volts and is sufficiently accurate for precisely setting calculated dipole fields. The control system calibration was used to obtain a "coarse" field setting and the final "fine" setting

was achieved with reference to the voltmeter. To further insure that any nonlinearity effects were minimized, the separator calibration was checked using stable mass beams as close as possible to the desired mass settings. For example, for a survey of the potassium isotope yields, the spectrometer was calibrated using beams of stable ^{39}K and ^{41}K. Similarly, for yield measurements in the rubidium mass region, beams of ^{85}Rb and ^{87}Rb would be used for calibration.

Data Acquisition:

Once the proton beam was positioned on target and the separator tuned and calibrated using stable masses, Faraday cup 1 would be inserted to block the ion beam from entering the dipole magnet. The dipole and quadrupoles would then be tuned to settings corresponding to the desired ion mass and Faraday cup 1 would be removed from the beamline to allow the ion beam to be deposited on an aluminum foil covering Faraday cup 4 at the final focus position.

Faraday cup 4 consists of an aluminum frame approximately 3.5" in diameter, covered with aluminum foil. The product beams were deposited on the aluminum foil which was changed periodically to prevent buildup of long lived activities. Faraday cup 4 is centered in a beamline "T" and is inclined at 45° to the incident ion beam. This allows a silicon surface barrier detector to be mounted orthogonal to the ion

beam axis, facing the center of the Faraday cup foil. The detector is mounted (in the beamline vacuum) on a blank-off plate covering one of the arms of the beamline "T". This detector was used to determine the activity deposited by beams of the ionized alpha emitting isotopes: primarily ^{8}Li, ^{9}Li and ^{20}Na. The energy calibration and detection efficiency of the detector were determined by counting a calibrated ^{241}Am source placed at the center of the collection foil - in the position corresponding to the beam spot.

The activities of the majority of the collected isotope beams were determined by gamma spectroscopy. An upright Ge(Li) detector was positioned immediately under the center of the beamline "T" containing Faraday cup 4. At each mass postion, the elements that could be successfully extracted and ionized were identified by known gamma rays specific to nuclides of that mass. As with the Si detector, the energy calibration and detection efficiency of the Ge(Li) detector were determined by counting calibrated gamma sources in the beam spot position. The detector configuration with respect to the collection foil and ion beam is shown in Figure 17.

Both gamma and alpha spectra were accumulated using a multichannel analyser PCA-8000 board and software (from The Nucleus) installed in a Multiterm AT personal computer (IBM clone). All spectra were stored on diskettes for subsequent analysis. Gamma spectra were collected in 4096 channels and analysed using the GAMANAL spectral analysis code (Gu72)

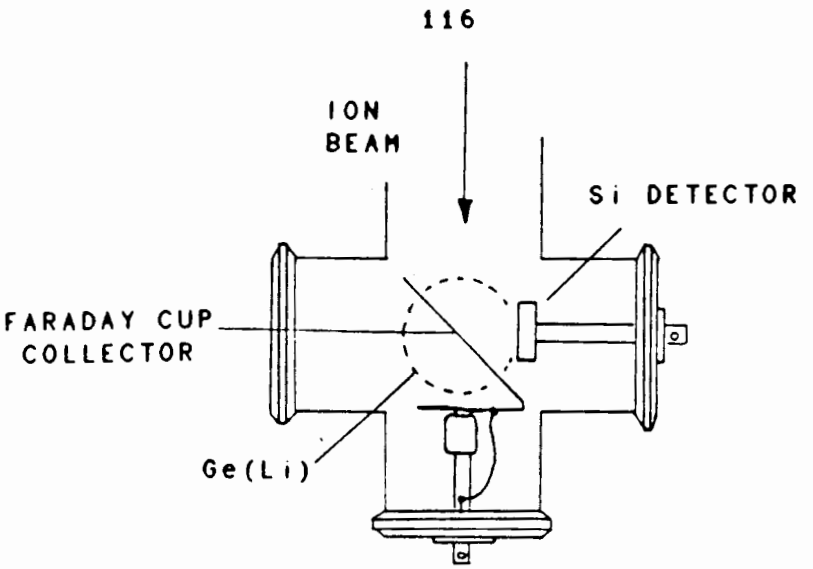

alpha - gamma detector configuration

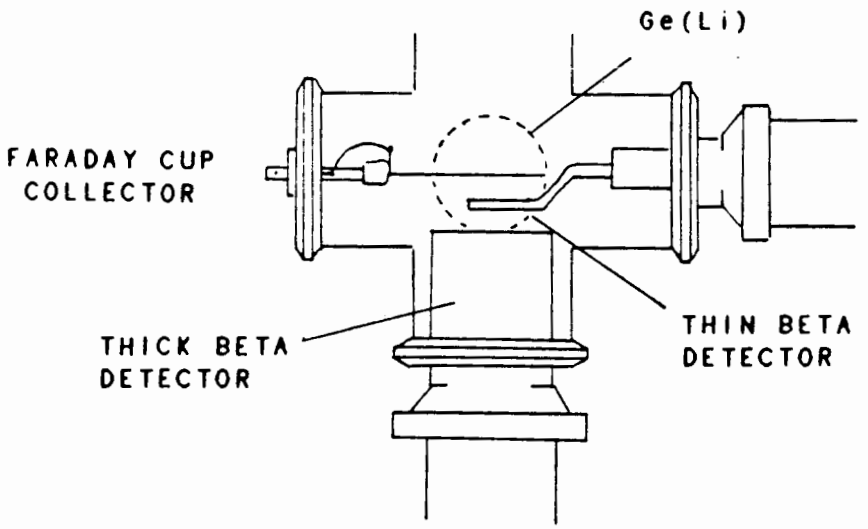

beta telescope detector configuration

Figure 17: Detector configurations at collection point. The dotted circle represents a Ge(Li) detector positioned under the collection foil.

running on the Simon Fraser University mainframe computer. Alpha spectra were simply integrated using the PCA-8000 software.

Besides alpha and gamma spectroscopy, beta counting using two plastic scintillator detectors was also employed. A ∂E-E detector telescope consisting of thin and thick scintillators was used to verify the detection of ^{8}Li and ^{9}Li and attempt to detect ^{11}Li. This detector telescope was not energy or efficiency calibrated and was used simply to count all energetic betas in a multiscaling mode. During a collection period for one of the lithium nuclides, the total beta activity would be multiscaled while the ion beam would be periodically deflected off the collector foil (and the ∂E-E telescope) using one set of the electrostatic deflection plates. The deflection was synchronized with the multiscaling, and the entire data collection sequence could be cycled repetitively to achieve better counting statistics. The decrease of total beta activity during the beam deflection period was analysed and the decay constants used to verify the presence of ^{8}Li and ^{9}Li and ^{24m}Na. This method failed to verify the presence of ^{11}Li.

Data Analysis:

Gamma and alpha spectra were collected in either of two modes, the choice of mode depending on the half-life and the observed production yield of the isotope being counted.

For beams of moderate acivity and longer half-lives, the gamma or alpha count would be simultaneous with the collection period. The isotope beam would begin depositing activity with the opening of Faraday cup 1 and the multichannel analyser would be simultaneously switched into acquire mode. The spectrum would be monitored for the signature gammas or alphas expected of the nuclides at that mass position and when sufficient statistics were obtained, acquisition would be terminated. The ion beam would be intercepted again by Faraday cup 1 and the the separator tuned for another mass.

The average yield of a nuclide was determined according to the following method. For a steady rate of production, the activity of a specific separated nuclide at time (t) after the beginning of a collect/count period is:

$$A(t) = Y(1-\exp\{-\lambda t\})$$

where $A(t) \equiv$ activity (count/sec)

$Y \equiv$ average yield of nuclide (nuclei/sec)

$\lambda \equiv$ decay constant of nuclide (sec^{-1})

$t \equiv$ collect/count time

The total number of counts observed over a collect/count interval of (t) seconds duration is the sum :

$$\int_0^t A(t)dt = Y\int_0^t (1-\exp\{-\lambda t\})dt$$

or:

$$A(t)t = Y\left[t + \frac{\exp\{-\lambda t\} - 1}{\lambda}\right]$$

rearranging to solve for Y and correcting for detector effficiency and branching ratios gives:

$$Y = \frac{N}{\epsilon(B.R.)}\left[\frac{\lambda}{(t\lambda + \exp\{-\lambda t\} - 1)}\right]$$

where:

Y ≡ average yield of nuclide (nuclei/sec)

ϵ ≡ detector efficiency

B.R. ≡ Branching ratio of radiation

N ≡ counts in time (t)

t ≡ collect/count time (sec)

For nuclides of short half-life and high production yield, the observed activities were high enough to overload the Ge(Li) detector. To decrease detector dead times and distortion of spectral peak shapes, a different collection and counting method was used. First, the nuclide of interest would be collected by removing Faraday cup 1 from the ion beam. Next, with Faraday cup 1 inserted, the collected activity would be allowed to decay for some time interval. Then, the MCA would be turned on and the sample counted. If the collected activity was sufficiently high, several successive spectra could be obtained from one collection. For this method, the average yield was

calculated in the following manner:

At the beginning of the collection time (t_0) the number of nuclei collected is N_0 — obviously, $N_0 = 0$. During the collection interval the number of nuclei present is the sum of the nuclei deposited and those that have decayed. Assuming a steady rate of production and collection, the number of nuclei collected at t_1 is given by:

$$N_1 = \frac{Y}{\lambda} \cdot (1 - \exp\{-\lambda t_1\})$$

where: $Y \equiv$ average yield of nuclide (nuclei/sec)

$\lambda \equiv$ decay constant of nuclide (sec^{-1})

$t_1 \equiv$ time after collection start when collection stops

After t_1 no more nuclei are collected and those present are decaying. After a decay interval, a count is taken starting at time (t_2), when N_2 nuclei are present; the count stops at time (t_3) when N_3 nuclei are present. The number of nuclei present at the beginning of the count interval (t_2) and at its end (t_3) is given by:

$$N_2 = N_1(1 - \exp\{-\lambda t_2\})$$

$$N_3 = N_1(1 - \exp\{-\lambda t_3\})$$

The difference of the two is the number of nuclei that have decayed in the count time:

$$N_3 - N_2 = \frac{\text{counts}}{(t_3 - t_2)} = A$$

where: $A \equiv$ observed activity (counts/sec)

On substitution and rearrangement:

$$A = N_1(\exp\{-\lambda(t_3-t_1)\} - \exp\{-\lambda(t_2-t_1)\})$$

and:

$$N_1 = \frac{Y}{\lambda}(1 - \exp\{-\lambda t_1\}) \quad \text{as before}$$

Solving for Y and correcting the count for branching ratios and detector efficiency:

$$Y = \frac{A \cdot \lambda \cdot (1 - \exp\{-\lambda t_1\})^{-1}}{\epsilon \cdot B.R. \cdot (\exp\{-\lambda(t_3-t_1)\} - \exp\{-\lambda(t_2-t_1)\})}$$

Calculation Methods & Uncertainty Estimates:

In practice, yield estimates for both types of counting methods were calculated by using a spreadsheet type of calculation. For the simultaneous collect/count calculation, the input parameters consisted of the nuclide half-life, gamma energy, gamma branching ratio, integrated gamma count and relative uncertainties, count time and proton flux. The half-lives, gamma energies and branching ratio values were from the 1983 compilation in Atomic Data & Nuclear Data Tables and from the Table of Isotopes, 7th ed. (Re83, Le78) The integrated gamma counts and uncertainties were from the output of the GAMANAL spectral analysis program. For each gamma ray associated with a collected nuclide, a yield (and uncertainty) was calculated in terms of both the absolute observed yield (nuclei/sec) and the

normalized yield (nuclei/sec/μA protons). In the case of more than one identifying gamma, the weighted mean of all yield values was calculated. Obviously, the number of gammas observed per nuclide varied; the presence of some nuclei was inferred from only one gamma ray while the presence of others was confirmed by as many as 15-20 peaks.

Estimates of the relative uncertainties of the yields were based on the uncertainties of the integrated counts, the uncertainty of the detector efficiency for a particular gamma energy, the gamma branching ratio uncertainty, the uncertainty in the count time and the uncertainty in the proton flux. The GAMANAL relative errors in peak counts varied from ± 0.5% up to ± 50%, depending on the statistics obtained. The relative detector efficiency error varied from ± 1.4% at 100 keV, to ± 3.7% at 3000 keV. An average gamma branching ratio error of ± 10% was used for all gammas. An absolute uncertainty of ± 2 seconds in the collect/count times was chosen to take into account any discrepancy in the simultaneity of the count and collect times. Finally, an absolute error of ± 10 nA in the proton flux was used to account for fluctuations in the SEM scaler reading.

For the collect-wait-count data acquisitions, the time components of the the spreadsheet equations were written in terms of the collect time, the count time and (t_2) the beginning of the count time. Yield uncertainty calculations

included the previously discussed errors as well as a ± 2 second absolute error for each of the three time components. Part of a sample spreadsheet calculation is shown in Appendix A.

Comparisons with Calculated Values:

In order to estimate the overall performance of the separator and the target/ion sources, the experimentally measured yields must be compared to some reasonable estimates of expected yields. Given known target thicknesses and proton fluxes, the expected production yields can be calculated if the proper reaction cross-sections are known. Some cross-sections are available from experimental studies, however, cross-sections for the entire range of possible target-product combinations at all incident proton energies have not been determined. In order to successfully calculate production yield estimates for the broad range of products from proton spallation reactions, theoretical values of reaction cross-sections must be used.

The most reasonable means of calculating the required cross-sections is by the semiempirical method of Silberberg and Tsao. (Si73a, Si73b, Si77, Si83) This method uses a series of equations and parameters to calculate the reaction cross-sections as a function of the target and product compositions and the incident proton energy. The forms of the equations and the values of the parameters used are derived

from fits to available experimental measurements. While other semiempirical formulae have been proposed for prediction of spallation yields, (Ru66) the Silberberg-Tsao equations are the most detailed, defining over a dozen target-product mass domains each with specific calculation methods. As well, production by more than one mechanism is taken into account; for a target such as ^{238}U, both spallation and fission contributions are considered.

The targets considered valid within the Silberberg-Tsao formulae range from lithium to uranium. The possible products range from the target mass down to A = 6. Valid energies of incident protons are limited to $E_p \geq 100$ MeV. Generally, the predictions give acceptable results of mass distributions for a particular product element. For specific products at intermediate energies the comparisons with experimental values agree within a factor of two. (Si73b, Si77) For the conditions important to the present experiments the quoted ratios of calculated to experimental cross-sections are given in Table 3.

Also, for products with masses close to that of the target, further deviations from the predicted cross-sections can be expected in the present case. With thicker targets, the possibility of secondary reactions becomes significant; the Silberberg-Tsao calculations make no provision for such reactions.

Table 3

Silberberg-Tsao Cross-Section Uncertainties

Reaction	Deviation from unity of $\sigma_{calc}/\sigma_{exp}$
spallation, $\partial A \leq 50$	+0.5, -0.3
spallation, $\partial A \geq 50$	+1, -0.5
fission, $A_{target} \leq 210$	+2, -0.7
fragmentation, evaporation ($A \leq 55$, $Z \geq 6$)	+1, -0.5
^{238}U fission	+0.6, -0.4
peripheral, $Z_{target} \geq 29$	+0.5, -0.3

The Silberberg-Tsao cross-sections used for comparisons with experimental yields were calculated by means of the computer code SILT running on the SFU mainframe computer. Where target elements consisted of more than one isotope, contributions to the cross-section from all composite target species were summed. The expected production yields (nuclei/sec/μA) were calculated as the product of the target thickness (nuclei/cm^2), the SILT cross-section (cm^2) and a proton flux (protons/sec) equivalent to 1 μA.

Release Time & Efficiency Estimates:

With the availability of experimental and theoretical yield estimates, it becomes possible to estimate the overall efficiency for combined target/ion source and separator

systems. For any product element, the ratio of calculated to measured yields should reflect the overall efficiency of extracting, ionizing and separating that element. This overall efficiency would presumably reflect the ionization efficiency of the product element as well as any losses due to chemical reactions or leaks in the system. Such component losses can be expected to be essentially equivalent for all isotopes of a product element. However, the losses due to radioactive decays in a range of isotopes will not be equivalent, but will be reflective of the half-life of each. If the delay time of each isotope of a given element in transit through a specific target matrix is taken to be equivalent, it becomes possible to estimate the mean release time for that element by comparison of the overall efficiency observed for each isotope with its half-life. Clearly, this is not a foolproof method and a more direct measurement of release times would be preferable. However, in the present configuration of TISOL, it is not possible to estimate the release times in any other way.

To obtain the maximum efficiency and release time estimates, the experimental/calculated yield ratios for the isotopes of each element observed from a target were plotted as a function of the isotope half-lives. A non-linear iterative least squares fit of efficiency vs. halflife was obtained using a function of the form:

$$\text{Efficiency} = \text{Eff}_{max} \cdot (1-\exp\{-t_{1/2}/\tau\})$$

where: Eff_{max} ≡ maximum efficiency (Efficiency —> Eff_{max}, as $t_{1/2}$ —> ∞)

$t_{1/2}$ ≡ halflife of isotope

τ ≡ mean release time of element

RESULTS & DISCUSSION

The Titanium Foils Target Runs:

While the first successful observation of on-line isotope separation at TISOL used a Sc_2O_3/graphite target, no systematic yields were obtained. The earliest quantitative studies used a titanium metal foil target. The target consisted of 13 disks of a 0.25mm thick, 99.7% pure Ti foil purchased from the AESER division of Johnson Matthey Inc. The disks were 13 mm in diameter and were stacked in a graphite crucible separated by 1 mm thick graphite spacer rings; the target had a total thickness of 1.48 g/cm^2. The crucible was open at the top and was placed inside the graphite oven of the McGill surface ionization source; the Ti foil target runs were the only ones using the Mcgill surface source instead of the TRIUMF surface source. A total of three on-line runs were made using the Ti foil target. Two runs (on July 12 and July 29, 1988) used a tungsten ionizing foil rolled in a heated tantalum tube. The third run (August 4, 1988) used a rhenium foil inside a tantalum tube. In all runs, the estimated temperature of

the target was about 1400 - 1500° C.

Table 4

Results of Ti Foil Target Runs:

	July 12/88	July 29/88	Aug 4/88
Ionizer:	W	W	Re
Nuclide	Yields (nuclei/sec/μA protons)		
Li-8	-	~ $2.8 \cdot 10^5$	~ $3.3 \cdot 10^5$
Na-20	$6.8 \cdot 10^2$ ± 22%	$1.4 \cdot 10^3$ ± 21%	$4.8 \cdot 10^2$ ± 21%
Na-21	$3.3 \cdot 10^4$ ± 18%	$7.3 \cdot 10^4$ ± 18%	-
Na-25	$1.1 \cdot 10^5$ ± 10%	$2.9 \cdot 10^5$ ± 10%	$6.0 \cdot 10^4$ ± 10%
Na-26	$4.2 \cdot 10^3$ ± 22%	$1.7 \cdot 10^4$ ± 21%	$3.3 \cdot 10^3$ ± 14%
Na-27	$5.5 \cdot 10^2$ ± 21%	$1.5 \cdot 10^3$ ± 20%	$4.8 \cdot 10^2$ ± 12%
Al-28	-	$2.7 \cdot 10^2$ ± 20%	$2.2 \cdot 10^2$ ± 21%
Al-29	$4.5 \cdot 10^2$ ± 24%	$5.9 \cdot 10^2$ ± 21%	-
K-35	$3.1 \cdot 10^2$ ± 29%	$1.4 \cdot 10^2$ ± 22%	-
K-36	$1.6 \cdot 10^4$ ± 11%	$1.9 \cdot 10^4$ ± 12%	$5.4 \cdot 10^3$ ± 14%
K-37	$5.1 \cdot 10^5$ ± 23%	-	$2.8 \cdot 10^5$ ± 22%
K-38g	$3.3 \cdot 10^6$ ± 22%	-	-
K-42	$9.6 \cdot 10^7$ ± 21%	-	-
K-47	-	-	$4.4 \cdot 10^3$ ± 11%

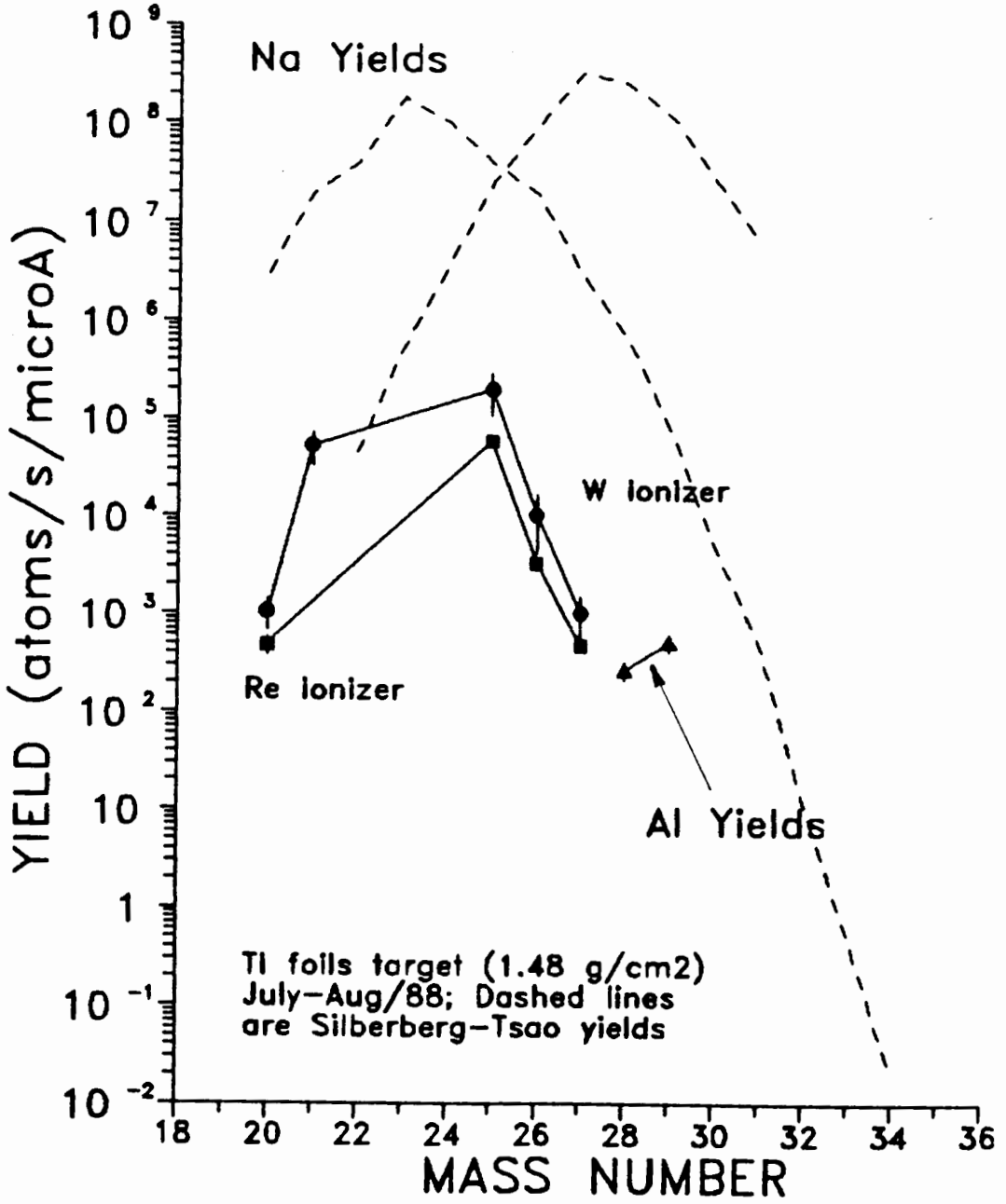

Figure 18: Yields of Na & Al from a Ti foils target.

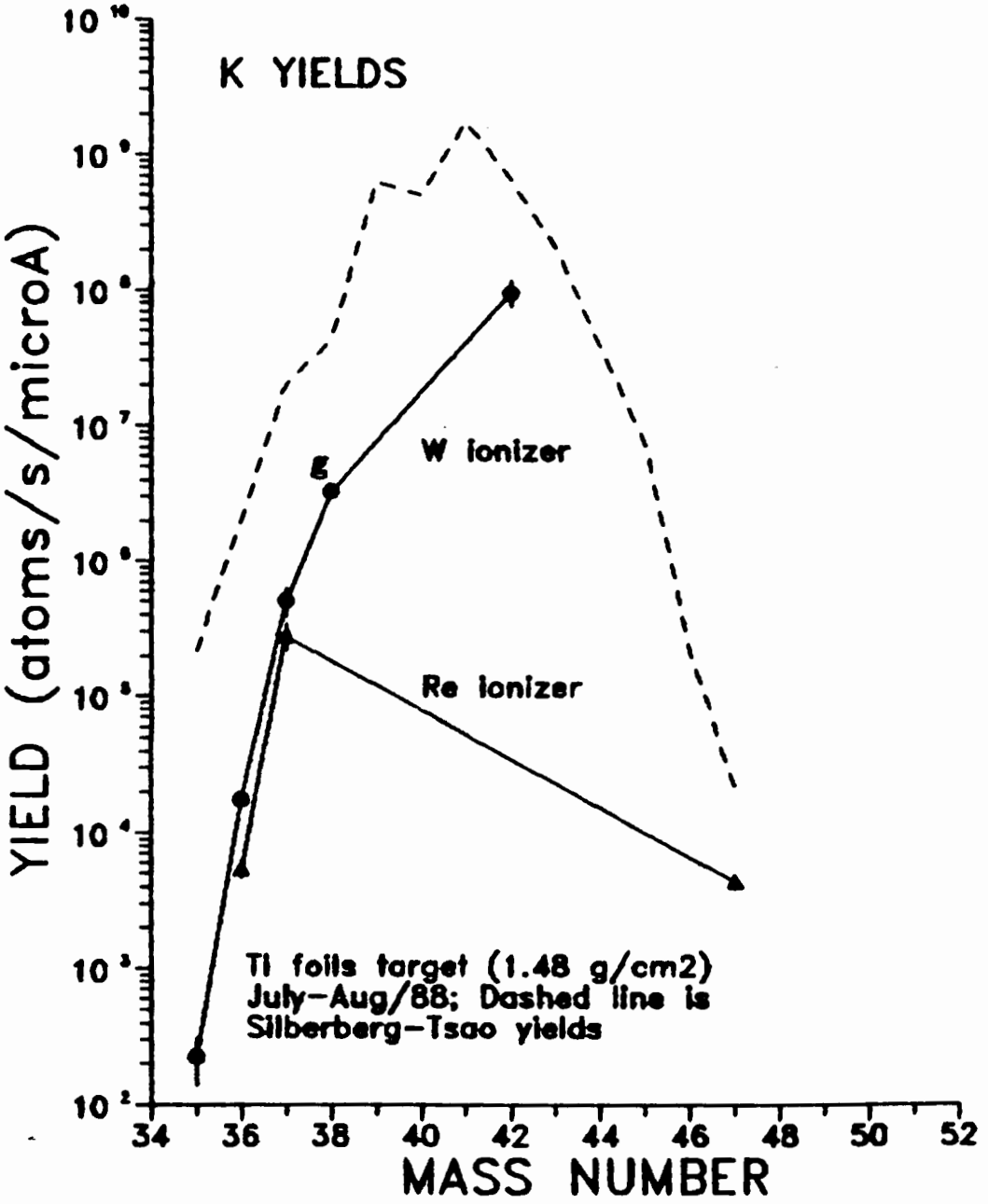

Figure 19: Yields of K from a Ti foils target.

For the Ti foil target, the observed separated isotopes were Li, Na, Al & K. The experimental yields are presented in Table 4. The comparisons with calculated Silberberg-Tsao yields are presented in Figures 18 and 19. The two tungsten ionizer run results have been averaged for display purposes.

For both the Na and K isotopes, the W ionizer yields are consistently higher than those obtained with the Re ionizer. Since the work function of rhenium is greater than that of tungsten, this behavior is contrary to that predicted by the Saha-Langmuir formula, which predicts greater ionization from a Re surface. This enhanced ionization may result from the formation of a tungsten-molecular oxygen layer (with a higher work function than that of the metal) or from plasma-like effects near the walls of the hot W foil. Unfortunately, while the observed enhancement is interesting, it is of too low an order to be considered significant. In some instances the difference in yields is within the combined uncertainties of the two values; in all cases the addition of relatively small errors would account for the differences. Such errors can easily be ascribed to differences in proton beam positions or ion beam tunes that have not been included in the yield calculations.

The calculated conversion efficiencies (observed yields/predicted yields) for Na and K isotopes as a function of isotope half-life are displayed in Figures 20 and 21

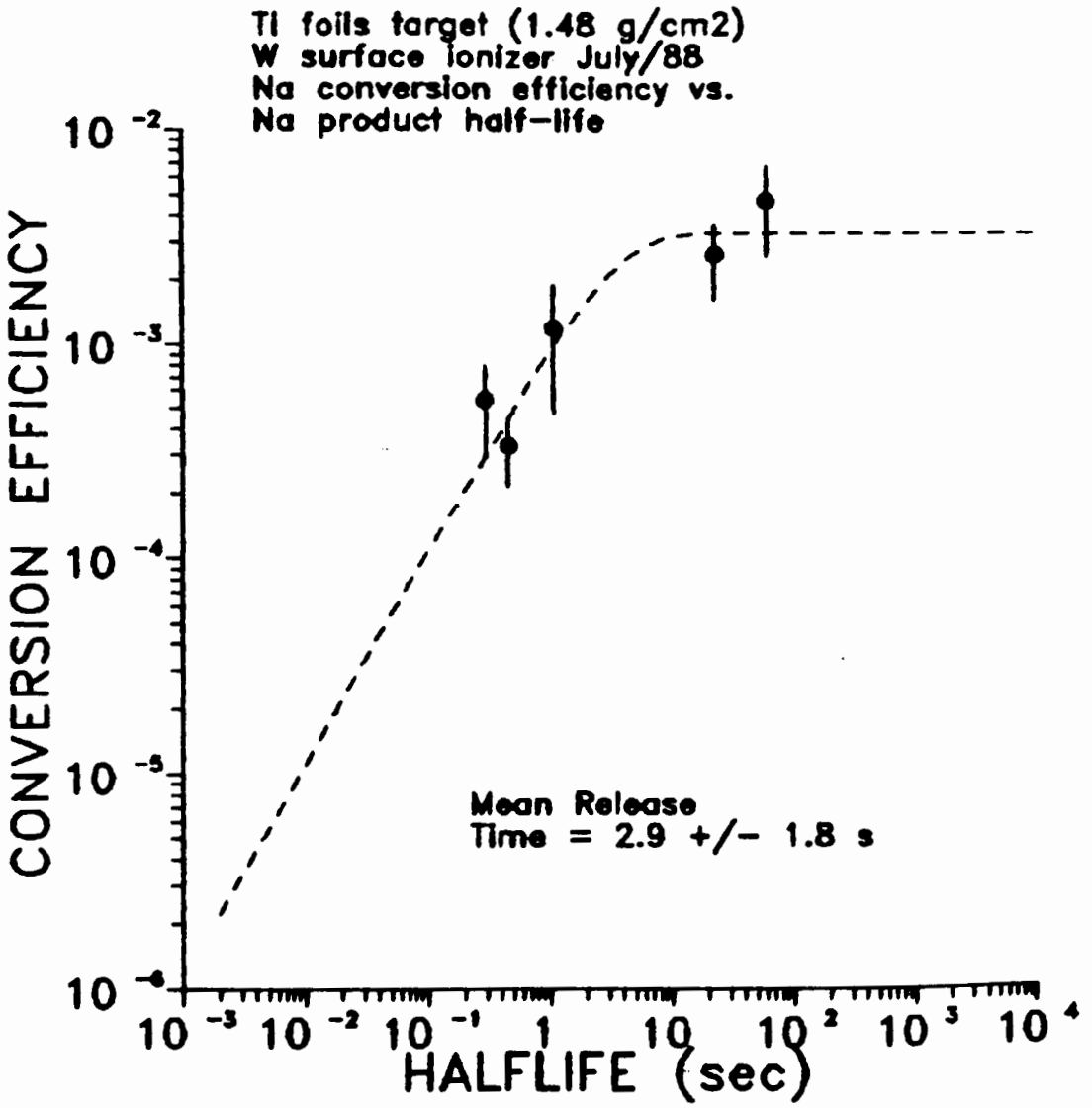

Figure 20: Graph of conversion efficiency vs. nuclide half-life for Na isotopes from a Ti foil target.

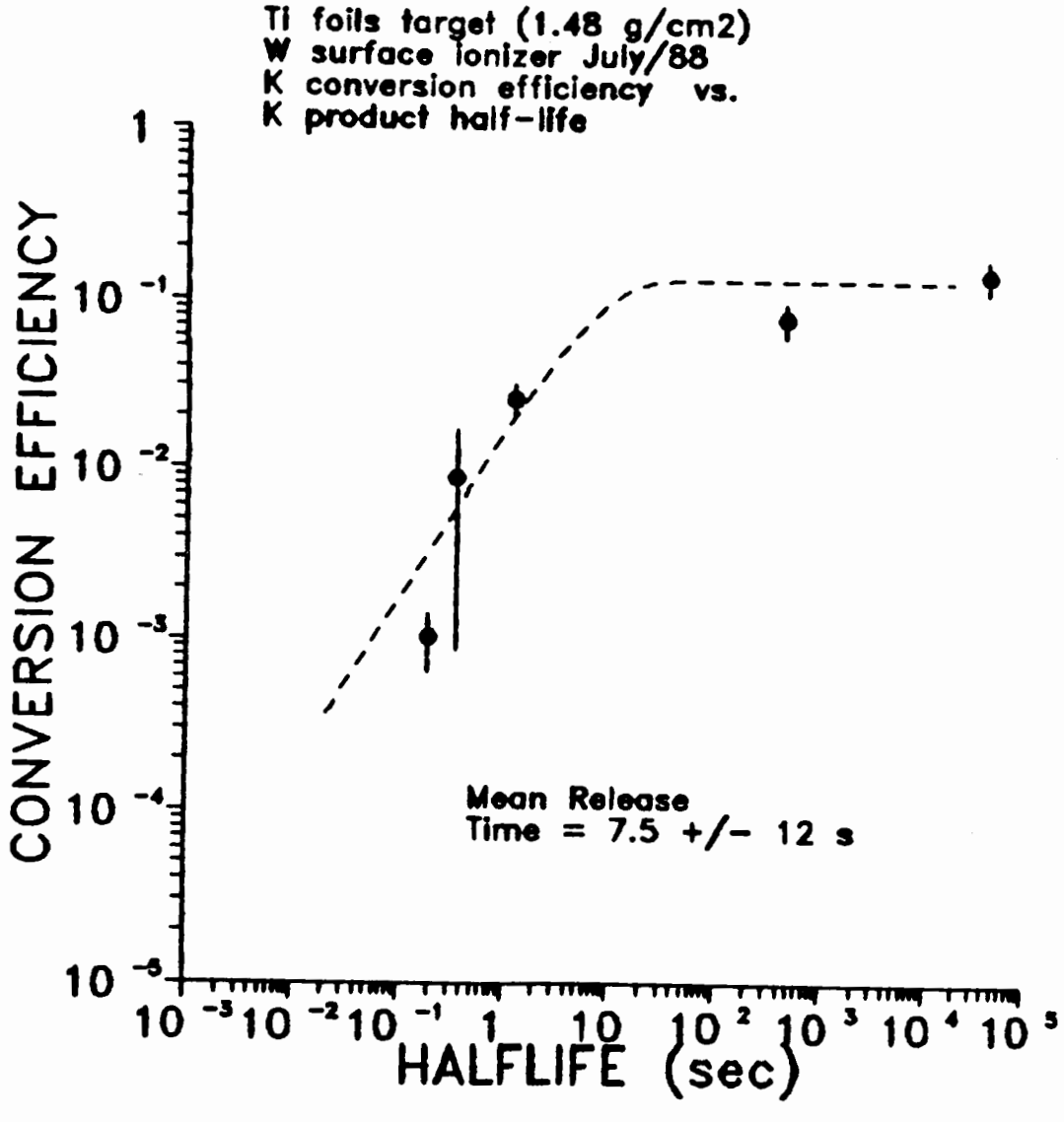

Figure 21: Graph of conversion efficiency vs. nuclide half-life for K isotopes from a Ti foil target.

respectively, along with the derived least square fits of Eff_{max} and mean release time. For aluminum, only two points were available for a fit and only approximate estimates (without corresponding uncertainties) were obtained. The fit for the sodium isotopes gives reasonable values for both parameters. However, the fit for the potassium isotopes, while producing a reasonable estimate of Eff_{max}, produces a large uncertainty for the mean release time estimate. The least squares estimates are shown in Table 5 along with the efficiencies predicted by the Saha-Langmuir formula.

Table 5

Maximum Efficiencies & Mean Release Times

for Elements from the Ti Foils Targets

Element	τ_{mean} (sec)	Eff_{max} (%)	Saha-Langmuir[a] (%)
Na	2.9 ± 1.8	0.33 ± 0.08	1.6
Al	~ 480	~ $1.0 \cdot 10^{-6}$	0.02
K	7.5 ± 12	13.2 ± 4.6	54

a: Ionization efficiency predicted by Saha-Langmuir formula at 1900 °C

The calculated maximum efficiency for both Na and K is well below that predicted by the Saha-Langmuir formula. Since the calculated release times are much shorter than the half-lives of the longest lived isotopes observed, it is likely that the losses are due to effects other than decay in transit.

The Zirconium Foils Target Run:

A single run using zirconium foils as a target was conducted on December 12, 1988. This run used a Re ionizer and the TRIUMF surface ionization source. The zirconium foil was from the same supplier as the previous titanium foil and the target was constructed as before. A total of thirty-nine 0.25 mm thick disks were used, giving a target thickness of 6.32 g/cm^2. The estimated target temperature was 1900° to 2000° C.

Yields for sodium, potassium, rubidium and strontium isotopes were obtained. It was assumed that all of the strontiums observed were the result of direct production and not the decay products of rubidium parents. For isotopes lighter than ^{85}Sr, this is indeed the case; for neutron rich strontiums, the observed yield may be a combination of directly produced and decay product components. Estimates of the magnitude of the decay component were made for all cases where Rb —> Sr or Sr —> Rb decay could contribute to the yield of the daughter. For all cases, except that of

$^{91}Rb \longrightarrow {}^{91}Sr$ decay, the estimated contribution was less than 1%. For the mass 91 case, up to 27% of the observed ^{91}Sr yield may be due to decay of ^{91}Rb. For this, and all other runs, no attempt was made to separate these components. Similarly, in cases where both the ground and metastable isomeric states were observed for a nuclide, no attempt was made to extract the decay contribution to the yield of the ground state; both states were assumed to be produced independently. The yields are presented graphically in Figures 22 - 25 and numerically in Table 6. The yields of ground and metastable isomers have been summed for display and for the least squares fits.

The general shapes of the mass distributions for the rubidium and potassium yields agree quite well with the predictions of the Silberberg-Tsao formulae. For the strontium and sodium cases, insufficient data prevents a meaningful comparison. For both the potassium and rubidium cases the yields of the heavier isotopes seem to be underestimated by the SILT calculations. The experimental enhancement of neutron-rich rubidium yields may be attributed to contributions from secondary reactions occurring in a thick target. Such reactions would be expected to increase yields of neutron-rich products close to the target mass. As well, the Silberberg-Tsao formalism predicts contributions from both spallation reactions and peripheral reactions for this target/product combination. For a

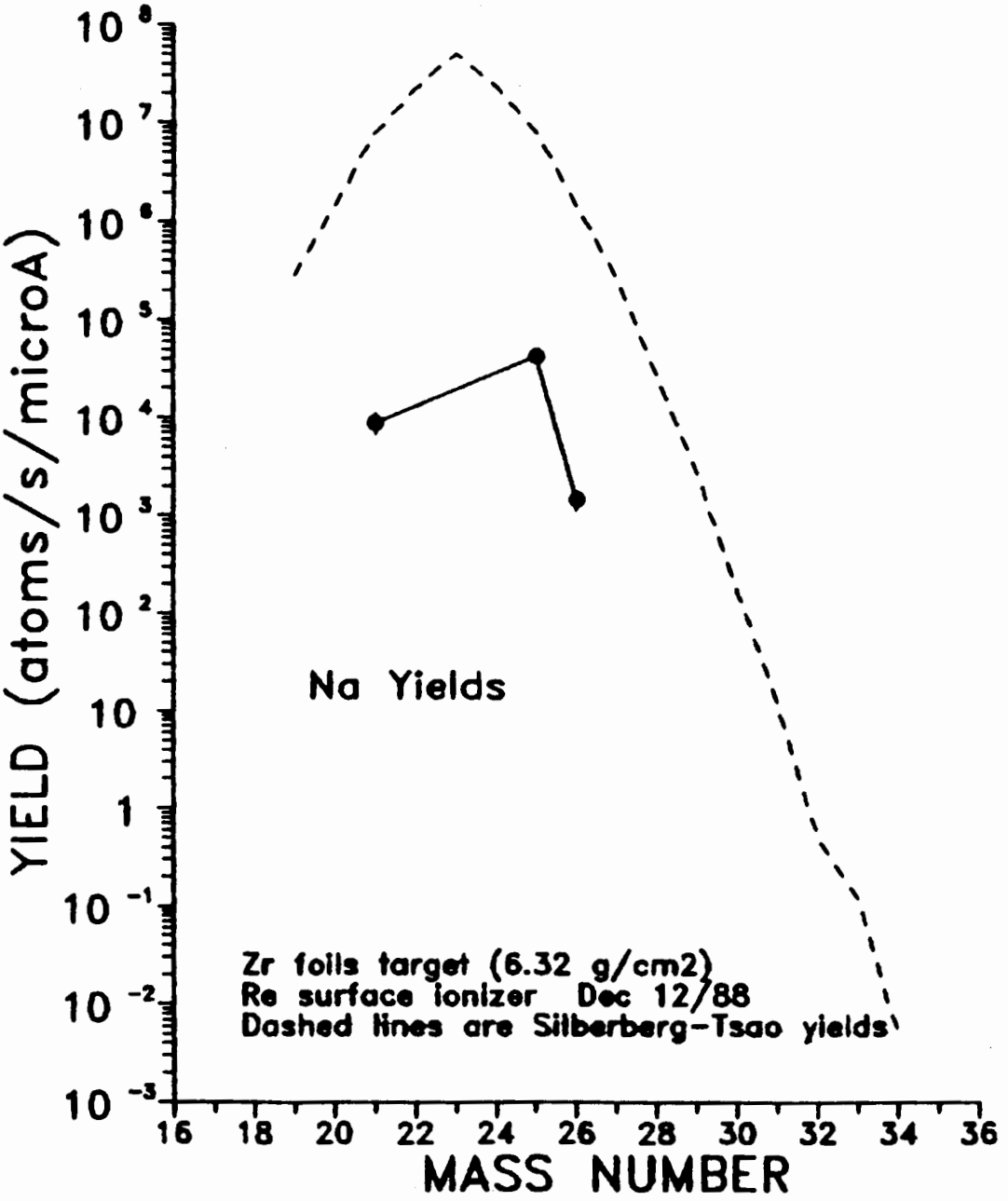

Figure 22: Yields of Na from a Zr foils target.

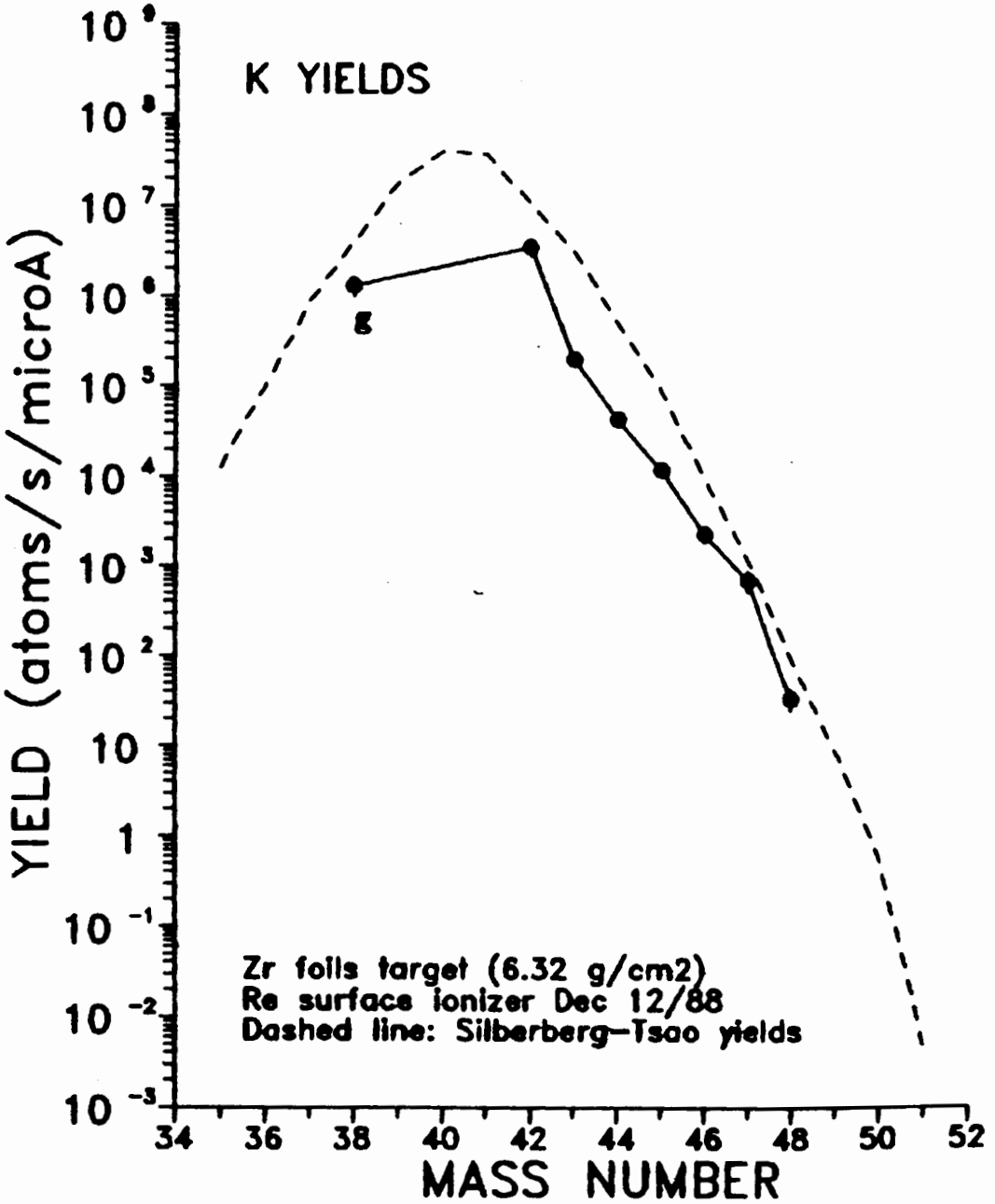

Figure 23: Yields of K from a Zr foils target.

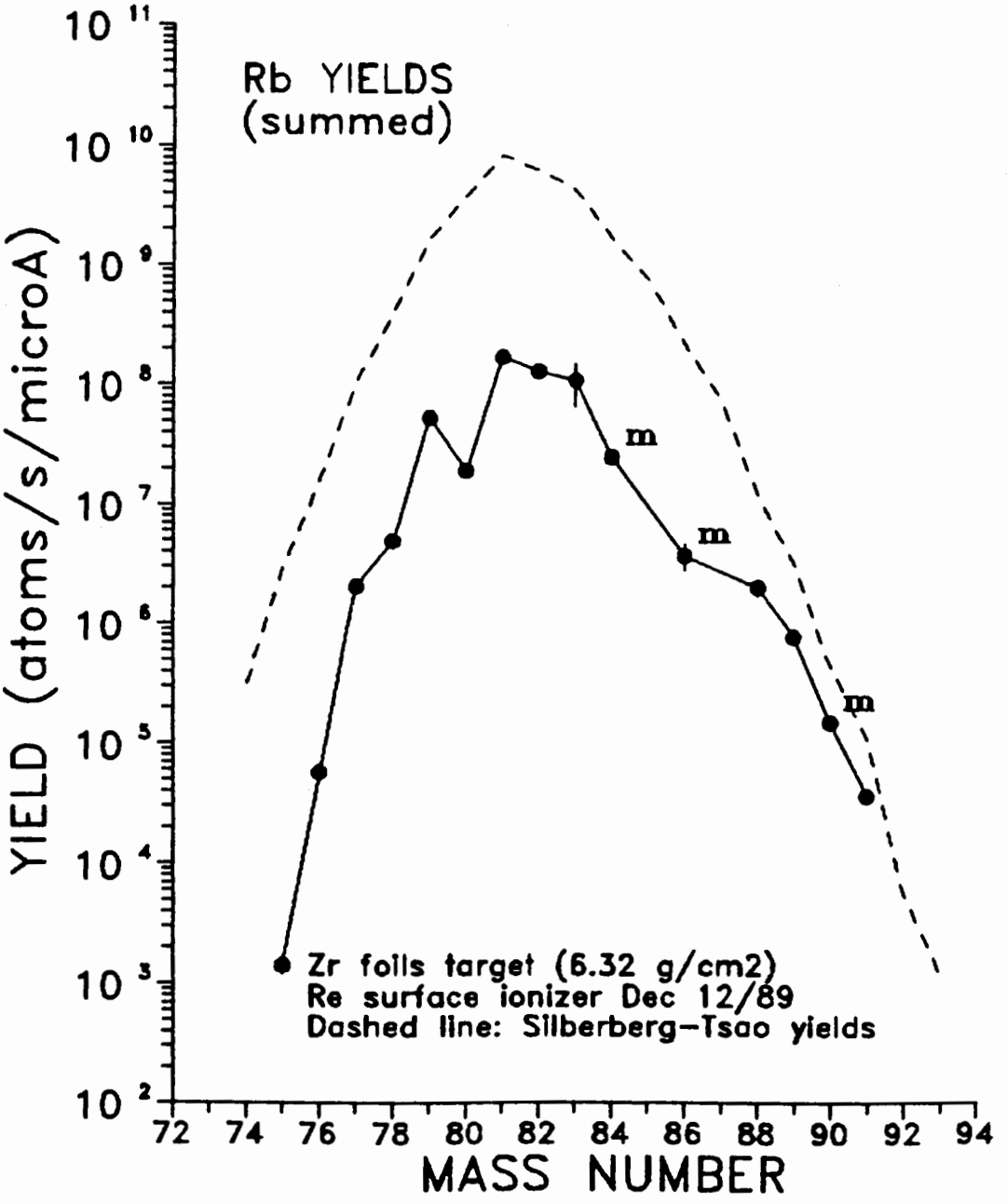

Figure 24: Yields of Rb from a Zr foils target.

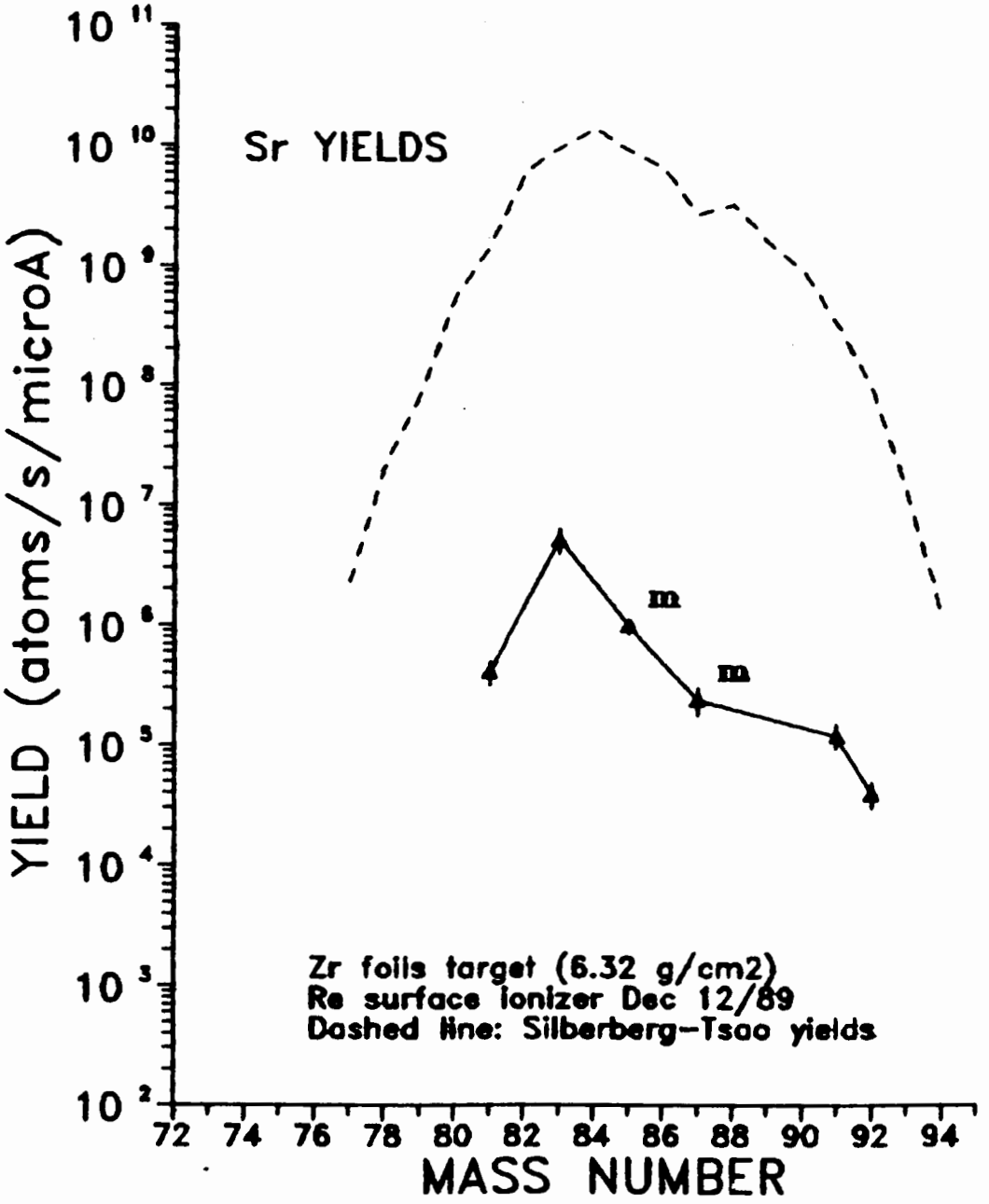

Figure 25: Yields of Sr from a Zr foils target.

Table 6

Results of Zr Foils Run

Nuclide	Yield (nuclei/sec/μA)	Nuclide	Yield (nuclei/sec/μA)
Na-21	$8.9 \cdot 10^{3}$ ± 23%	Rb-75	$1.4 \cdot 10^{3}$ ± 11%
Na-25	$4.4 \cdot 10^{4}$ ± 10%	Rb-76	$5.6 \cdot 10^{4}$ ± 6%
Na-26	$1.5 \cdot 10^{3}$ ± 22%	Rb-77	$2.0 \cdot 10^{6}$ ± 5%
		Rb-78g	$1.7 \cdot 10^{6}$ ± 30%
K-38g	$1.3 \cdot 10^{6}$ ± 23%	Rb-78m	$3.1 \cdot 10^{6}$ ± 7%
K-42	$3.5 \cdot 10^{6}$ ± 22%	Rb-79	$5.2 \cdot 10^{7}$ ± 4%
K-43	$2.0 \cdot 10^{5}$ ± 16%	Rb-80	$1.9 \cdot 10^{7}$ ± 8%
K-44	$4.3 \cdot 10^{4}$ ± 10%	Rb-81g	$1.4 \cdot 10^{8}$ ± 9%
K-45	$1.2 \cdot 10^{4}$ ± 13%	Rb-81m	$3.1 \cdot 10^{7}$ ± 17%
K-46	$2.3 \cdot 10^{3}$ ± 18%	Rb-82g	$1.2 \cdot 10^{7}$ ± 25%
K-47	$7.0 \cdot 10^{2}$ ± 14%	Rb-82m	$1.2 \cdot 10^{8}$ ± 8%
K-48	$3.4 \cdot 10^{1}$ ± 26%	Rb-83	$1.1 \cdot 10^{8}$ ± 39%
		Rb-84m	$2.5 \cdot 10^{7}$ ± 11%
Sr-81	$4.1 \cdot 10^{5}$ ± 22%	Rb-86m	$3.7 \cdot 10^{6}$ ± 24%
Sr-83g	$5.2 \cdot 10^{6}$ ± 23%	Rb-88	$2.0 \cdot 10^{6}$ ± 13%
Sr-83m	$3.1 \cdot 10^{3}$ ± 21%	Rb-89	$7.8 \cdot 10^{5}$ ± 8%
Sr-85m	$1.0 \cdot 10^{6}$ ± 14%	Rb-90m	$1.5 \cdot 10^{5}$ ± 11%
Sr-87m	$2.4 \cdot 10^{5}$ ± 26%	Rb-91	$3.6 \cdot 10^{4}$ ± 9%
Sr-91	$1.2 \cdot 10^{5}$ ± 25%		
Sr-92	$3.9 \cdot 10^{4}$ ± 23%		

reaction of the type (p, ypxn), the condition where $x \leq x_{max}$, (x ≡ number of neutrons emitted by the target) is described by a periferal cross-section formula; for $x > x_{max}$, a spallation formula takes over. Unfortunately, for the condition where $y \geq 4$ (y ≡ number of protons emitted by target), no formulas exist in the Silberberg-Tsao formalism; none were deduced for lack of experimental data. Consequently, the predictions for rubidium yields are not valid for a zirconium target since y = 4.

The apparent enhancement of neutron-rich potassium yields cannnot be attributed to secondary reactions, but only to the inadequacy of the predictions. Within the Silberberg-Tsao formalism, the combination of a target mass ~ 95 and a product mass ~ 45 falls on a boundary region between two defined domains of reaction mechanisms: the breakup region and the spallation region. Near such boundaries, the predictions are not expected to be accurate.

The most significant result of the rubidium yield measurements is the observation of $1.4 \cdot 10^3$ nuclei/sec/μA of the isotope ^{75}Rb. This nuclide is only one neutron removed from the lightest previously observed rubidium isotope, that is, ^{74}Rb. Attempts were made to detect ^{74}Rb by tuning the separator to the mass = 74 position and searching for the gammas associated with its daughter ^{74}Kr ($t_{1/2}$ = 11.5 min), however, no signature could be detected. The gamma background at the Ge(Li) position was reduced by turning off

the proton beam, but still, no ^{74}Kr could be detected.

The plots of conversion yields as a function of half-life for Rb, Sr, K and Na are shown in Figures 26 - 29. The least squares fit to the rubidium data included only the nuclides lighter than ^{86}Rb. When the heavier nuclides are excluded, a reasonable fit is obtained. For the strontium case, the two yields where only the metastable isomers were observed were likewise excluded from the least squares fit. Here again, a reasonable fit is obtained when only the remaining nuclides are used. For the potassium yields, no fit could be obtained. It may be that the SILT predictions are inadequate for this case, or it may be that the mean release time for K from Zr is so short that a decrease in yield is not observed for any of the isotopes separated. At best, a maximum efficiency of ~ 10 % and a release time < 4 seconds might be estimated for potassium. Only three sodium isotopes were observed. A fit using all three conversion yield values could not be obtained and an estimate was made using only the ^{21}Na and ^{26}Na values. The results are displayed in Table 7. As with the Ti foil runs, the deduced efficiency is far below the predicted ionization efficiency.

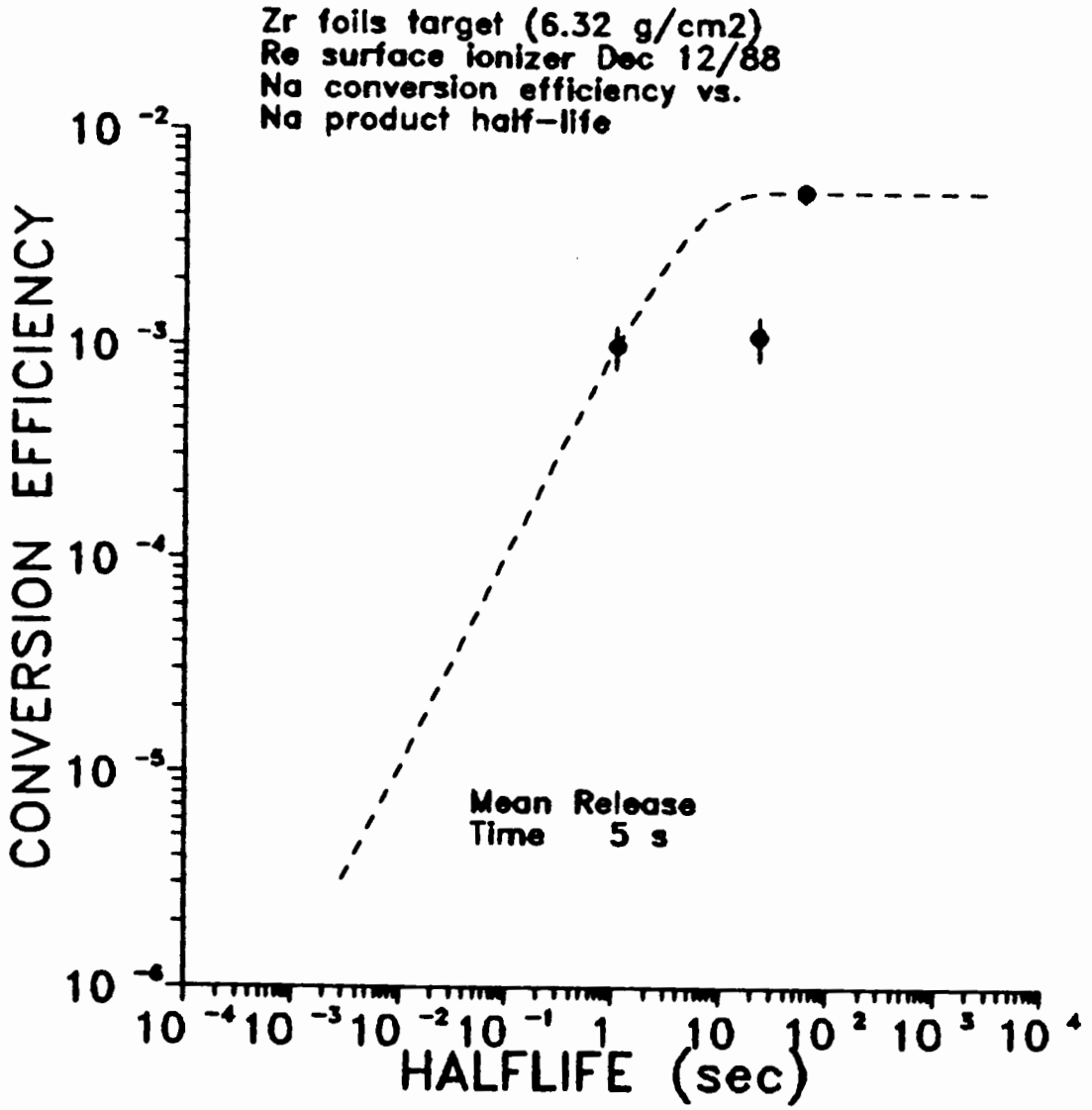

Figure 26: Conversion efficiencies for Na from a Zr foils target.

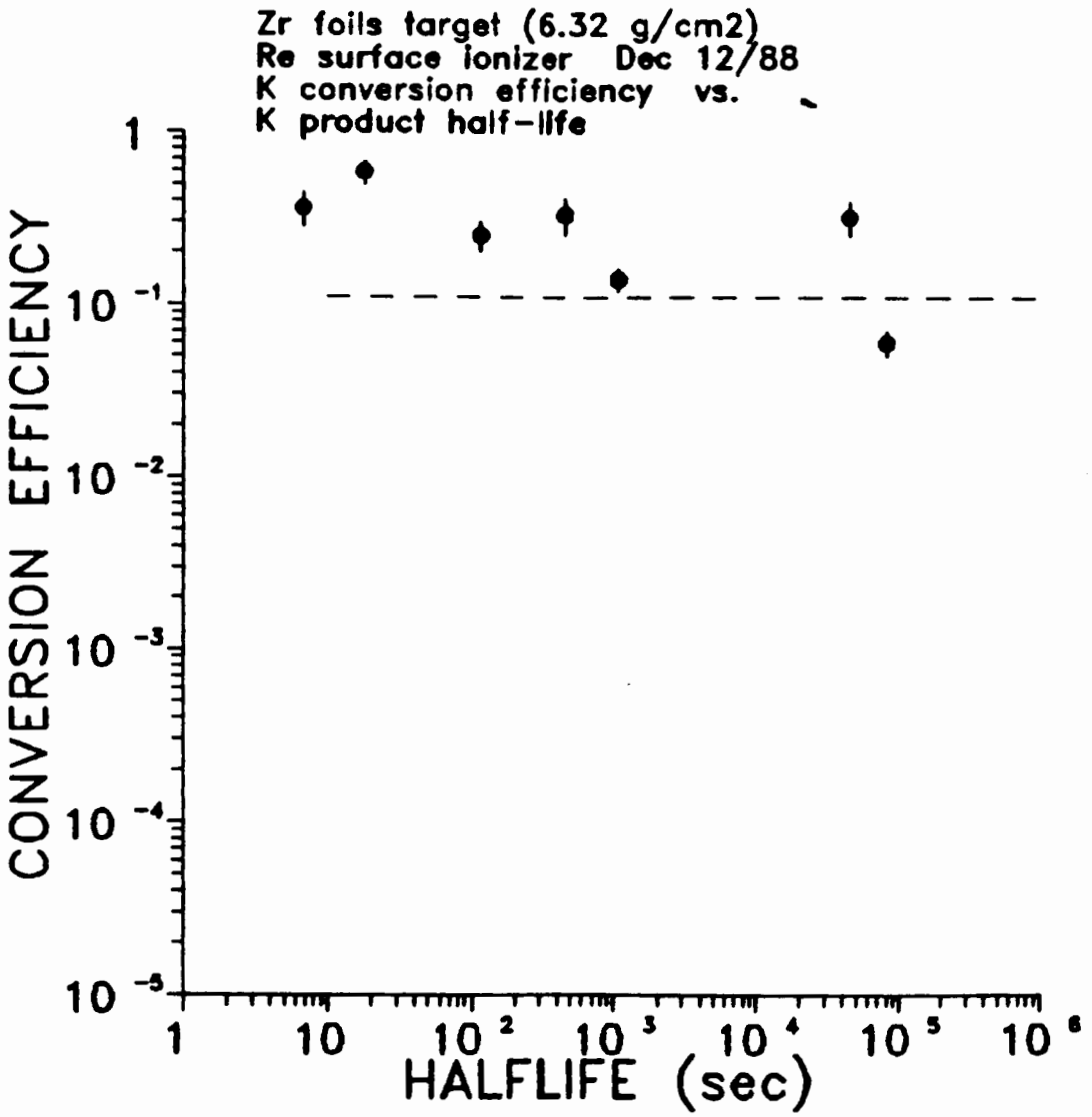

Figure 27: Conversion efficiencies for K from a Zr foils target.

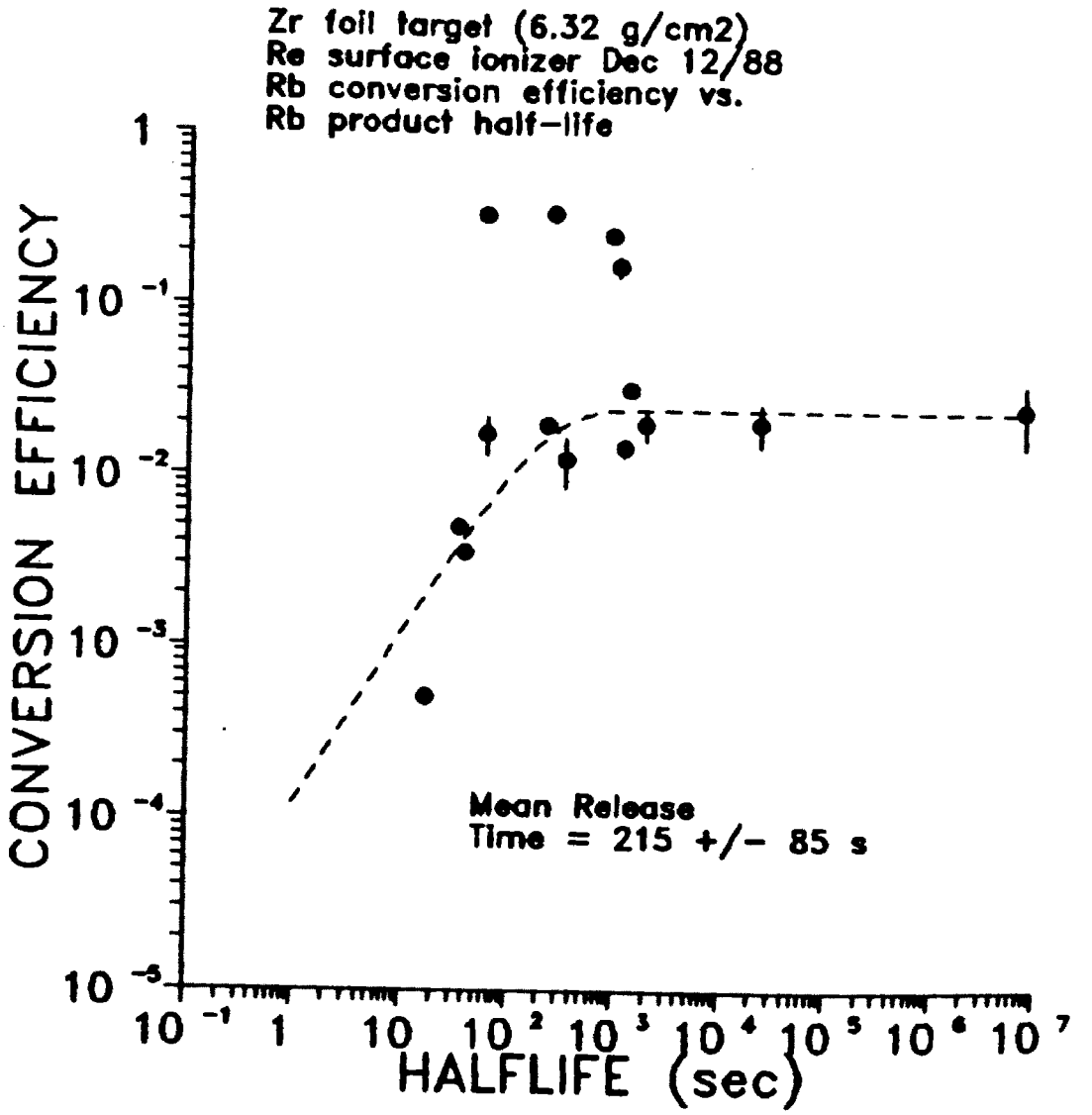

Figure 28: Conversion efficiencies for Rb from a Zr foils target.

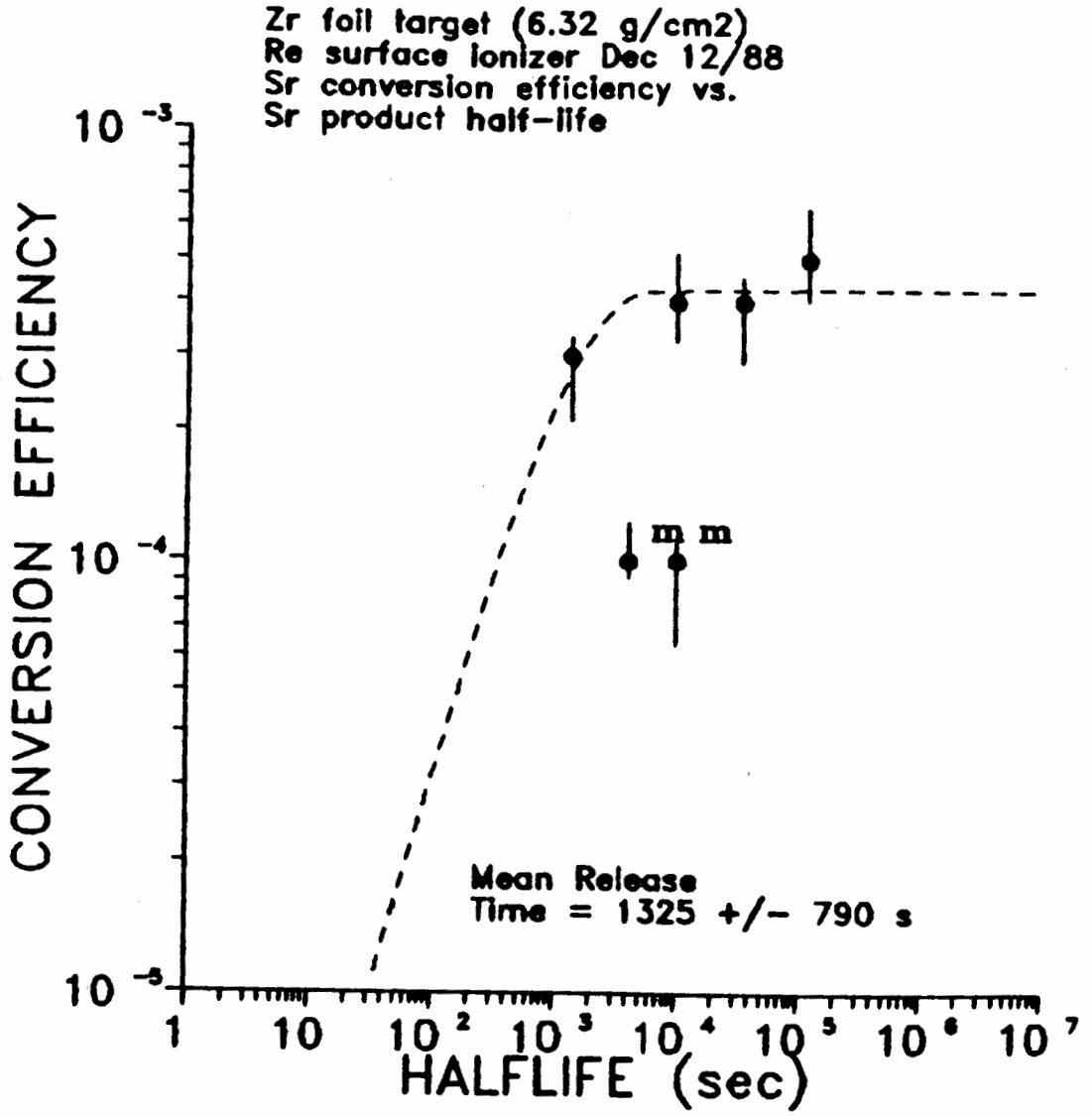

Figure 29: Conversion efficiencies for Sr from a Zr foils target.

Table 7

Maximum Efficiencies & Mean Release Times

for Elements from the Zr Foils Target

Element	τ_{mean} (sec)	Eff_{max} (%)	Saha-Langmuir[a] (%)
Na	~ 5	~ 0.5	30
K	< 4	~ 10	97
Rb	215 ± 85	2.4 ± 0.4	99
Sr	1325 ± 790	0.4 ± .006	8

a: Ionization efficiency predicted by Saha-Langmuir formula at 1900 °C

The Niobium Foils Target Run:

On December 19, 1988, Li, Na, K, Rb and Sr isotope yields were measured from a target of niobium foils. The Nb foils were 0.24mm thick disks 13mm in diameter and were obtained from the same source as the previous target disks. Fifty-four foils were stacked in a graphite target crucible for a total target thickness of 11.6 g/cm^2. A Re ionizer foil was used in the surface source and the target temperature was estimated to be between 1900° and 2000° C. The yields from the niobium target would be expected to be comparable to those from the zirconium target as the elements are adjacent in the periodic table. The purpose of running both targets

was to see if any differences in yields or release times could be observed.

The measured yields are shown in Table 8 and in Figures 30 to 33. As with the previous targets, the metastable and ground state yields have been summed for display.

Any differences in yields from the Zr and Nb targets should be most noticeable for rubidium and strontium products. The experimental yields of the rubidium isotopes from each target are compared in Figure 34, along with the SILT predictions. On the proton-rich side of stability, the experimental yields from the two targets are essentially identical, however, on the neutron-rich side the yields from zirconium are much larger. To some extent this is expected, since the isotopic distribution of zirconium includes ^{94}Zr and ^{96}Zr, which would produce more of the heavier rubidiums. However, the enhancement in yield seems to begin at mass 84 which should be easily produced by both targets. It is unfortunate that only the yields to metastable isomers of ^{84}Rb and ^{86}Rb were observed for both targets. The apparent discrepancy in yields may be due to some nuclear structure effects for the target/daughter combinations that enhance yields to the isomeric state in some cases and to the ground state in others. An alternate explanation may be that the higher yields of heavy rubidiums from Zr are due to the previously discussed secondary reactions. If such is the case, it would seem the contribution from the heavier Zr

Table 8

Results of Nb Foils Run

Nuclide	Yield (nuclei/sec/μA)	Nuclide	Yield (nuclei/sec/μA)
Li-8	$3.7 \cdot 10^4$ ± 21%	Rb-75	$1.1 \cdot 10^3$ ± 19%
Na-25	$1.6 \cdot 10^4$ ± 14%	Rb-76	$6.4 \cdot 10^4$ ± 7%
Na-26	$3.5 \cdot 10^2$ ± 34%	Rb-77	$2.1 \cdot 10^6$ ± 5%
K-37	$5.3 \cdot 10^3$ ± 64%	Rb-78g	$5.4 \cdot 10^6$ ± 7%
K-38g	$3.1 \cdot 10^5$ ± 21%	Rb-78m	$9.4 \cdot 10^6$ ± 4%
K-42	$1.1 \cdot 10^5$ ± 82%	Rb-79	$7.0 \cdot 10^7$ ± 3%
K-44	$2.4 \cdot 10^4$ ± 21%	Rb-80	$6.2 \cdot 10^6$ ± 12%
K-45	$3.9 \cdot 10^3$ ± 30%	Rb-81g	$3.7 \cdot 10^8$ ± 6%
K-46	$6.5 \cdot 10^2$ ± 49%	Rb-81m	$8.5 \cdot 10^7$ ± 14%
K-47	$2.2 \cdot 10^2$ ± 41%	Rb-82g	$7.0 \cdot 10^6$ ± 29%
Sr-77	$8.4 \cdot 10^3$ ± 18%	Rb-82m	$2.7 \cdot 10^8$ ± 7%
Sr-79	$1.2 \cdot 10^5$ ± 44%	Rb-83	$1.4 \cdot 10^8$ ± 47%
Sr-80	$1.1 \cdot 10^7$ ± 43%	Rb-84m	$7.7 \cdot 10^6$ ± 11%
Sr-81	$1.5 \cdot 10^6$ ± 9%	Rb-86m	$1.5 \cdot 10^5$ ± 25%
Sr-83g	$1.3 \cdot 10^7$ ± 18%	Rb-88	$3.4 \cdot 10^4$ ± 21%
Sr-83m	$4.8 \cdot 10^3$ ± 19%		
Sr-85m	$3.3 \cdot 10^6$ ± 12%		
Sr-87m	$7.0 \cdot 10^4$ ± 38%		

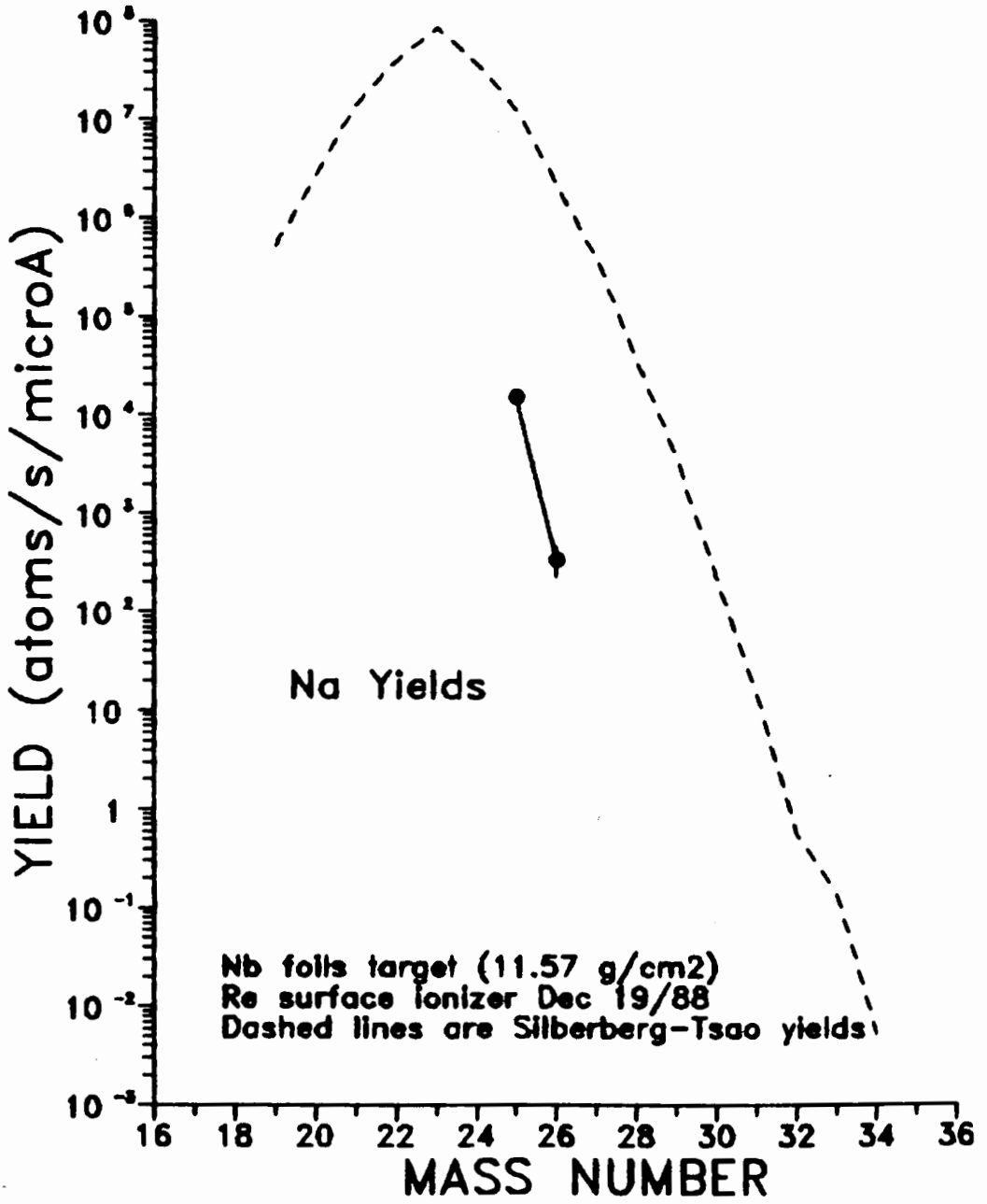

Figure 30: Yields of Na from a Nb foils target.

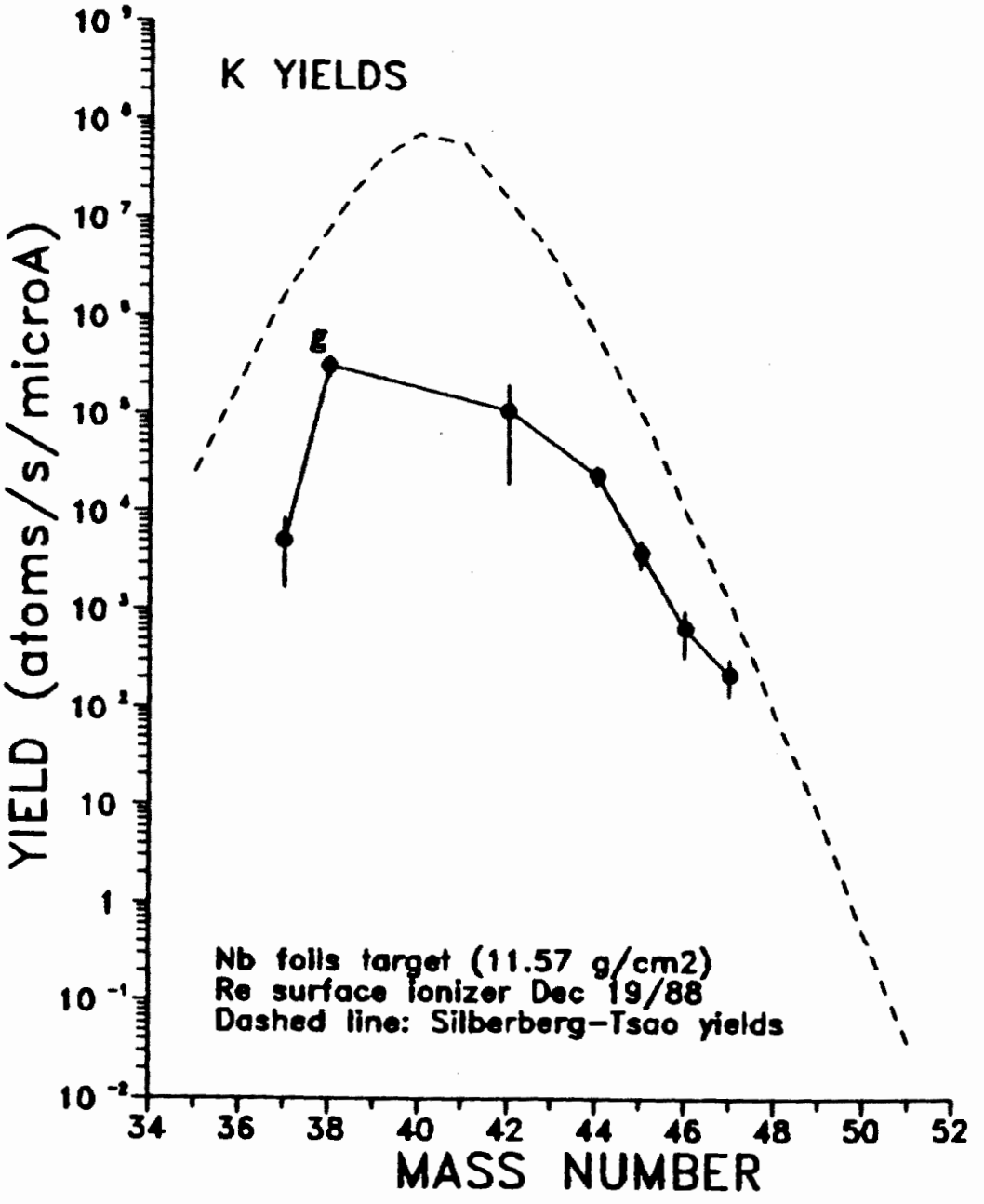

Figure 31: Yields of K from a Nb foils target.

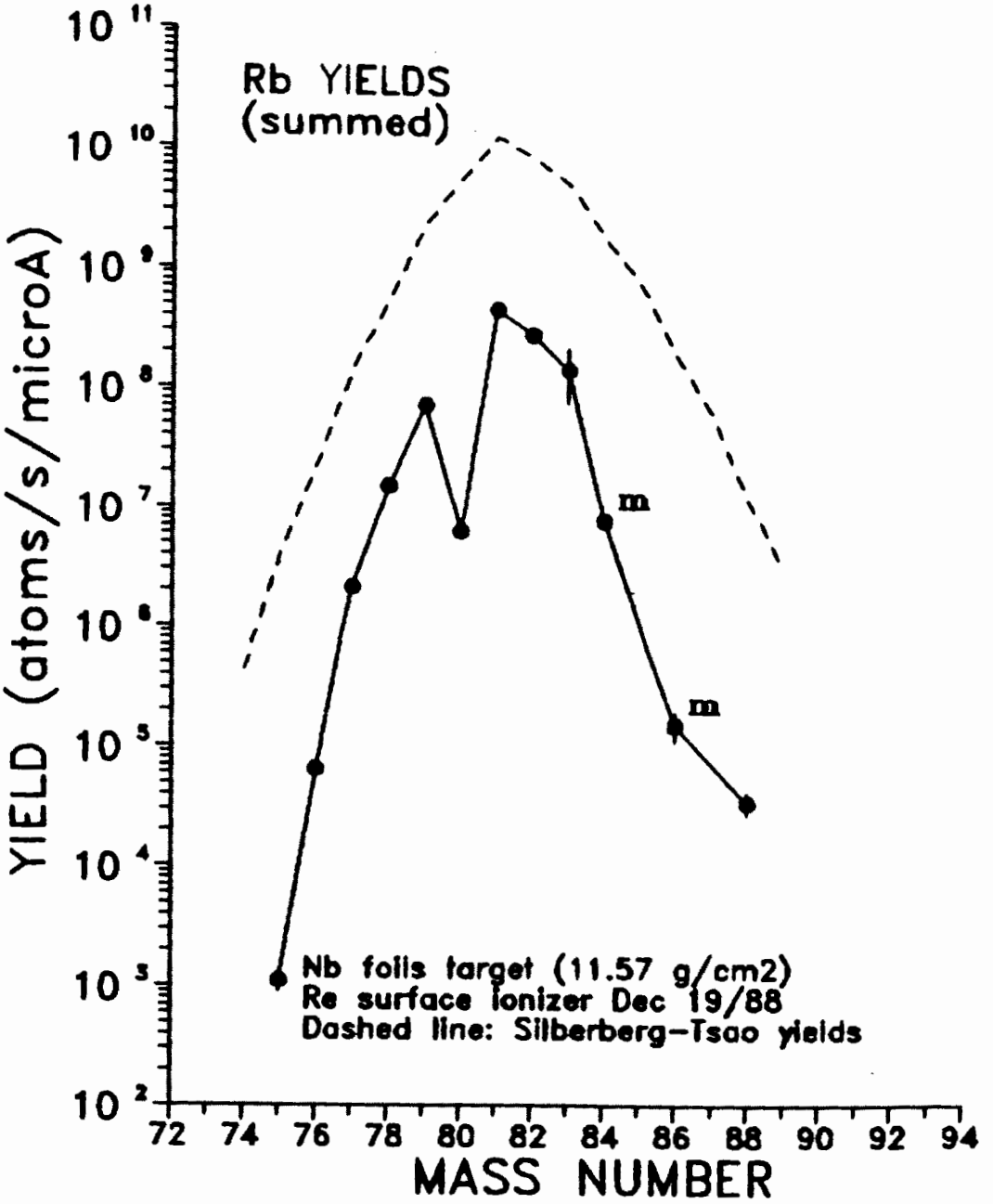

Figure 32: Yields of Rb from a Nb foils target.

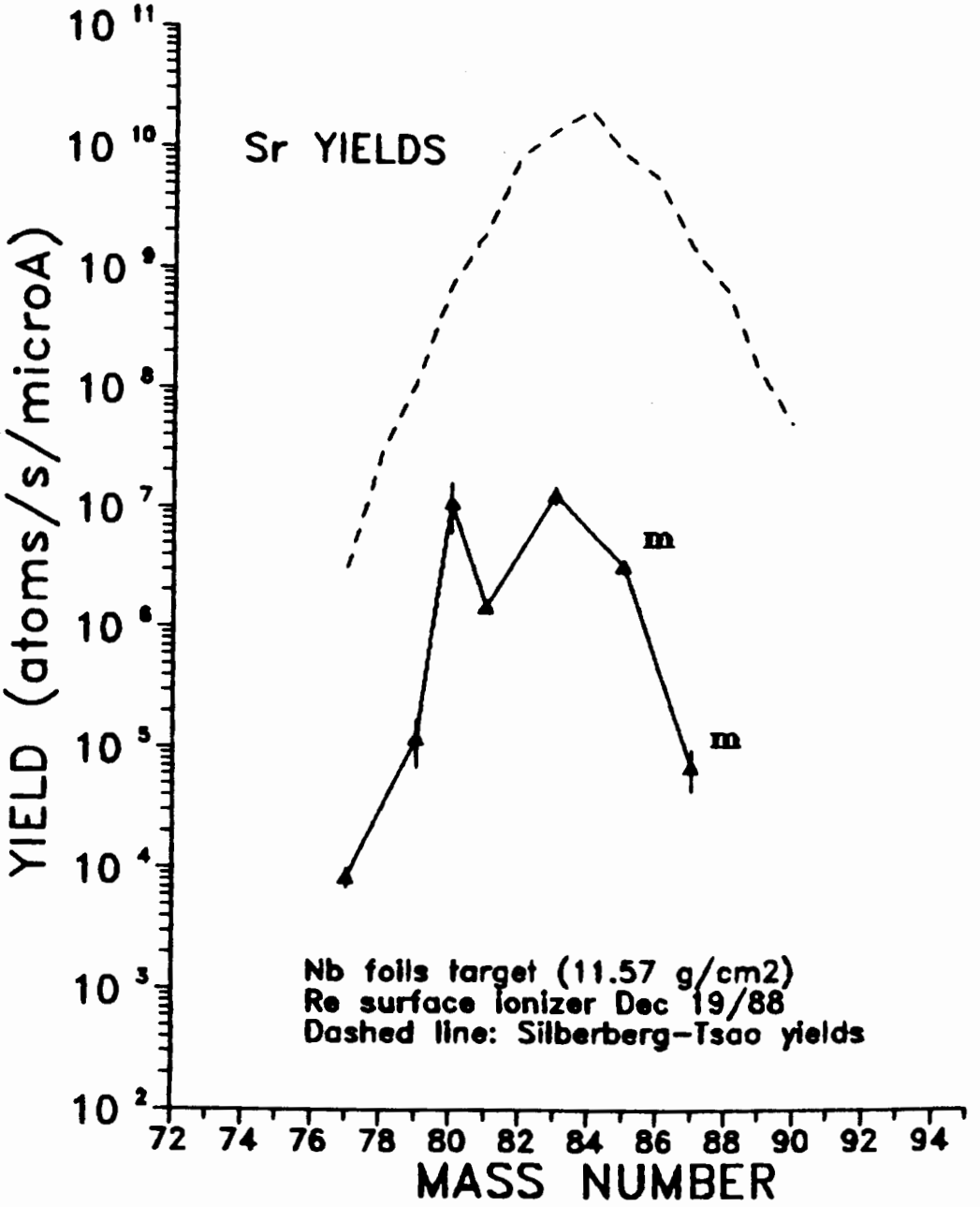

Figure 33: Yields of Sr from a Nb foils target.

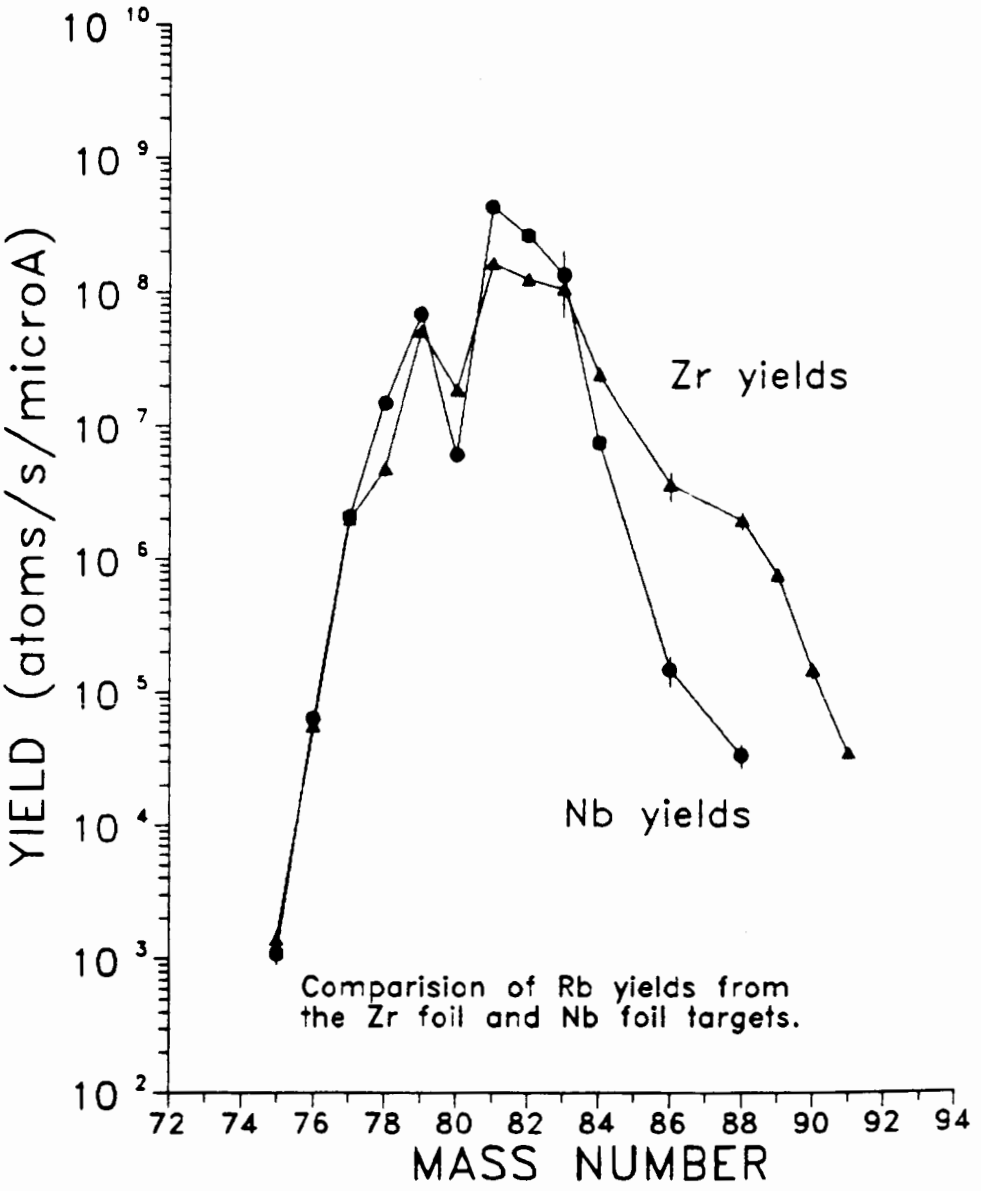

Figure 34: Comparison of Rb yields from Zr & Nb foils targets.

isotopic components of the target is significant. In any case, the Silberberg-Tsao predictions of Rb yields are not expected to be entirely accurate for either target for reasons discussed previously. From the experimental yields, it appears that production of the lighter rubidiums is about the same from both targets, while heavier rubidiums are better produced by a Nb target. No significant release differences are immediately apparent from the mass distributions from the two targets at the temperatures involved.

The case of Sr yields is also ambiguous. The measured yields and predicted yields are displayed in Figure 33. As with the rubidium products, production cross-sections for Sr from Nb are not considered valid. However, only 3 protons are emitted from Zr to produce Sr and here the SILT formulas for peripheral reactions are included in the prediction. While the comparison of experimental yields does not show any clear trends, it seems that the Zr target is better for neutron-rich Sr products.

No great differences are to be expected for the sodium or potassium yields from those observed from the zirconium target and the measured values are indeed of the same order of magnitude. A reasonable fit for efficiency vs. half-life was obtained for the rubidium yields and it is displayed in Figure 35. No fit could be obtained for the strontium case as can be predicted from the data displayed

in Figure 36. Clearly, the difference resulting from the exclusion of the peripheral reactions cross-sections in the SILT calculations makes a significant difference. A fit for the potassium efficiencies (Figure 37) could only be obtained by exclusion of the 47K data point and even then the uncertainty is greater than the value. Since only two sodium yields were measured, only an estimate of release time was calculated; the fit is displayed in Figure 38. The results of the fits are displayed in Table 9. Sodium release and efficiency is comparable to that of the Zr target. The estimated potassium release time is the same as for the Ti foils targets but in both cases the uncertainties

Table 9

Maximum Efficiencies & Mean Release Times

for Elements from the Nb Foils Target

Element	τ_{mean} (sec)	Eff_{max} (%)	Saha-Langmuir[a] (%)
Na	~ 8	~ 0.12	30
K	7.1 ± 7.8	4.3 ± 0.5	97
Rb	1370 ± 950	3.8 ± 1.5	99
Sr	?	?	8

a: Ionization efficiency predicted by Saha-Langmuir formula at 1900 °C

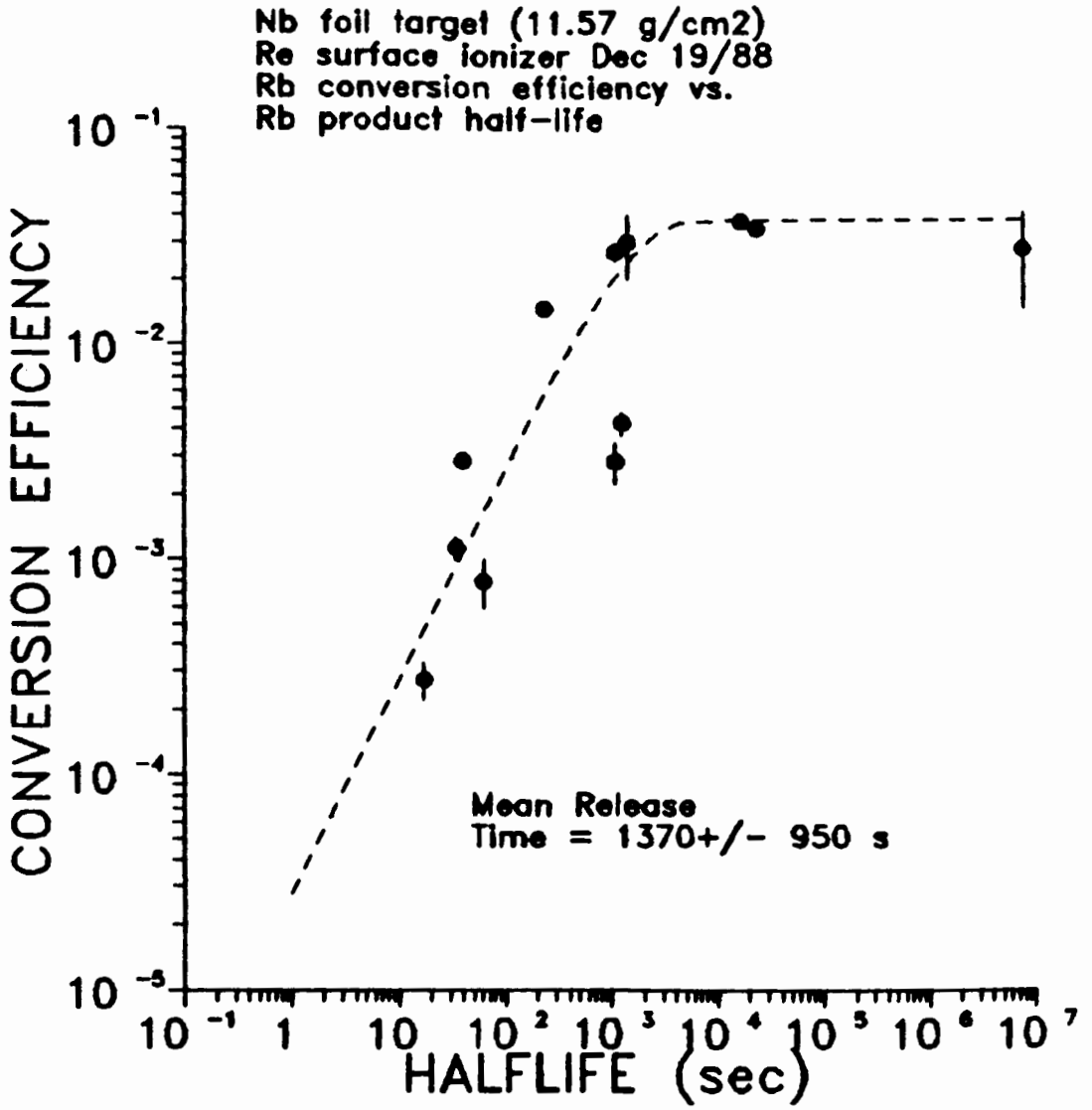

Figure 35: Conversion efficiencies for Rb from a Nb foils target.

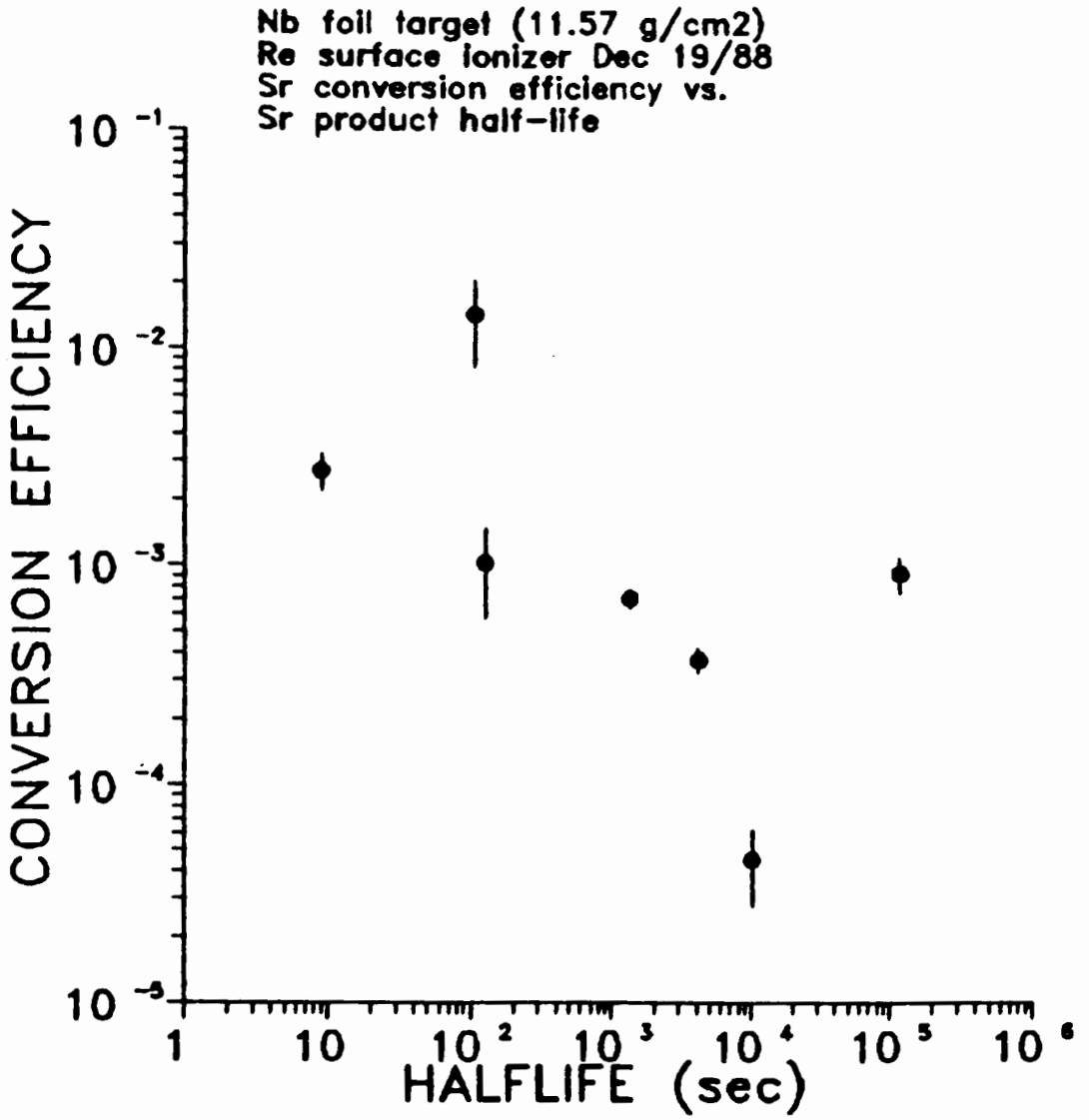

Figure 36: Conversion efficiencies for Sr from a Nb foils target.

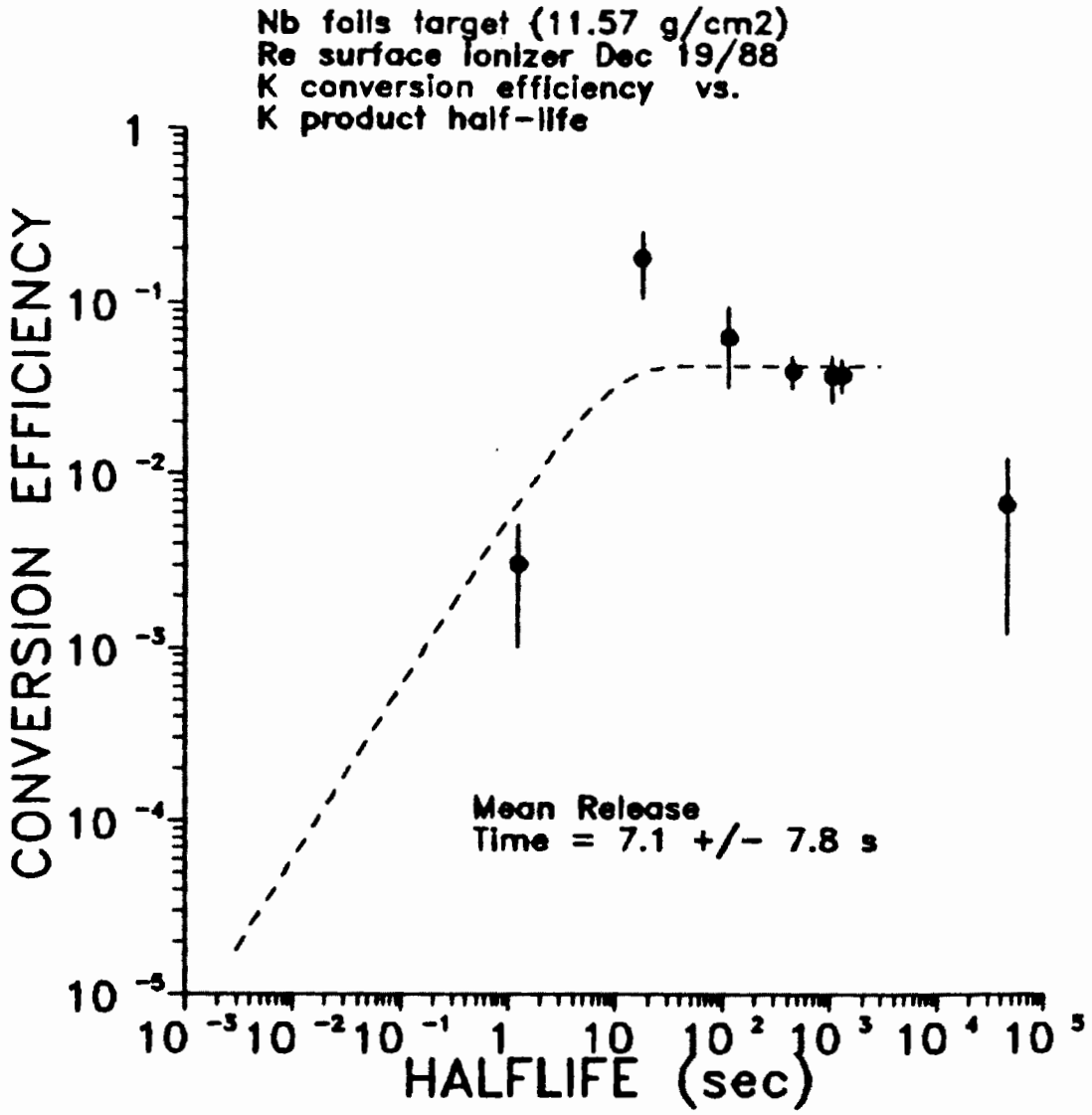

Figure 37: Conversion efficiencies for K from a Nb foils target.

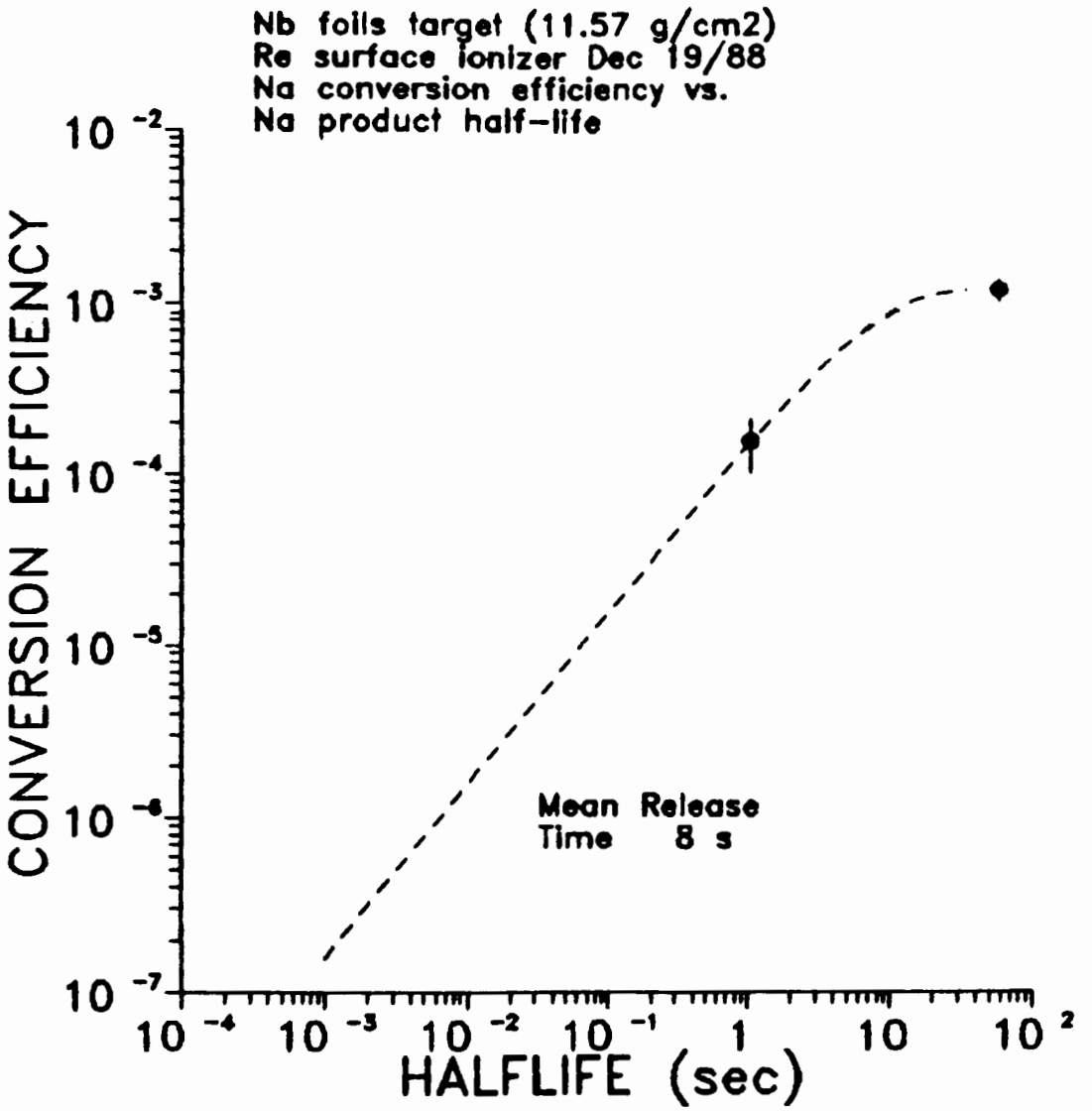

Figure 38: Conversion efficiencies for Na from a Nb foils target.

are greater than the values. For rubidium, the maximum efficiencies are about the same for Zr and Nb; the uncertainty in the Nb target Rb release time is 70% making any comparison somewhat dubious.

The Hafnium Foils Target Run:

A target of fifty stacked 0.25mm thick hafnium foil disks was used in a TISOL run on January 30, 1989. A rhenium ionizer foil was used in the surface ionization source and the estimated target temperature was 1800° - 1900° C. The intent of running this target was to look for yields of cesium isotopes and possibly rare earth product such as Sm, Eu, Tm and Yb which have sufficient vapor pressures to be released at this temperature. Of historical significance is the fact that TISOL operation was deemed sufficiently safe by the TRIUMF safety group to allow the irradiation of a fissionable target for the first time. Yields of Li, Na, K, Rb, Cs and Yb were measure. No strontium separation was observed, nor any lanthanides other than Yb.

The results are displayed in Table 10 and in Figures 39 - 43. The sodium yields are of the same order of magnitude as with the previous targets and seem to generally follow the predicted mass distribution, though the production of proton-rich isotopes seems enhanced over the neutron-rich isotopes. The sharp discontinuities in the predicted yield curve are due to a change of semiempirical parameters at

mass 20 and 30. All of the observed sodium yields lie in the domain of one parameter value, but it is impossible to comment on the validity of the predictions for sodium species from the Hf target.

Only three yields were measured for potassium species in this run; the ^{38g}K yield exceeds the SILT predictions while the ^{44}K and ^{45}K yields fall short by 2 to 3 orders of magnitude. In the niobium target run the ^{38g}K yield also seemed high. There is no simple explanation for this phenomenon. Since ^{38m}K decays entirely by β^+ emission, there can be no contribution to the ground state yield from decay of the metastable isomer. One possible explanation is that the yield is enhanced by decay of ^{38}Ca into ^{38}K, though no activity attributable to any calcium isotope was observed in any of the target runs. However, this does not mean that Ca isotopes were not being separated. Calcium has a first ionization potential of 6.1 eV while that of Yb is 6.2 eV. Since Yb was ionized and separated, it is possible that calcium may have been as well, even if it was not detected. The calciums from mass 40 to mass 48 are all either stable or so long-lived that they are virtually non-detectable during any count interval used in this study. Calcium 39 is a β^+ - only emitter, while the isotopes lighter than mass 37 are delayed proton emitters. Of the calciums on the proton-rich side of stability, only ^{38}Ca is likely to be detected by the gamma counting techniques used. On the neutron-rich

Table 10

Results of Hf Foils Run

Nuclide	Yield (nuclei/sec/μA)	Nuclide	Yield (nuclei/sec/μA)
Li-8	$4.0 \cdot 10^5$ ± 28%	K-38g	$6.0 \cdot 10^5$ ± 22%
		K-44	$2.6 \cdot 10^4$ ± 15%
Na-20	$4.0 \cdot 10^2$ ± 40%	K-45	$1.5 \cdot 10^4$ ± 17%
Na-21	$1.5 \cdot 10^4$ ± 24%		
Na-25	$1.2 \cdot 10^4$ ± 11%	Cs-119	$1.9 \cdot 10^2$ ± 56%
Na-26	$8.7 \cdot 10^2$ ± 26%	Cs-120	$1.4 \cdot 10^3$ ± 27%
Na-27	$2.7 \cdot 10^2$ ± 55%	Cs-121m	$2.6 \cdot 10^3$ ± 40%
		Cs-122m	$8.8 \cdot 10^2$ ± 28%
Rb-77	$7.6 \cdot 10^3$ ± 14%	Cs-123g	$7.3 \cdot 10^3$ ± 28%
Rb-78g	$1.1 \cdot 10^4$ ± 19%	Cs-124g	$7.1 \cdot 10^3$ ± 21%
Rb-78m	$4.7 \cdot 10^4$ ± 19%	Cs-125	$5.4 \cdot 10^4$ ± 18%
Rb-79	$4.6 \cdot 10^5$ ± 6%	Cs-126	$2.3 \cdot 10^4$ ± 17%
Rb-80	$1.7 \cdot 10^5$ ± 12%	Cs-128	$1.1 \cdot 10^4$ ± 17%
Rb-81g	$1.1 \cdot 10^5$ ± 17%		
Rb-81m	$5.8 \cdot 10^5$ ± 31%	Yb-159	$4.9 \cdot 10^2$ ± 35%
Rb-82g	111310^5 ± 31%	Yb-160	$2.8 \cdot 10^3$ ± 15%
Rb-82m	$2.6 \cdot 10^6$ ± 7%	Yb-161	$7.3 \cdot 10^3$ ± 21%
Rb-84m	$4.9 \cdot 10^5$ ± 10%	Yb-162	$3.4 \cdot 10^4$ ± 13%
Rb-86m	$3.4 \cdot 10^4$ ± 19%	Yb-163	$6.7 \cdot 10^4$ ± 17%
Rb-88	$3.4 \cdot 10^4$ ± 24%	Yb-167	$5.9 \cdot 10^4$ ± 9%
Rb-89	$1.3 \cdot 10^4$ ± 16%		
Rb-90	$3.3 \cdot 10^3$ ± 34%		

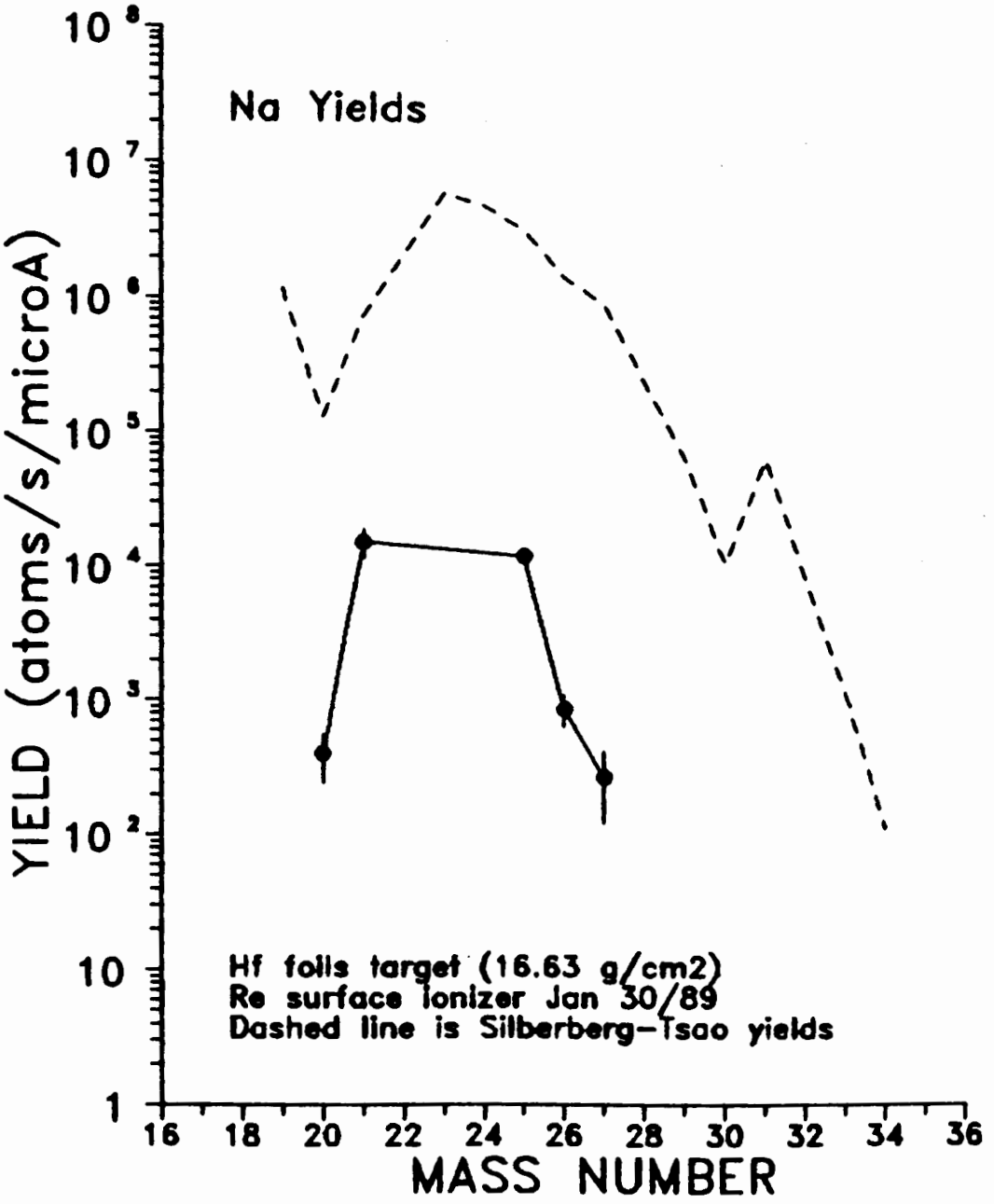

Figure 39: Yields of Na from a Hf foils target.

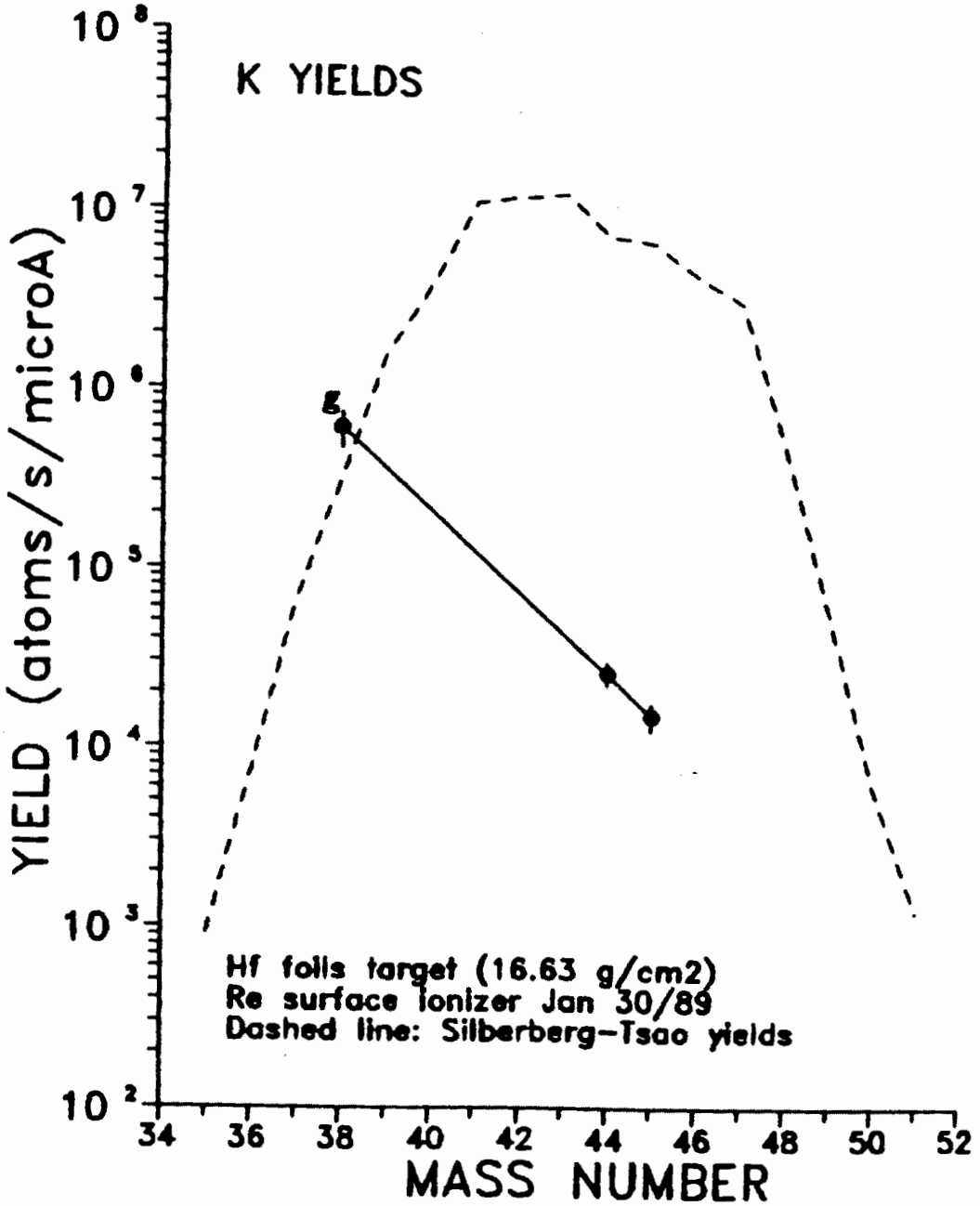

Figure 40: Yields of K from a Hf foils target.

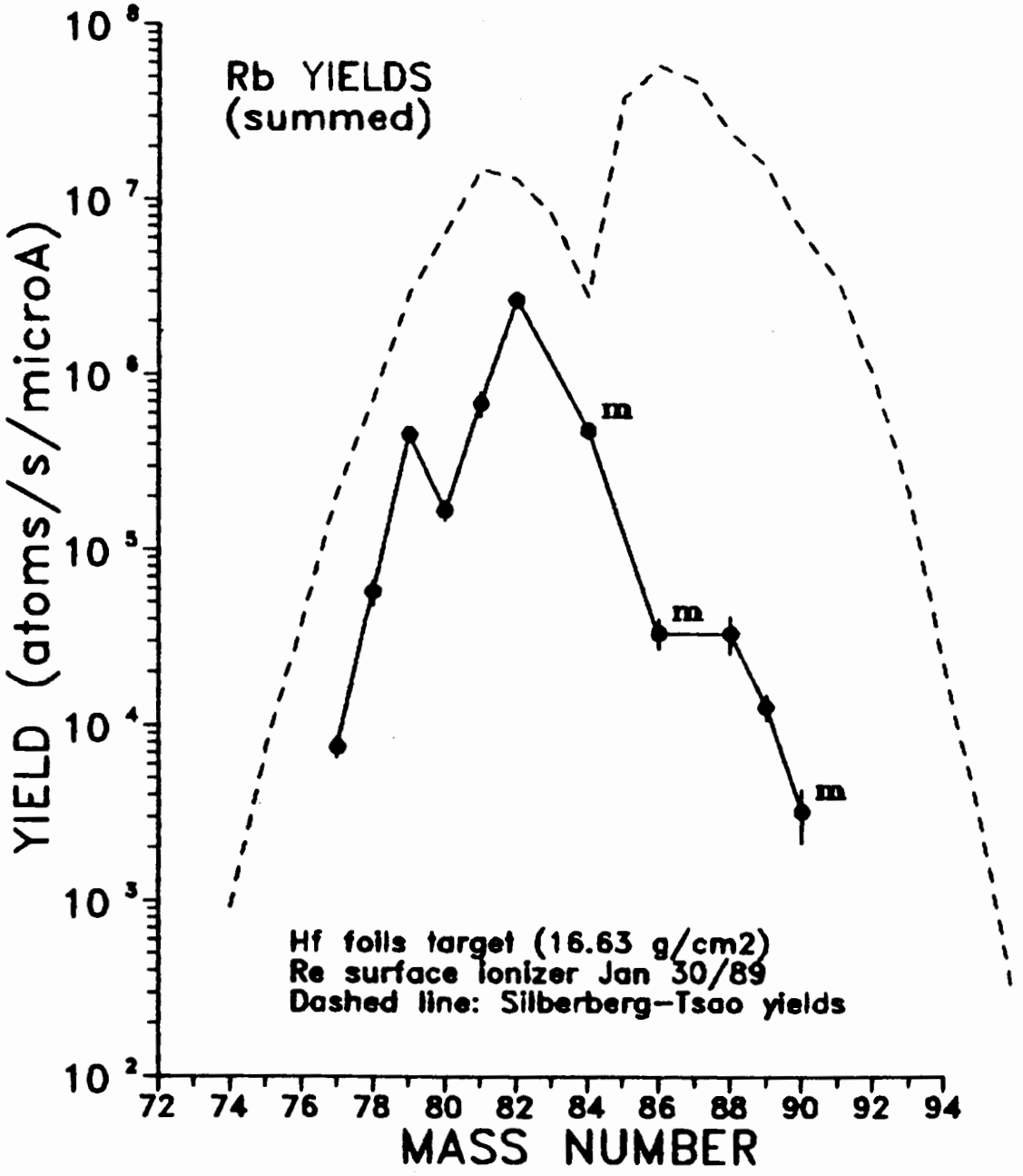

Figure 41: Yields of Rb from a Hf foils target.

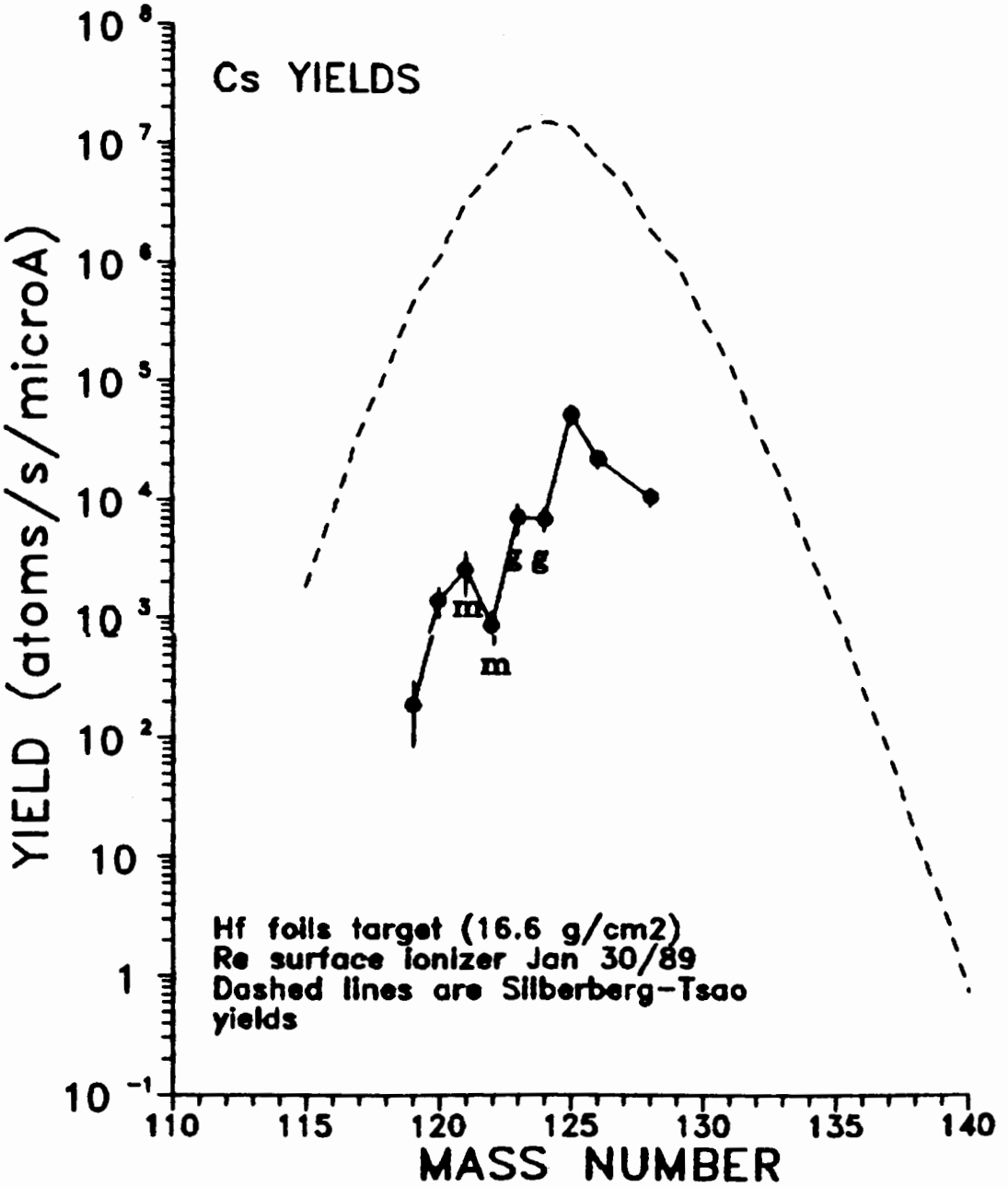

Figure 42: Yields of Cs from a Hf foils target.

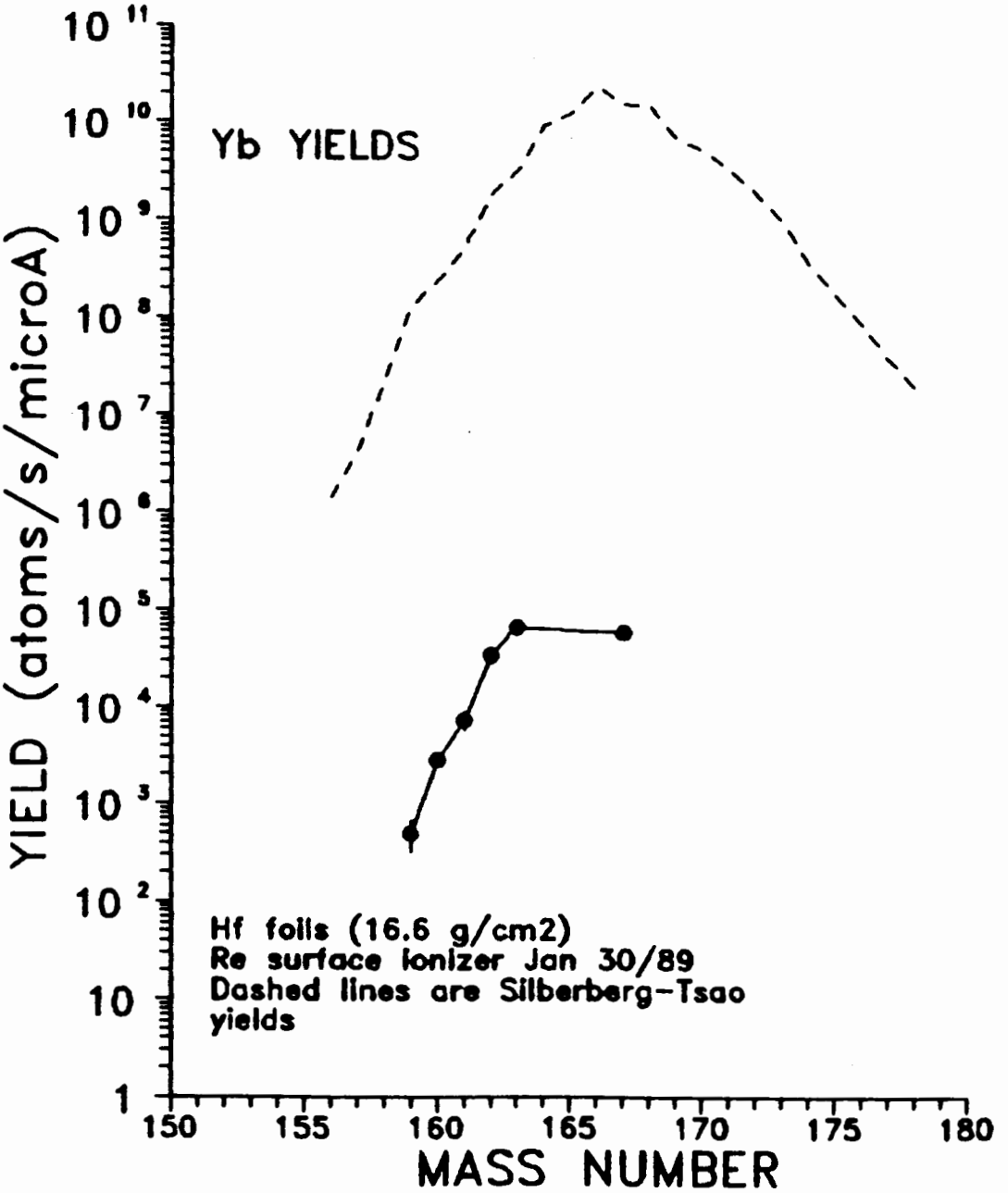

Figure 43: Yields of Yb from a Hf foils target.

side of stability, only isotopes heavier than mass 49 would be detectable. However, since no potassium heavier than mass 47 was observed, no search for these heavier calciums was conducted. No extensive study of the potassium yields was conducted since hafnium is expected to be a poor target for production of potassium isotopes. The Silbergerg-Tsao formulae predict target breakup to be the dominant reaction mechanism for potassium products lighter than mass 41 with peripheral reaction mechanisms contributing for potassiums heavier than mass 41; neither production mechanism is expected to give high yields. Comparison with The titanium target yields (where spallation reactions are the dominant production mechanism) shows yield differences on the order of 1 - 2 orders of magnitude.

The rubidium yields displayed in Figure 41 are generally high when compared to the SILT predictions. The double peaked shape of the predicted mass distribution is due to the summed contributions from both spallation and fission reactions on the target. Comparison with the experimental mass yields shows a good agreement for the lighter rubidiums that are produced mainly by spallation and a large over-estimation of the fission yield for the heavier isotopes.

The cesium yields are shown in Figure 42. For four of the measured yields only ground state or isomeric state yields could be determined. However, the general distribution follow the predictions, especially if a small

allowance is made for yields to the missing isomers. The SILT formulae predict spallation and peripheral reaction mechanisms for Cs production. The yields are much lower than would be predicted by the expected ionization efficiency for cesium.

The ytterbium yields are shown in Figure 43. Though about 5 orders of magnitude less than the SILT predictions the yields follow the calculated mass distribution. The ytterbiums are expected to be produced by both spallation and peripheral reactions. Since only three protons are emitted in a (p, ypxn) reaction for a Yb product, the SILT prediction can be considered valid. No other lanthanides were observed from this target.

The conversion efficiency vs. half-life least squares fits are shown in Figures 44 - 48; the results are given in Table 11. For the sodium isotopes, the calculated release time is shorter than the estimates for the Zr or Nb targets, but the uncertainty is greater than the value. For potassium, the ^{38g}K point was excluded from the fit and only crude estimates were made. For the rubidium data, the four lowest points were excluded from the fit; these correspond to yields of heavy rubidiums were the SILT prediction from fission yields seems to be grossly over-estimated. For the cesium fit, the ^{122m}Cs and ^{123g}Cs points were omitted from the fit as was the ^{167}Yb point from the fit to the ytterbium values. Attempts were made to fit the data using all

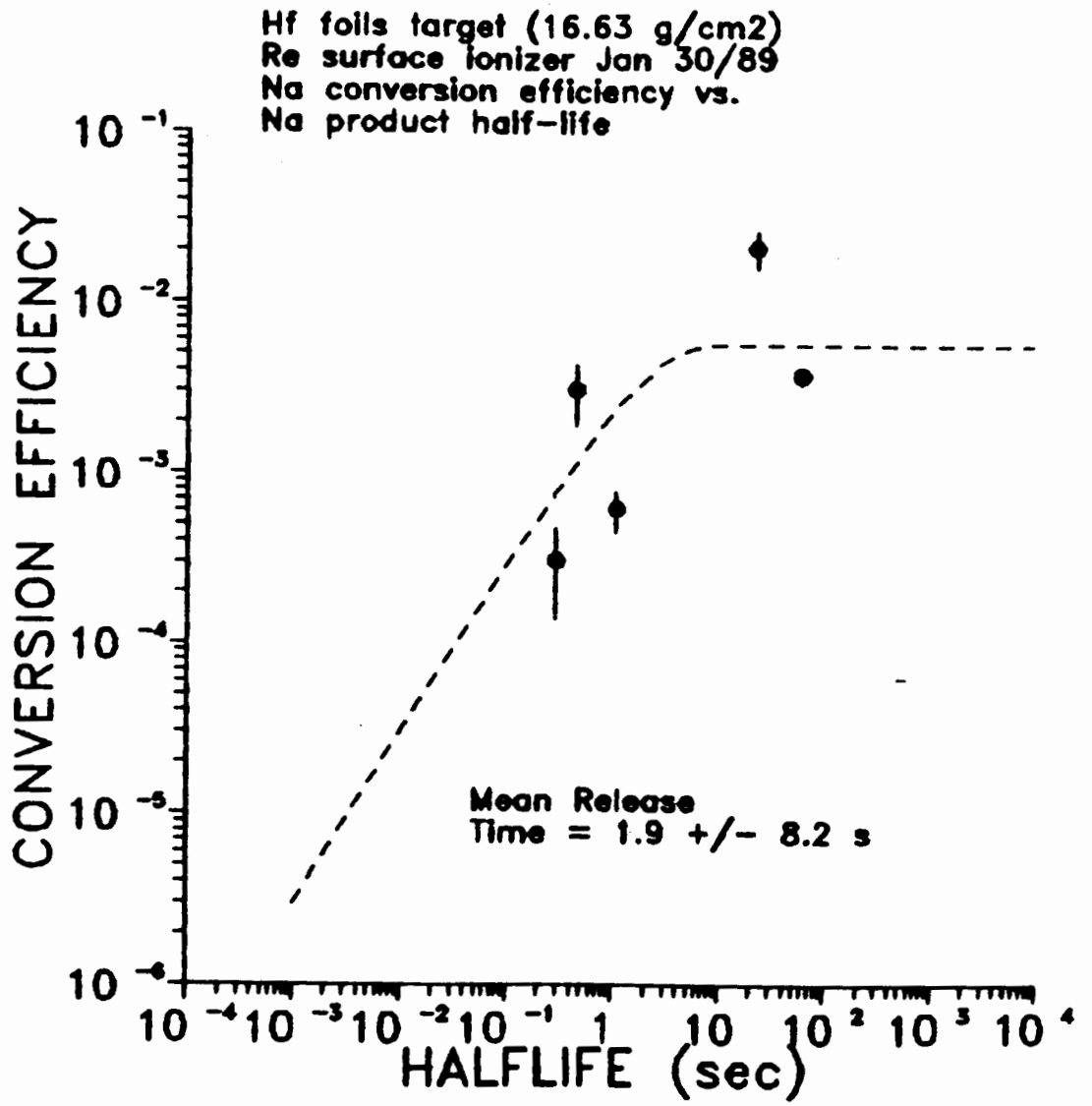

Figure 44: Conversion efficiencies for Na from a Hf foils target.

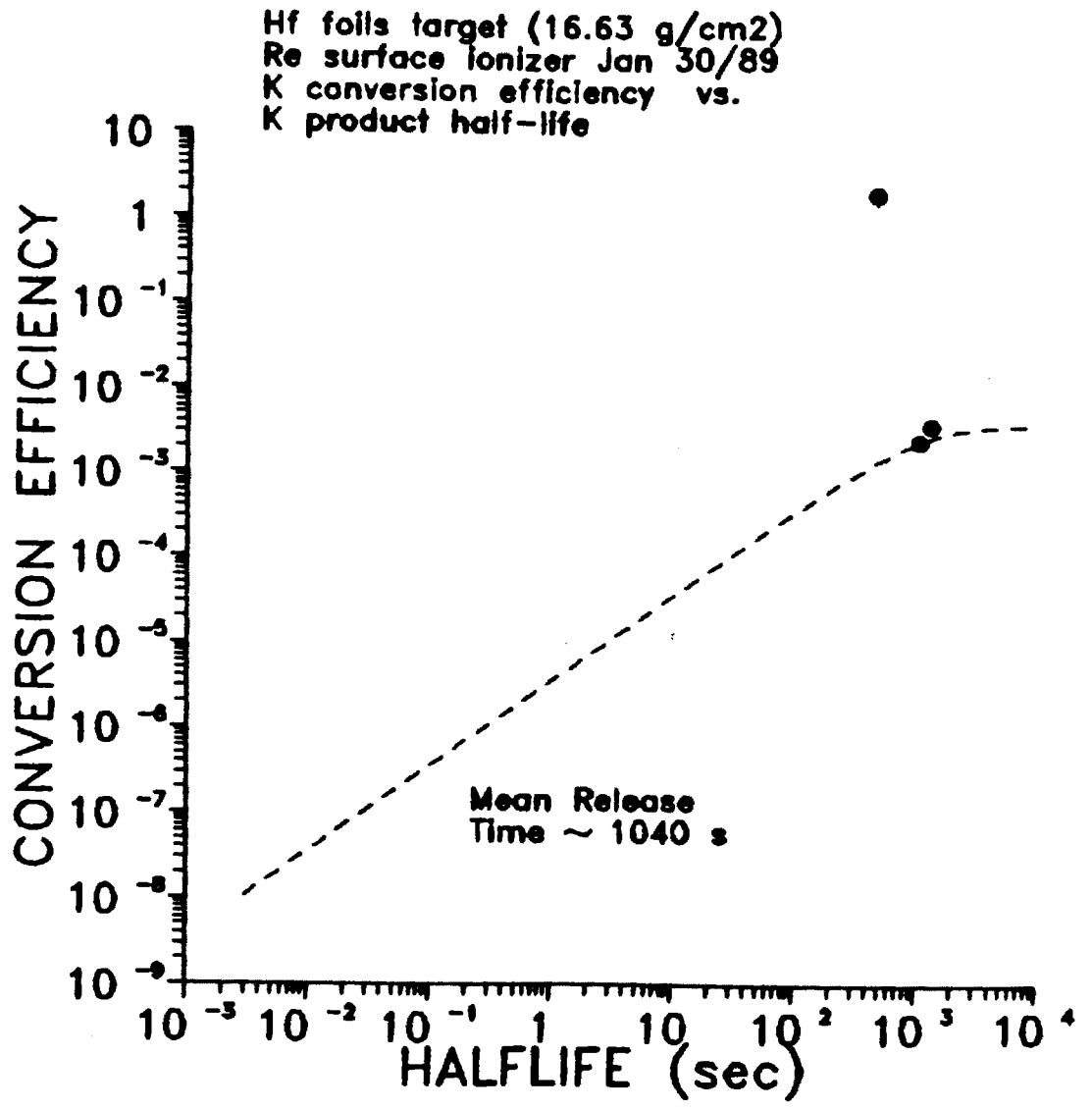

Figure 45: Conversion efficiencies for K from a Hf foils target.

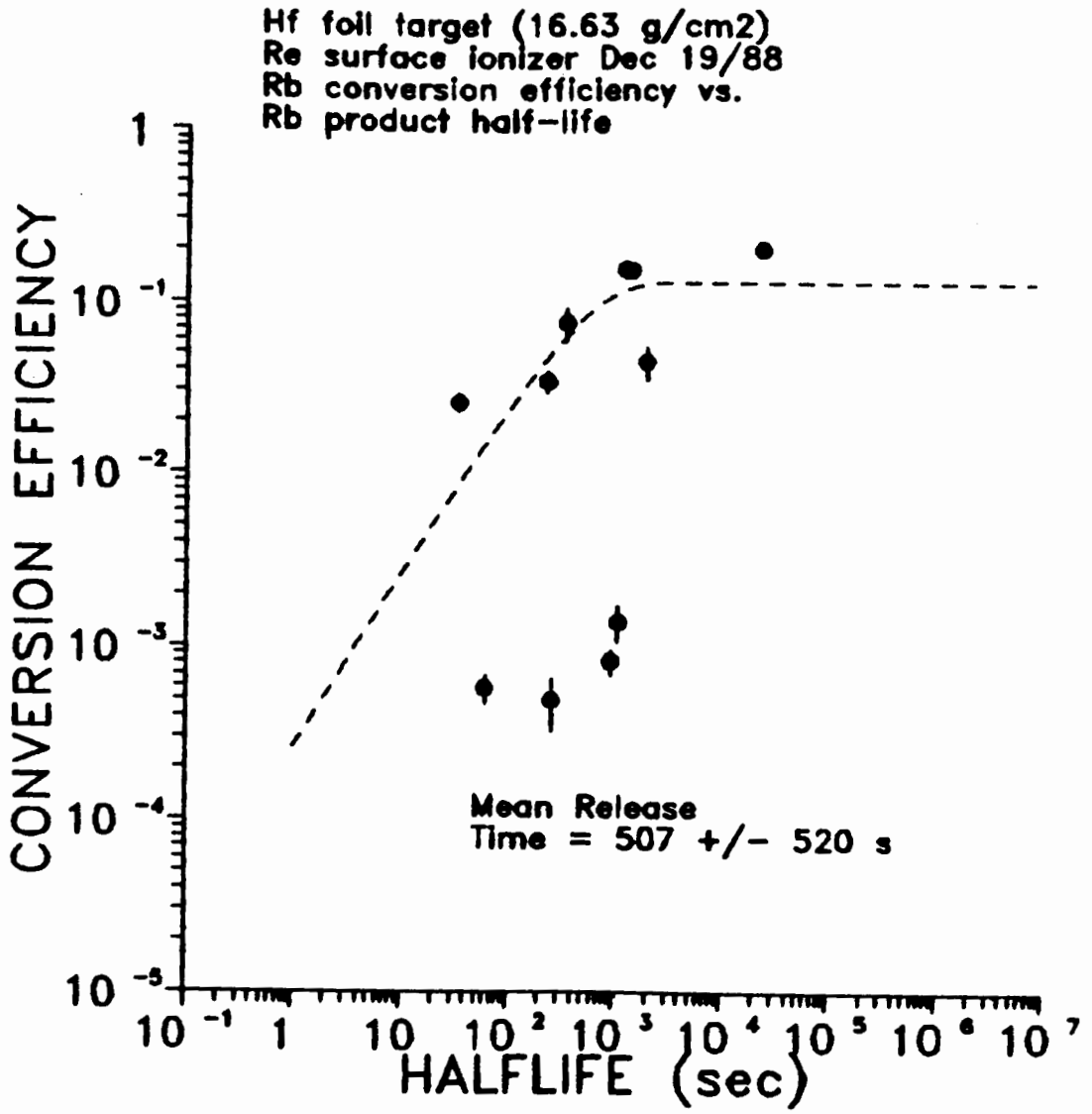

Figure 46: Conversion efficiencies for Rb from a Hf foils target.

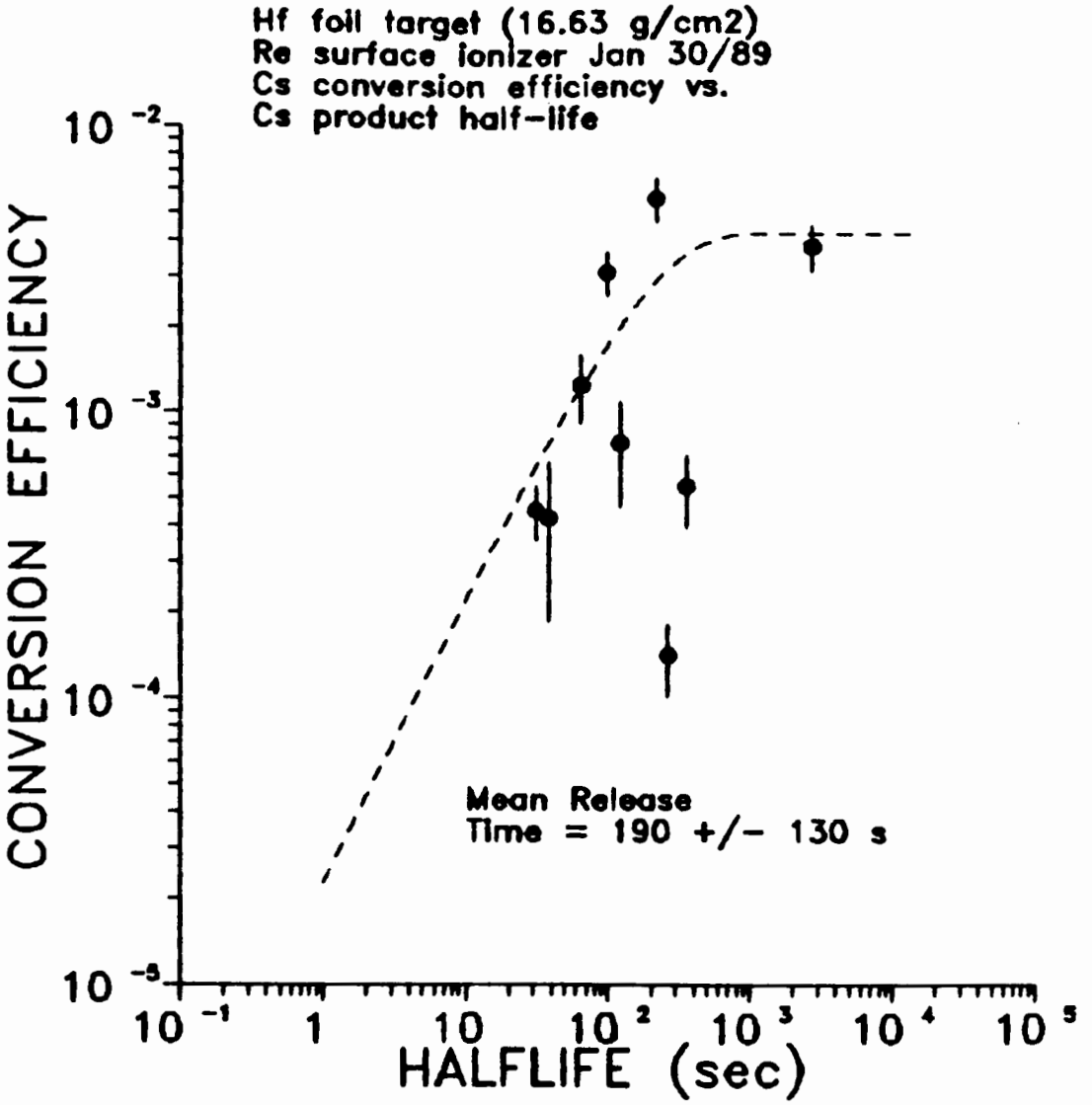

Figure 47: Conversion efficiencies for Cs from a Hf foils target.

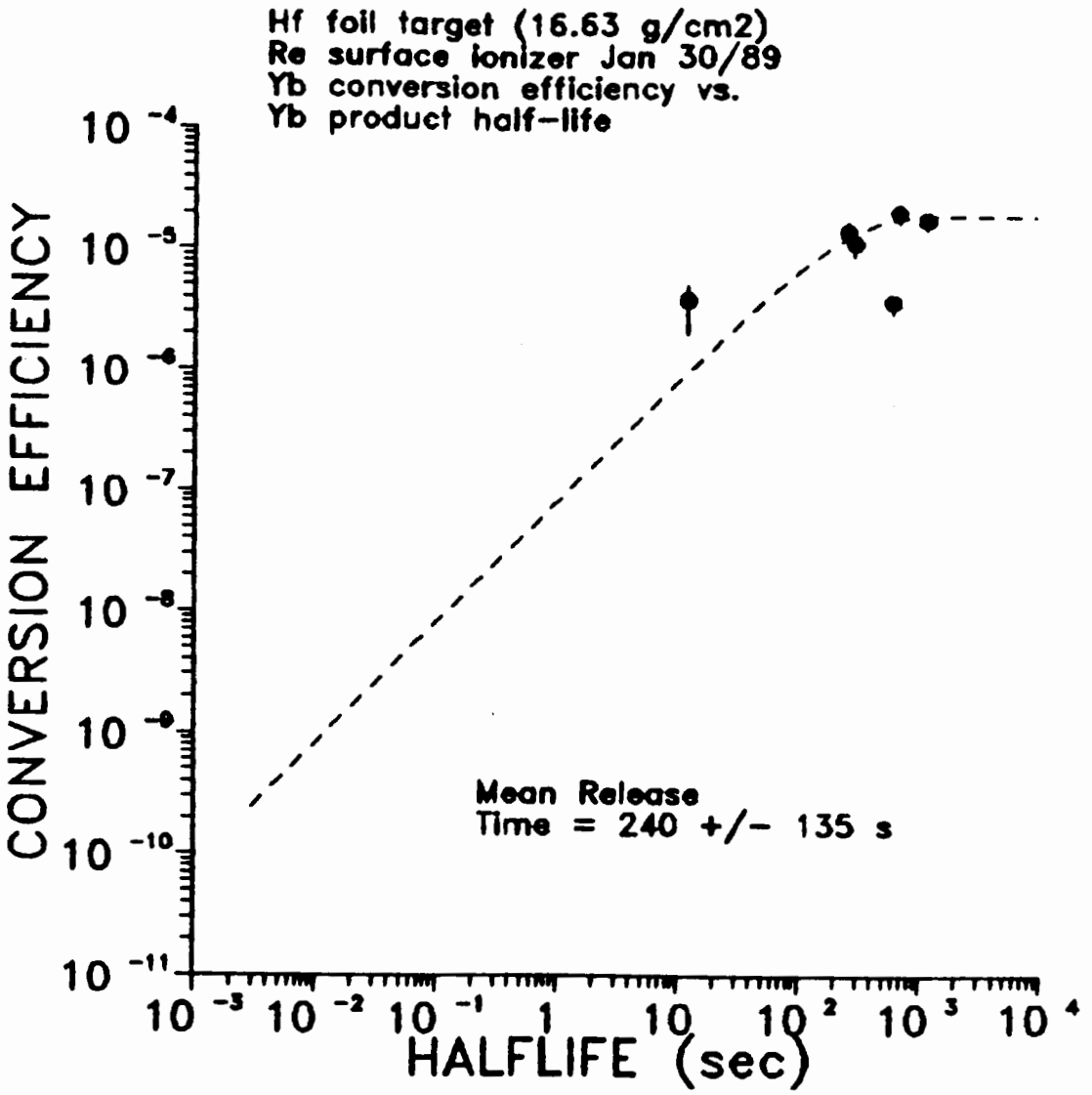

Figure 48: Conversion efficiencies for Yb from a Hf foils target.

Table 11

Maximum Efficiencies & Mean Release Times

for Elements from the Hf Foils Target

Element	τ_{mean} (sec)	Eff_{max} (%)	Saha-Langmuir[a] (%)
Na	1.9 ± 8.2	0.6 ± 0.5	30
K	~ 1040	~ 0.4	97
Rb	507 ± 520	13 ± 4.4	99
Cs	190 ± 130	0.4 ± 0.2	100
Yb	240 ± 135	.002 ± 0.0004	0.6

a: Ionization efficiency predicted by Saha-Langmuir formula at 1900 °C

experimental points for all cases. When no fit could be obtained, individual points were excluded until a fit could be obtained.

The Uranium Oxide/Carbon Target Run:

On May 4, 1989, a target composed of pressed pellets of uranium oxide mixed with carbon lamp black was irradiated for TISOL yield determinations. Approximately 2 grams of UO_2 was mixed with an equal weight of carbon lamp black. A small amount of albumen (egg white) was added until the Powder just began to cake. The mixture was then gently pressed into loose pellets, 13 mm in diameter. The pellets

were dried under a heat lamp and placed in a graphite target crucible with graphite sheet spacers. The target had an estimated thickness of 1.6 g U/cm^2. Pressed pellets, rather than a loose powder, were used for safety reasons. With a loose powder target, the possibility of contamination from the spilled uranium dust was deemed too great; it was reasoned that the pellet target could be better contained. Once in the TISOL target chamber, the target was slowly heated to about 1800° C. During heating to this temperature, the uranium oxide is converted to uranium carbide with release of gaseous carbon oxides. As well, the albumen is presumably carbonized.

Yields of Li, Na, Al, Ga, Rb, Cs and In were measured for this target. The potassium were not expected to be significant from this target and were not measured. During the determination of neutron-rich rubidium yields, gammas from isotopes of strontium were observed. However, unlike the previous targets, no strontium signatures were observed on the proton-rich side of stability. Estimates of strontium yields from decays of their rubidium parents showed that the strontiums could be entirely accounted for by rubidium decay. The yields are given in Table 12 and displayed in Figures 49 - 53.

Sodium, aluminum and potassium are all predicted to be produced by breakup reactions by the Silberberg-Tsao formulae. As with the Hf target, discontinuities in the SILT

predictions at mass 20 and 30 of the Na and Al distributions are present. The Na and Al yield distributions do not seem to fit the SILT curves.

The lithium yields are primarily attributed to evaporation of light fragments from the target. Both the ^{8}Li and ^{9}Li yields were estimated from the alpha spectra obtained at each mass. In each case the high energy alpha spectrum was simply summed and corrected for detector efficiency. Multiscaled beta spectra were also obtained at each mass setting to verify the identity of the species by its halflife.

The production of Ga, Rb, Cs and In results from proton induced fission of uranium. Both the Rb and In yield distributions show excellent agreement with the SILT predictions. The apparent jump in ^{99}Rb yield is undoubtedly the result of errors in the assigned branching ratios for the gammas observed. The determination of a ^{99}Rb yield, just one mass short of the present limit of known neutron-rich rubidiums, leaves only the lightest (^{74}Rb) and heaviest (^{100}Rb) rubidium isotopes unobserved using the TISOL system. For indium, the observed mass distribution stops at ^{131}In, again just one mass short of the heaviest known isotope. The cesium mass distribution also agrees well with the SILT predictions; the drop in yields above mass 142 can be attributed to delay losses incurred due to the shorter halflives of the heavier isotopes. Again, the limit of known

Table 12

Results of UO_2/C Foils Run

Nuclide	Yield (nuclei/sec/μA)	Nuclide	Yield (nuclei/sec/μA)
Li-8	$2.1 \cdot 10^5$ ± 29%	Rb-96	$3.4 \cdot 10^4$ ± 26%
Li-9	$7.5 \cdot 10^3$ ± 27%	Rb-97	$5.6 \cdot 10^3$ ± 15%
		Rb-98	$2.7 \cdot 10^2$ ± 37%
Na-21	$2.6 \cdot 10^4$ ± 19%	Rb-99	$9.3 \cdot 10^2$ ± 30%
Na-25	$1.3 \cdot 10^5$ ± 10%		
Na-26	$1.3 \cdot 10^4$ ± 19%	Cs-124	$1.5 \cdot 10^6$ ± 35%
Na-27	$3.2 \cdot 10^3$ ± 20%	Cs-125	$3.1 \cdot 10^6$ ± 31%
		Cs-126	$7.1 \cdot 10^5$ ± 16%
Al-28	$1.3 \cdot 10^3$ ± 24%	Cs-127	$2.5 \cdot 10^6$ ± 41%
Al-29	$5.9 \cdot 10^2$ ± 30%	Cs-128	$3.2 \cdot 10^6$ ± 14%
Rb-80	$3.4 \cdot 10^4$ ± 22%	Cs-129	$4.9 \cdot 10^6$ ± 21%
Rb-81g	$1.1 \cdot 10^5$ ± 17%	Cs-130	$3.7 \cdot 10^6$ ± 12%
Rb-86m	$8.6 \cdot 10^6$ ± 42%	Cs-132	$1.6 \cdot 10^7$ ± 28%
Rb-88	$2.0 \cdot 10^7$ ± 15%	Cs-139	$1.9 \cdot 10^7$ ± 12%
Rb-89	$2.1 \cdot 10^7$ ± 9%	Cs-140	$5.0 \cdot 10^6$ ± 8%
Rb-90g	$8.3 \cdot 10^6$ ± 28%	Cs-141	$1.7 \cdot 10^6$ ± 13%
Rb-90m	$1.8 \cdot 10^7$ ± 8%	Cs-142	$1.1 \cdot 10^5$ ± 15%
Rb-91	$1.2 \cdot 10^7$ ± 7%	Cs-143	$1.3 \cdot 10^5$ ± 9%
Rb-92	$2.5 \cdot 10^6$ ± 50%	Cs-144	$8.2 \cdot 10^4$ ± 14%
Rb-93	$3.1 \cdot 10^6$ ± 13%	Cs-145	$1.4 \cdot 10^4$ ± 16%
Rb-94	$9.7 \cdot 10^5$ ± 19%	Cs-146	$5.4 \cdot 10^2$ ± 28%
Rb-95	$1.3 \cdot 10^5$ ± 12%		

Table 12 (cont'd)

Results of UO_2/C Foils Run

Nuclide	Yield (nuclei/sec/μA)
In-120b	$2.8 \cdot 10^5$ ± 21%
In-120c	$9.6 \cdot 10^5$ ± 10%
In-121g	$1.1 \cdot 10^6$ ± 15%
In-122b	$8.5 \cdot 10^4$ ± 32%
In-122c	$4.6 \cdot 10^5$ ± 16%
In-123g	$5.4 \cdot 10^5$ ± 15%
In-124g	$9.2 \cdot 10^4$ ± 16%
In-124m	$1.5 \cdot 10^5$ ± 8%
In-125g	$1.6 \cdot 10^5$ ± 11%
In-125m	$2.6 \cdot 10^3$ ± 42%
In-126g	$3.2 \cdot 10^4$ ± 9%
In-126m	$3.3 \cdot 10^4$ ± 18%
In-127g	$2.3 \cdot 10^4$ ± 12%
In-127m	$1.9 \cdot 10^3$ ± 33%
In-128g	$7.4 \cdot 10^3$ ± 28%
In-128m	$8.5 \cdot 10^3$ ± 21%
In-129g	$4.7 \cdot 10^3$ ± 15%
In-130a	$1.7 \cdot 10^2$ ± 65%
In-130b	$1.2 \cdot 10^3$ ± 51%
In-130c	$5.6 \cdot 10^2$ ± 28%
In-131	$2.5 \cdot 10^2$ ± 33%

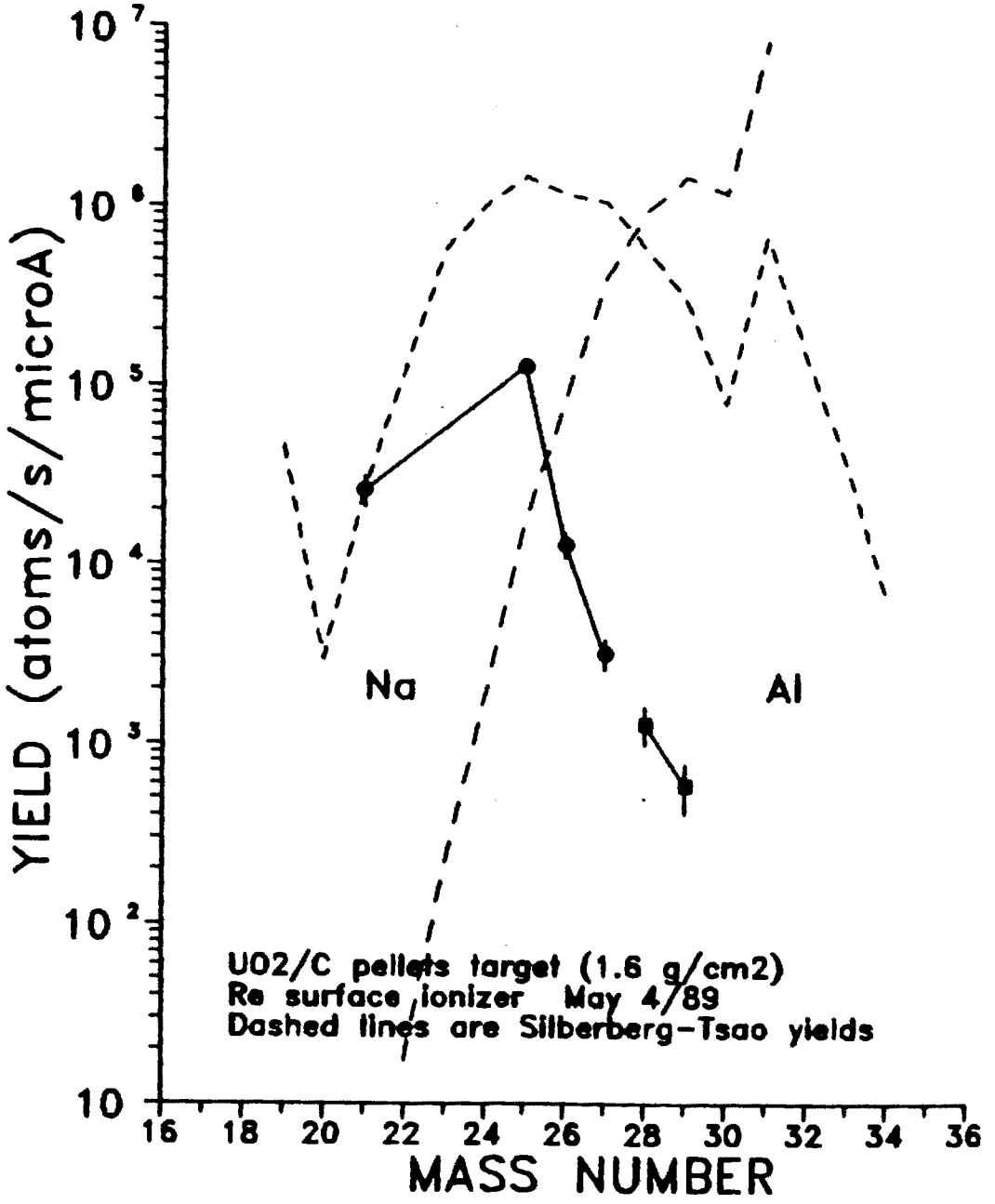

Figure 49: Yields of Na & Al from a UO_2/C target.

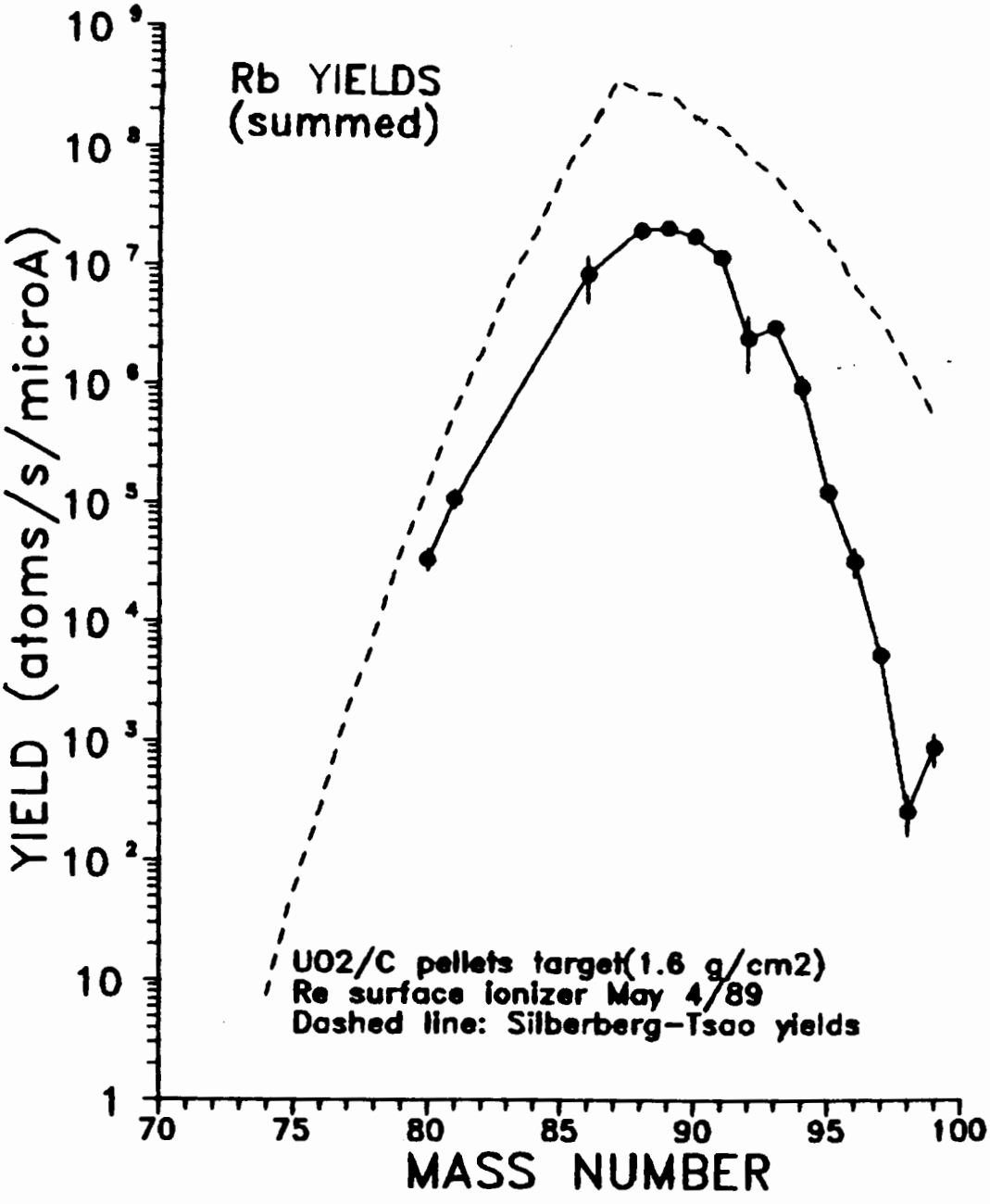

Figure 50: Yields of Rb from a UO_2/C target.

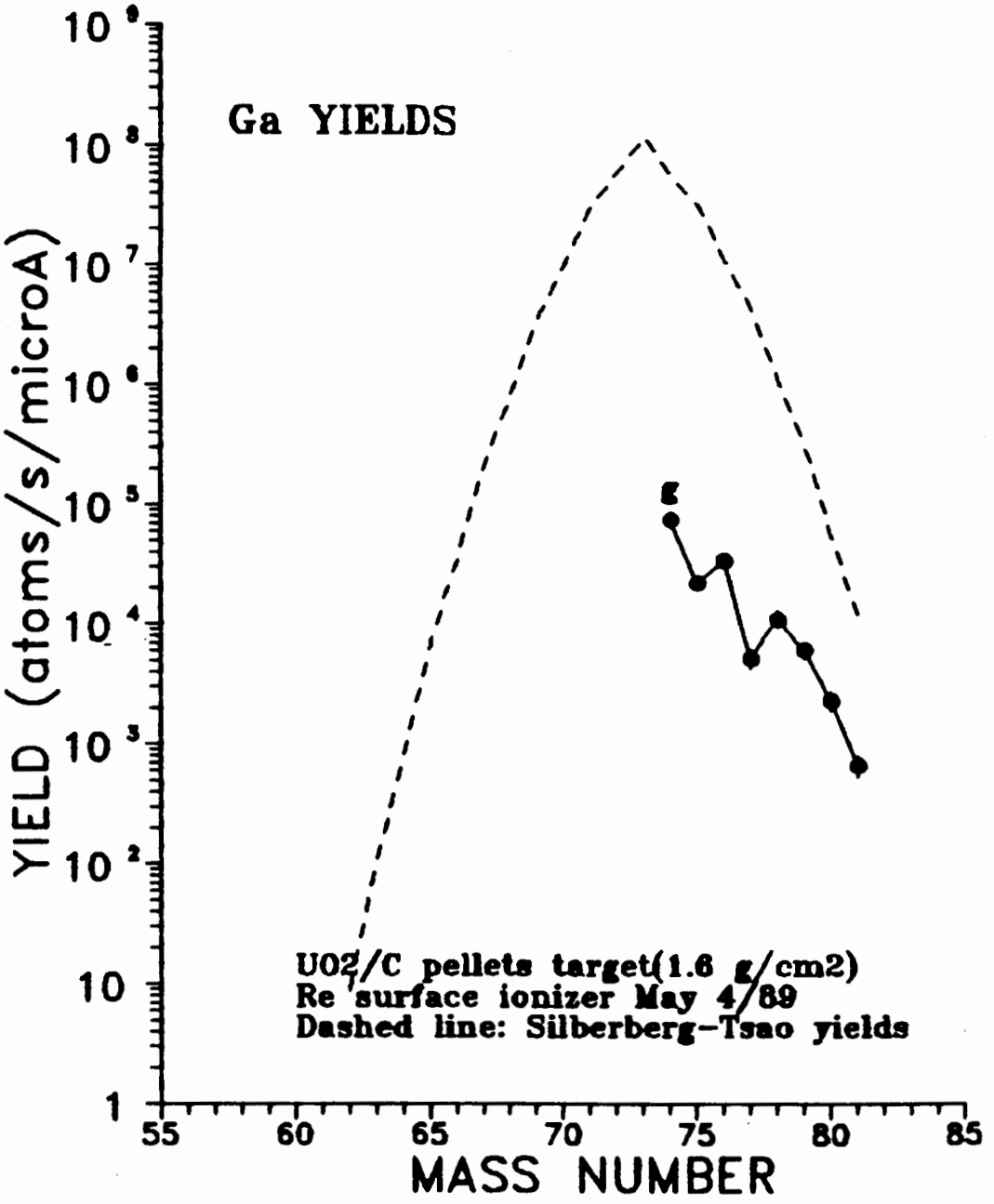

Figure 51: Yields of Ga from a UO_2/C target.

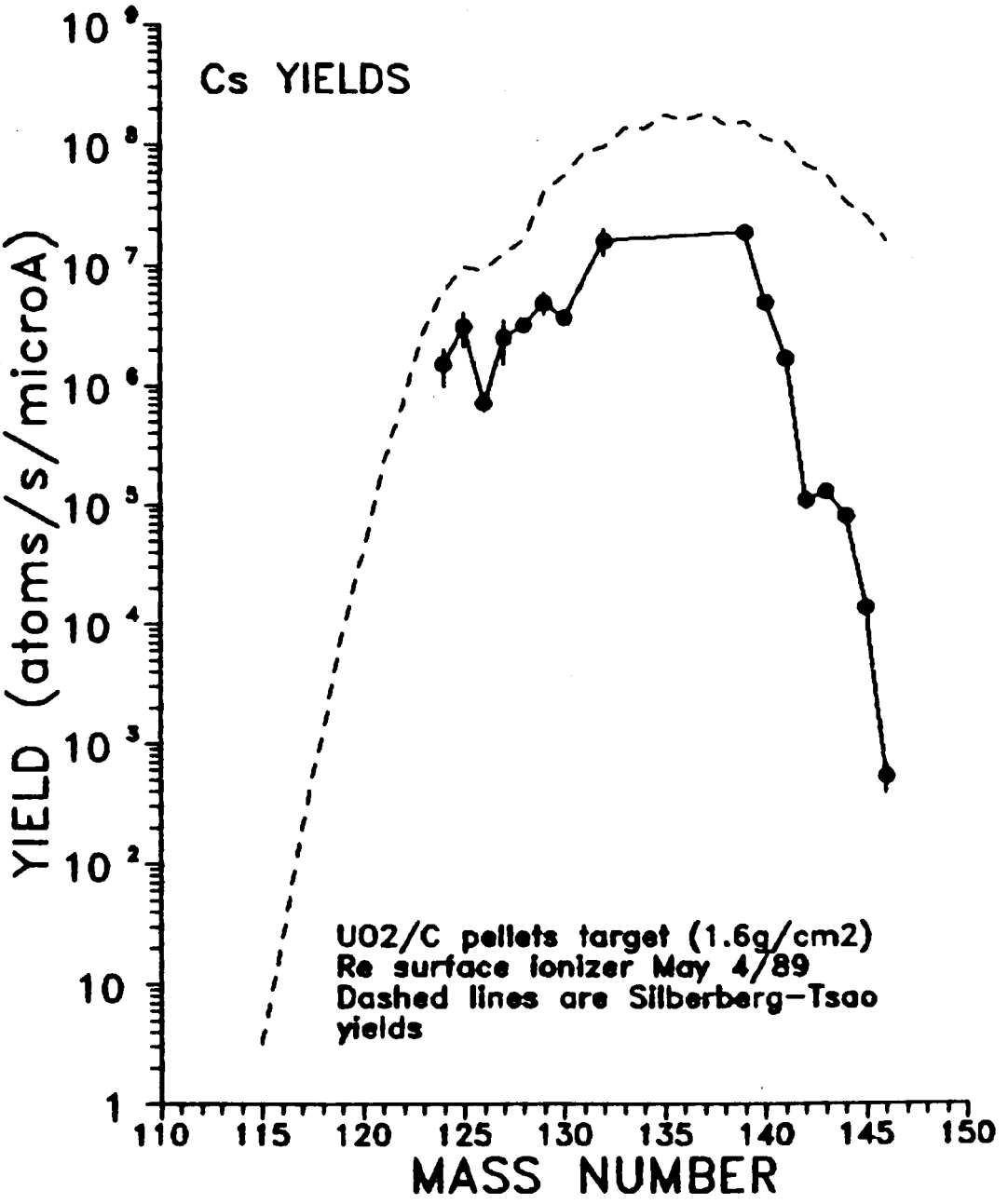

Figure 52: Yields of Cs from a UO_2/C target.

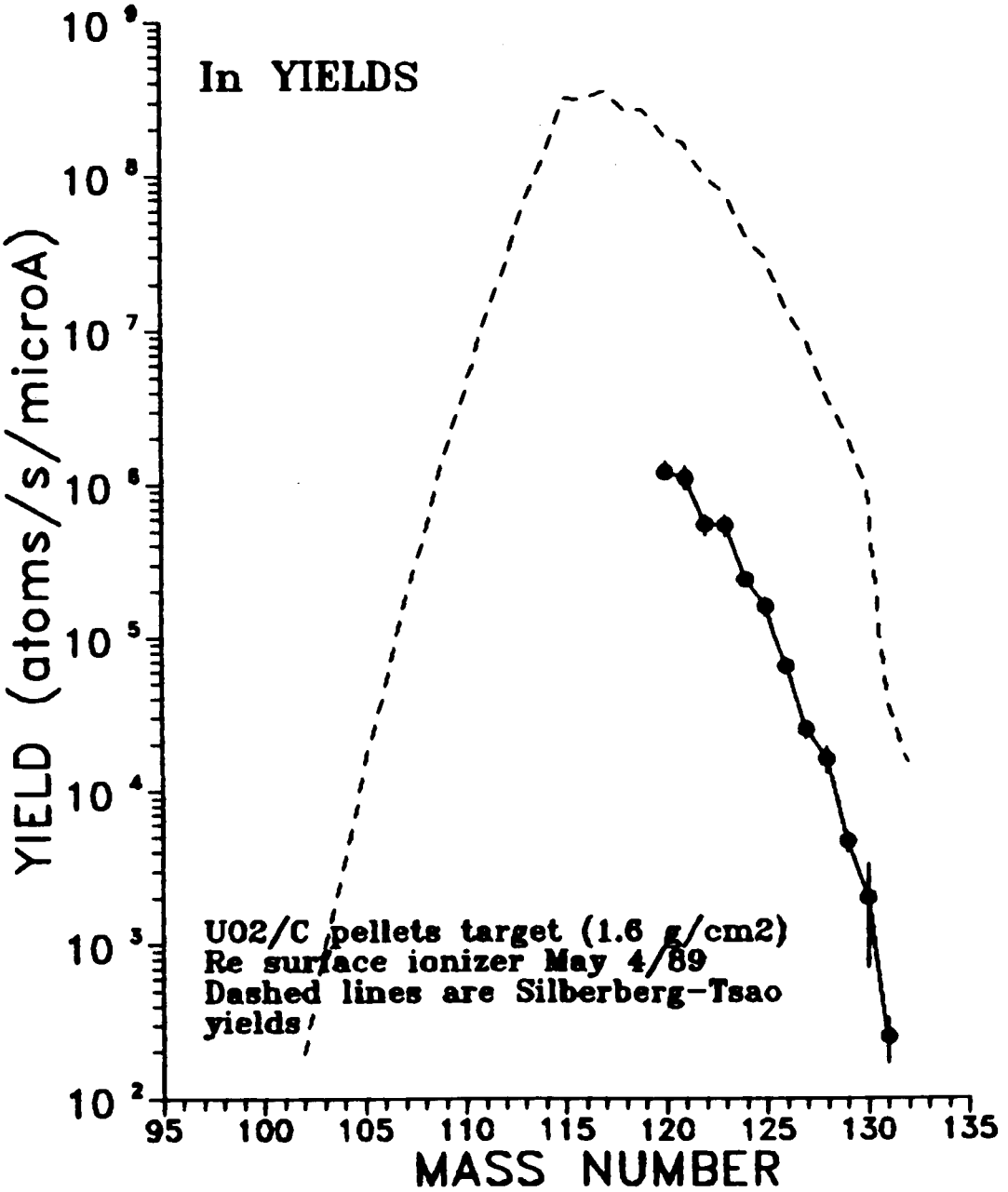

Figure 53: Yields of In from a UO_2/C target.

isotopes is approached, ^{146}Cs is just two masses short of the heaviest known cesium. For gallium , the experimental yields generally follow the distribution predicted by the SILT formulae, but show a shallower decrease at higher masses than predicted. Since this results in conversion efficiencies that increase with shorter half-life, no release time estimates could be obtained. However, the trend seen in the Rb, In and Cs production yields is again present, ^{81}Ga is just two masses short of the heaviest known gallium isotope.

The UO_2/C target has an estimated thickness of $4.5 \cdot 10^{21}$ target nuclei/cm^2. All the previous targets had thicknesses of ~ 10^{22} target nuclei/cm^2. Yet, the Cs yields from this target are three orders of magnitude greater than those from the Hf foils target, even though the number of target atoms is one tenth that of the hafnium target. Clearly, the UO_2/C target is much superior for the release of cesium. The sodium and rubidium yields are also greater than those from the Hf target, but by smaller amounts. For these three alkali elements, it appears that the UO_2/C mixture makes a much better target than Hf foil.

The results of the least squares fits are presented in Table 13 and Figures 54 - 59. A suitable fit could not be obtained for the sodium data, even excluding the high ^{21}Na point; only rough estimates are given. No fits could be obtained for either the aluminum or gallium yield data.

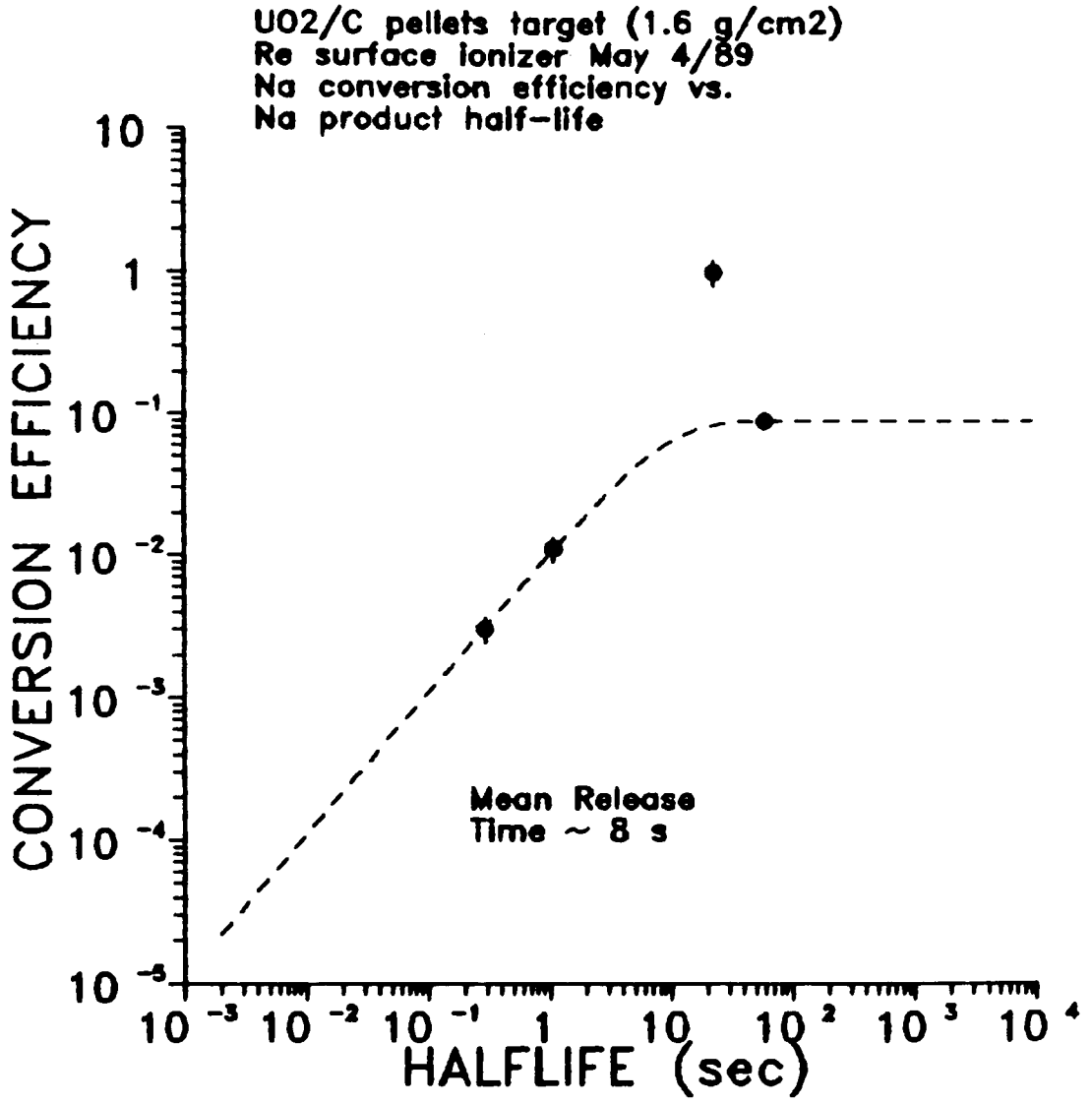

Figure 54: Conversion efficiencies for Na from a UO_2/C target.

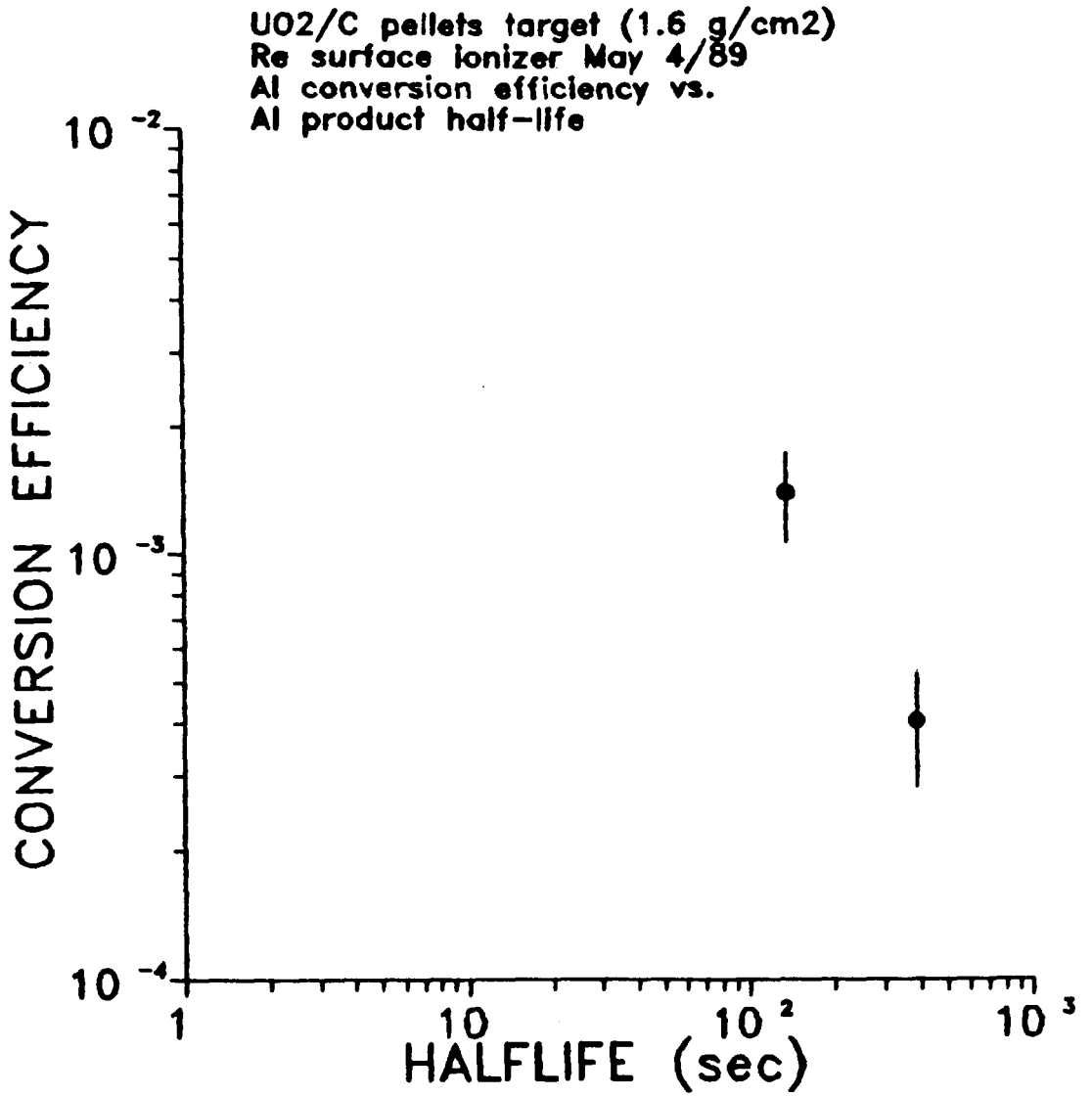

Figure 55: Conversion efficiencies for Al from a UO_2/C target.

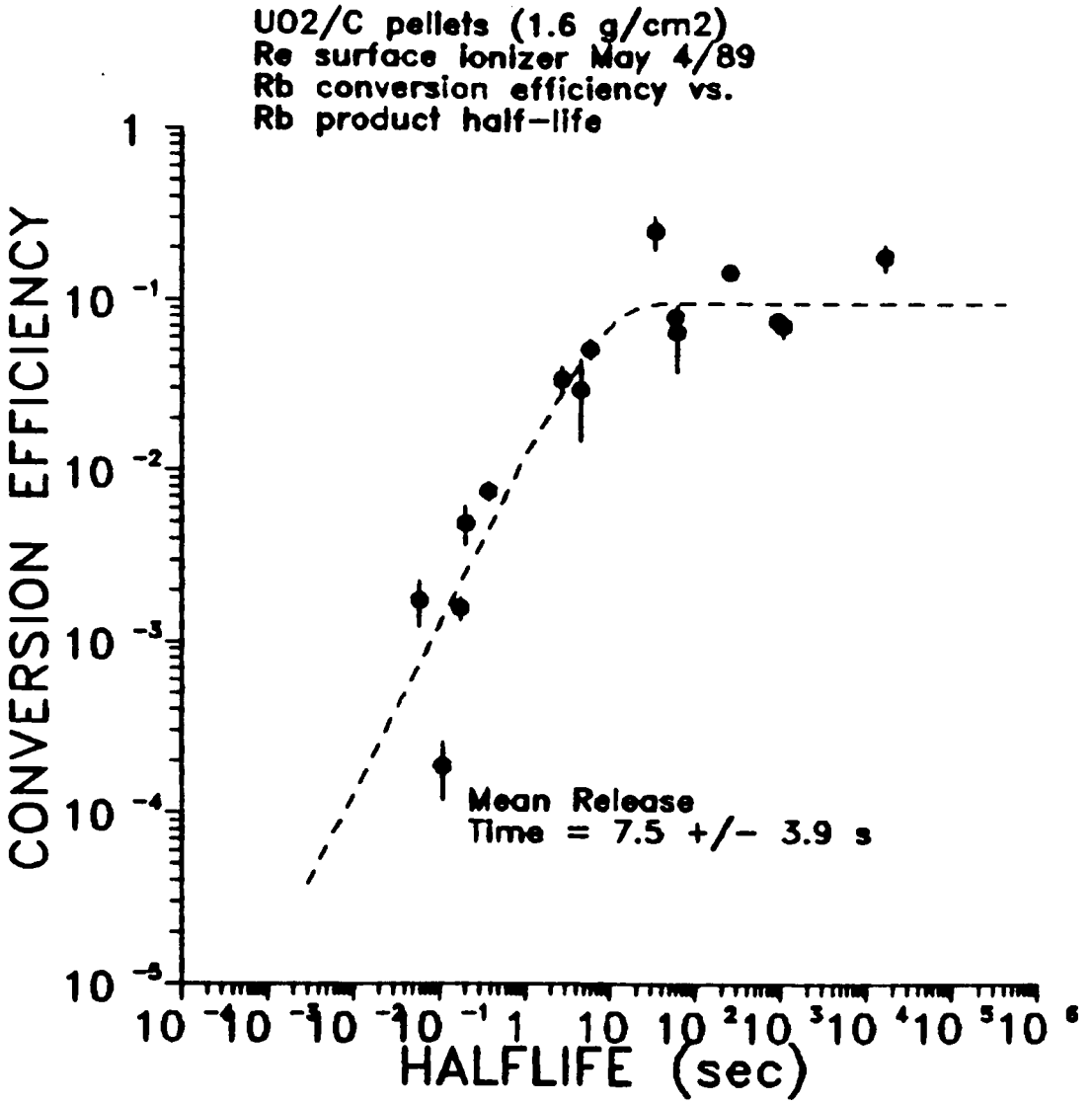

Figure 56: Conversion efficiencies for Rb from a UO_2/C target.

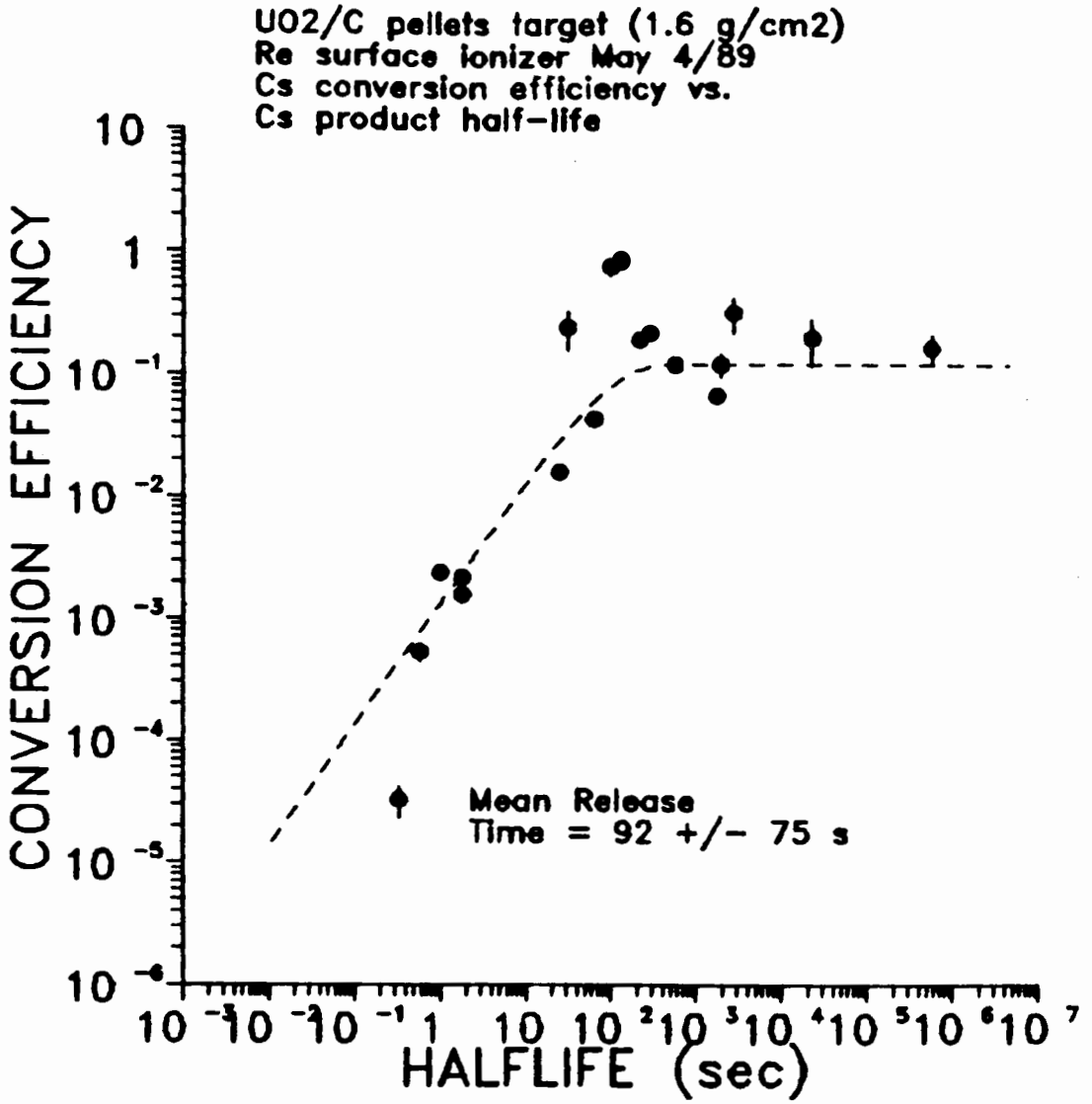

Figure 57: Conversion efficiencies for Cs from a UO_2/C target.

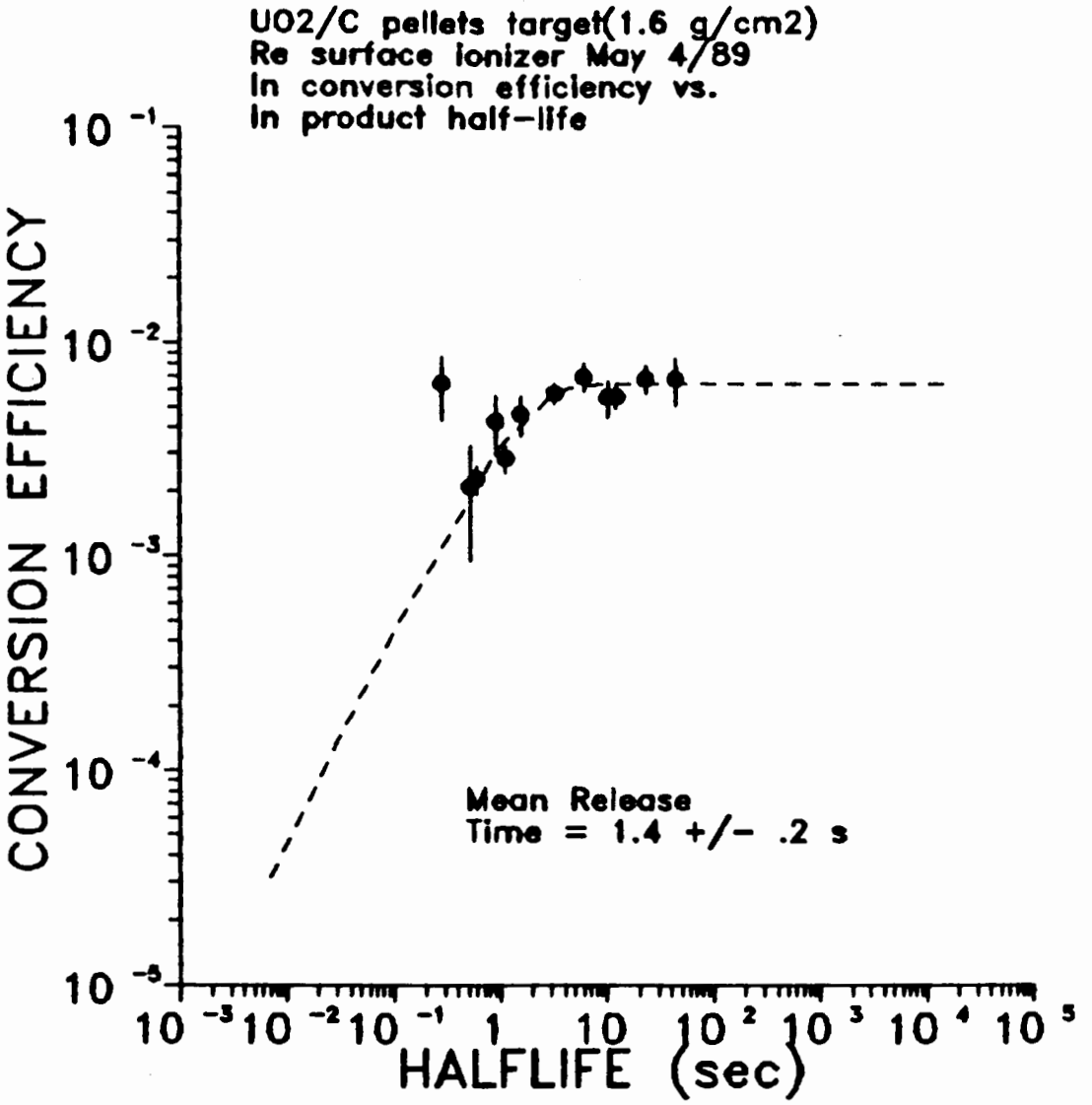

Figure 58: Conversion efficiencies for In from a UO_2/C target.

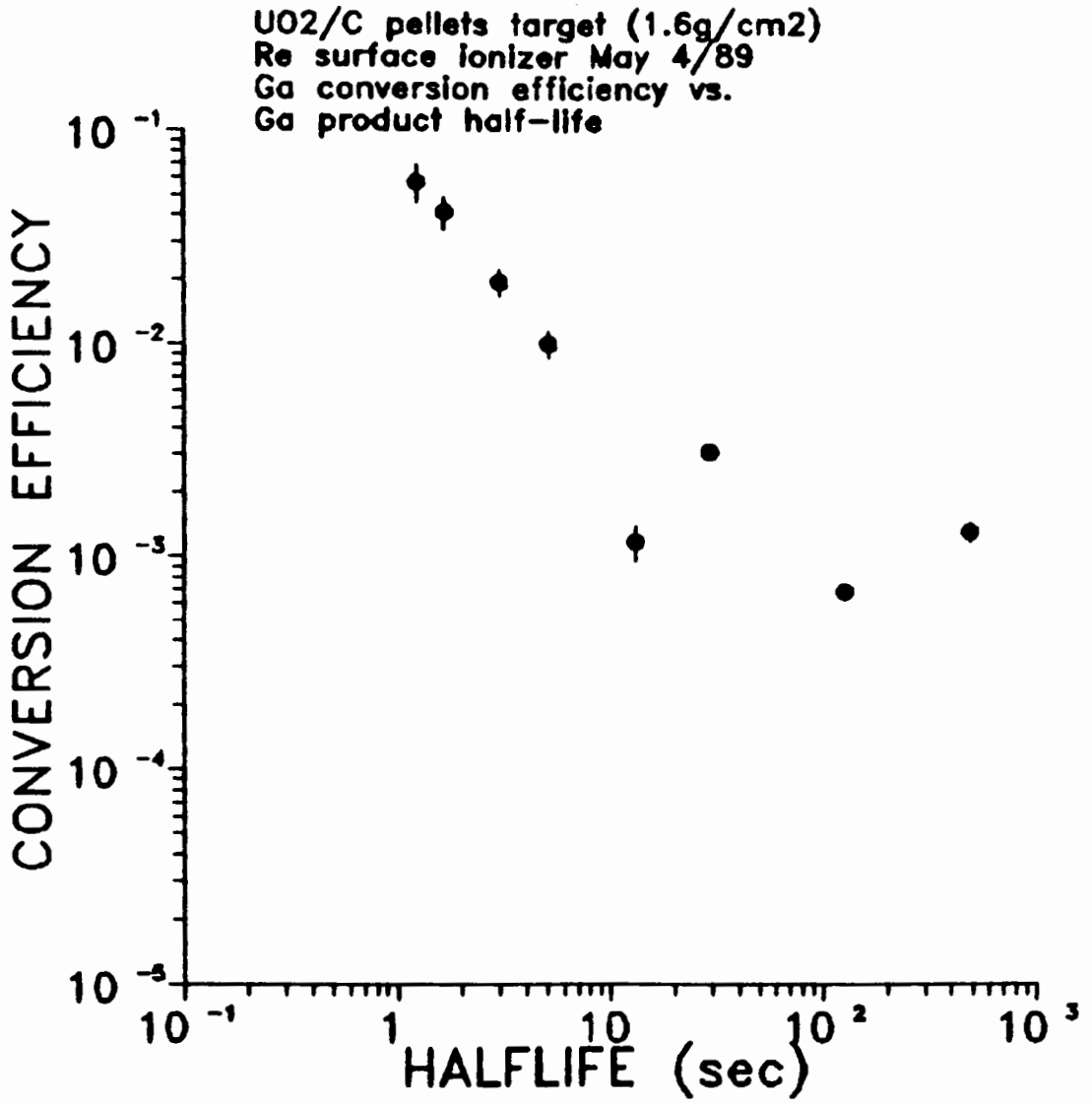

Figure 59: Conversion efficiencies for Ga from a UO_2/C target.

However, the calculated curves for the rubidium, indium and cesium yields seem to fit the data rather well.

Table 13

Maximum Efficiencies & Mean Release Times

for Elements from the UO_2/C Pellets Target

Element	τ_{mean} (sec)	Eff_{max} (%)	Saha-Langmuir[a] (%)
Na	~ 8	~ 9	30
Al	?	?	0.5
Ga	?	?	0.4
Rb	7.5 ± 3.9	9.6 ± 1.3	96
Cs	92 ± 75	12 ± 3.9	99
In	1.4 ± 0.2	0.6 ± 0.04	1.4

a: Ionization efficiency predicted by Saha-Langmuir formula at 1900 °C

The Zirconium Carbide Target Run:

On April 17, 1989, a target of pressed pellets of ZrC was investigated in order to compare its production yields with those of the Zr foil target. Powdered ZrC (5 micron, from CERAC) was mixed with a minimum of albumen and lightly pressed into 13 mm diameter pellets. After drying under a heat lamp, the pellets were placed in a target crucible

inside the target/ion source and slowly heated *in situ*. The total target thickness was 14.9 g Zr/cm^2. As with the Zr foil target, yields of Na, K, Rb and Sr were measured; ^{8}Li, ^{9}Li, ^{28}Al and ^{29}Al were also observed.

Though the ZrC target was only twice as thick (in Zr) as the Zr foils target, the yields of the sodium isotopes are about one order of magnitude greater. However, the potassium yields are roughly the same for the two targets. The yields of the longer lived rubidium isotopes are also about one order of magnitude higher than those from the Zr foils target, but the yields of the short lived species are comparable from both targets. This suggests a somewhat shorter rubidium release time from the ZrC powder, but not significantly short enough to make much difference for the release properties of isotopes with halflives shorter than a few minutes. Presumably, the release time is also shorter for sodium from a ZrC target, since the yields of Na isotopes with half-lives less than one minute are enhanced. The release time for potassiums must be roughly the same for the two targets since their yields are similar. The strontium yields are of the same order as those from both the Zr and Nb foil targets, again suggesting similar release properties. The yield distributions are displayed in Figures 60 - 63 and listed in Table 14.

Table 14

Results of ZrC Pellets Run

Nuclide	Yield (nuclei/sec/μA)	Nuclide	Yield (nuclei/sec/μA)
Li-8	$2.6 \cdot 10^6 \pm 28\%$	Rb-75	$1.3 \cdot 10^3 \pm 15\%$
Li-9	$1.7 \cdot 10^5 \pm 28\%$	Rb-76	$8.7 \cdot 10^4 \pm 8\%$
		Rb-77	$1.3 \cdot 10^6 \pm 6\%$
Na-20	$3.2 \cdot 10^3 \pm 15\%$	Rb-78g	$7.0 \cdot 10^6 \pm 20\%$
Na-21	$5.5 \cdot 10^4 \pm 20\%$	Rb-78m	$9.8 \cdot 10^6 \pm 7\%$
Na-25	$2.3 \cdot 10^5 \pm 10\%$	Rb-79	$7.7 \cdot 10^7 \pm 44\%$
Na-26	$1.2 \cdot 10^4 \pm 22\%$	Rb-80	$8.9 \cdot 10^6 \pm 8\%$
Na-27	$9.8 \cdot 10^2 \pm 22\%$	Rb-81g	$1.1 \cdot 10^9 \pm 8\%$
		Rb-81m	$1.2 \cdot 10^8 \pm 16\%$
Al-28	$1.1 \cdot 10^3 \pm 26\%$	Rb-82g	$1.4 \cdot 10^7 \pm 29\%$
Na-26	$1.3 \cdot 10^3 \pm 32\%$	Rb-82m	$4.5 \cdot 10^8 \pm 7\%$
		Rb-83	$1.0 \cdot 10^9 \pm 17\%$
K-37	$4.7 \cdot 10^4 \pm 30\%$	Rb-84g	$3.7 \cdot 10^8 \pm 40\%$
K-38g	$4.3 \cdot 10^6 \pm 26\%$	Rb-84m	$6.8 \cdot 10^7 \pm 11\%$
K-44	$4.1 \cdot 10^4 \pm 16\%$	Rb-86m	$6.3 \cdot 10^6 \pm 23\%$
K-45	$1.8 \cdot 10^4 \pm 12\%$	Rb-88	$2.2 \cdot 10^6 \pm 5\%$
K-46	$2.4 \cdot 10^3 \pm 23\%$	Rb-89	$1.1 \cdot 10^6 \pm 8\%$
		Rb-90g	$3.0 \cdot 10^4 \pm 52\%$
Sr-77	$9.0 \cdot 10^3 \pm 18\%$	Rb-90m	$1.4 \cdot 10^5 \pm 22\%$
Sr-80	$1.3 \cdot 10^7 \pm 70\%$	Rb-91	$1.1\ 10^4 \pm 26\%$
Sr-81	$1.7 \cdot 10^7 \pm 12\%$		
Sr-83g	$2.5 \cdot 10^7 \pm 16\%$		
Sr-87m	$5.2 \cdot 10^5 \pm 21\%$		
Sr-91	$1.2 \cdot 10^5 \pm 22\%$	Sr-92	$3.9 \cdot 10^4 \pm 23\%$

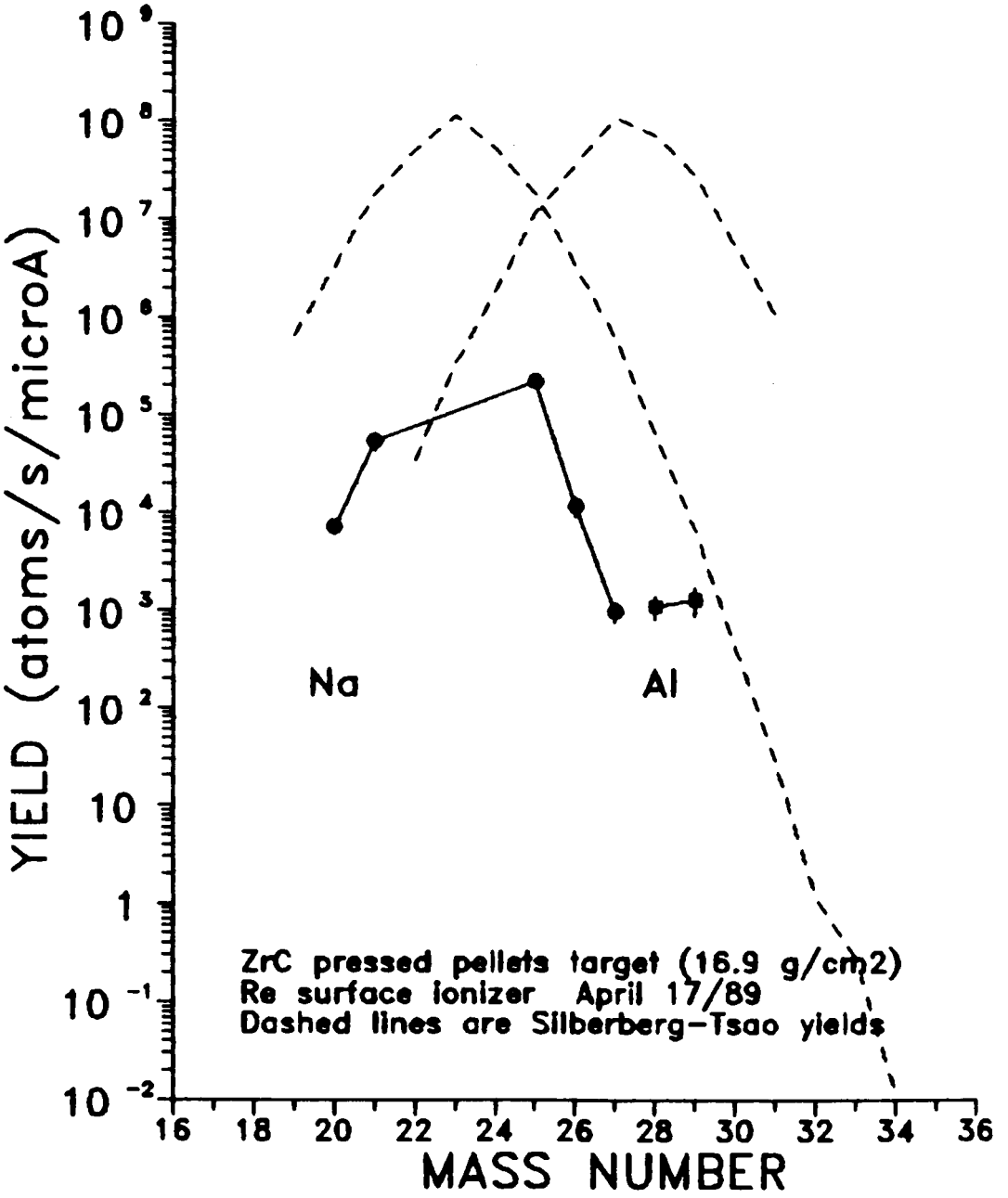

Figure 60: Yields of Na & Al from a ZrC target.

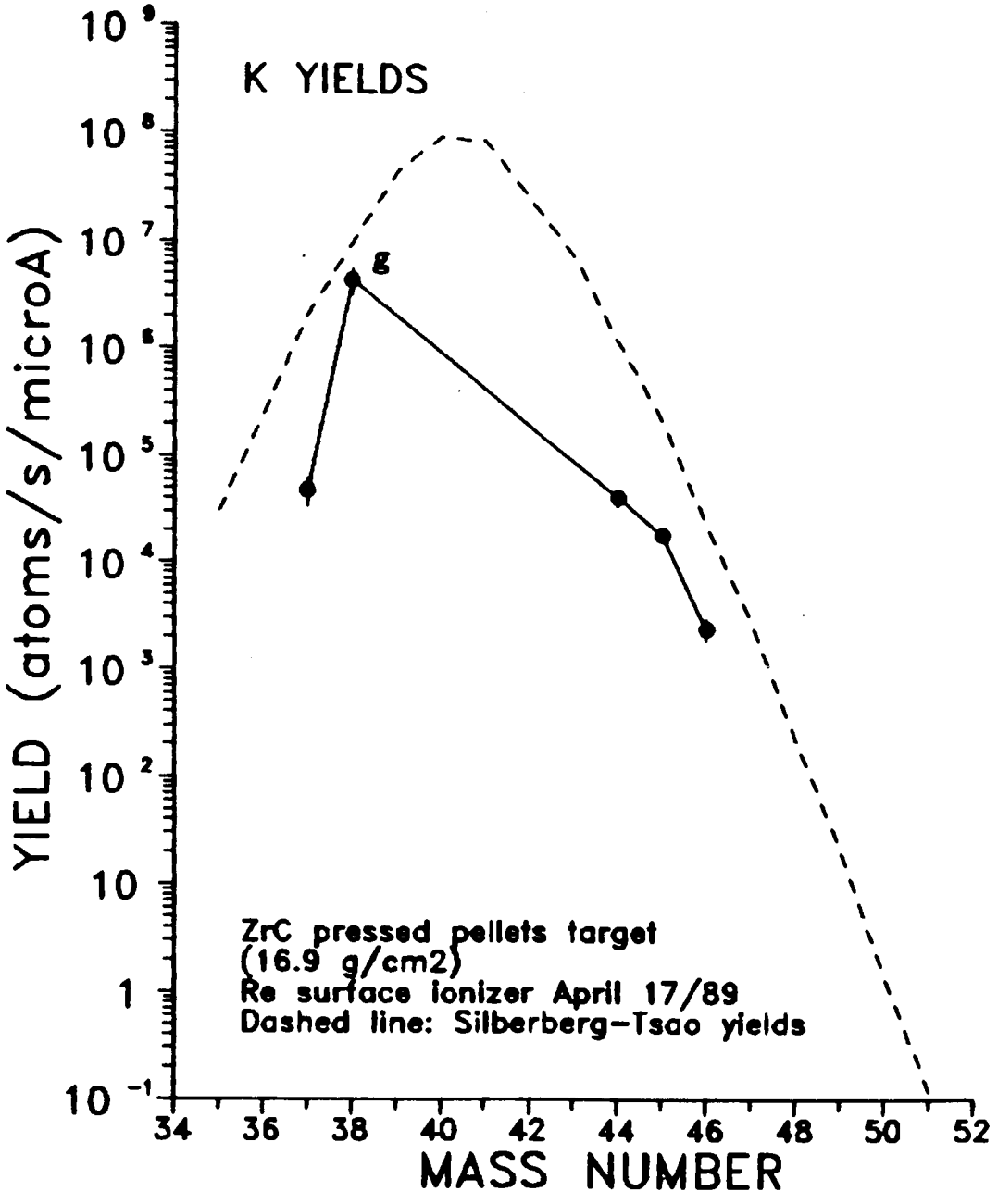

Figure 61: Yields of K from a ZrC target.

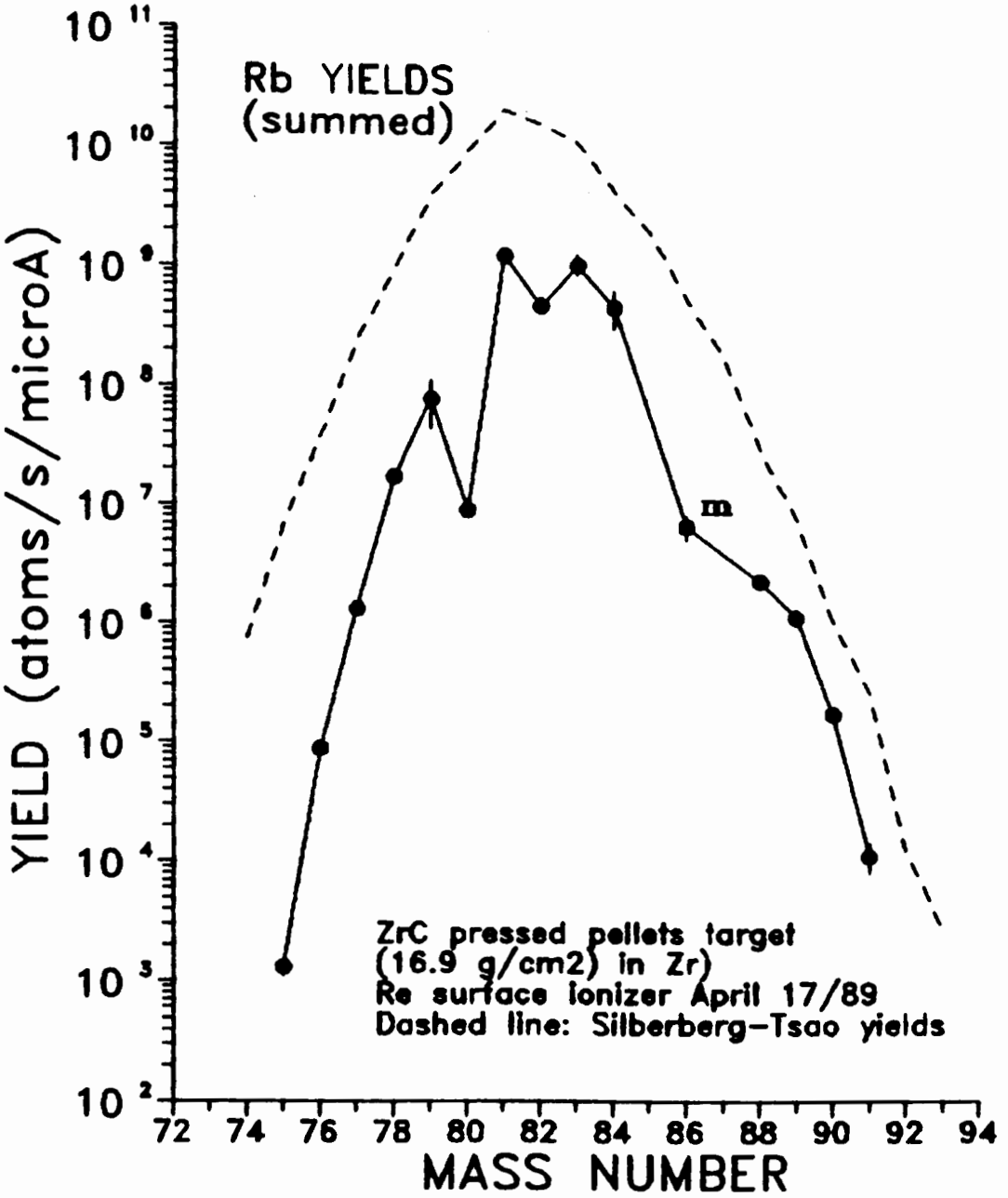

Figure 62: Yields of Rb from a ZrC target.

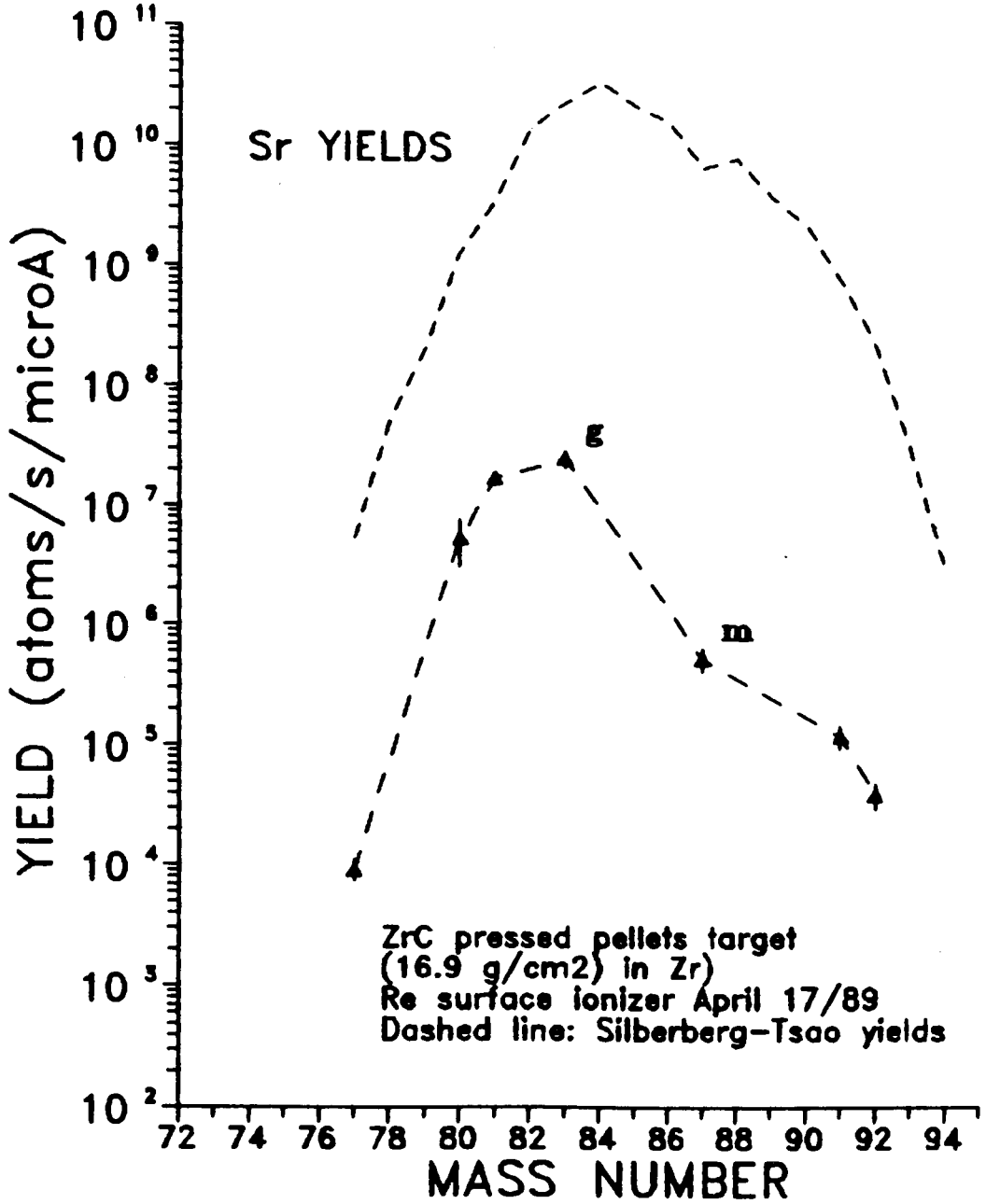

Figure 63: Yields of Sr from a ZrC target.

The results of the least-squares fits for maximum efficiency and mean release time are listed in Table 15 and displayed in Figures 64 - 67.

Table 15

Maximum Efficiencies & Mean Release Times

for Elements from a ZrC Pellets Targets

Element	τ_{mean} (sec)	Eff_{max} (%)	Saha-Langmuir[a] (%)
Na	1.7 ± 2.3	0.6 ± 0.5	30
Al	~ 90	~ 0.002	0.5
K	2.5 ± 6.3	6.0 ± 3.0	97
Rb	1000 ± 900	7.4 ± 3.5	99
Sr	~ 23	~ 0.5	8

a: Ionization efficiency predicted by Saha-Langmuir formula at 1500 °C

The rubidium and sodium fits are reasonable, though the uncertainties are high. The release time for sodium is slightly faster than the estimate for the Zr foils target. For rubidium, it is impossible to make a meaningful comparison with the Zr foils target. For potassium, the release times and efficiencies for both targets are comparable. As with all previous cases, the aluminum estimates are base on only two points and cannot be

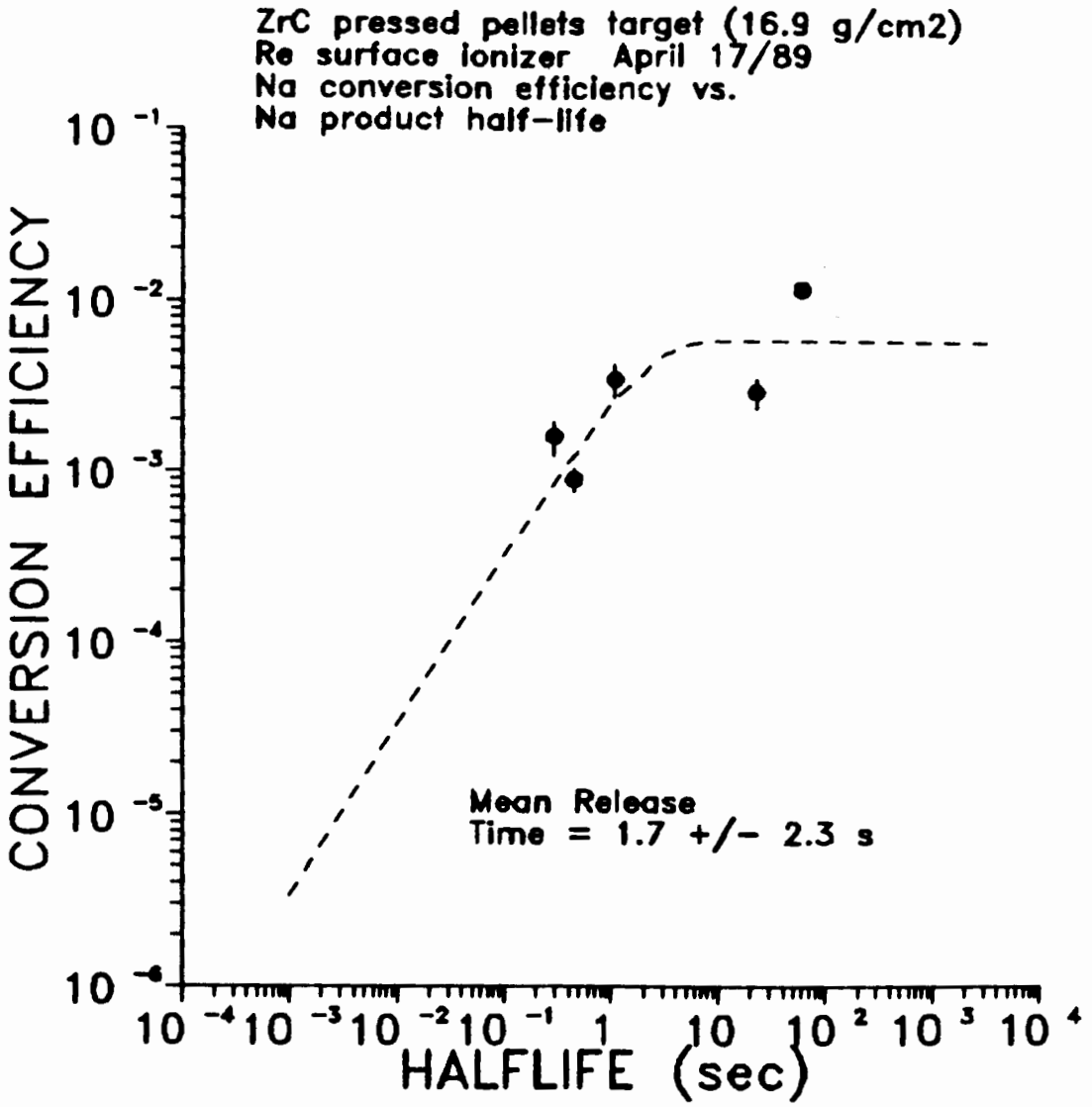

Figure 64: Conversion efficiencies for Na from a ZrC target.

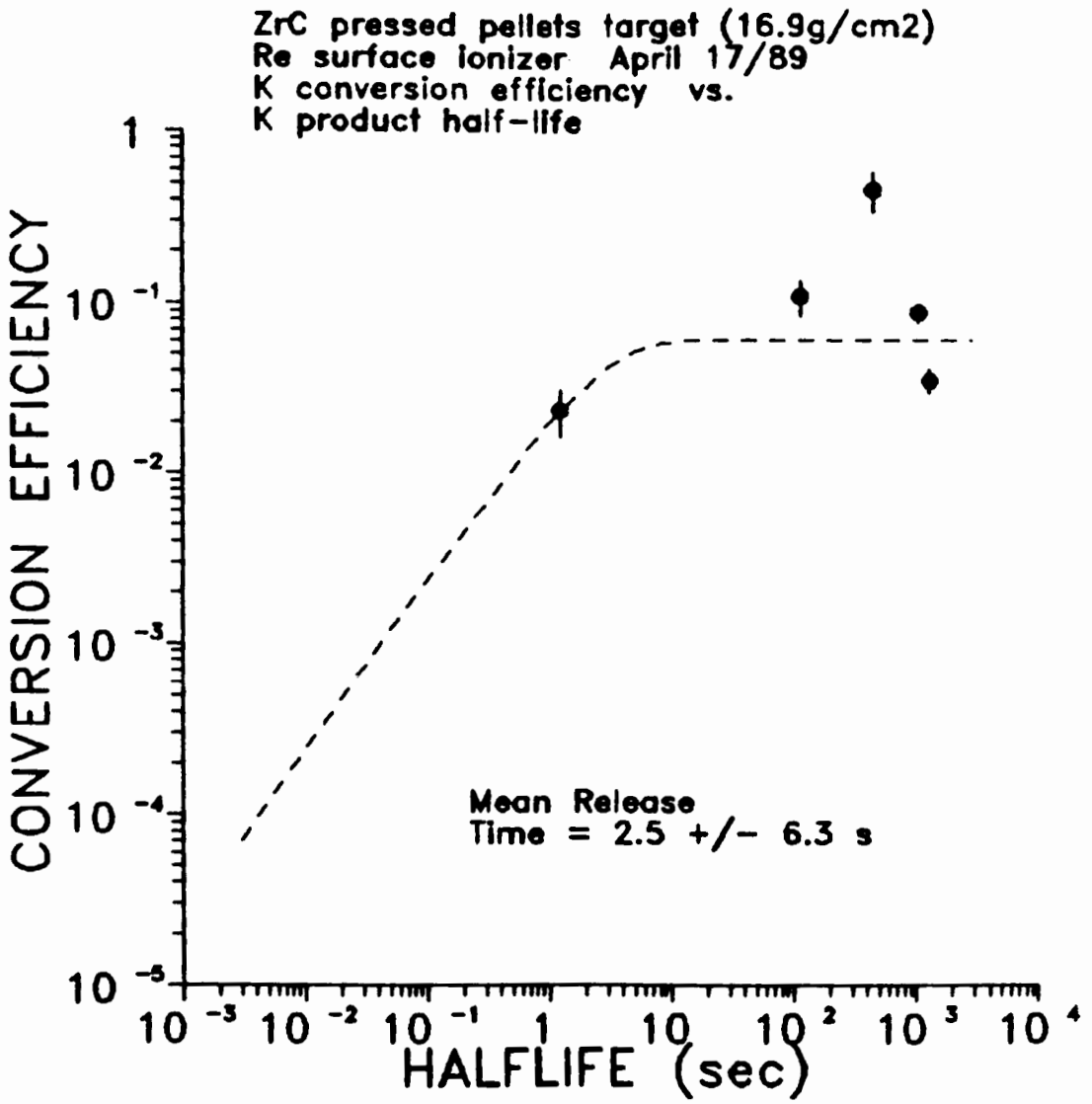

Figure 65: Conversion efficiencies for K from a ZrC target.

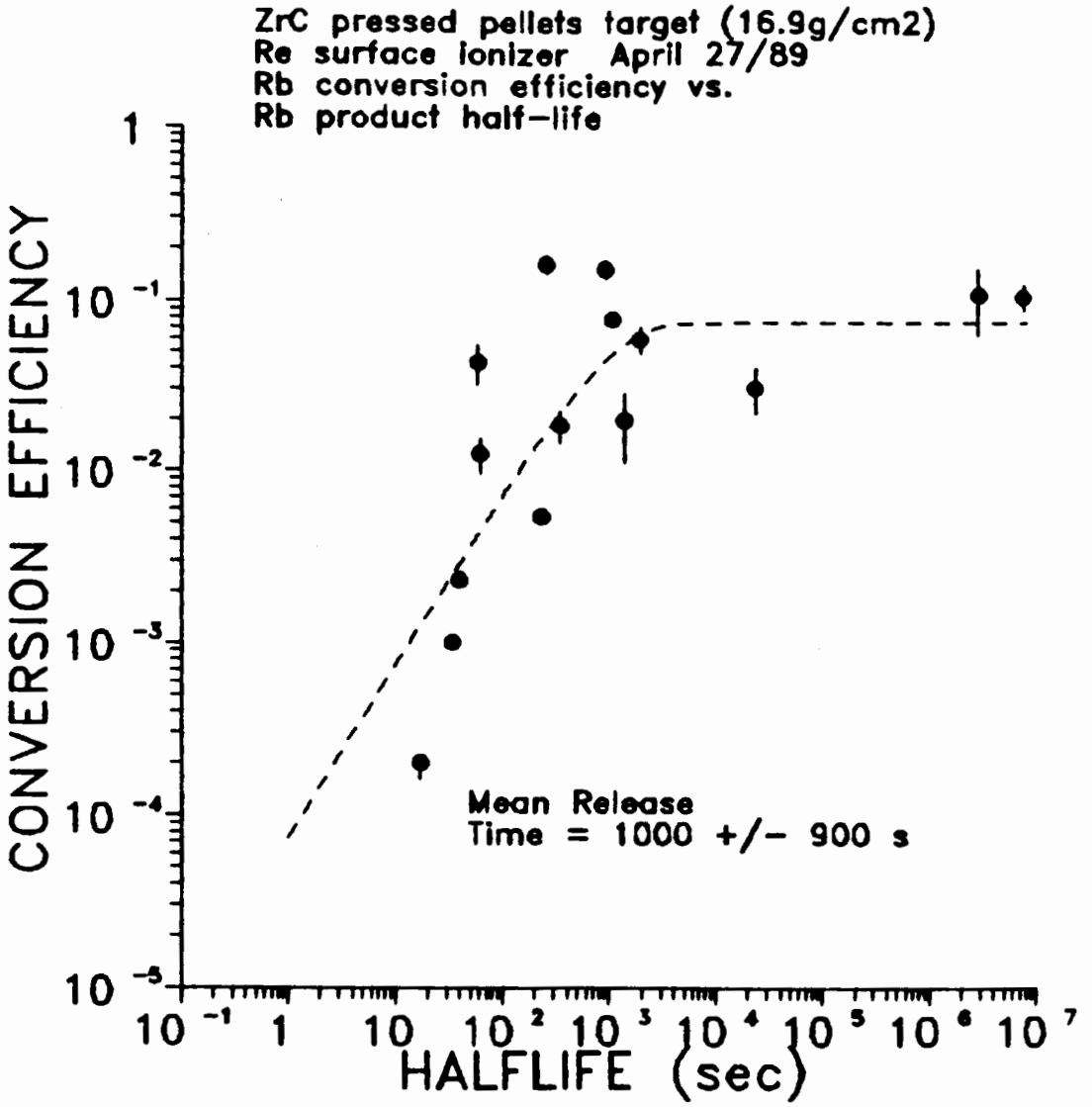

Figure 66: Conversion efficiencies for Rb from a ZrC target.

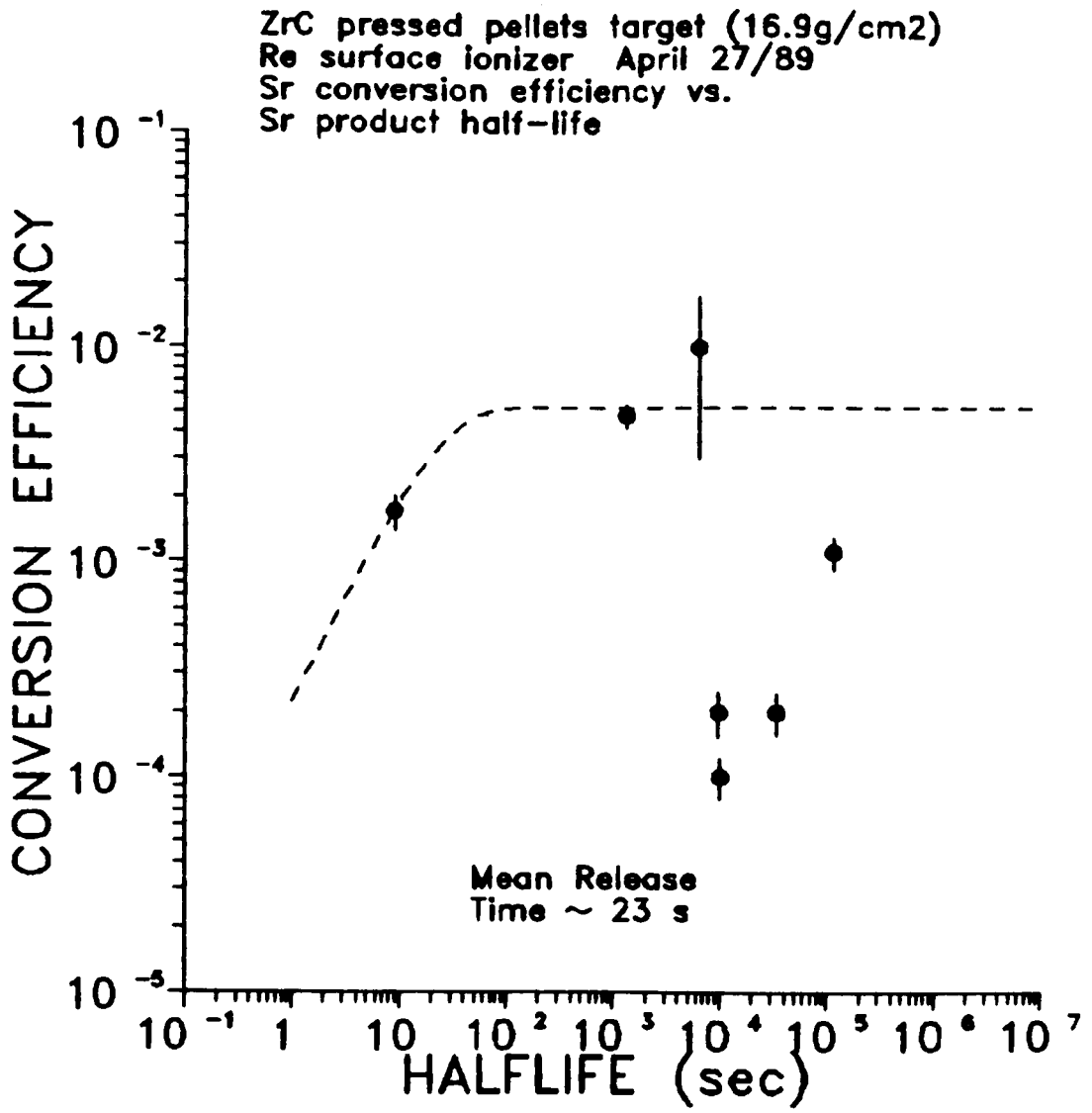

Figure 67: Conversion efficiencies for Sr from a ZrC target.

considered accurate. For the strontium fit, the points from the heavier isotopes had to be excluded in order to obtain a fit. Even then, only a rough estimate could be obtained. Altogether, the results indicate that ZrC is a better target than Zr foil for Na, Rb and Sr products; for K, the targets are comparable.

The Silicon Carbide Target Run:

The last target to be investigated using the surface ionization source was made of pressed pellets of SiC. Eighteen pellets of powdered SiC were lightly pressed with a minimum of albumen, as before. The dried pellets were placed in the target/ion source and conditioned *in situ*. 8.05 g of SiC were used for a total target thickness of 6.06 g Si/cm^2. The primary purpose of investigating this target was to measure the yields of Li, Na and Al from a lighter mass target than before. Previously, the observed light elements were the spallation and evaporation products of heavier target nuclei and the cross-sections for their production were not favourable. With a target just higher in mass than the desired products, the spallation cross-sections should be significantly enhanced.

The measured yields are given in Table 16 and Figure 68. With the exception of the mass 24 yield, the sodium and aluminum yields follow the mass distribution predicted by

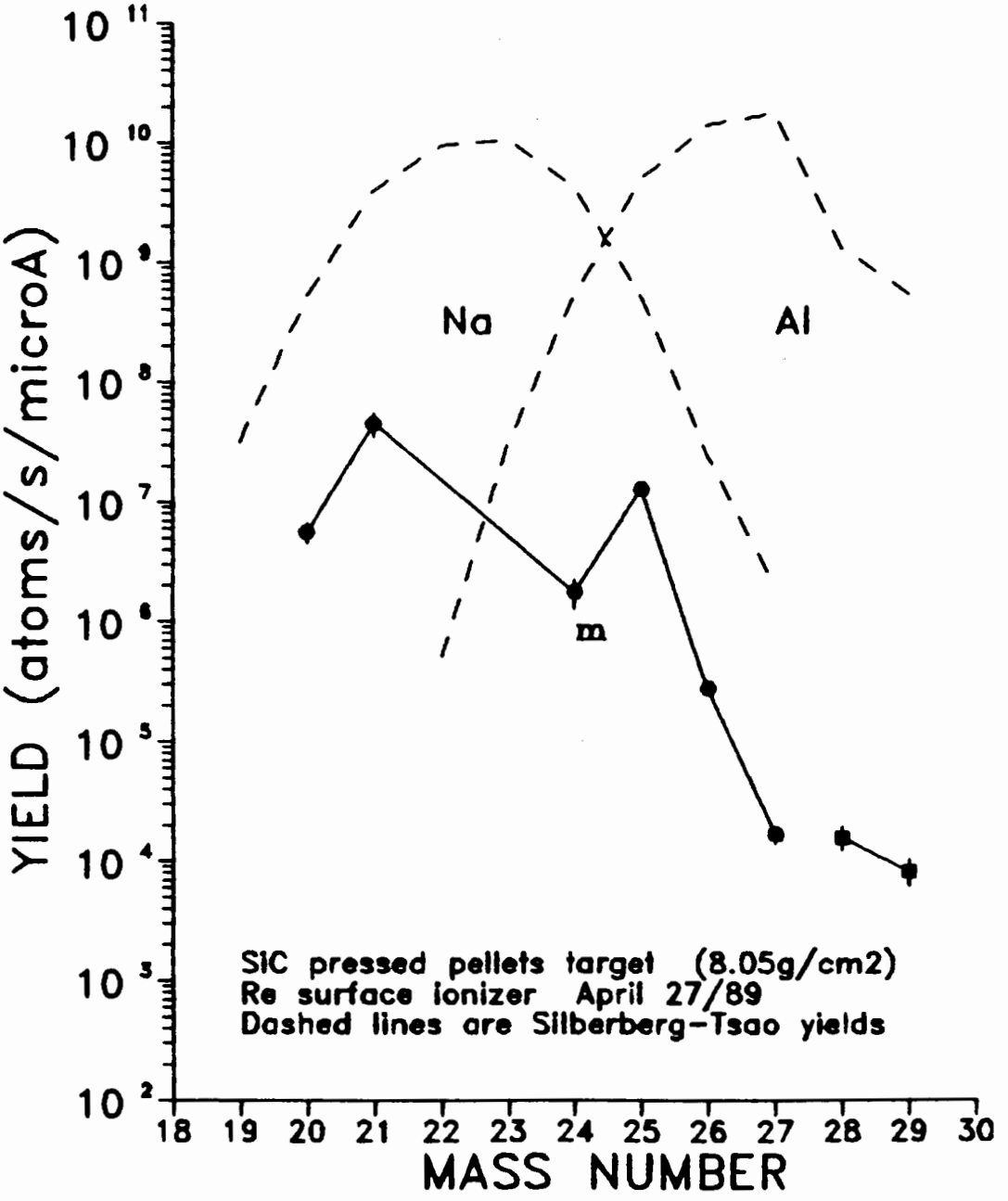

Figure 68: Yields of Na & Al from a SiC target.

the Silberberg-Tsao formulae. The low value for mass 24 is understandable, since only the yield of ^{24m}Na was determined. If the ^{24g}Na yield had been included, the mass

Table 16

Results of SiC Pellets Run

Nuclide	Yield (nuclei/sec/μA)	Nuclide	Yield (nuclei/sec/μA)
Li-8	$5.6 \cdot 10^6$ ± 19%	Na-20	$1.2 \cdot 10^6$ ± 14%
Li-8	$1.2 \cdot 10^5$ ± 27%	Na-21	$4.5 \cdot 10^7$ ± 22%
		Na-24m	$1.8 \cdot 10^6$ ± 27%
Al-28	$1.6 \cdot 10^4$ ± 22%	Na-25	$1.3 \cdot 10^7$ ± 10%
Al-29	$8.3 \cdot 10^3$ ± 24%	Na-26	$2.8 \cdot 10^5$ ± 10%
		Na-27	$1.7 \cdot 10^4$ ± 16%

yield would be greatly increased. Also, the ^{24m}Na yield can be expected to be diminished due to the very short half-life of this isomer. The measurement of this yield is significant. The half-life of the metastable isomer is only 20.2 milliseconds, this makes it the shortest lived species to have been successfully separated at TISOL.

As expected, the yields of both sodium and aluminum are much higher than those measured with the previous targets. Some of this is due to the fact that (in terms of nuclei/cm^2) this target is an order of magnitude thicker

than those previously used. However, the yields are about two orders of magnitude greater than before, and the difference must be attributed to the much higher production cross sections. The yields of the two lithium isotopes are about the same as with the previous targets, where lithium production was attributed to evaporation reaction mechanisms. For SiC, the production is attributed to a mixture of evaporation and spallation reactions. In all previous runs, no effort was made to establish the release times or efficiencies for the lithium since the source of the lithiums is not known. As well as being produced from the target nuclei, the lithium isotopes can be produced from virtually every material in the target/ion source. Under these conditions, it is impossible to estimate any release properties.

The least-squares fit results are given in Table 17 and Figures 69 and 70. The estimated release time for sodium is of the same order as with the Ti, ZrC and Hf targets. The maximum efficiency is the second highest, exceeded only by that of the UO_2/C target. For aluminum, the estimated release time is about the same as for the Ti and ZrC targets; the efficiency is similar to that from the ZrC target.

Table 17

Maximum Efficiencies & Mean Release Times

for Elements from the SiC Pellets Target

Element	τ_{mean} (sec)	Eff_{max} (%)	Saha-Langmuir[a] (%)
Na	1.6 ± 1.1	2.0 ± 0.5	30
Al	~ 300	~ $4.3 \cdot 10^{-3}$	0.5

a: Ionization efficiency predicted by Saha-Langmuir formula at 1900 °C

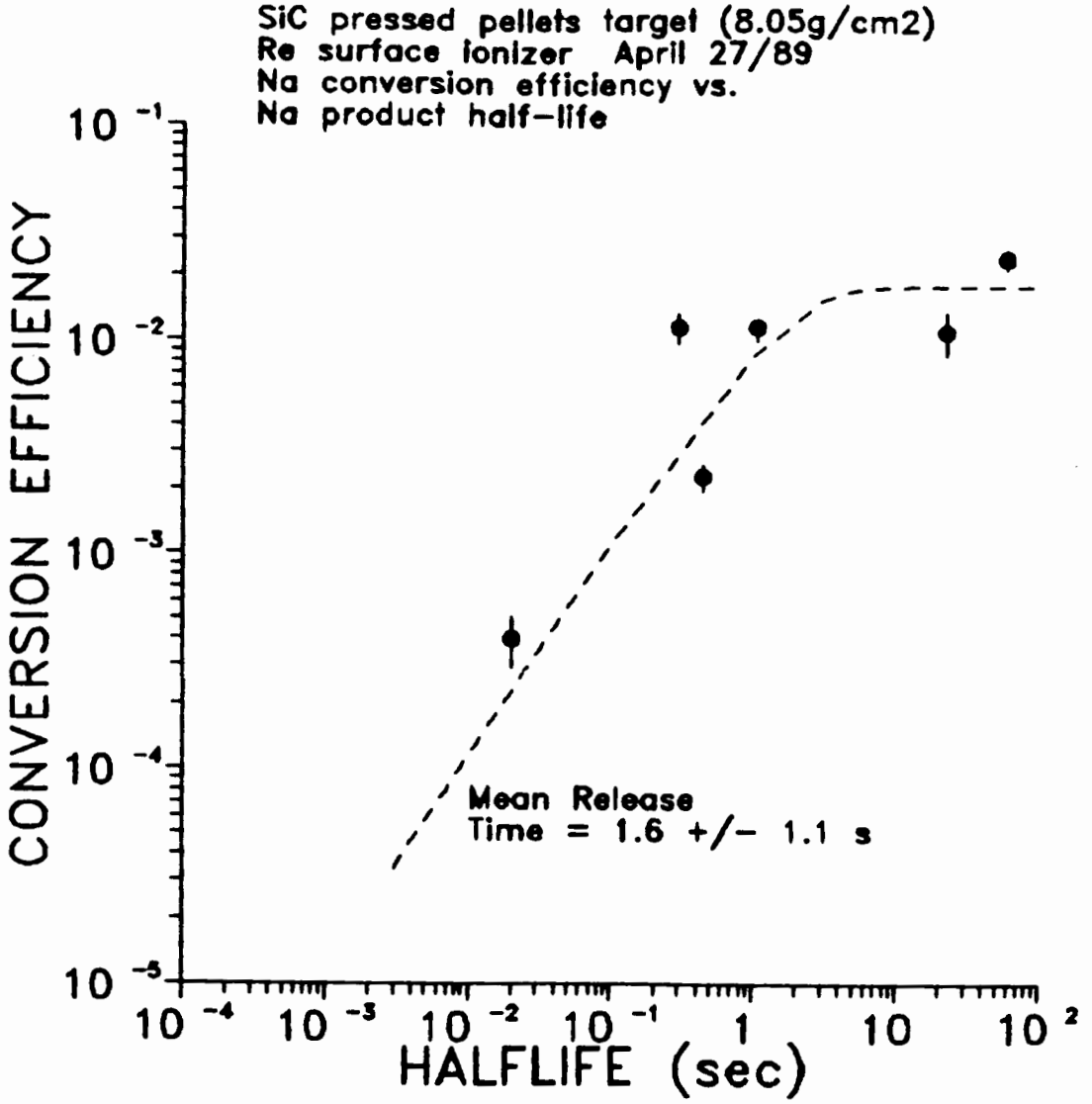

Figure 69: Conversion efficiencies for Na from a SiC target.

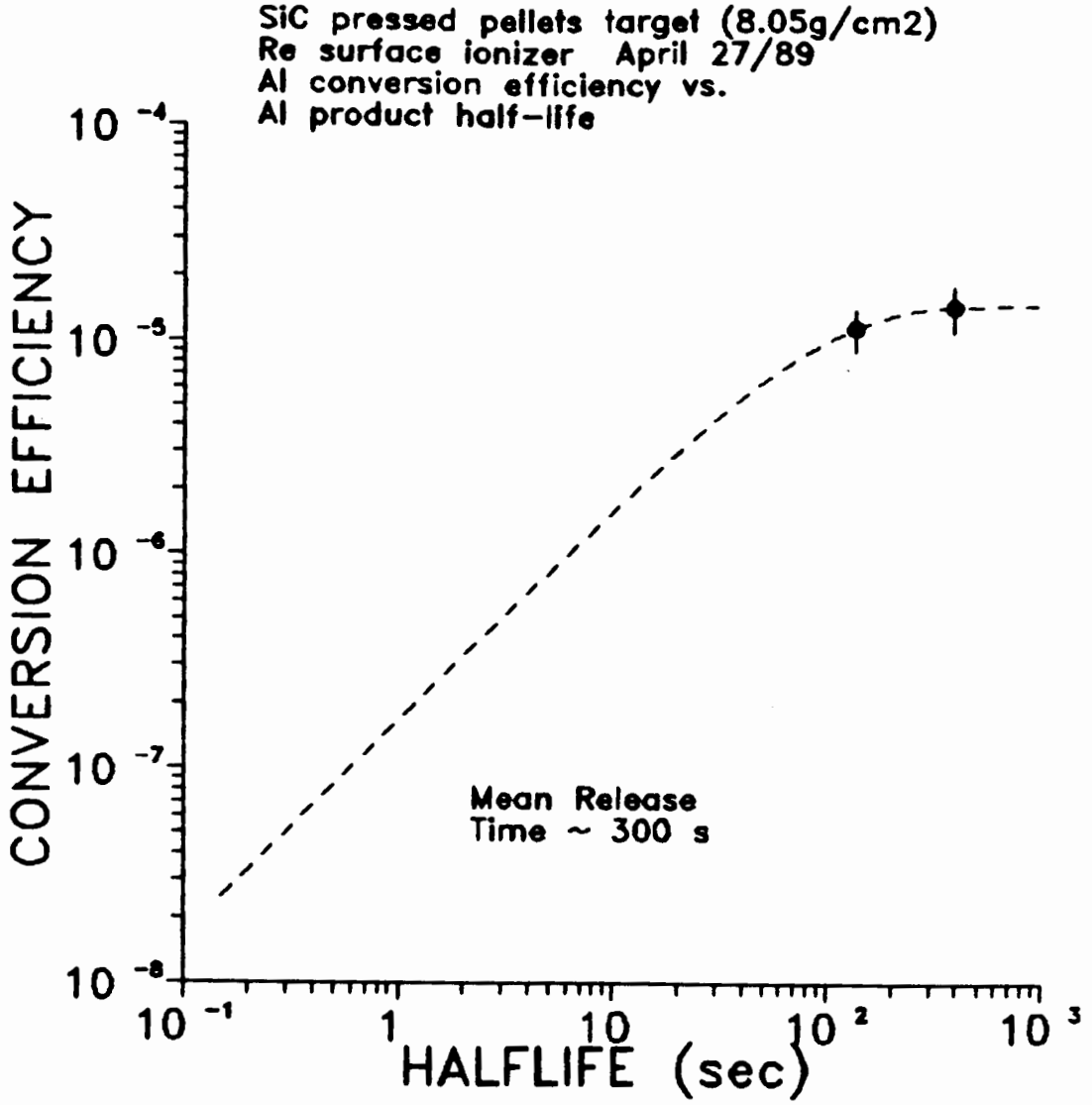

Figure 70: Conversion efficiencies for Al from a SiC target.

SUMMARY

The TISOL system has been shown to be capable of producing good yields of separated radioactive beams. With a slit exit geometry on the ion source, the measured performance of the separator has not matched that predicted by initial calculations. However, with a circular exit orifice, the performance is better than initially expected.

Seven target materials have been investigated and yields of over 120 nuclides have been measured. Estimates of mean release times for eight elements from the targets investigated have been made by comparison with theoretical production yields. A summary of these release estimates is given in Table 18.

Where comparisons can be made with targets previously investigated at ISOLDE (CERN), the ISOLDE release time estimates are listed. Unlike the TISOL estimates, the ISOLDE release time values were obtained by measuring the decrease in activity with time. This direct method is undoubtedly more accurate than the estimation method based on the Silberberg-Tsao predictions. Still, the agreement between the two methods is surprisingly good. The only case where there is significant disagreement is for the SiC target. There are two other estimates of sodium release time from targets of uranium and silicon deposited on carbon slabs. The Orsay collaboration at CERN (To81) have measured

Table 18

Summary of Release Time Estimates

Nuclide	t_{mean} (sec)	Eff^{max} (%)	Target	ISOLDE t^{mean}* (sec)
Na	1.6 ± 1.1	2.0 ± 0.5	SiC (p)	~ 2740 (Ho84)
	1.7 ± 2.3	0.6 ± 0.08	ZrC (p)	
	1.9 ± 8.2	0.6 ± 0.5	Hf (f)	
	2.9 ± 1.8	0.3 ± 0.08	Ti (f)	
	~ 5	~ 0.5	Zr (f)	
	~ 8	~ 0.1	Nb (f)	
	~ 8	~ 9	UO_2/C (f)	~ 4 (Ca79)
Al	~ 90	~ .002	ZrC (p)	
	~ 300	~ .004	SiC (p)	
	~ 480	~ $1.3 \cdot 10^{-6}$	Ti (f)	
K	2.5 ± 6.3	6.0 ± 3.0	ZrC (p)	
	< 4	~ 10	Zr (f)	
	7.1 ± 7.8	4.3 ± 0.5	Nb (f)	
	7.5 ± 12	13 ± 5	Ti (f)	
	~ 1040	~ 0.4	Hf (f)	

(p) ≡ pellets, (f) ≡ foils
* ISOLDE data are for powder targets.

Table 18 (cont'd)

Rb	7.5 ± 3.9	9.6 ± 1.3	UO_2/C (f)	3-7 (Ca76)
	215 ± 85	2.4 ± 0.4	Zr (f)	
	507 ± 520	13 ± 4.4	Hf (f)	
	1000 ± 900	7.4 ± 3.5	ZrC (p)	~ 1200 (Ho84)
	1370 ± 950	3.8 ± 1.5	Nb (f)	~ 1700 (Ca78)
Sr	~ 23	~ 0.5	ZrC (p)	
	1325 ± 790	0.4 ± 0.01	Zr (f)	
In	1.4 ± 0.2	0.6 ± 0.04	UO_2/C (f)	
Cs	92 ± 75	12 ± 3.9	UO_2/C (f)	~ 475 (Ca76)
				~ 35 (Ho84)
	190 ± 75	0.4 ± 0.2	Hf (f)	
Yb	240 ± 135	0.002 ± 0.0004	Hf (f)	100-200 (Ca78)

(p) ≡ pellets, (f) ≡ foils
* ISOLDE data are for powder targets.

Na release times of 70 - 350 ms and ~ 90 ms from U/C and Si/C targets respectively; these times do not agree with either the ISOLDE or TISOL estimates.

For most elements, where comparisons can be made, the release times of the pelleted powder targets seem to be faster than those of the foil targets. However, with the large uncertainties, no valid conclusions can be made. The

release times for the alkalis seem to follow a general trend: Na < K < Rb; again, the large uncertainties preclude a valid conclusion.

The observation of nuclides with halflives below one second (as short as 20.2 ms for ^{24m}Na) shows that TISOL is a viable system for separating short lived species. That nuclei at the far edges of stability can be successfully produced and separated is further shown by the observation of the rubidium isotope chain from ^{75}Rb to ^{99}Rb. This is just one isotope short of the known limits on both the proton-rich and neutron-rich sides of stability. Similarly, the observed heavy cesiums and indiums approach the heaviest experimentally observed stable nuclides.

The surface ionization source used in the yield measurements, while adequate, is far from ideal. Many improvements can be envisaged based on its past performance and evident problems. It is conceivable that with an improved source, the heaviest known stable alkali elements may be reached.

FUTURE CONSIDERATIONS

Though the work described in this thesis stopped in the spring of 1989, the development of TISOL has not stopped. In 1989, the surface ionization source measurements were concluded and on-line development using an ECR source began. The TIS chamber was replace with a smaller chamber that

accepts targets horizontally. Two new magnetic quads, with larger central gap (4" ø) and shorter length, replaced the 3" ø gap magnets; this allowed the ECR source to be installed and increased the beam transmission to the dipole.

Perhaps the most significant results of the TISOL development program have come with the instalation of the ECR source. The TISOL ECR is the first on-line ECR source coupled to an ISOL. Already, targets of Ti, SiC, UO_2/C, MgO, CaO and LaC_2 have been investigated. Ion beams of Xe (A = 115 - 140), Kr (A = 89 - 93), Ar (A = 33 - 46) and Ne (A = 17 - 25) have been observed. Furthermore, the observation of short-lived gamma rays at A = 26 & 27 suggest that a detailed study of the previously uncharacterized ^{26}Ne and ^{27}Ne is possible. A preliminary determination of the ionization efficiency for Ne gives a very good value of 30%. Recently, a yield of ~ 10^4 nuclei/sec/μA was observed for 119 ms ^{8}He from a LaC_2 target; the He ionization efficiency has not yet been determined.

As well as ionizing noble gases, the ECR has high efficiency for most gaseous species. The current goal of the ECR developement program is to produce intense beams of nitrogen. Already, yields of nitrogen (A = 13-17, as N^+, N_2^+, CN^+, NH_3^+ and NO_2^+) have been observed. Other light elements such as carbon (A = 10, 11, 15, as CO^+ and CO_2^+), and chlorine (as Cl^+ and HCl^+) have also been produced. The successful extraction of short lived gaseous species with

high ionization efficiency using the ECR source suggests that TISOL can be used for research that may not be feasible at other ISOL facilities.

While TISOL is still a test facility, a modest research program is starting based on the production of the above mentioned neutron-rich gaseous elements. Furthermore, proposals to use TISOL, with a surface source, for decay studies of proton-rich rubidiums is under consideration.

In order to accommodate the anticipated growth of the research program, an expansion of TISOL is planned for 1990-1991. A reorientation and extension of the electrostatic beamline, to bring the TISOL beam into the TRIUMF proton hall extension, has been approved. The beam transport would include a switching magnet capable of directing the beam to any of three collection stations in a much larger experimental area.

Further planned upgrades include the 4A proton beamline. Currently, beamline 4A is limited to currents below 2 μA; or more realistically below 1 μA. This level is due to excessive neutron fluxes measured above the beamline shielding blocks. If the shielding could be improved, currents as high as 5 μA (or possibly even 10 μA) would be possible. With these higher beam currents, TISOL production yields would be greatly enhanced.

DEC 19/88 RUN: Nb foil target (11.57 g/cm2)
Gamma Efficiency = exp(-0.959*ln(Energy)+0.923) ; Energy in keV.
Back FC4 used, ie: the 45 deg collector allowing alpha counting.

NUCLIDE	T 1/2 (sec)	GAMMA ENERGY (keV)	BRANCH RATIO	COUNTS	RELATIVE ERROR	COUNT TIME (sec)	p+ FLUX (microA)	EFFICIENCY	YIELD (nuc/s /microA)	ERROR/ SIGMA (%)		weighted mean	sigma (%)
Na-25	59.6	389.7	0.1340	730	0.219	200	0.350	8.25E-03	1.5E+04	28.4			
Na-25	59.6	585.1	0.1380	689	0.186	200	0.350	5.59E-03	2.1E+04	26.5			
Na-25	59.6	974.8	0.1400	318	0.177	200	0.350	3.42E-03	1.5E+04	26.5			
Na-25	59.6	1611.8	0.0950	120	0.179	200	0.350	2.11E-03	1.4E+04	27.3			
---									---				
Na-25 average									1.6E+04	16.0	avg	1.6E+04	13.7
Na-26	1.07	1808.6	0.9900	67	0.270	300	0.345	1.89E-03	3.5E+02	34.1			
K-37	1.23	2796.0	0.0180	8	0.638	200	0.350	1.25E-03	5.1E+03	67.4			
K-38g	458.4	2168.0	0.9990	4680	0.017	200	0.345	1.59E-03	3.1E+05	21.3			
K-42	44496	1524.6	0.1830	19	0.795	400	0.345	2.23E-03	1.1E+05	82.1			
K-44	1327.8	1157.0	0.5820	276	0.186	300	0.345	2.90E-03	2.1E+04	27.4			
K-44	1327.8	2150.8	0.2280	85	0.226	300	0.345	1.60E-03	3.0E+04	31.0			
---									---				
K-44 average									2.6E+04	17.5	avg	2.4E+04	20.8
K-45	1068	174.3	0.7530	509	0.743	400	0.345	1.78E-02	2.3E+03	76.2			
K-45	1068	1705.6	0.5330	91	0.268	400	0.345	2.00E-03	5.2E+03	33.9			
K-45	1068	2353.6	0.1430	17	0.665	400	0.345	1.47E-03	4.9E+03	69.9			
---									---				
K-45 average									4.1E+03	31.4	avg	3.9E+03	30.1
K-46	108	1346.0	1.0000	49	0.448	200	0.345	2.51E-03	6.5E+02	49.2			
K-47	17.5	585.7	0.8500	390	0.2994	200	0.375	5.58E-03	1.3E+03	35.3			
K-47	17.5	2013.1	1.0000	20	0.4759	200	0.375	1.71E-03	1.8E+02	52.0			
---									---				
K-47 average									7.2E+02	75.1	avg	2.2E+02	40.6
Rb-75 A	21.4	178.9	1.0000	1151	0.0800	200	0.360	1.74E-02	1.1E+03	18.5			
Rb-76	37	346.1	0.0620	2938	0.0416	300	0.330	9.24E-03	6.3E+04	18.3			
Rb-76	37	354.9	0.1000	4360	0.0304	300	0.330	9.02E-03	5.9E+04	18.2			
Rb-76	37	424.2	0.4800	17684	0.0101	300	0.330	7.60E-03	5.9E+04	18.3			
Rb-76	37	454.0	0.0260	944	0.1136	300	0.330	7.12E-03	6.3E+04	21.6			
Rb-76	37	612.0	0.0150	446	0.1321	300	0.330	5.35E-03	6.8E+04	23.0			
Rb-76	37	767.9	0.0180	320	0.2211	300	0.330	4.30E-03	5.1E+04	29.3			
Rb-76	37	799.9	0.0350	849	0.0676	300	0.330	4.14E-03	7.2E+04	20.5			
Rb-76	37	885.0	0.0440	894	0.0676	300	0.330	3.76E-03	6.6E+04	20.7			
Rb-76	37	919.1	0.0360	757	0.1070	300	0.330	3.62E-03	7.1E+04	22.3			
Rb-76	37	974.0	0.0210	364	0.1506	300	0.330	3.43E-03	6.2E+04	24.8			
Rb-76	37	1219.0	0.0230	438	0.1470	300	0.330	2.76E-03	8.5E+04	24.9			
---									---				
Rb-76 aver ge									6.5E+04	12.8	avg	6.4E+04	6.5
Rb-77	222	66.5	0.5900	11245	0.0360	60	0.355	4.50E-02	2.3E+05	16.9	ign		
Rb-77	222	149.9	0.0470	2948	0.0730	60	0.355	2.06E-02	1.6E+06	19.1			
Rb-77	222	178.8	0.2400	16934	0.0231	60	0.355	1.74E-02	2.2E+06	18.1			
Rb-77	222	254.4	0.0260	1429	0.1146	60	0.355	1.24E-02	2.4E+06	21.7			

Rb-77	222	393.3	0.1100	3923	0.0316	60	0.355	8.18E-03	2.3E+06	19.4		
Rb-77	222	433.0	0.0100	268	0.3258	60	0.355	7.46E-03	1.9E+06	37.9		
Rb-77	222	469.0	0.0120	500	0.1753	60	0.355	6.91E-03	3.2E+06	26.2		
Rb-77	222	545.2	0.0120	310	0.1674	60	0.355	5.98E-03	2.3E+06	25.9		
Rb-77	222	608.5	0.0270	767	0.0817	60	0.355	5.38E-03	2.8E+06	21.5		
Rb-77	222	626.7	0.0330	835	0.0780	60	0.355	5.23E-03	2.6E+06	21.4		
Rb-77	222	647.9	0.0280	751	0.0729	60	0.355	5.07E-03	2.8E+06	21.3		
Rb-77	222	666.9	0.0140	316	0.2164	60	0.355	4.93E-03	2.4E+06	29.5		
Rb-77	222	779.8	0.0110	314	0.3289	60	0.355	4.24E-03	3.6E+06	38.7		
Rb-77	222	805.6	0.0260	413	0.0906	60	0.355	4.11E-03	2.1E+06	22.3		
Rb-77	222	834.1	0.0020	85	0.3867	60	0.355	3.98E-03	5.7E+06	43.7		
Rb-77	222	860.0	0.0065	104	0.3212	60	0.355	3.86E-03	2.2E+06	38.1		
Rb-77	222	910.2	0.0065	95	0.3252	60	0.355	3.66E-03	2.1E+06	38.5		
Rb-77	222	958.7	0.0180	276	0.1263	60	0.355	3.48E-03	2.3E+06	24.2		
Rb-77	222	970.8	0.0280	441	0.0846	60	0.355	3.44E-03	2.4E+06	22.4		
Rb-77	222	988.3	0.0400	298	0.1284	60	0.355	3.38E-03	1.2E+06	24.4		
Rb-77	222	1012.4	0.0110	128	0.2419	60	0.355	3.30E-03	1.9E+06	31.9		
Rb-77	222	1037.4	0.0130	192	0.1971	60	0.355	3.23E-03	2.4E+06	28.7		
Rb-77	222	1067.8	0.0075	101	0.3084	60	0.355	3.14E-03	2.3E+06	37.2		
Rb-77	222	1153.8	0.0110	132	0.2365	60	0.355	2.91E-03	2.2E+06	31.6		
Rb-77	222	1606.0	0.0042	41	0.4359	60	0.355	2.12E-03	2.5E+06	48.6		
Rb-77	222	2508.0	0.0013	13	0.7240	60	0.355	1.38E-03	3.9E+06	75.8		
---									---			
Rb-77 average									2.5E+06	33.5	avg 2.1E+06	5.4
Sr-77	9	146.9	1.0000	2948	0.0730	60	0.355	2.10E-02	8.4E+03	18.4		
Rb-83	7447680	520.4	0.4610	279	0.4338	200	0.380	6.25E-03	1.4E+08	47.2		
Sr-83g	116640	381.5	0.1730	1053	0.2273	200	0.380	8.42E-03	1.6E+07	29.0		
Sr-83g	116640	418.4	0.0457	181	0.6921	200	0.380	7.70E-03	1.1E+07	71.6		
Sr-83g	116640	762.7	0.2970	711	0.1329	200	0.380	4.33E-03	1.2E+07	23.4		
---									---			
Sr-83g average									1.3E+07	15.2	avg 1.3E+07	17.8
Sr-83m	4.95	259.3	0.8750	3722	0.0701	200	0.380	1.22E-02	4.8E+03	18.7		
Sr-85g	6E+08	868.1	0.0001	57	1.02	200	0.380	3.83E-03	1.3E+13	103.9		
Sr-85m	4059.6	151.2	0.1280	10304	0.0445	200	0.380	2.04E-02	3.1E+06	17.1		
Sr-85m	4059.6	231.9	0.8440	54222	0.0121	200	0.380	1.36E-02	3.7E+06	17.3		
---									---			
Sr-85m average									3.4E+06	3.5	avg 3.3E+06	12.2
Rb-86m	63.6	556.1	0.9810	1382	0.105	30	0.355	5.86E-03	1.5E+05	24.9		
Sr-87m	10080	388.4	0.8180	514	0.331	300	0.355	8.27E-03	7.0E+04	37.7		
Rb-88	1068	1836.0	0.2210	41	0.375	200	0.380	1.87E-03	2.1E+04	42.9		
Rb-88(89)	1068	898.0	0.1450	163	0.463	300	0.380	3.70E-03	2.9E+04	50.2		
Rb-88(89)	1068	1836.0	0.2210	132	0.176	300	0.380	1.87E-03	3.1E+04	27.3		
Rb-88(89)	1068	2677.9	0.0202	16	0.576	300	0.380	1.30E-03	5.9E+04	61.6		
---									---			
Rb-88 average (from A-99 spectrum)									3.9E+04	34.2	avg 3.4E+04	20.5

NUCLIDE	T 1/2 (sec)	GAMMA ENERGY (KeV)	BRANCH RATIO	COUNTS	RELATIVE ERROR	COUNT TIME (sec)	p+ FLUX (microA)	EFFICIENCY	COLLECT TIME (sec)	T2 (sec)	YIELD (nuc/s /microA)	ERROR (%)	weighted mean	sigma (%)
Rb-78m A	345.6	341.3	0.0152	498	0.251	60	0.330	9.37E-03	10	35	9.9E+06	31.6		
Rb-78m A	345.6	725.1	0.0620	902	0.084	60	0.330	4.55E-03	10	35	9.1E+06	22.1		
Rb-78m A	345.6	753.4	0.0392	552	0.097	60	0.330	4.38E-03	10	35	9.1E+06	22.7		
Rb-78m A	345.6	848.6	0.0066	90	0.621	60	0.330	3.91E-03	10	35	9.9E+06	65.5		
Rb-78m A	345.6	1199.3	0.0723	704	0.067	60	0.330	2.81E-03	10	35	9.8E+06	22.3		
Rb-78m A	345.6	1232.4	0.0133	146	0.305	60	0.330	2.73E-03	10	35	1.1E+07	37.2		
Rb-78m A	345.6	1265.6	0.0125	88	0.342	60	0.330	2.67E-03	10	35	7.5E+06	40.3		
Rb-78m A	345.6	1270.2	0.0135	97	0.313	60	0.330	2.66E-03	10	35	7.7E+06	37.9		
Rb-78m A	345.6	1375.6	0.0122	77	0.399	60	0.330	2.46E-03	10	35	7.3E+06	45.3		
Rb-78m A	345.6	1529.8	0.0177	135	0.238	60	0.330	2.22E-03	10	35	9.7E+06	32.2		
Rb-78m A	345.6	1630.3	0.0488	326	0.119	60	0.330	2.09E-03	10	35	9.1E+06	24.9		
Rb-78m A	345.6	1644.6	0.0710	475	0.077	60	0.330	2.07E-03	10	35	9.2E+06	23.2		
Rb-78m A	345.6	1796.2	0.0134	106	0.309	60	0.330	1.91E-03	10	35	1.2E+07	38.0		
Rb-78m A	345.6	1952.9	0.0172	105	0.330	60	0.330	1.76E-03	10	35	9.9E+06	39.7		
Rb-78m A	345.6	2013.2	0.0325	220	0.182	60	0.330	1.71E-03	10	35	1.1E+07	28.7		
Rb-78m A	345.6	2222.5	0.0093	90	0.296	60	0.330	1.55E-03	10	35	1.8E+07	37.1		
Rb-78m A	345.6	2626.9	0.0280	113	0.207	60	0.330	1.32E-03	10	35	8.7E+06	30.7		
Rb-78m A	345.6	3270.3	0.0066	34	0.386	60	0.330	1.07E-03	10	35	1.4E+07	45.0		
Rb-78m A	345.6	3319.5	0.0292	95	0.149	60	0.330	1.06E-03	10	35	8.7E+06	27.5		
Rb-78m B	345.6	725.1	0.0620	523	0.104	60	0.330	4.55E-03	10	335	9.6E+06	22.9		
Rb-78m B	345.6	753.4	0.0392	319	0.133	60	0.330	4.38E-03	10	335	9.6E+06	24.4		
Rb-78m B	345.6	848.6	0.0066	41	0.956	60	0.330	3.91E-03	10	335	8.2E+06	97.8		
Rb-78m B	345.6	1199.3	0.0723	369	0.098	60	0.330	2.81E-03	10	335	9.4E+06	23.4		
Rb-78m B	345.6	1232.4	0.0133	60	0.393	60	0.330	2.73E-03	10	335	8.5E+06	44.7		
Rb-78m B	345.6	1529.8	0.0177	47	0.414	60	0.330	2.22E-03	10	335	6.2E+06	46.8		
Rb-78m B	345.6	1630.3	0.0488	194	0.210	60	0.330	2.09E-03	10	335	9.9E+06	30.3		
Rb-78m B	345.6	1644.6	0.0710	284	0.103	60	0.330	2.07E-03	10	335	1.0E+07	24.2		
Rb-78m B	345.6	1796.2	0.0134	35	0.517	60	0.330	1.91E-03	10	335	7.1E+06	56.2		
Rb-78m B	345.6	1952.9	0.0172	53	0.353	60	0.330	1.76E-03	10	335	9.1E+06	41.7		
Rb-78m B	345.6	2013.2	0.0325	104	0.275	60	0.330	1.71E-03	10	335	9.7E+06	35.3		
Rb-78m B	345.6	2222.5	0.0093	51	0.392	60	0.330	1.55E-03	10	335	1.8E+07	45.1		
Rb-78m B	345.6	2626.9	0.0280	69	0.216	60	0.330	1.32E-03	10	335	9.6E+06	31.3		
Rb-78m B	345.6	3270.3	0.0066	15	0.536	60	0.330	1.07E-03	10	335	1.1E+07	58.3		
Rb-78m B	345.6	3319.5	0.0292	43	0.307	60	0.330	1.06E-03	10	335	7.2E+06	38.4		
Rb-78m C	345.6	725.1	0.0620	983	0.065	200	0.330	4.55E-03	10	515	8.9E+06	20.3		
Rb-78m C	345.6	753.4	0.0392	687	0.114	200	0.330	4.38E-03	10	515	1.0E+07	22.4		
Rb-78m C	345.6	848.6	0.0066	206	0.283	200	0.330	3.91E-03	10	515	2.0E+07	34.4		
Rb-78m C	345.6	1199.3	0.0723	724	0.083	200	0.330	2.81E-03	10	515	9.1E+06	21.8		
Rb-78m C	345.6	1232.4	0.0133	173	0.290	200	0.330	2.73E-03	10	515	1.2E+07	35.4		
Rb-78m C	345.6	1529.8	0.0177	162	0.264	200	0.330	2.22E-03	10	515	1.1E+07	33.5		
Rb-78m C	345.6	1630.3	0.0488	440	0.111	200	0.330	2.09E-03	10	515	1.1E+07	23.6		
Rb-78m C	345.6	1644.6	0.0710	604	0.075	200	0.330	2.07E-03	10	515	1.0E+07	22.1		
Rb-78m C	345.6	1796.2	0.0134	82	0.387	200	0.330	1.91E-03	10	515	8.2E+06	44.0		
Rb-78m C	345.6	1952.9	0.0172	115	0.250	200	0.330	1.76E-03	10	515	9.7E+06	32.7		

Rb-78m	C	345.6	2013.2	0.0325	220	0.215	200	0.330	1.71E-03	10	515	1.0E+07	30.1			
Rb-78m	C	345.6	2222.5	0.0093	105	0.320	200	0.330	1.55E-03	10	515	1.9E+07	38.5			
Rb-78m	C	345.6	2626.9	0.0280	135	0.202	200	0.330	1.32E-03	10	515	9.3E+06	29.6			
Rb-78m	C	345.6	3319.5	0.0292	96	0.183	200	0.330	1.06E-03	10	515	7.9E+06	28.7			
Rb-78m	D	345.6	725.1	0.0620	302	0.131	200	0.330	4.55E-03	10	995	7.2E+06	23.3			
Rb-78m	D	345.6	753.4	0.0392	239	0.168	200	0.330	4.38E-03	10	995	9.3E+06	25.6			
Rb-78m	D	345.6	1199.3	0.0723	334	0.182	200	0.330	2.81E-03	10	995	1.1E+07	27.2			
Rb-78m	D	345.6	1232.4	0.0133	54	0.427	200	0.330	2.73E-03	10	995	9.9E+06	47.3			
Rb-78m	D	345.6	1529.8	0.0177	56	0.483	200	0.330	2.22E-03	10	995	9.5E+06	52.5			
Rb-78m	D	345.6	1630.3	0.0488	142	0.207	200	0.330	2.09E-03	10	995	9.3E+06	29.3			
Rb-78m	D	345.6	1644.6	0.0710	236	0.139	200	0.330	2.07E-03	10	995	1.1E+07	25.0			
Rb-78m	D	345.6	1952.9	0.0172	64	0.419	200	0.330	1.76E-03	10	995	1.4E+07	46.9			
Rb-78m	D	345.6	2013.2	0.0325	103	0.288	200	0.330	1.71E-03	10	995	1.2E+07	35.7			
Rb-78m	D	345.6	2222.5	0.0093	59	0.352	200	0.330	1.55E-03	10	995	2.7E+07	41.2			
Rb-78m	D	345.6	2626.9	0.0280	52	0.346	200	0.330	1.32E-03	10	995	9.4E+06	40.8			
Rb-78m	D	345.6	3319.5	0.0292	37	0.314	200	0.330	1.06E-03	10	995	8.0E+06	38.4			
Rb-78m	average							ERR				1.0E+07	33.3	avg 9.4E+06	4.0	
Rb-78g	A	1059.6	562.1	0.1140	420	0.214	60	0.330	5.80E-03	10	35	5.1E+06	29.4			
Rb-78g	A	1059.6	1821.7	0.0110	38	0.647	60	0.330	1.88E-03	10	35	1.5E+07	68.4			
Rb-78g	A	1059.6	2137.4	0.0174	24	0.667	60	0.330	1.61E-03	10	35	6.9E+06	70.4			
Rb-78g	A	1059.6	2420.3	0.0456	29	0.734	60	0.330	1.43E-03	10	35	3.6E+06	76.8			
Rb-78g	A	1059.6	2514.1	0.0331	41	0.524	60	0.330	1.38E-03	10	35	7.2E+06	57.1			
Rb-78g	A	1059.6	2982.4	0.0519	42	0.378	60	0.330	1.17E-03	10	35	5.5E+06	44.3			
Rb-78g	A	1059.6	3084.0	0.0469	27	0.386	60	0.330	1.13E-03	10	35	4.1E+06	45.0			
Rb-78g	A	1059.6	3438.2	0.1080	77	0.208	60	0.330	1.02E-03	10	35	5.6E+06	31.2			
Rb-78g	B	1059.6	562.1	0.1140	344	0.155	60	0.330	5.80E-03	10	335	5.1E+06	25.4			
Rb-78g	B	1059.6	2420.3	0.0456	31	0.588	60	0.330	1.43E-03	10	335	4.6E+06	63.0			
Rb-78g	B	1059.6	2514.1	0.0331	35	0.497	60	0.330	1.38E-03	10	335	7.5E+06	54.6			
Rb-78g	B	1059.6	2982.4	0.0519	29	0.412	60	0.330	1.17E-03	10	335	4.7E+06	47.2			
Rb-78g	B	1059.6	3084.0	0.0469	26	0.553	60	0.330	1.13E-03	10	335	4.8E+06	60.0			
Rb-78g	B	1059.6	3438.2	0.1080	60	0.198	60	0.330	1.02E-03	10	335	5.3E+06	30.5			
Rb-78g	C	1059.6	562.1	0.1140	1048	0.101	200	0.330	5.80E-03	10	515	5.5E+06	21.4			
Rb-78g	C	1059.6	2420.3	0.0456	85	0.280	200	0.330	1.43E-03	10	515	4.5E+06	35.3			
Rb-78g	C	1059.6	2514.1	0.0331	86	0.286	200	0.330	1.38E-03	10	515	6.5E+06	35.8			
Rb-78g	C	1059.6	2982.4	0.0519	73	0.278	200	0.330	1.17E-03	10	515	4.1E+06	35.4			
Rb-78g	C	1059.6	3084.0	0.0469	103	0.239	200	0.330	1.13E-03	10	515	6.7E+06	32.5			
Rb-78g	C	1059.6	3438.2	0.1080	255	0.092	200	0.330	1.02E-03	10	515	8.0E+06	24.0			
Rb-78g	D	1059.6	562.1	0.1140	767	0.082	200	0.330	5.80E-03	10	995	5.5E+06	20.5			
Rb-78g	D	1059.6	2420.3	0.0456	70	0.280	200	0.330	1.43E-03	10	995	5.1E+06	35.3			
Rb-78g	D	1059.6	2514.1	0.0331	59	0.351	200	0.330	1.38E-03	10	995	6.1E+06	41.2			
Rb-78g	D	1059.6	2982.4	0.0519	62	0.296	200	0.330	1.17E-03	10	995	4.8E+06	36.9			
Rb-78g	D	1059.6	3084.0	0.0469	64	0.267	200	0.330	1.13E-03	10	995	5.7E+06	34.6			
Rb-78g	D	1059.6	3438.2	0.1080	186	0.130	200	0.330	1.02E-03	10	995	8.0E+06	25.7			
Rb-78g	average											6.0E+06	35.3	avg 5.4E+06	6.8	
Rb-79	A	1374	129.7	0.1090	35662	0.021	200	0.350	2.37E-02	10	18	4.1E+07	16.5			
Rb-79	A	1374	154.8	0.0804	32192	0.015	200	0.350	2.00E-02	10	18	6.0E+07	16.7			
Rb-79	A	1374	160.8	0.0874	36459	0.019	200	0.350	1.93E-02	10	18	6.5E+07	16.8			
Rb-79	A	1374	182.8	0.1950	83374	0.019	200	0.350	1.70E-02	10	18	7.5E+07	17.0			

Rb-79	A	1374	286.2	0.0092	2315	0.180	200	0.350	1.11E-02	10	18	6.8E+07	25.2
Rb-79	A	1374	350.6	0.0736	17560	0.018	200	0.350	9.13E-03	10	18	7.8E+07	18.1
Rb-79	A	1374	397.6	0.0616	12299	0.028	200	0.350	8.09E-03	10	18	7.4E+07	18.4
Rb-79	A	1374	401.8	0.0082	1723	0.180	200	0.350	8.01E-03	10	18	7.9E+07	25.6
Rb-79	A	1374	461.5	0.0125	2139	0.106	200	0.350	7.01E-03	10	18	7.3E+07	21.3
Rb-79	A	1374	486.8	0.0023	322	0.491	200	0.350	6.66E-03	10	18	6.3E+07	52.5
Rb-79	A	1374	524.2	0.0022	390	0.473	200	0.350	6.21E-03	10	18	6.6E+07	50.8
Rb-79	A	1374	533.3	0.0132	1976	0.078	200	0.350	6.11E-03	10	18	7.3E+07	20.2
Rb-79	A	1374	558.3	0.0026	460	0.299	200	0.350	5.84E-03	10	18	9.1E+07	35.3
Rb-79	A	1374	603.2	0.0068	1020	0.124	200	0.350	5.42E-03	10	18	8.3E+07	22.6
Rb-79	A	1374	622.2	0.0893	12693	0.026	200	0.350	5.27E-03	10	18	8.1E+07	19.2
Rb-79	A	1374	688.1	0.2350	31178	0.018	200	0.350	4.78E-03	10	18	8.3E+07	19.2
Rb-79	A	1374	774.1	0.0061	702	0.152	200	0.350	4.27E-03	10	18	8.1E+07	24.6
Rb-79	A	1374	786.0	0.0016	462	0.227	200	0.350	4.21E-03	10	18	2.1E+08	29.9
Rb-79	A	1374	915.8	0.0061	616	0.113	200	0.350	3.63E-03	10	18	8.3E+07	22.7
Rb-79	A	1374	921.6	0.0045	415	0.123	200	0.350	3.61E-03	10	18	7.6E+07	23.2
Rb-79	A	1374	934.9	0.0033	288	0.167	200	0.350	3.56E-03	10	18	7.3E+07	25.8
Rb-79	A	1374	941.2	0.0018	147	0.266	200	0.350	3.54E-03	10	18	6.9E+07	33.1
Rb-79	A	1374	1137.7	0.0012	91	0.376	200	0.350	2.95E-03	10	18	7.7E+07	42.6
Rb-79	A	1374	1184.1	0.0025	218	0.209	200	0.350	2.84E-03	10	18	9.2E+07	29.0
Rb-79	A	1374	1298.3	0.0013	98	0.472	200	0.350	2.60E-03	10	18	8.7E+07	51.4
Rb-79	A	1374	1480.3	0.0017	45	0.428	200	0.350	2.29E-03	10	18	3.5E+07	47.5
Rb-79	A	1374	1504.7	0.0010	64	0.403	200	0.350	2.26E-03	10	18	8.5E+07	45.3
Rb-79	B	1374	129.7	0.1090	41877	0.017	200	0.350	2.37E-02	10	333	5.7E+07	16.4
Rb-79	B	1374	154.8	0.0804	29503	0.020	200	0.350	2.00E-02	10	333	6.4E+07	16.7
Rb-79	B	1374	160.8	0.0674	32930	0.022	200	0.350	1.93E-02	10	333	6.9E+07	16.8
Rb-79	B	1374	182.8	0.1950	72589	0.027	200	0.350	1.70E-02	10	333	7.7E+07	17.1
Rb-79	B	1374	286.2	0.0092	2290	0.251	200	0.350	1.11E-02	10	333	7.9E+07	30.7
Rb-79	B	1374	350.6	0.0736	15235	0.024	200	0.350	9.13E-03	10	333	8.0E+07	18.1
Rb-79	B	1374	397.6	0.0616	10844	0.019	200	0.350	8.09E-03	10	333	7.6E+07	18.3
Rb-79	B	1374	401.8	0.0082	1492	0.128	200	0.350	8.01E-03	10	333	8.0E+07	22.2
Rb-79	B	1374	461.5	0.0125	1847	0.097	200	0.350	7.01E-03	10	333	7.4E+07	20.9
Rb-79	B	1374	486.8	0.0023	302	0.413	200	0.350	6.66E-03	10	333	6.9E+07	45.3
Rb-79	B	1374	524.2	0.0022	256	0.472	200	0.350	6.21E-03	10	333	6.6E+07	50.8
Rb-79	B	1374	533.3	0.0132	1943	0.074	200	0.350	6.11E-03	10	333	8.5E+07	20.1
Rb-79	B	1374	558.3	0.0026	338	0.301	200	0.350	5.84E-03	10	333	7.8E+07	35.5
Rb-79	B	1374	603.2	0.0068	910	0.166	200	0.350	5.42E-03	10	333	8.7E+07	25.1
Rb-79	B	1374	622.2	0.0893	10951	0.022	200	0.350	5.27E-03	10	333	8.2E+07	19.1
Rb-79	B	1374	688.1	0.2350	26674	0.019	200	0.350	4.78E-03	10	333	8.3E+07	19.3
Rb-79	B	1374	774.1	0.0061	572	0.122	200	0.350	4.27E-03	10	333	7.7E+07	22.9
Rb-79	B	1374	786.0	0.0016	330	0.267	200	0.350	4.21E-03	10	333	1.7E+08	33.0
Rb-79	B	1374	915.8	0.0061	607	0.079	200	0.350	3.63E-03	10	333	9.6E+07	21.2
Rb-79	B	1374	921.6	0.0045	417	0.109	200	0.350	3.61E-03	10	333	9.0E+07	22.5
Rb-79	B	1374	934.9	0.0033	342	0.152	200	0.350	3.56E-03	10	333	1.0E+08	24.9
Rb-79	B	1374	941.2	0.0018	188	0.246	200	0.350	3.54E-03	10	333	1.0E+08	31.6
Rb-79	B	1374	1137.7	0.0012	91	0.339	200	0.350	2.95E-03	10	333	9.0E+07	39.4
Rb-79	B	1374	1184.1	0.0025	174	0.160	200	0.350	2.84E-03	10	333	8.6E+07	25.7
Rb-79	B	1374	1298.3	0.0013	99	0.472	200	0.350	2.60E-03	10	333	1.0E+08	51.4
Rb-79	B	1374	1480.3	0.0017	98	0.235	200	0.350	2.29E-03	10	333	8.8E+07	31.2
Rb-79	B	1374	1504.7	0.0010	48	0.496	200	0.350	2.26E-03	10	333	7.5E+07	53.7

Rb-79 average											8.2E+07	30.1	avg 7.0E+07	3.3
Sr-79 A	138	135.0	0.1200	632	0.644	200	0.350	2.28E-02	10	18	1.1E+05	66.4		
Sr-79 A	138	324.1	0.1500	367	0.661	200	0.350	9.84E-03	10	18	1.2E+05	68.4		
Sr-79 B	138	324.1	0.1500	420	0.580	200	0.350	9.84E-03	10	333	6.7E+05	60.6		
Sr-79 average											3.0E+05	86.8	avg 1.2E+05	43.5
Rb-80 A	34	616.7	0.2600	6389	0.020	30	0.365	5.31E-03	14	68	6.8E+06	22.6		
Rb-80 A	34	639.6	0.0160	289	0.128	30	0.365	5.13E-03	14	68	5.2E+06	25.9		
Rb-80 A	34	704.3	0.0180	360	0.105	30	0.365	4.68E-03	14	68	6.3E+06	25.0		
Rb-80 A	34	1257.1	0.0060	49	0.259	30	0.365	2.68E-03	14	68	4.5E+06	35.0		
Rb-80 B	34	616.7	0.2600	528	0.053	30	0.365	5.31E-03	14	248	2.2E+07	23.1		
Rb-80 B	34	639.6	0.0160	37	0.325	30	0.365	5.13E-03	14	248	2.6E+07	39.5		
Rb-80 B	34	704.3	0.0180	35	0.400	30	0.365	4.68E-03	14	248	2.4E+07	46.0		
Rb-80 B	34	1257.1	0.0060	7	0.918	30	0.365	2.68E-03	14	248	2.5E+07	94.7		
Rb-80 average											1.5E+07	62.6	avg 6.2E+06	11.8
Sr-80 A	6372	175.0	0.1030	251	0.608	30	0.365	1.78E-02	14	248	8.5E+06	64.8		
Sr-80 A	6372	235.9	0.0420	131	0.654	30	0.365	1.33E-02	14	248	1.4E+07	69.3		
Sr-80 A	6372	414.1	0.0303	70	0.797	30	0.365	7.78E-03	14	248	1.8E+07	83.0		
Sr-80 average											1.4E+07	29.5	avg 1.1E+07	43.2
Rb-81g	16488	190.4	0.6433	105252	0.014	200	0.365	1.64E-02	10	24	3.3E+08	17.0		
Rb-81g	16488	244.3	0.0031	518	0.355	200	0.365	1.29E-02	10	24	4.2E+08	39.5		
Rb-81g	16488	357.7	0.0076	749	0.140	200	0.365	8.95E-03	10	24	3.6E+08	22.8		
Rb-81g	16488	389.0	0.0046	511	0.232	200	0.365	8.26E-03	10	24	4.4E+08	29.4		
Rb-81g	16488	446.3	0.2330	17501	0.010	200	0.365	7.24E-03	10	24	3.4E+08	18.4		
Rb-81g	16488	456.9	0.0303	2117	0.043	200	0.365	7.08E-03	10	24	3.2E+08	18.9		
Rb-81g	16488	476.8	0.0053	423	0.216	200	0.365	6.80E-03	10	24	3.8E+08	28.4		
Rb-81g	16488	499.4	0.0012	433	0.254	200	0.365	6.50E-03	10	24	1.8E+09	31.5		
Rb-81g	16488	537.6	0.0242	1450	0.061	200	0.365	6.06E-03	10	24	3.2E+08	19.7		
Rb-81g	16488	548.9	0.0047	687	0.082	200	0.365	5.94E-03	10	24	8.1E+08	20.5		
Rb-81g	16488	568.9	0.0058	333	0.138	200	0.365	5.74E-03	10	24	3.3E+08	23.3		
Rb-81g	16488	729.1	0.0030	253	0.147	200	0.365	4.52E-03	10	24	6.1E+08	24.2		
Rb-81g	16488	803.5	0.0084	451	0.099	200	0.365	4.12E-03	10	24	4.3E+08	21.8		
Rb-81g	16488	834.8	0.0082	357	0.113	200	0.365	3.97E-03	10	24	3.6E+08	22.5		
Rb-81g	16488	977.1	0.0057	223	0.169	200	0.365	3.42E-03	10	24	3.8E+08	26.1		
Rb-81g	16488	1041.1	0.0054	209	0.148	200	0.365	3.21E-03	10	24	3.9E+08	24.8		
Rb-81g average											5.0E+08	71.8	avg 3.7E+08	5.9
Rb-81M	1818	86.2	0.0472	34129	0.018	200	0.365	3.51E-02	10	24	7.8E+07	15.8		
Rb-81M	1818	643.6	0.0010	363	0.133	200	0.365	5.10E-03	10	24	2.7E+08	23.2		
Rb-81M average											1.7E+08	55.1	avg 8.5E+07	14.2
Sr-81	1332	147.8	0.3140	3468	0.051	200	0.365	2.09E-02	10	24	1.5E+06	17.3		
Sr-81	1332	153.5	0.3520	3480	0.062	200	0.365	2.02E-02	10	24	1.4E+06	17.7		
Sr-81	1332	443.3	0.1820	803	0.155	200	0.365	7.29E-03	10	24	1.7E+06	24.0		
Sr-81	1332	523.7	0.0139	62	0.636	200	0.365	6.21E-03	10	24	2.0E+06	66.3		
Sr-81	1332	574.7	0.0702	221	0.198	200	0.365	5.68E-03	10	24	1.6E+06	27.3		
Sr-81	1332	711.9	0.0144	34	0.878	200	0.365	4.63E-03	10	24	1.4E+06	89.9		

Sr-81	1332	720.8	0.0368	109	0.342	200	0.365	4.57E-03	10	24	1.8E+06	39.3			
Sr-81	1332	909.0	0.0283	64	0.392	200	0.365	3.66E-03	10	24	1.7E+06	43.8			
Sr-81	1332	938.5	0.0307	54	0.430	200	0.365	3.55E-03	10	24	1.4E+06	47.3			
---											---				
Sr-81 average											1.6E+06	12.8	avg 1.5E+06	9.3	
Rb-82g	76.2	1395.0	0.0051	108	0.202	200	0.365	2.43E-03	5	25	7.0E+06	28.8			
Rb-82m	23292	182.9	0.0205	887	0.225	200	0.365	1.70E-02	5	25	2.3E+08	28.1			
Rb-82m	23292	221.5	0.0206	635	0.270	200	0.365	1.42E-02	5	25	2.0E+08	32.0			
Rb-82m	23292	454.9	0.0085	868	0.174	200	0.365	7.11E-03	5	25	1.3E+09	25.3			
Rb-82m	23292	554.3	0.6280	9778	0.020	200	0.365	5.88E-03	5	25	2.4E+08	18.9			
Rb-82m	23292	606.3	0.0184	415	0.235	200	0.365	5.40E-03	5	25	3.9E+08	30.2			
Rb-82m	23292	619.1	0.3920	5613	0.028	200	0.365	5.29E-03	5	25	2.5E+08	19.2			
Rb-82m	23292	827.8	0.2150	2454	0.036	200	0.365	4.00E-03	5	25	2.6E+08	19.8			
Rb-82m	23292	1007.6	0.0737	704	0.087	200	0.365	3.32E-03	5	25	2.7E+08	21.7			
Rb-82m	23292	1044.0	0.3220	3026	0.026	200	0.365	3.21E-03	5	25	2.7E+08	20.1			
Rb-82m	23292	1081.4	0.0138	136	0.277	200	0.365	3.10E-03	5	25	2.9E+08	34.2			
Rb-82m	23292	1100.0	0.0033	104	0.406	200	0.365	3.05E-03	5	25	9.6E+08	45.3			
Rb-82m	23292	1191.3	0.0025	65	0.431	200	0.365	2.82E-03	5	25	8.5E+08	47.5			
Rb-82m	23292	1317.5	0.2400	1858	0.035	200	0.365	2.56E-03	5	25	2.8E+08	20.6			
Rb-82m	23292	1475.8	0.1550	1080	0.036	200	0.365	2.30E-03	5	25	2.8E+08	20.9			
Rb-82m	23292	1650.3	0.0114	84	0.214	200	0.365	2.07E-03	5	25	3.3E+08	29.8			
Rb-82m	23292	1779.6	0.0026	55	0.276	200	0.365	1.92E-03	5	25	1.0E+09	34.6			
---											---				
Rb-82m average											4.7E+08	73.9	avg 2.7E+08	6.5	
Rb-84m	1215.6	215.6	0.2640	49878	0.017	200	0.355	1.46E-02	23	223	1.7E+07	17.2			
Rb-84m	1215.6	248.0	0.5900	39087	0.011	200	0.355	1.27E-02	23	223	6.7E+06	17.4			
Rb-84m	1215.6	463.6	0.3540	13618	0.014	200	0.355	6.98E-03	23	223	7.1E+06	18.5			
---											---				
Rb-84m average											1.0E+07	45.5	avg 7.7E+06	10.8	

REFERENCES

(Al68) T.Alväger & J.Uhler, in Progress in Nuclear Techniques and Instrumentation (F.J.M.Farley, ed.) Vol. 3, J.Wiley & Sons, New York (1968) p.161

(An76) G.Andersson, M.Ashgar, A.Emsallem, E.Hagberg & B.Jonson, Phys. Lett. B61 234 (1976)

(An78) G.Andersson, M.Ashgar, A.Emsallem, E.Hagberg, B. Jonson & P.Tidemand-Petersson, Phys. Scr. 18 165 (1978)

(As78) M.Ashgar, A.Emsallem, E.Hagberg, B.Jonson & P. Tidemand-Petersson, Z. Phys. A288 45 (1978)

(Az79) R.E.Azuma, L.C.Carraz, P.G.Hansen, B.Jonson, K.L.Kratz, S.Mattsson, G.Nyman, H.Ohm, H.L.Ravn, A.Schroder & W.Zeigart, Phys. Rev. Lett. 43 1652 (1979)

(Az80) R.E.Azuma, T.Bjornstad, H.A.Gustafsson, P.G.Hansen, B.Jonson, S.Mattsson, G.Nyman, A.M.Poskanzer, & H.L.Ravn, Phys. Lett. 96B 31 (1980)

(Be75) G.J.Beyer, E.Herrmann, A.Piotrowski, V.I.Raiko, & H.Tyrroff, Nucl. Instr. Meth. 96 437 (1971)

(Bj81) T.Bjørnstad, L.C.Carraz, H.A.Gustafsson, J.Heinemeier, B.Jonson, O.C.Jonsson, V.Lindfors, S.Mattsson & H.L.Ravn, Nucl. Instr. Meth. 186 391 (1981)

(Br73) K.L.Brown, F.Rothacker, D.C.Carey & Ch.Iselin, CERN Report 73-16 (Nov 1973)

(Ca78) L.C.Carraz, I.R.Haldorsen, H.L.Ravn, M.Skarestad & L.Westgaard, Nucl. Instr. Meth. 148 217 (1978)

(Ca79) L.C.Carraz, S.Sundell, H.L.Ravn, M.Skarestad & L.Westgaard, Nucl. Instr. Meth. 158 69 (1979)

(Ca82) M.D.Cable, J.Honkanen, R.F.Parry, H.M.Thierens, J.M.Wouters, Z.Y.Zhou & J.Cerny, Phys. Rev. C26 1778 (1982)

(Ca83) M.D.Cable, J.Honkanen, R.F.Parry, S.H.Zhou, Z.Y. Zhou & J.Cerny, Phys. Lett. 123B 25 (1983)

(Da90) J.M.D'Auria, M.Dombsky, L.Buchmann & J.S.Vincent, Nucl. Instr. Meth. A288 354 (1990)

(De80) C.Detraz, M.Epherre, D.Guillemaud, P.G.Hansen, B. Jonson, R.Klapisch, M.Langevin, S.Mattsson, F. Naulin, G.Nyman, A.M.Paskanzer, H.L.Ravn, M.de Saint-Simon, K.Takahashi, C.Thibault & F.Touchard, Phys. Lett. 94B 307 (1980)

(Eb79) P.Eberhardt, M.H.A.Jungck, L.O.Mercer & F.Mederer, Astophys. J. Lett. 234 L169 (1979)

(Em81) Proc. of the 10th Inter. EMIS Conf., Zinal, Switz. (1980) (E.Kugler, H.L.Ravn & S.Sundell, ed.) Nucl. Instr. Meth., 186 1 (1981)

(Em87) Proc. of the 11th Inter. EMIS Conf., Los Alamos N.M., (1986) (W.Talbert ed.) Nucl. Instr. Meth., B26 1 (1987)

(Em87) Proc. of the 11th Inter. EMIS Conf.,

(Ep79) M.Epherre, G.Audi, C.Thibault, R.Klapisch, G.Huber, F.Touchard & H.Wollnik, Phys. Rev. C19 1504 (1979)

(Fa83) T.Faestermann, A.Gillitzer, K.Hartel, P.Kienle & E. Nolte, Proc. Int. Conf. on Nucl. Physics, Vol 1 (Compositori Tipografia, Bologna) p. B263

(Fa84) T.Faestermann, A.Gillitzer, K.Hartel, P.Kienle & E. Nolte, Phys. Lett. 137B 23 (1984)

(Fo74) S.Foster, L.Root & C.Kost, TRIUMF (1974) unpublished.

(Ha79) P.G.Hansen, Ann. Rev. Nucl. Part. Sci., 29 69 (1979)

(Ha81) A.K.Haynes, TRIUMF (1981) unpublished.

(Ha85a) E.Hagberg, J.Hardy, G.Audi & H.Schmeing, Proc. of the Accelerated Radioactive Beams Workshop, Parksville, B.C. (1985), (L.Buchmann & J.M.D'Auria eds.) TRIUMF TRI-85-1

(Ha85b) J.H.Hamilton, P.G.Hansen & E.F.Zganjars, Rep. Prog. Phys. 48 631 (1985)

(Ho82) S.Hofmann, W.Reisdorf, G.Münzenberg, F.P.Hessberger, J.R.H.Schneider & P.Armbruster, Z. Phys. A304 111 (1982)

(Ho84) P.Hoff, O.C.Jonsson, E.Kugler & H.L.Ravn, Nucl. Instr. Meth. 221 313 (1984)

(Kl82) O.Klepper, T.Batsch, S.Hofmann, R.Kirschner, W. Kurcewicz, W.Reisdorf, E.Roeckl, D.Schardt & G. Nyman, Z. Phys. A305 125 (1982)

(Ko84) C.Kost & P.Reeve, TRIUMF Report TRI-DN-82-28 (Oct. 1984)

(Jo73) P.G.Johnson, A.Bolson & C.M.Henderson, Nucl. Instr. Meth. 106 83 (1973)

(Jo81) B.Jonson, H.A.Gustafsson, P.G.Hansen, P.Hoff, P.O.Larsson, S.Mattsson, G.Nyman, H.L.Ravn & D.Schardt, Proc. 4th Int. Conf. Nuclei Far From Stability, Helsingo/r, (1981): CERN Geneva 1981, 81-09 p.265

(Ke87) R.Keitel & L.Wilson, IEEE Trans. Nucl. Sci. NS-34 (4) 849 (1987)

(Ke90) R.Keitel & D.Harrison, Nucl. Instr. Meth. (in press)

(Ki78) R.Kirchner & A.Piotrowski, Nucl. Instr. Meth. 153 291 (1978)

(Ki81) R.Kirchner, Nucl. Instr. Meth. 186 275 (1981)

(Kl65) R.Klapisch & R.Bernas, Nucl. Instr. Meth. 38 291 (1965)

(Kl69) R.Klapisch, Ann. Rev. Nucl. Sci., 19 33 (1969)

(Ko51a) O.Kofoed-Hansen & K.O.Neilsen, Phys. Rev. 82 96 (1951)

(La25) I.Langmuir & K.H.Kingdon, Proc. Roy. Soc. London, 107 61 (1925)

(La75) A.Latuszynski & V.I.Raiko, Nucl. Instr. Meth. 125 61 (1975)

(La84) M.Langevin, C.Detraz, M.Epherre, D.Guillemaud, B.Jonson, C.Thibault & the ISOLDE Collaboration, Phys. Lett. 146B 176 (1984)

(Le78) Table of Isotopes, 7th ed. (C.M.Lederer & V.S.Shirley, eds.) J.Wiley & Sons, New York (1978)

(Ni84) J.M.Nitschke, Proc. of the TRIUMF-ISOL Workshop, Mont Gabriel Que., (1984) (J.Crawford, J.M.D'Auria & J.Lee, eds.) TRIUMF TRI-84-1

(Op22) Optomux is a trademark of OPTO22, Huntington Beach, CA, USA

(Ox87) K.Oxorn, J.E.Crawford, H.Dautet, J.K.P.Lee, R.B.Moore & L.Nikkinen, Nucl. Instr. Meth. B26 143 (1987)

(Pr85) P.B.Price, J.D.Stevenson, S.W.Barwick & H.L.Ravn, Phys. Rev. Lett. 54 297 (1985)

(Pu81) J.C.Putaux, J.Obert, L.Kotfila, B.Roussiere, J.Sauvage-Letessier, C.F.Liang, A.Peghaire, P.Paris, J.Giroux & the ISOCELE collaboration, Nucl. Instr. Meth. 186 321 (1981)

(Ra79) H.L.Ravn, Phys. Rep., 54 203 (1979)

(Ra87) H.L.Ravn, T.Bjørnstad, P.Hoff, O.C.Jonsson, E.Kugler, S.Sundell, B.Vosicki & the ISOLDE collaboration, Nucl. Instr. Meth. B26 183 (1987)

(Ra89) H.L.Ravn & B.W.Allardyce, in Treatise on Heavy Ion Science (D.A.Bromley, ed.) Vol. 8, Plenum Press, New York (1989) p.363-439

(Re81) PL.Reeder, R.L.Warner, T.R.Yeh, R.E.Chrien, R.L.Gill, M.Schmid, H.I.Liou & M.L.Stelts, Phys. Rev. Lett. 47 483, (1981)

(Re83) U.Reus & W.Westmeir, Atom. Data & Nucl. Data Tables 29 194 (1983)

(Re84) P.L.Reeder & R.A.Warner, Nucl. Sci. Eng. 87 181 (1984)

(Ri75) B.W.Ridley, D.E.Prull, R.J.Peterson, E.W.Stoub & R.A.Emigh, Nucl. Instr. Meth. 130 79 (1975)

(Ro84) H.J.Rose & G.A.Jones, Nature 307 245 (1984)

(Ru66) G.Rudstam, Z.Naturforsch. 219 1027 (1966)

(Sa20) M.N.Saha, Phil. Mag. 40 472 (1920)

(Sa21) M.N.Saha, Z. Phys. 6 40 (1921)

(Sa23) M.N.Saha, Phil. Mag. 46 534 (1923)

(Se68) G.T.Seaborg, Ann. Rev. Nucl. Sci. 18 53 (1968)

(Si73a) R.Silberberg & C.H.Tsao, Astrophys. J. Suppl. 25 315 (1973)

(Si73b) R.Silberberg & C.H.Tsao, Astrophys. J. Suppl. 25 335 (1973)

(Si77) R.Silberberg & C.H.Tsao, Astrophys. J. Suppl. 35 129 (1977)

(Si83) R.Silberberg, C.H.Tsao & J.R.Letaw, p321 in Composition & Origin of Cosmic Rays (M.M.Shapiro ed.) D.Reidel, Dortrecht (1983)

(Ta85a) I.Tanihata, H.Hamagaki, O.Hashimoto, S.Nagamiya, Y.Shida, N.Yoshikawa, O.Yamakawa, K.Sugimoto, Y.Kobayashi, D.E.Greiner, N.Takahashi & Y.Nojiri, Phys. Lett. 160B 380 (1985)

(Ta85b) I.Tanihata, H.Hamagaki, O.Hashimoto, Y.Shida, N. Yoshikwaa, K.Sugimoto, O.Yamakawa, Y.Kobayashi & N.Takahashi, Phys. Rev. Lett. 55 2676 (1985)

(Ta89) I.Tanihata, in Treatise on Heavy Ion Science (D.A.Bromley, ed.) Vol. 8, Plenum Press, New York (1989) p.363-439

(Th75) C.Thibault, R.Klapisch, C.Rigaud, A.M.Poskanzer, R.Pprieels, L.Lesard & W.Reisdorf, Phys. Rev., C12 644 (1975)

(To81) F.Touchard, J.Biderman, M.de Saint Simon, C.Thibault, G.Huber, M.Epherre & R.Klapisch, Nucl. Instr. Meth. 186 329 (1981)

(Tr85) The TRIUMF-ISOL Facility, A Proposal for an Intense Radioactive Beams Facility (1985)